Investigating the effects of magnesium on the structure and durability of radioactive waste glasses by solid-state NMR

Rui Guo

Selwyn College

This dissertation is submitted for the degree of

Doctor of Philosophy

February 2019

Declaration

This dissertation is the result of my own work and includes nothing which is the outcome of work done in collaboration except as declared in the Preface and specified in the text. It is not substantially the same as any that I have submitted, or, is being concurrently submitted for a degree or diploma or other qualification at the University of Cambridge or any other University or similar institution except as declared in the Preface and specified in the text. I further state that no substantial part of my dissertation has already been submitted, or, is being concurrently submitted for any such degree, diploma or other qualification at the University of Cambridge or any other University or similar institution except as declared in the Preface and specified in the text. It does not exceed the prescribed word limit for the relevant Degree Committee.

Summary

Investigating the effects of magnesium on the structure and durability of radioactive waste glasses by solid-state NMR

Rui Guo

In the current GDF concepts, the main mechanism by which the release of immobilised radionuclides from the vitrified waste forms in long-term would be dissolution of the host glasses, when in contact with groundwater. The presence of Mg in glasses as opposed to Ca, as the alkaline-earth constituent, has been found to deteriorate their dissolution resistance. The UK Magnox waste glasses contain Mg (~4.5 oxide wt%) that entrains from the fuel cladding material used in the Magnox reactors. A series of 6/7-component simplified counterparts of the full-component non-radioactive surrogate MW25 glass were used to separately study the effects of Mg on glass structures, initial and long-term dissolution behaviours. Both the pristine and altered structures of the simplified glass(es), especially the Mg endmember (MgEM), were thoroughly characterised, primarily, using multinuclear solid-state NMR techniques to provide atomistic level insights into its structural features and help explain its dissolution.

The proportion of $^{[3]}$B increases as the relative Mg content increases in the simplified glasses. However, this is not due to the competition for the charge compensator Na but its own poorer charge compensating capability relative to Ca. As a minor constituent, La also adopts different structural roles depending in the relative Mg content, which corroborates some Mg being network former. Nevertheless, these structural changes have little impact on the primary dissolution of these glasses. From 1 to 16 week(s), however, the MgEM glass exhibits a much higher degree of dissolution compared with the CaEM glass, with almost an order of magnitude difference at the longest available experimental period. The inferior aqueous durability of Mg-containing glasses lies in the secondary effects, mainly the gel layer formation and precipitation. While XRD could not provide any structural information on these secondary phases, a Mg silicate phase (precipitated) that has a local crystallographic structure resembling that of talc is uncovered by ^{17}O, ^{25}Mg, ^{29}Si and ^{1}H solid-state NMR. Semi-quantitative ^{1}H NMR results are also able to observe other hydrogenated species and their temporal evolution in the altered glass, which in turn shed light upon the intricate glass-water interactions. The precipitation reactions are likely to inhibit the local saturation of Si needed for densification of the hydrolysed glass and hence reduce its protectiveness against further dissolution. NMR calculations based on Ab

initio density function theory serve both as a complementary method and as a benchmark for interpreting complex experimental NMR spectra.

Acknowledgements

Firstly, I would like to thank my supervisor, Prof. Ian Farnan, for introducing me to the fascinating solid-state NMR world. The immense help and wise advice he offered, especially in my difficult times, had been truly educational in both science and life respects. Secondly, I am grateful to Dr. Clive Brigden for his prior work, without which my work presented in this thesis would not be possible. Besides, I need to thank the diverse people in my research group for their continual feedback on my work, inadvertent or otherwise, which quite often had been practically helpful and/or intellectually stimulating. In particular, Tom Goût, who helped me set up my leaching experiments and constantly held interesting discussions with me on glass dissolution, and Giles Rought-Whitta, who frequently and patiently shared his knowledge in computational NMR and crystallography with me. My special gratitude towards Dr. David Halat should also be noted here for him offering me the precious spectrometer time and hardware support in his laboratory at the Department of Chemistry. The spectrometer time granted at the UK 850 MHz solid-state NMR Facility (University of Warwick) was essential for me to obtain the ^{25}Mg NMR results, and is also acknowledged here. Last but not the least, I am extremely grateful to my PhD funding bodies: EPSRC and the Department of Earth Sciences, for awarding me a Cambridge International Scholarship so that my pursuit of a PhD degree at Cambridge became financially viable. The generosity shown by Selwyn College and Cambridge Philosophical Society during my write-up period is also greatly appreciated.

Outside science, I have many people to be thankful to with the following four being the most important. I have been lucky enough to keep receiving my parents' encouragement to pursue what I think matters to me. Their total understanding has more or less given me the freedom to complete my PhD journey. I also would like to thank my good friend Shen Xiang, who, quite often, was happy and keen to share his perspectives on life with me. The sincerity of our friendship indeed inspired me when my self-doubts hit hard. Lastly and most importantly, I must express my highest gratitude to my ex-girlfriend, Yue (Sophie) Zhang, for the unreserved love and support she had been showing to me throughout. Those walks and strolls we took by the Thames River on those sunny weekend days, were the loveliest and most beautiful moments in my times of struggle. Our unforgettable time together will forever be enshrined in my head. I wish her the true happiness she has been longing for and deserves.

Abstract

Radioactive waste glasses containing Mg have been shown to have much poorer (~one order of magnitude) aqueous durability in long-term, compared with those have a similar amount of Ca as the alkaline-earth constituent. This is the case between two non-radioactive research surrogates: MW glasses produced in the UK and SON68 glass produced in France. With the latter being the most widely researched and understood nuclear glass to date, advances in understanding and modelling MW glass dissolution require special account for Mg. Mg-containing clay precipitates observed on glass surface after reaching the residual rate regime have been thought to be the cause. However, precipitation initiated from early stages when the supposedly protective gel layer is forming and growing has not been studied. Solid-state NMR is extensively applied to characterise the altered glass surface in this thesis for its power in providing atomic-level structural insights with amorphous materials being amenable to it. Its quantitative nature also affords extra advantages over other spectroscopic techniques.

Simplified MW25 glass (MgEM) and the series with various degree of Ca substitution were made to separately investigate the effects of Mg, firstly, on the pristine glass structure. The relative fraction of boron in 3- and 4-fold coordination changes as the relative amount of Mg (Ca) content changes in the glass. This is driven by the different structural roles (network forming/modifying) between the two alkaline-earth elements. The representative rare-earth element, La, also adopts different structural roles between MgEM and its counterpart CaEM, accordingly. However, the initial dissolution rates measuring their primary leaching kinetics do not reflect the varying structural features elucidated by ^{11}B, ^{27}Al, ^{23}Na, ^{25}Mg and ^{139}La NMR.

Longer dissolution experiments up to 16 weeks are carried out to measure the extent of leaching with the feedback of secondary effects. The least durable MgEM glass is investigated in detail. Utilisation of ^{25}Mg-enriched MgEM glass as well as ^{17}O-enriched water as the leaching agent facilitates solid-state NMR experiments selectively characterising the alteration layers. Although suffering from low sensitivity, ^{1}H-^{25}Mg and ^{1}H-^{17}O cross-polarisation as well as ^{17}O multiple-quantum magic angle spinning NMR act as the surface probe. Coupled with ^{1}H and ^{29}Si NMR results, the altered glass and precipitates structures and the corresponding implications for glass dissolution kinetics are discussed at length. Aside from experimental results, NMR calculations based on ab initio density functional theory are performed to assist with explaining the complex ^{25}Mg and ^{17}O NMR spectra and hence identifying the precipitates.

Contents

List of Figures

List of Tables

Chapter 1

1. Introduction

Handling of radioactive wastes that arose from operation of civil nuclear power plants and nuclear weapon programs in the past has become a sensitive issue facing many developed nuclear countries. Primarily, a safe and efficient handling strategy for these wastes is essential for reducing the radioactivity-related hazards that they would impose on the environment and human societies. Besides, the future development and promotion of civil nuclear energy capacity hinges upon the demonstration of our ability to address this issue now.

In broad terms, these wastes can be categorised into exempt, low, intermediate and high-level waste (LLW, ILW and HLW) based on their level of activity or hazard with the exact category boundaries being regulated at the national level. While LLWs and ILWs constitute the vast majority of the radioactive waste in volume terms, they contain less than 10% of the total radioactivity. Volumes of HLWs are small in comparison, but are far more hazardous and difficult to handle as they contain more than 90% of the total radioactivity (Ojovan and Lee, 2005). HLWs are those characterised as containing large concentrations of short and long lived radionuclides, fission and activation products hence generating large quantities of heat due to β and γ decay: they need to be properly cooled, contained and isolated in short-term and, as an international consensus, to be disposed of eventually in deep geological disposal facilities (GDF) (IAEA, 2009). Typical HLWs that originate from the operation of various nuclear power plants include spent nuclear fuel (SNF)[*], where it is designated as waste, and aqueous waste generated from re-processing of SNF. In a closed nuclear fuel cycle, re-processing is the chemical process to extract Pu and U from the SNF in order to reutilise the unburnt fissile materials e.g. to manufacture mixed oxide (MOX) fuel. Unlike SNF, which is already in solid form as e.g. UO_2 pellets, the concurrent highly corrosive, toxic and radioactive fluid by-products from re-processing need to be conditioned (solidified) for both interim storage and final disposal.

1.1. Glass as a wasteform

The most common means of re-processing SNF is the so-called PUREX (Plutonium and Uranium Recovery Extraction) process: the stripped (from cladding) SNF pellets are firstly

[*] SNF is not universally regarded as waste as it still contains a significant amount of U and Pu depending on the burn-up, reactor type and lifetime etc. In this regard, the fuel (resource) is being recycled, which leads to a so-called closed nuclear fuel cycle.

dissolved in nitric acid and then followed by liquid-liquid solvent extraction of Pu and U. Consequently, the raffinate is a liquidus HLW containing fission products, minor actinides, alloying elements from the SNF and pipework, organic solvent in the nitric matrix as well as activation products through neutron capture (Cochran and Tsoulfanidis, 1999). Re-processing SNF has been practised in countries including the USA, Russia, Japan, Germany, France and the UK from the operation of different types of gas cooled reactors and light water reactors for more than 4 decades. In almost all cases, the highly radioactive liquid wastes were managed and eventually vitrified (see 1.2) to reduce the volume and highly mobile hazards by incorporating and/or encapsulating the radionuclides into solid glass structures to be immobilised (Ojovan and Lee, 2005). Before final deep geological disposal, these solid wasteforms are typically stored in dry casks in interim storage facilities with active air cooling to allow the dissipation of decay heat from the short-lived fission products such as ^{137}Cs and ^{90}Sr (Grambow, 2006).

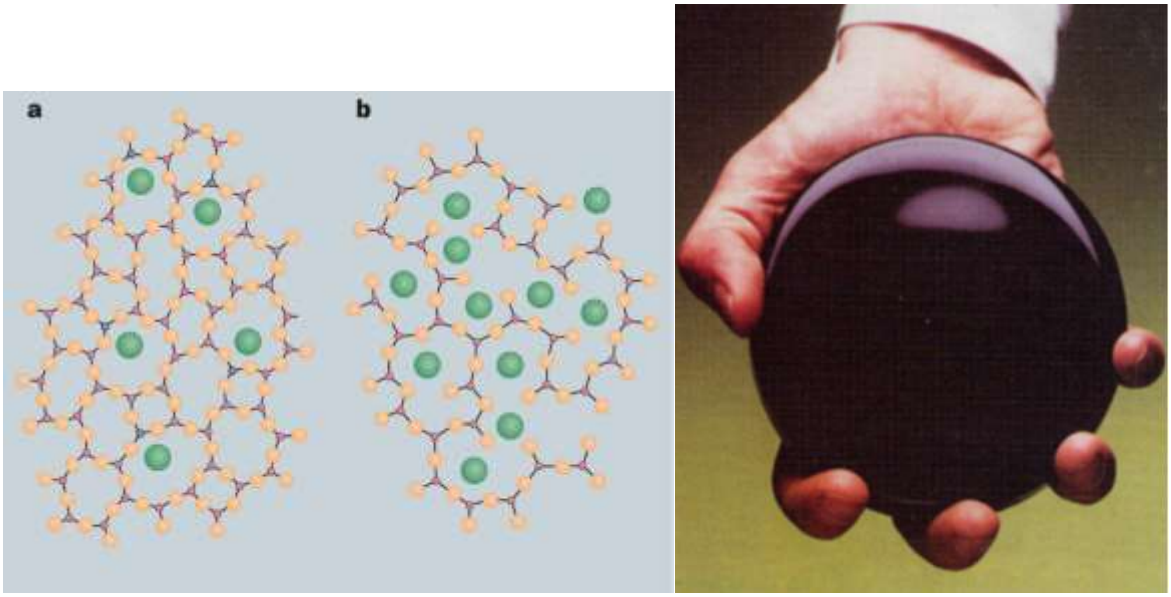

Figure 1-1 Left: a 2D schematic illustration of (a) a borosilicate glass and (b) the corresponding silicate glass without boron (grey). Network modifier (green) charge-compensates over-coordinated boron in structure (a) and associates exclusively with non-bridging oxygens in structure (b) (silicon, purple; oxygen, orange) (adapted from (Farnan, 1997)**); Right: a simulant vitrified borosilicate glass wasteform (adapted from** (Ojovan and Lee, 2005)**).**

The suitability of borosilicate glasses as a wasteform has been widely accepted and adopted by the abovementioned countries except Russia who opted for alumina-phosphate glasses (Gin, Abdelouas, *et al.*, 2013). Figure 1-1 shows a typical alkali-silicate glass microstructure model and a simulant vitrified borosilicate glass product. Compositional and structural variations, for example, Na cations in Figure 1-1 could be other alkalis e.g. Li, K, Cs and alkaline earth such as Ca, Sr and their relative concentrations to Si (B), could alter the glass density, degree of disorder and network connectivity. The adaptability and flexibility in both structure and composition

provide the general advantages of using borosilicate glasses as the wasteform including their waste load flexibility and diversity, good glass forming ability at manageable temperatures, excellent chemical durability as well as thermal and radiation stability (Donald, Metcalfe and Taylor, 1997). However, the timescale involved in radioactive waste glass disposal i.e. up to 10^6 years depending on the exact waste load, means that water ingress and contact with the glass is highly likely. Aqueous glass dissolution would then eventually lead to the release of confined radionuclides.

1.2. Radioactive waste glasses produced in the UK

The research into vitrification of highly radioactive liquids from SNF re-processing in the UK was initiated from the 1950s, following the operation of the first-generation Magnox reactors. Magnox reactors used natural abundance, metallic uranium fuel cladded with a non-oxidising Mg-based alloy. The high moderation efficiency of graphite exempted the need for ^{235}U enrichment while fission heat was exchanged and transferred by CO_2 gas as the coolant. Vitrification of the effluent from re-processing Magnox metallic spent fuel had been carried out since the late 1980s at the Sellafield Waste Vitrification Plant (WVP) using the French second-generation two-stage AVH (Atelier Vitrification La Hague) process, where calcination of the effluent and final melting with the glass frit were separated (see Figure 1-2). Based on the composition and waste loading (see later), the typical melting temperature was ~1050℃ in order to achieve a balance between ease of manufacture, glass homogeneity, production rate (viscosity-related) and volatilisation of both radioactive and non-radioactive constituents (Ojovan and Lee, 2005; Harrison, 2014). The majority of glass produced so far was targeted at 25 wt% waste loading and there were more than 2700 canisters (more than 2200 tonnes[†]) as of 2015 waiting to be finally disposed of in GDFs (Schofield *et al.*, 2016).

The utilisation of the non-oxidising Mg alloy as the fuel cladding material led to the incorporation of Mg in the final vitrified wasteform. For the full-component inactive simulant Magnox waste glass vitrified at the WVP with 25 wt% waste loading (herein referred to as MW25), the final Mg content is ~4.5 MgO wt% and the full composition is listed in Table 1-1. Compared with the most widely studied French SON68 glass the full-component inactive simulant to R7T7 glass, which was also vitrified using the AVT processes, there is a presence of an approximately equivalent amount of Mg in place of Ca (Table 1-1). Glass compositions has been regarded as the first-order parameter in determining the respective dissolution

[†] This also includes other glasses produced at the WVP from re-processing SNF from operation of Advanced Gas-cooled Reactors and Pressurised Water Reactors (PWR) in the UK.

mechanisms and the corresponding aqueous durability (Frugier *et al.*, 2005; Grambow, 2006; Gin *et al.*, 2012; Mike T. Harrison, 2014). Mg, in particular, has attracted extra attention because of the observed faster long-term dissolution and extensive secondary precipitation reactions for Mg-containing glasses as well as when Mg is present in the leaching agent. The former effect is also relevant to some French first-generation AVM (Atelier Vitrification Marcoule) glasses and there is ~100 mg/L Mg in the Callovo-Oxfordian clay groundwater at the proposed French GDF site (Curti *et al.*, 2006; Thien *et al.*, 2010, 2012; Jollivet *et al.*, 2012; Fleury *et al.*, 2013; Gin *et al.*, 2013).

Table 1-1 Oxide wt% and cation mol% of full-component MW25 and SON68 glasses (Scales, 2011; Jollivet, Gin and Schumacher, 2012).

Oxide wt%	MW25	SON68	Cation mol%	MW25	SON68
CaO	-	4.07	Ca	-	3.68
MgO	4.50	-	Mg	5.27	-
Al_2O_3	4.30	5.00	Al	4.00	4.97
B_2O_3	16.70	14.14	B	22.64	20.58
BaO	0.52	0.62	Ba	0.16	0.20
CeO_2	1.10	0.97	Ce	0.30	0.28
Cr_2O_3	0.64	0.53	Cr	0.40	0.35
Cs_2O	1.00	1.12	Cs	0.33	0.40
Fe_2O_3	3.00	3.03	Fe	1.77	1.92
La_2O_3	0.56	0.93	La	0.16	0.29
Li_2O	4.00	1.99	Li	12.63	6.75
MoO_3	1.40	1.78	Mo	0.46	0.63
MnO_2	-	0.39	Mn	-	0.23
Na_2O	8.50	10.22	Na	12.94	16.71
Nd_2O_3	1.60	2.04	Nd	0.45	0.61
NiO	0.48	0.43	Ni	0.30	0.29

P_2O_5	-	0.29	P	-	0.21
Pr_2O_3	0.52	0.46	Pr	0.15	0.14
RuO_2	0.49	-	Ru	0.17	-
SiO_2	47.10	45.85	Si	36.99	38.67
Sm_2O_3	0.36	-	Sm	0.10	-
SrO	0.29	0.35	Sr	0.13	0.17
TeO_2	0.17	0.23	Te	0.05	0.07
Y_2O_3	0.17	0.20	Y	0.07	0.09
ZrO_2	1.40	2.75	Zr	0.54	1.13
Ag_2O	-	0.03	Ag	-	0.01
ZnO	-	2.53	Zn	-	1.58
CdO	-	0.03	Cd	-	0.01
SnO	-	0.02	Sn	-	0.01

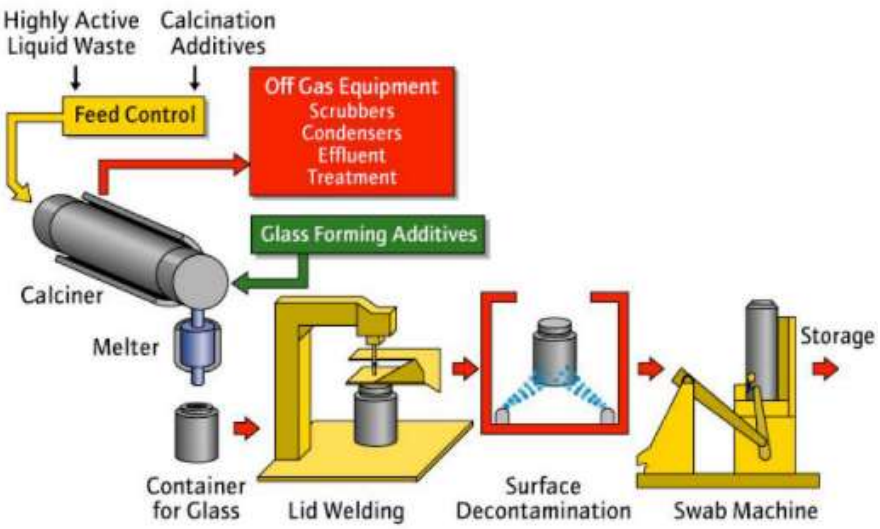

Figure 1-2 AVH-based vitrification and packing flowchart at Sellafield WVP (adapted from (Harrison, 2014a)**).**

In the UK, despite no specific site being selected to date for the development of the GDF for SNF and HLW glasses, a generic single disposal, multilayer concept based on the Swedish KBS-3 design has been established for performance assessment (Nirex, 2005). In such a concept as illustrated in Figure 1-3, the HLW steel canisters (Figure 1-2) would be sealed in an outer copper canister with cast iron as another layer of insert in between. Further, a buffer layer

of bentonite clay would be filled between the copper canisters and the host rock. Typically, the GDF in the current design concept would be located 300~1000 m deep in the ground depending on the rock type and hydrological environments (Change, 2014; NDA, 2016).

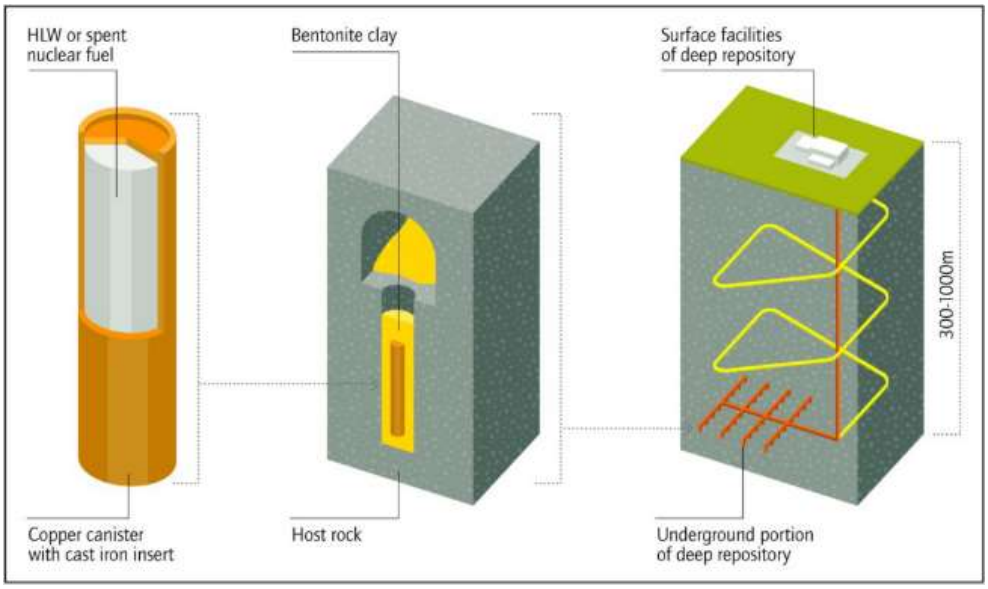

Figure 1-3 GDF concept for UK SNF and HLW glasses based on the KBS-3 design.

1.3. Durable but dissolvable glasses

Despite being more chemically durable than most other materials, glass would still dissolve when exposed to aqueous environments and the rate at which this happens depends on a series of factors including pH, temperature, *SA*/*V* (surface area-to-volume ratio) etc. (Scholze, 1988; Grambow, 2006; Conradt, 2008). Outside the nuclear waste community, aqueous dissolution of glass has been a well-known phenomenon and has a wide range of scientific and engineering implications. For example, the dissolution of basaltic glass in the oceans is crucial for the carbon cycle on earth (Kump, Brantley and Arthur, 2013) and it is important to understand the degradation of bioglass in the human body to improve product quality and compatibility (Filgueiras, La Torre and Hench, 1993).

As a natural occurrence, volcanic glasses such as basaltic and rhyolite glasses have endured in nature for geological timescales and provided scientific evidence for validating the concept of safe disposal of glass wasteforms (Dickin, 1981; Lutze *et al.*, 1985). However, the very high SiO_2 contents in these glasses are not necessarily representative of most nuclear waste glasses produced to date. The nuclear waste glasses are designed to immobilise the radioactive fission products, activation products and minor actinides. Disintegration or destruction of these glasses is highly undesirable and would lead to re-mobilisation and, hence, release of radionuclides into the environment. Since deep geological disposal has been accepted widely for the management

of HLWs in the long-term, interactions between the glass wasteform and geological environments must be investigated. The only conceivable mechanism by which the radionuclides would escape from the glass wasteform after the other natural and engineering barriers being breached is glass-groundwater interaction, which would lead to alteration and dissolution of the glass structures. In order to demonstrate the safety case for GDF design and assessment in terms of HLW glasses, it is crucial that the glass-groundwater interaction mechanisms are understood and could be controlled by engineering means.

1.3.1. Glass dissolution theories

In the past 30~40 years, there has been an enormous amount of research being carried out in an effort to understand both the short-term and long-term nuclear waste glass dissolution, particularly borosilicate glasses, including kinetics as well as mechanisms across the whole glass composition and aqueous environment spectrum. The international nuclear waste glass community has reached some consensus in terms of the kinetic stages involved in glass dissolution even though the associated exact mechanisms are still open to discussion. There are numerous reviews on the state-of-the-art status in terms of our understanding of nuclear waste glass dissolution including Van Iseghem *et al.* (2006); Grambow (2006); Vienna *et al.* (2013); Gin *et al.* (2013, 2016); Gin, Jollivet, Fournier, Berthon, *et al.* (2015a). The following discussions are based on but not limited to these works.

When in contact with dilute aqueous solutions, ion-exchange reactions tend to take place between proton species in water (H^+, H_3O^+) and mobile and reactive alkali cations (Li^+, Na^+) at borosilicate glass surface by means of inter-diffusion. The only way by which this process would take place is for water and proton species to be present at the reactive sites i.e. hydration of the glass network. The initial hydration and ion-exchange processes can be described by Equation 1-1 below and the exact alkali to proton ratio depends on the partial molar volumes of the released alkali cations and the charge balancing need fulfilled by protons (Ferrand, Abdelouas and Grambow, 2006).

$$\text{Si-O-(Li, Na etc.)} + H_3O^+ \rightarrow \text{Si-O-H} + (Li^+, Na^+ \text{ etc.}) + H_2O$$

Equation 1-1

Inter-diffusion reactions would drive the solution pH to increase, hence promoting hydrolysis reactions where bridging oxygen bonds are broken and subsequent release of orthosilicic acid (H_4SiO_4) and other glass network formers (Al, B etc.) that are connected to Si by bridging oxygens. The competition between these two processes would lead to a dynamic steady-state

that defines the initial rate r_0 as shown in Figure 1-4, where the dissolution is mechanistically congruent. Furthermore, because of the nature of these two processes, water diffusion and dissociation are regarded as the rate-limiting steps for this early stage of glass dissolution. It is worth noting that B concentration in solution, as a network former, has been widely accepted as the glass dissolution identifier because of its structural role, high solubility (in aqueous environments relevant to nuclear waste glass dissolution) and extreme low retention in the altered glass structure (Scheetz *et al.*, 1984; Gin, Jollivet, Fournier, Angeli, *et al.*, 2015).

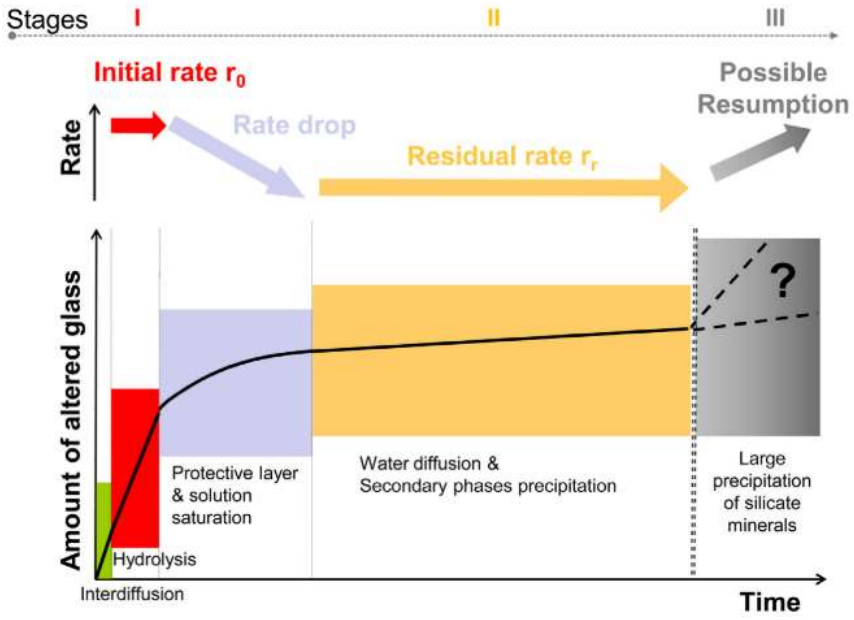

Figure 1-4 Typical stages of nuclear waste glass dissolution and the related potential rate-limiting mechanisms. The duration of each stage depends on glass composition and leaching conditions (adapted from (Gin, Abdelouas, *et al.*, 2013)**).**

The following rate drop has historically caused extensive controversies regarding the fundamental mechanisms of a reduction in dissolution rate. This is important to understand because it serves as the intermediate between the fast r_0 and the 3~4 order of magnitude lower residual rate r_r, the latter of which are thought to control the long-term dissolution behaviour over GDF design lifetime. With the build-up of Si concentration in the solution, the reactions below in Equation 1-2 start to dominate the hydrolysis reaction and apparent Si saturation status would lead to the re-construction of the hydrated and/or disrupted glass network as well as condensation and resorption of the previously dissolved orthosilicic acid phase. This separate newly formed phase is called the gel layer in most of the literature. After the demonstration that fresh SON68 glass dissolves in the apparent Si saturated prior leaching solution as fast as the initial rate r_0, the affinity related argument for the rate drop was affirmed to be minor compared with the protectiveness provided by the gel layer (Vernaz *et al.*, 2001). However, it was later

proved that both factors should be considered in developing a complete and valid glass dissolution model (Van Iseghem *et al.*, 2009).

$$\mathrm{Si{-}OH + HO{-}X \rightarrow Si{-}O{-}X + H_2O\ (X = Si, Al\ etc.)}$$

$$\mathrm{H_4SiO_4 + Si\text{-}OH \rightarrow Si\text{-}O\text{-}Si(OH)_3 + H_2O}$$

$$\mathrm{H_4SiO_4 + H_4SiO_4 \rightarrow 2SiO_2 + 4H_2O}$$

Equation 1-2

The porous, hydrated and amorphous gel layer, upon densification, acts as a passivating barrier between the reaction front at the pristine glass boundary and the leaching solution to limit the transport of both dissolved glass constituents outwards and water inwards. This has been observed for SON68 and its representative simplified 6-component counterpart ISG (International Simple Glass[‡]) and other similar glasses which are readily leached in neutral conditions typically at 90 ℃ (Cailleteau *et al.*, 2008; Gin, Ryan, *et al.*, 2013; Gin, Jollivet, Fournier, Angeli, *et al.*, 2015; Collin *et al.*, 2018). On the other hand, the structural and chemical role of the gel layer is also important in the sense that it provides resorption and precipitation sites for radionuclides and their compounds with low solubility to retain them on the glass surface.

1.3.2. Interfacial dissolution-precipitation mechanism

A completely different mechanism for nuclear waste glass dissolution was proposed mainly by the geochemical community as an extension from silicate mineral weathering and dissolution, in contrast with the well-established theories outlined in 1.3.1, called interfacial dissolution-precipitation (IDP). In short, based on the nanometre scale chemical gradient of mobile elements such as B and Na at the mineral/glass-solution interface observed using techniques with extremely high spatial and mass resolution, Hellmann *et al.* (2012) postulated that congruent dissolution instead of inter-diffusion is the dominant process upon silicate mineral-water interaction. Specifically, as schematically illustrated in Figure 1-5, precipitation reactions taking place within a thin layer of interfacial water film (a few nanometres) are spatially and temporally coupled with the congruent dissolution of the underlying mineral. Consequently, the precipitates, mainly silica, would grow inwards to form a precipitated layer while the thin film of water persists to drive such reactions. The driving force for precipitation to take place is the

[‡] Production of ISG was initiated in the nuclear waste glass community to provide a benchmark material for inter-laboratory research. It was formulated according to the composition of SON68 with the major cation ratios between them kept the same. 50 kg of ISG was produced in one batch to provide glass homogeneity and product consistency (Gin, Abdelouas, *et al.*, 2013).

solubility difference between the parent phase and silica, and the close coupling between dissolution and precipitation only requires the interfacial fluid layer to be super-saturated (Hellmann *et al.*, 2012; Daval *et al.*, 2013; Putnis, 2014; Ruiz-Agudo *et al.*, 2016). Geisler *et al.* (2010, 2015), Hellmann *et al.* (2015) extended the argument and characterisation techniques to the synthetic and nuclear waste glasses domain to advocate the IDP mechanism to be considered in glass dissolution models. However, by using ^{29}Si isotope as a solution tracer and H profiling on leached SON68 and ISG, Gin, Jollivet, Fournier, Angeli, *et al.* (2015) and Gin *et al.* (2016) rebuffed the idea that the alteration layer is formed by IDP, at least not completely, and stressed the importance of experimental setup to distinguish far from and close to saturation leaching conditions.

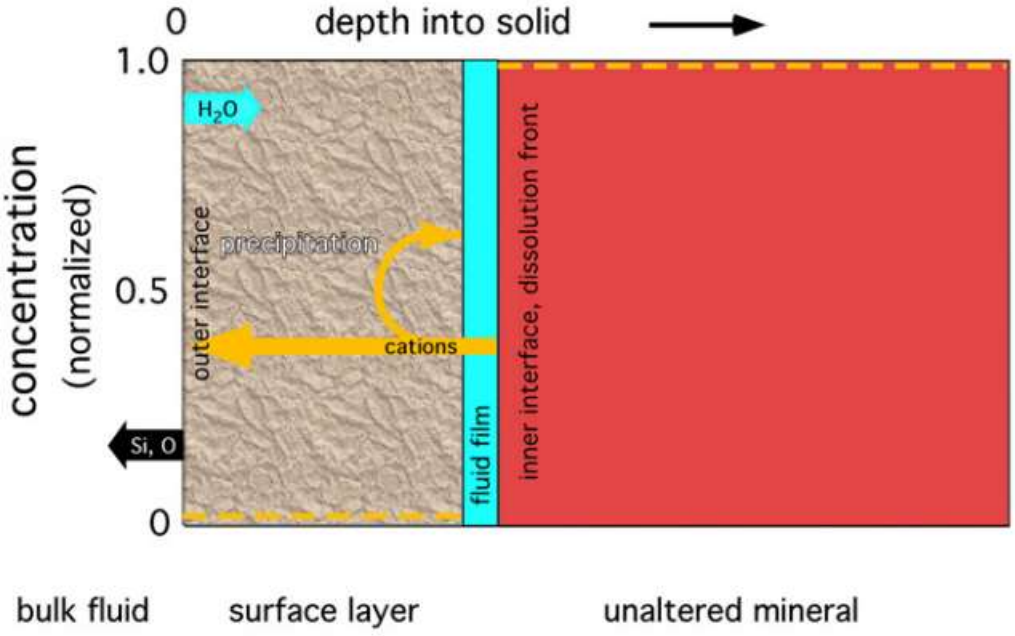

Figure 1-5 An illustration of the different layers at the silicate mineral-water interfaces according to the IDP model (adapted from (Hellmann *et al.*, 2012)**).**

In either glass dissolution scenario, the gradual rate drop is, at least partly, induced by the secondary alteration layer(s) formation, which grows and limits the transport of aqueous species to the reaction front. In other words, whilst these two mechanisms differ from each other significantly, the differences are more in a thermodynamics sense instead of kinetics. Nevertheless, it is essential to identify the chemical nature of the altered glass surface to make progress with understanding the mechanism and/or to assist with modelling.

1.4. The effect of Mg on glass dissolution

1.4.1. Literature survey

There were only a few studies before the launch of the RWM (Radioactive Waste Management) programme focusing on the dissolution of MW glasses. The programme launched in 2011 for the HLW stream was aimed at systematically investigating the MW glasses produced at the Sellafield WVP, to gather more data and better understand the glass and groundwater compositional (and pH) effects on their dissolution behaviour. More importantly, how does it compare between MW glasses and the widely-studied SON68 glass (Schofield *et al.*, 2016)? One of the key objectives was to investigate the effect of Mg on surface alteration, which is the only pathway for the glass dissolution to initiate and proceed. Among the sparse published work, at least two studies have shown that MW glasses that contain Mg (and nominally no calcium (Ca)) have significantly poorer aqueous durability compared with Ca-based glasses such as SON68. This was embodied by approximately one order of magnitude higher boron concentration in the leachate for the former in both short-term (tens of days) and long-term (up to 12.2 years) (see Figure 1-6) (Abraitis *et al.*, 2000; Curti *et al.*, 2006). It was also shown that after 12.2 years of dissolution in water at 90℃, secondary clay formed on the MW glass surface has a composition between Mg-rich saponites, hectorites and montmorillonites. In another earlier study by Zwicky *et al.* (1988), Mg enrichment was observed and a hectorite-like precipitated phase was identified at the outermost 2-6 μm of the 'corrosion layer' after 185 days leaching of a MW glass at 110℃ with a SA/V of 10 m^{-1}. In both cases, it is unclear at which stage the clay minerals started to form or their structural and/or chemical roles in influencing the dissolution kinetics.

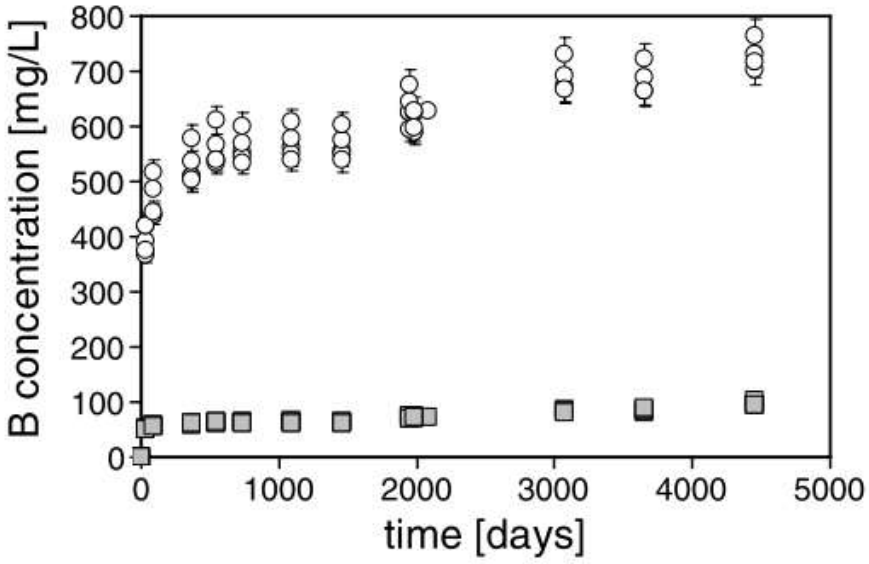

Figure 1-6 B concentration vs leaching time in Curti *et al.* (2006) **where open circles represent the data for a MW glass and filled square for SON68 glass. The leaching experiments were carried out with an initial solution of pure water and a temperature of 90**℃ **(Adapted from** (Curti *et al.*, 2006)**).**

Gin, Ribet and Couillard (2001) and Lemmens (2001) both observed that the densification of the gel layer, which makes it protective, depends on the Si concentration and the precipitation and/or presence of phyllosilicate (clay) phases. The concurrently precipitated phyllosilicates are not protective in nature and could consume the Si needed for the local saturation to occur, which is required for the gel layer to densify. In this regard, Mg present in the leachant has been found to catalyse the formation of Mg-containing clay minerals by co-precipitating with the dissolved silica at solid-solution interface under conditions relevant to nuclear waste glass disposal: neutral to slightly alkaline pH (7~10) and moderate temperatures (60~90℃) (Harder, 1972; Debure *et al.*, 2012; Jollivet *et al.*, 2012; Fleury *et al.*, 2013). This process, however, should be distinguished from the extensive secondary precipitation that leads to the potential resumption of dissolution after the residual rate regime being reached and sustained (see Figure 1-4). Instead, it is concerned with the rate drop regime where the protective gel layer is supposed to form.

1.4.2. Previous work

In 2012, under the commercial contract with Amec Foster Wheeler to investigate the effect of magnesium on the chemical durability of UK ILW and HLW glasses, the RWM programme included making a series of 6/7-component simplified glasses to set up a separate effect study of Mg on dissolution of the full-component MW25 glass. The work was published in the form of a technical report (Brigden and Farnan, 2014). In the 15-month postdoctoral period, the simplified glasses were made according to the composition of MW25 with the sole

compositional variable as Mg/Ca ratio. Static batch leaching experiments using deionised water at 90℃ in closed systems were conducted on the simplified as well as MW25 and SON68 glass powders for different durations. In addition, the MgEM glass was also leached in ^{17}O-enriched water to facilitate ^{17}O NMR experiments. The main findings from the leaching experiments include: 1. The extent of dissolution of Mg-containing glasses is much greater than of Ca-containing glasses from 1 week up to 16 weeks, with Mg endmember (MgEM) glass showing an order of magnitude higher normalised release of B than Ca endmember (CaEM) glass at the end of 16 weeks; 2. Dissolved Mg from Mg-containing glasses re-precipitate onto the glass surface and is incorporated into the alteration products, with the most significant extent observed for MgEM glass. These key findings were consistent with the ^{1}H and ^{17}O[§] NMR signal intensities where significantly more proton and oxygen-17 (primarily from the enriched water) atoms were detected for Mg-containing glasses as a result of dissolution. However, detailed characterisation of the alteration products was not performed.

1.4.3. Scope of the thesis

Predicting the long-term nuclear waste glass dissolution over geological time in the context of GDF ultimately needs to rely on credible performance assessment models. Despite decades of effort and a reasonable consensus on the nuclear waste glass dissolution stages, except for the very short (typically a few hours) initial dissolution, the exact rate limiting mechanisms and their couplings are still not clear (Collin *et al.*, 2018). At least, they are believed to be dependent on factors including glass composition and specific experimental parameters such as leaching temperature, pH and *SA*/*V* etc. One of the difficulties in developing a mechanistic model is the general lack of generic knowledge about the protective gel and precipitate compositions and/or structures even within known glass composition domains (Gin *et al.*, 2016). These secondary phases must be characterised as they appear to control the solution chemistry and limit the transport of aqueous species to the glass surface and release of soluble radionuclides from the glass (Curti *et al.*, 2006; Cailleteau *et al.*, 2008; Gin *et al.*, 2011; Vienna *et al.*, 2013; Gin, Jollivet, Fournier, Angeli, *et al.*, 2015).

The promising results from the abovementioned commercial contracted work created the framework for academic research on the mechanisms of gel formation and its structure, as well as the influence of the nature of precipitates on its protectiveness. In particular, in the context of Mg-containing glass, a detailed characterisation of these altered phases would provide useful

§ ^{17}O-enriched (45%) water was also used for leaching the powders of CaEM and MgEM glasses to facilitate the ^{17}O NMR experiments.

insights into the dissolution of Magnox waste glasses (MW25) as opposed to the well-studied SON68 (Mg-free). Some of this thesis is based upon the methodology and materials originating from the previous work, which is properly quoted/referenced wherever necessary. In order to achieve the abovementioned goals and ambition, the scope of this thesis will mainly include the following aspects: Chapter 2 details the relevant theoretical background and experimental techniques of solid-state NMR, which is the primary investigation method for characterising the pristine glass and altered glass structures. As a supplementary to experiments, the ab initio density functional theory (DFT) electronic structure code CASTEP is also introduced, with its applicability and capability to calculate NMR parameters. In addition, the method of treating and presenting leaching data is briefly outlined. Chapter 3 describes the procedures for sample preparation, leaching experiments setup, solution- and solid-state characterisation methodologies as well as CASTEP NMR calculations. Chapter 4 focuses on the multinuclear NMR characterisation of a series of 6/7-component simplified glasses with Mg/Ca substitution based on the MW25 glass (MgEM) composition. The initial dissolution rates of these glasses are then collectively related to the composition and structural variation. Chapter 5 is largely devoted to explaining and exploring the previous leaching data and to presenting the new leaching data of ^{25}Mg-enriched MgEM glass. Chapter 6 takes up the most space of this thesis as a chapter and is devoted to elucidating the altered glass structure, primarily, by mutually complementary ^{25}Mg, ^{29}Si, ^{1}H and ^{17}O NMR techniques, entailing various 1D and 2D MQMAS pulse sequences. In Chapter 7, the calculated ^{25}Mg and ^{17}O NMR parameters and the corresponding simulated spectra of a few Mg silicates are presented, together with some of the results from Chapter 6 for comparison. Finally, Chapter 8 has concluding remarks, discusses the findings from Chapter 4-7 and outlines the future work prospects.

Chapter 2

2. Theory

2.1. Introduction

The lack of long-range translational order in glasses and other forms of non-crystalline solid materials has imposed difficulties in describing their structures. For the same reason, common laboratory techniques that rely on Bragg diffraction principles are incapable of deciphering such amorphous states. Based on structural roles for oxide glasses, it has become conventional to assign the different cations to network formers (e.g. Si, B, P) and network modifiers or charge compensators (e.g. Li, Na, Ca). These roles are closely related to the valence states and ionic radii and usually characterised by the number of nearest-neighbour oxygen anion, known as the coordination number (Zarzycki, 1991). Besides, it has been established in silicate glasses that the arrangements of next-nearest-neighbour (NNN) Si and the distribution of O-Si-O bond angle and distance could embody the level of order/disorder at medium- and long-range (Stebbins, 2007). Typical glass characterisation techniques include X-ray absorption, Raman, infrared and NMR (Nuclear Magnetic Resonance) spectroscopy, among others. NMR spectroscopy is of particular interest in the respect that the results are element/isotope specific and inherently quantitative [*]. Its sensitivity to the short- to medium-range chemical environments of the nuclei under investigation makes solid-state NMR an imperative experimental tool to interrogate glass structures. As a supplementary means to experiments, theoretical calculation has become an invaluable tool in materials structure characterisation and prediction. In the NMR community, it has become practically possible to calculate chemical shielding and other NMR parameters of periodic solids beyond molecular systems with the introduction of GIPAW (Gauge Including Projector Augmented Wave) method by Pickard and Mauri (2001).

2.2. Fundamentals of NMR spectroscopy

Classically speaking, NMR spectroscopy is realised by registering the precession frequencies of magnetic nuclei in an applied magnetic field. This mechanism does limit the NMR active nuclei to those with non-zero spin numbers (see 2.2.2). Fortunately, the majority of elements in

[*] In an NMR spectrum, signal intensity is proportional to the number of nuclei giving rise to it. More strictly speaking, it is proportional to the total magnetisation giving rise to the corresponding signal. The compromises in quantitation, as explained in many cases later, are mainly due to excitation and acquisition efficiency.

the periodic table have non-zero spin isotopes and in principle the precession frequencies of all could be detected in a magnetic field. Since nuclei are directly used as the microscopic structure probes in solid-state NMR experiments, a sample's crystallinity is not a prerequisite for obtaining NMR spectra. On the contrary, its sensitivity to short- and medium-range structures could help elucidate local structural features such as bond length, coordination and order/disorder. Therefore, it is a very useful tool for characterising proto-crystalline and amorphous state materials that lack long-range translational symmetry. Having said that, NMR spectra of disordered materials are often complex and require additional work to interpret their structural origins, compared with their crystalline counterparts.

2.2.1. Classical descriptions of NMR

The magnetic moment $\vec{\mu}$ of a nucleus arises from its spin angular momentum $\vec{J}$ which in turn stems from its intrinsic spin $\vec{I}$ (see 2.2.2). $\vec{\mu}$ and $\vec{J}$ are related via the gyromagnetic ratio γ, which is unique for each nuclide, by

$$\vec{\mu} = \gamma\vec{J}.$$

Equation 2-1

When a magnetic field $\vec{B}$ (Tesla) is present, a dipole with its own angular momentum like a magnetic nucleus would precess around the field at an angular frequency ω (rad·s^{-1}) that determined by γ (rad·s^{-1}·T^{-1}):

$$\omega = -\gamma\left|\vec{B}\right|.$$

Equation 2-2

This frequency is usually referred to as the nuclear Larmor frequency. The overall motion could be comprehensively described by

$$\frac{d\vec{\mu}}{dt} = \gamma\vec{J} \times \vec{B} = \vec{\mu} \times \vec{B}.$$

Equation 2-3

In a macroscopic sample, the total nuclear magnetisation $\vec{M}$ is made up of all the individual nuclear magnetic moments as their vectorial sum $\sum_n \mu_n$. The presence of an external magnetic field $\vec{B}$ would induce an anisotropic net macroscopic $\vec{M}$ in its direction from originally randomly distributed, i.e. isotropic nuclear magnetic moments. In other words, the nuclear

ensembles exhibit paramagnetism. Ultimately, this macroscopic magnetisation is what would be manipulated and observed in an NMR experiment. The way in which this is carried out practically in its simplest form is described in 2.2.3.

2.2.2. Quantum mechanical aspects of NMR

Having stated that a nuclear magnetic moment originates from a nucleus' intrinsic spin angular momentum, we do not explore the origin of this purely quantum property. All we need to know from a practical point of view is that other than the physical motion that we could visualise, nuclear spin is an intrinsic quantum mechanical property that many nuclides possess (nuclear spin arises from combined spins of protons and neutrons that make up the nucleus and their individual angular momentum states) and gives rise to a final value of spin angular momentum, *I*. Thus, nuclear spin is characterised by a spin number *I* from which the magnitude of the total angular momentum *J* could be calculated by

$$J = \hbar\sqrt{I(I+1)},$$

Equation 2-4

where ħ is the reduced Planck constant. *I* could be either an integer or half integer positive number.

Unlike classical angular momentum that an object possesses when it rotates, nuclear spin and angular momentum are quantised. Nuclides with a spin number *I* have $2I + 1$ discrete energy levels, each of which could be assigned a quantum number *m*. m takes the value from $-I$ to *I* at an increment of 1. When a magnetic field is absent, these energy levels are degenerate. However, if they interact with a magnetic field, $2I$ equally spaced energy gaps would be lifted between neighbouring energy levels. Such an interaction is called Zeeman interaction and is illustrated in Figure 2-1 for an $I = ½$ spin (assumed positive γ and hereafter).

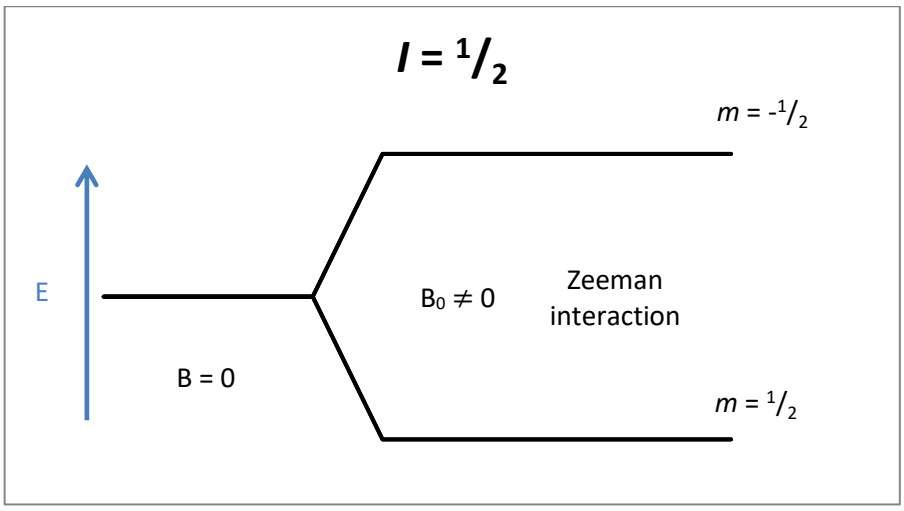

Figure 2-1 The degeneracy of energy levels $m = -1/2$ and $m = 1/2$ when no magnetic field is present and the effect of the Zeeman interaction when a magnetic field is applied.

In quantum mechanical terms, the state of a system is described by a wavefunction ψ. At equilibrium, a spin system would be in one of its eigenstates each of which is described by an eigenfunction $\psi_{I,m}$. Furthermore, if we want to know certain spin properties of a spin system in a specific environment, we conduct the corresponding spin operations on the wavefunction (eigenfunctions) that is described in that environment. For example, by applying the particular spin operator $\hat{I}^2$ on the eigenfunction $\psi_{I,m,}$ we get the square of the magnitude of spin angular momentum by

$$\hat{I}^2 \psi_{I,m} = \hbar^2 I(I+1) \psi_{I,m}.$$

Equation 2-5

Similarly, we can obtain the energy values of the non-degenerate energy levels, each of which is an eigenstate of the spin system, in a magnetic field. The energy operator (Hamiltonian) $\hat{H}$ for an isolated (i.e. not perturbed by other interactions) nuclear spin in a magnetic field B_0 is represented by

$$\hat{H} = -\hat{\mu} \cdot B_0,$$

Equation 2-6

where $\hat{\mu}$ is the nuclear magnetic moment operator. $\hat{\mu}$, in turn, is related to the spin operator $\hat{I}$ by

$$\hat{\mu} = \gamma \hbar \hat{I}.$$

Equation 2-7

At this stage, we define the direction in which the magnetic field is applied as Z. Then, nuclear spin quantisation would be along Z and so is the Zeeman interaction. By applying the z component of the nuclear spin operator $\hat{I}_z$ on the eigenfunction $\psi_{I,\,m,}$ we could obtain the corresponding quantum number *m* as follows

$$\hat{I}_z\,\psi_{I,\,m} = m\,\psi_{I,\,m}.$$

Equation 2-8

Eventually, the energy of each eigenstate $E_{I,\,m}$ can be evaluated by comparing Equation 2-6, 7, 8:

$$E_{I,\,m} = -\gamma\hbar\,B_0 m.$$

Equation 2-9

Again, let's take the $I = ½$ spin for instance, the energies of the two eigenstates $\psi_{1/2,\,-1/2}$ and $\psi_{1/2,\,1/2}$ are $\frac{1}{2}\gamma\hbar B_0$ and $-\frac{1}{2}\gamma\hbar B_0$, respectively. Therefore, the energy gap between the two energy levels is $\gamma\hbar B_0$. Quantum mechanically, the well-known Planck equation $E = \hbar\nu$ states that the energy of a photon is proportional to its frequency. Comparing the energy gap with Equation 2-2, we conclude that the photon absorbed/emitted associated with the transitions between the two Zeeman states has a frequency the same as the precession frequency in a classical picture.

Unsurprisingly, the macroscopic magnetisation $\vec{M}$ also finds its root in quantum mechanics. In a nuclear spin ensemble at equilibrium, the Zeeman states are populated following Boltzmann distribution as

$$\frac{N_{m-1}}{N_m} = e^{-\gamma\hbar B_0/k_B T}$$

Equation 2-10

where *N* represents the population of spins, k_B is the Boltzmann constant and T is the absolute temperature. In the case of $I = ½$, according to the population distribution law, the state $m = ½$ is more populated than its counterpart $m = -1/2$ as it is the more energy favoured state. The biased distribution towards lower energy state leads to the net magnetisation $\vec{M}$.

Some of the quantum mechanical concepts mentioned above are stated briefly and loosely in a practical frame , and therefore should not be taken rigorously from a physicist point of view.

2.2.3. Single-pulse NMR

We already defined the direction in which the external magnetic field B_0 is applied as Z. In a classical picture, the approach to acquire signals on an NMR spectrometer is to nutate the net macroscopic magnetisation towards the X-Y plane (X-Y-Z forms the laboratory frame (LAB)) and register its precession frequency within the plane. In practice, in order to achieve magnetisation nutation, an electromagnetic radiation is applied to 'perturb' the equilibrium. Since the radiation is in the radiofrequency (RF) range of the electromagnetic spectrum and usually only turned on for a few microseconds, it is herein referred to as an RF pulse and conventionally named B_1. This process is schematically shown in Figure 2-2. If $\vec{M}$ is nutated into the X-Y plane, such a pulse is called a $\frac{\pi}{2}$ pulse reflecting the tip angle.

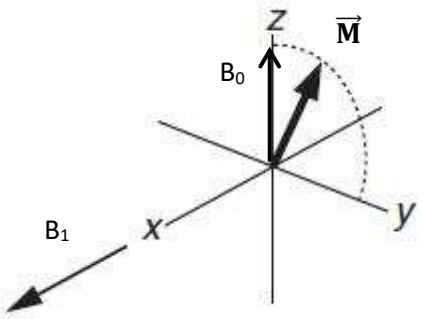

Figure 2-2 A schematic representation of the effect of application of an RF pulse on M in the vector model frame. B_0 and B_1 are not to scale.

Since the frequency of nutation υ_1 is proportional to B_1 ($\omega_1 = \gamma B_1$), it is customary to use υ_1 to represent the magnitude of RF pulse in frequency units. The RF pulses in an NMR experiment are always applied at a frequency close to that to be observed. The reason is that, firstly, we have a coordinate frame that is rotating at or close to the precession frequency of the net magnetisation so that $\vec{M}$ could be treated as 'static' in that frame since it does not precess as in Figure 2-2. Secondly, for multiple resonant frequencies to be detected, a uniform excitation profile is produced so that high experimental efficiency and quantification can be achieved.

After excitation, the RF pulse is turned off and $\vec{M}$ is allowed to precess freely during which time it decays in the X-Y plane and builds up again in the Z direction. Since, in principle, the accumulation of noise scales as the square root of scan number, n, whilst signal builds up linearly, the most straight forward way to increase signal-to-noise (S/N) ratio is to accumulate more scans i.e. $S/N \sim \sqrt{n}$. Ideally, allowing the spin system to restore its thermal equilibrium before repeating a scan, to achieve the desired S/N in a given time.

On a modern spectrometer, the oscillation of $\vec{M}$ is recorded digitally as a function of time known as free induction decay (FID), which contains all the information we need to know from an NMR experiment. However, it is difficult to decipher all the information in the time domain by human eyes, hence Fourier transform of the FID is needed to produce spectra that can be readily recognised as the frequency components of the decay.

The two concurrent events occur after an RF pulse: 1. Restoration of $\vec{M}$ in the Z direction and 2. Decay of $\vec{M}$ in the X-Y plane, are the two key dynamic processes characterised by the time constant T_1 (spin-lattice relaxation time) and T_2 (spin-spin relaxation time), respectively. Both relaxation mechanisms are induced by local magnetic field fluctuations and, hence, could provide dynamic insights into atomic level motions, which are not relevant to this thesis. However, it is important to note that they do have direct impacts on the quantitative nature of NMR and are pointed out in later chapters.

2.2.4. Chemical shifts

The usefulness of NMR spectroscopy would be null if the nuclei in a sample only interact with the external magnetic field as they would have exactly the same resonance frequency in that magnetic field. Apart from the Zeeman interaction, nuclei in a real sample interact with the magnetic field created by currents induced by their surrounding electrons, other nuclei and the local electric field gradient (EFG) for nuclei with an electric quadrupole moment ($I > ½$). These internal interactions (apart from EFG which will be discussed in detail in 2.3.2) generate magnetic fields at the nuclear site on top of B_0 so that the total magnetic fields experienced by nuclei in different chemical environments are slightly different. Indeed, by measuring the real resonance frequency resulting from these interactions, one can obtain atomistic level chemical information, which makes NMR such a powerful tool in the study of structure in materials.

The chemical bonds formed between nuclei are electronic in nature and they finally determine the majority of structural and chemical properties of a material. When placed in a magnetic field, the electrons that surround a nucleus are not impassive but react to the external field to create a secondary magnetic field called chemical shielding. The secondary field is typically $\sim 10^{-6} \sim 10^{-4}$ of B_0 but significant enough to result in measurable shifts in frequency. The corresponding Hamiltonian operator $\hat{H}_{cs}$ of this secondary field can be written as (similar to Equation 2-10)

$$\hat{H}_{cs} = -\gamma\hbar\hat{I} \cdot \sigma_{cs} \cdot B_0$$

Equation 2-11

where σ is the chemical shielding tensor and the other terms have their usual meanings. In the LAB, this tensor can be represented as a 3×3 matrix

$$\begin{Bmatrix} \sigma_{xx} & \sigma_{xy} & \sigma_{xz} \\ \sigma_{yx} & \sigma_{yy} & \sigma_{yz} \\ \sigma_{zx} & \sigma_{zy} & \sigma_{zz} \end{Bmatrix}.$$

Because of the chemical shielding effect, the total field B_{tot} experienced by a nucleus is

$$B_{tot} = (1 - \sigma_{cs}) \cdot B_0.$$

Equation 2-12

Since B_0 is applied in the Z (or 'zz') direction, only the σ_{xz}, σ_{yz} and σ_{zz} components are left over. Furthermore, only the 'zz' component matters as it is the part that aligns with B_0, which is in the direction of the quantization axis, while 'xz' and 'yz' parts only make secondary contributions (Duer, 2001; MacKenzie and Smith, 2002). As a result of this transformation, Equation 2-11 becomes

$$\hat{H}_{cs} = -\gamma\hbar\hat{I}\sigma_{zz}B_0.$$

Equation 2-13

We know from 2.2.2 that the Larmor frequency ω_0 of a bare nucleus is γB_0. Therefore, the deviation due to chemical shielding ω_{cs} can simply be written as

$$\omega_{cs} = \gamma B_0 \sigma_{zz}$$

Equation 2-14

and the magnitude of σ_{zz} determines how much the Zeeman levels are going to be shifted.

In a real-world experiment, we measure the frequency shift relative to a standard compound (reference) and represent the spectrum in a relative manner in parts-per-million (ppm) i.e. chemical shift δ as

$$\delta = \frac{\omega-\omega_{ref}}{\omega_{ref}} \times 10^6 = \frac{\gamma(1-\sigma_{zz})B_0 - \gamma(1-\sigma_{zz}^{ref})B_0}{\gamma(1-\sigma_{zz}^{ref})B_0} \times 10^6 = \frac{\sigma_{zz}^{ref}-\sigma_{zz}}{1-\sigma_{zz}^{ref}} \times 10^6 \approx (\sigma^{ref} - \sigma_{zz}) \times 10^{6\dagger}$$

Equation 2-15

On the other hand, it is possible to present the shielding tensor in a frame where all the off-diagonal components of the tensor matrix are zero as

$$\begin{Bmatrix} \sigma_{XX} & 0 & 0 \\ 0 & \sigma_{YY} & 0 \\ 0 & 0 & \sigma_{ZZ} \end{Bmatrix}$$

and this frame is called the principal axis frame (PAF). The key to working out the magnitude of σ_{zz} hence the chemical shift, lies in representing the principal values in the LAB through appropriate rotations. The important implication of this 'inconvenience' is exposed below and discussed in 2.3. As with the chemical shielding, the chemical shift should be regarded as a tensor in both frames. In the LAB, based on Equation 2-15, each component of the matrix is

$$\delta_{\alpha\beta} = \frac{\sigma^{ref}-\sigma_{\alpha\beta}}{1-\sigma_{\alpha\beta}} \approx \sigma^{ref} - \sigma_{\alpha\beta} \ (\alpha, \beta = x, y, z)$$

Equation 2-16

and in the PAF we have

$$\begin{Bmatrix} \delta_{XX} & 0 & 0 \\ 0 & \delta_{YY} & 0 \\ 0 & 0 & \delta_{ZZ} \end{Bmatrix}.$$

The isotropic chemical shift δ_{iso} is defined as the average of the three principal values i.e.

$$\delta_{iso} = \frac{\delta_{XX}+\delta_{YY}+\delta_{ZZ}}{3} = \sigma^{ref} - \sigma_{iso}{}^{\ddagger}.$$

Equation 2-17

The exact allocation of axes x, y and z differs in the literature according to different definitions. Here we adopt the Haeberlen notation (Haeberlen, 1976): $|\delta_{ZZ} - \delta_{iso}| \geq |\delta_{XX} - \delta_{iso}| \geq |\delta_{YY} - \delta_{iso}|$ and the anisotropy Δ_{cs} and asymmetry η_{cs} are accordingly defined as

$$\Delta_{cs} = \delta_{ZZ} - \delta_{iso}$$

† σ_{zz}^{ref} is usually 10^{-6}~10^{-4} of 1 hence the denominator can be approximated as 1.

‡ Similarly, σ_{iso} is the isotropic chemical shielding as the average of the three principle chemical shielding values.

$$\eta_{cs} = \frac{\delta_{YY} - \delta_{XX}}{\Delta_{cs}}$$ [§].

Equation 2-18

These three parameters are required to fully describe a chemical shift tensor. If we return to the point of the necessity to work out the σ_{zz} component to calculate the exact shift, using the defined parameters by the principal values as above, without step-by-step derivations as has been done by numerous authors (e.g. Duer, 2001; MacKenzie and Smith, 2002; Apperley, Harris and Hodgkinson, 2012 etc.), we have

$$\delta = \delta_{iso} + \frac{\Delta_{cs}}{2}(3\cos^2\theta - 1 + \eta_{cs} \sin^2\theta \cos 2\varphi)$$

where θ and φ are the polar and azimuthal angles describing the orientation of B_0 relative to the PAF[**]. Clearly, the exact frequency or shift from the reference frequency is orientation dependent.

2.3. Magic angle spinning solid-state NMR

In principle, solid-state NMR experiments should entail no further complications than their solution-state counterparts in terms of physical mechanisms. However, fundamental structural differences in these two states of matter impose some difficulties when trying to conduct a high resolution solid-state experiment or interpret a spectrum (the challenges associated with solution-state experiments are not addressed here).

Like the chemical shielding interaction discussed in 2.2.4, all the internal NMR interactions are anisotropic in the LAB. This is a problem in solids because: 1. Atomic mobility is limited due to rigid network structures and so the effects must be described by the associated interaction tensors; 2. Powders are used in almost all solid-state NMR experiments. The PAFs are confined in each crystallite in a powder-form sample and so would adopt all possible orientations with respect to the external magnetic field direction. Therefore, the orientation-dependent (anisotropic) interactions would alter the energy levels to different extent in a powder-form sample for differently orientated crystallites. Consequently, we observe different frequencies (shifts) even from a chemically identical site and the resulting broad lines are termed the powder-pattern lineshapes. In other words, one does not get high resolution due to these

[§] $0 \leq \eta_{cs} \leq 1$.

[**] Technically, we need to express the relative orientation between the two axis frames using three Euler angles. However, the z axis of LAB i.e. the B_0 direction is a symmetry axis for all tensors in their PAF so that the polar and azimuthal angles suffice.

'inconvenient' anisotropies. On the other hand, the fast atomic tumbling in liquids create an 'isotropic' environment in the sense that the anisotropies associated with these internal interactions are averaged out at the NMR timescale. Therefore, one usually gets narrow lines at the effectively averaged (isotropic) frequency from a liquid sample.

2.3.1. Magic angle spinning (MAS)

A powder solid sample is usually contained in a sealed ceramic tube conventionally called a 'rotor'. The most common method of averaging the internal interaction anisotropies (first-order) is by manipulating the spatial part of the anisotropy. This is achieved by physically spinning the rotor at $\theta_m = 54.736^o$ tilted from B_0 as illustrated in Figure 2-3. The reason is that under spinning conditions, the orientation of the internal interactions tensors become time-dependent and the anisotropic part is modulated by term $(3\cos^2\theta–1)$ where θ is the angle between rotor axis and B_0 (Andrew, Bradbury and Eades, 1958). Apparently, the anisotropies would be completely averaged to zero leaving only the isotropic part (like in a liquid sample) when this angle is set to be $\arccos\frac{\sqrt{3}}{3} \approx 54.736^o$: the so-called magic angle, which is between the spatial diagonal and one of the connected edges of a cube. However, if spun slower than the overall static linewidth, the FID decays rapidly, as in a static sample in the first half rotor period but a rotational echo would form as the sample returns to its initial state at the end of the second half rotor period. Fourier transform of the FID entrained with the rotational echo train would result in a spectrum formed of the isotropic line as well as the spinning sidebands separated at integer times of the spinning frequency (ω_r) from the isotropic line with the same line width (Maricq and Waugh, 1979).

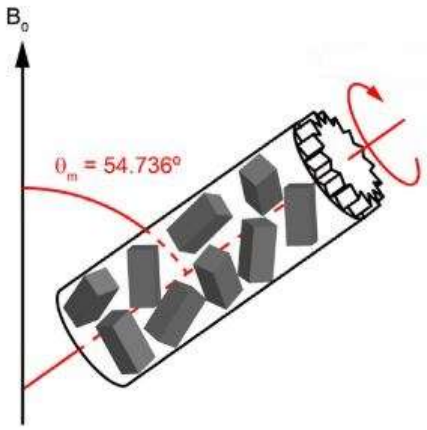

Figure 2-3 An illustration of the MAS practice. The rotating axis is tilted from B_0 by 54.736° (adapted from (Moran, Dawson and Ashbrook, 2017)**).**

2.3.2. MAS of quadrupole nuclei in solids

2.3.2.1. Theory

As mentioned above, nuclei with spin number $I > ½$ possess electric quadrupole moments so that they interact with EFGs present at the nuclear sites from surrounding charges. Like the chemical shielding interaction, we can represent the EFG as a tensor V in its own PAF as

$$\begin{Bmatrix} V_{XX} & 0 & 0 \\ 0 & V_{YY} & 0 \\ 0 & 0 & V_{ZZ} \end{Bmatrix}.$$

Since the EFG is the second derivative of electrostatic potential in space, it complies with the Laplace equation so that the trace of the V is zero, i.e. $V_{XX} + V_{YY} + V_{ZZ} = 0$. In the convention that $|V_{ZZ}| > |V_{XX}| > |V_{YY}|$ (Man, 2006), V can be described by its magnitude/anisotropy eq and asymmetry η_Q as

$$eq = V_{ZZ}$$

$$\eta_Q = \frac{V_{YY} - V_{XX}}{V_{ZZ}} \text{ ††}$$

Equation 2-19

The magnitude of the interaction called the quadrupole coupling constant, accordingly, is defined as

$$C_Q = \frac{e^2 Qq}{h}$$

where Q is the quadrupole moment of the nucleus and h the Planck constant such that it is in units of frequency.

Like other internal interactions, the effect of the quadrupolar interaction is to shift the Zeeman energy levels and hence change the observed frequency. However, the situation is slightly more complicated for quadrupolar nuclei because we now have $2I + 1$ discrete energy levels which means more than two when $I > ½$. Figure 2-4 illustrates the 4 energy levels associated with an $I = {}^3/_2$ nucleus e.g. ^{23}Na. First of all, Zeeman interaction splits the degenerate state into equally spaced energy levels associated with the Larmor frequency. In most cases where the magnitude of quadrupole coupling is much smaller (e.g. two orders of magnitude than that of the Zeeman interaction), the former can be treated as a perturbation to the Zeeman levels, as with the

†† $0 \leq \eta_Q \leq 1$.

chemical shielding effect. The full quadrupole coupling Hamiltonian is rather complex, as discussed and summarised in detail by Man (2006). Among other conventions, we adopt the most commonly used one introduced by Abragam (1961) to describe the quadrupole frequency ν_Q (Hz) in the PAF as

$$\nu_Q^{PAF} = \frac{3C_Q}{2I(2I-1)} \text{ (i.e. } \omega_Q^{PAF} = \frac{3C_Q\pi}{I(2I-1)} \text{ rad/s)}.$$

Equation 2-20

Without step-by-step derivations, the perturbation of the Zeeman levels by quadrupole coupling to Zeeman levels to first order is given by

$$\nu_Q = \frac{\nu_Q^{PAF}}{12}(3\cos^2\theta - 1 + \eta_{cs}\sin^2\theta\cos 2\varphi)\,(3m^2 - I(I+1)).$$

Equation 2-21

Here again, θ and φ are the polar and azimuthal angles describing the LAB (effectively the B_0 axis) in the PAF. Two points stand out from this mathematical representation: 1. First-order quadrupole coupling is orientation-dependent in the LAB and shifts different Zeeman levels to different extent based on *m*; 2. However, Zeeman levels with the same magnitude but opposite sign (e.g. for $m = -1/2$ and $1/2$) are shifted to the same extent, as the first-order coupling is quadratic about the z component of the spin angular momentum. Such a symmetry leads to the invariance of the central transition frequency, as schematically shown in Figure 2-4. Further, since it observes the same angular dependence in the LAB as with chemical shielding, MAS can average out the first-order quadrupole effect of the outer transitions (e.g. $-3/2 \leftrightarrow -1/2$ and $1/2 \leftrightarrow 3/2$) by making their orientations time-dependent in a polycrystalline sample and usually creates extensive sidebands because of the broad static pattern.

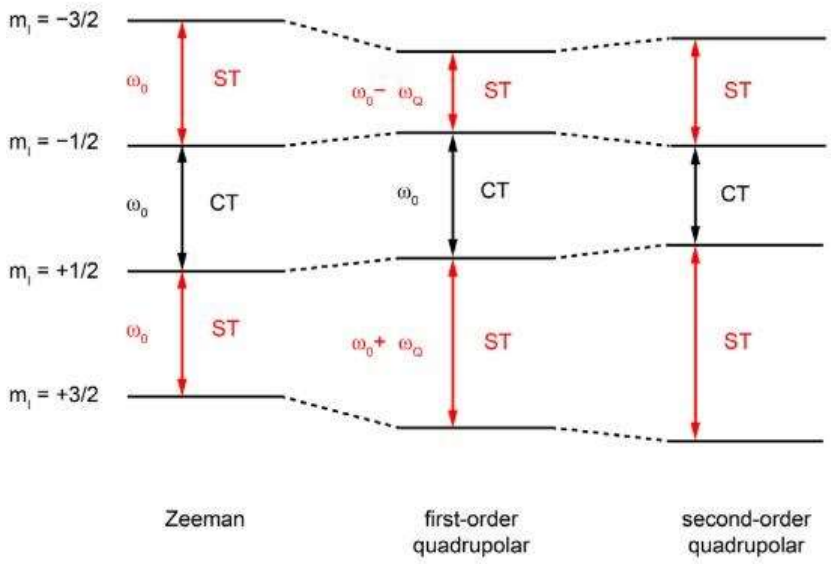

Figure 2-4 Effects of Zeeman interaction and both orders of quadrupole coupling on the energy levels of a $^3/_2$ spin nucleus. Modified from the Fig 4(a) in Moran, Dawson and Ashbrook (2017).

To further complicate the situation, in many cases the quadrupole coupling is so significant that second-order effects can no longer be omitted. As shown in Figure 2-4, both the satellite transitions are shifted further, hence their static, orientation-dependent, spectra are often broadened to tens of MHz which practically renders the observation impossible in pulsed NMR. Therefore, spectral acquisition is mostly focused on the central transition although the magnitude of the EFGs means that the central transition will also be subject to second-order quadrupole coupling. Under MAS conditions, the second-order quadrupole coupling is modulated, but the more complex angular dependence than its first-order counterpart makes MAS incapable of completely averaging out the associated anisotropy: for the central transition, the time-averaged second-order shift of each PAF orientation can be generalised in the form

$$\nu^{Q}_{-\frac{1}{2},\frac{1}{2}} = \frac{\omega_Q^2}{\omega_0}[A_0 C_0^I\left(\frac{1}{2}\right) + A_2(\theta, \varphi, \eta) C_2^I(\tfrac{1}{2}) P_2(\cos\beta) + A_4(\theta, \varphi, \eta) C_4^I(\tfrac{1}{2}) P_4(\cos\beta)]$$

Equation 2-22

when the sample was spun at the angle β inclined from B_0 axis (Frydman and Harwood, 1995). $C^I_{i=0,2,4}(m)$ coefficients are functions of spin number I and the transition -m↔m[‡‡]. A_2 and A_4 are the sources of the remaining second-order anisotropy hence residual broadening whilst A_0 is the isotropic quadrupole shift term. Importantly, the modulation terms $P_2(\cos\beta)$ and $P_4(\cos\beta)$ are the second- and fourth-rank of Legèndre polynomials i.e.

[‡‡] The angular dependence (anisotropy) associated with all symmetrical transitions, even not directly observable e.g. $-^2/_3 \leftrightarrow {}^2/_3$ follows Equation 2-22.

$$P_2(\cos\beta) = \frac{3\cos^2\beta - 1}{2}$$

$$P_4(\cos\beta) = \frac{35\cos^4\beta - 30\cos^2\beta + 3}{8}$$

and it is clear that the $P_4(\cos\beta)$ term is not reduced to zero by spinning at the magic angle while the $A_2(\theta, \varphi, \eta)$ term is eliminated. Therefore, there is a characteristic (η dependent) residual powder-pattern lineshape under MAS due to the second-order quadrupole coupling, whose breadth is determined by the magnitude of υ_Q.

It is worth noting that at geometrically and electrically symmetrical sites, EFG is essentially zero so that quadrupole interactions vanish. This usually occurs for quadrupole nuclei in tetrahedral or octahedral sites in solids with cubic symmetry.

2.3.2.2. Isotropic shift position as a result of MAS

For lines that are broadened by first-order interactions only, the position of their MAS spectra would be located at the centre of mass (CoM) and, hence, the isotropic position of the corresponding static spectra. However, the second-order quadrupole interaction broadened central lines are offset from the isotropic chemical shift position. Equation 2-22 shows that there is an isotropic shift associated with the second-order shift, which is not orientation-dependent (the first item in the square bracket). The so-called isotropic quadrupole shift has been shown (Freude and Haase, 1993) to be:

$$\nu_Q^{iso} = -\frac{\nu_Q^{PAF^2}}{30\upsilon_0}\left[I(I+1) - \frac{3}{4}\right]\left(1 + \frac{\eta^2}{3}\right)$$

Equation 2-23

for the central transition. As a result, the whole line is shifted to lower frequencies by the same amount depending on the EFG from the isotropic value hence the CoM of the central MAS line is $\delta_{iso} + \delta_Q^{iso}$ ($\delta_Q^{iso} \approx \frac{\nu_Q^{iso}}{\upsilon_0}$). Consequently, in order to obtain the true isotropic chemical shift position from a second-order quadrupole central transition spectrum, it is essential to simulate the spectrum and to extract the value from the fit.

2.3.3. Experimental aspects involving quadrupole nuclei

2.3.3.1. Excitation and quantification

Since there are more than two adjacent energy levels, there is more than one NMR transition for quadrupole nuclei. In most cases, the excitation and the subsequent observation of signal focus on the central transition only. Even so, the exact profile of central transition excitation still depends on the system under investigation and is not as trivial as described in 2.2.3 for one-half spins. Specifically, the nutation frequencies of nuclei in the m = ½ and -½ angular momentum states do not depend only on the magnitude of RF power but also on the relative magnitude between RF power and quadrupole coupling. In the case of $\nu_1 \gg \nu_Q$, the nutation frequency for the central transition remains invariant as ν_1, as if it was a one-half spin. This corresponds to a strong RF pulse and a weak quadrupole coupling and is conventionally called non-selective excitation. Opposite to this situation as $\nu_Q \gg \nu_1$ the nutation frequency of the central transition is effectively $(I + \frac{1}{2})$ faster than that which υ_1 would create for all transitions. In such a scenario the excitation is selective (Abragam, 1961). Accordingly, the corresponding $\frac{\pi}{2}$ pulse length is $(I + \frac{1}{2})$ times shorter. Moreover, the maximum intensity that can be obtained for a selective excitation is $(I + \frac{1}{2})$ times smaller than a maximum fictitious one-half intensity for the central transition only (Fukushima and Boden, 1982).

For samples in which more than one quadrupole site of different EFG magnitude coexist, it is crucial to apply 'very short' pulses, as indicated in Figure 2-5 by the red arrows, by which the excitation response is proportional to the pulse length regardless of the magnitude of quadrupole coupling. In other words, the same nuclei coupled to different magnitudes of EFG are excited to the same extent so that the signal intensity is proportional to the population of nuclei. It is worth noting that for intermediate RF power (or ν_Q), which is often encountered in real experiments, the excitation profiles fall in the limits of selective and non-selective limits (Vega, 2010). For pulses shorter than $\frac{1}{4\nu_1\left(I+\frac{1}{2}\right)}$ ($\frac{\pi}{2\left(I+\frac{1}{2}\right)}$), the errors in comparing the signal intensity (excitation response) are less than 10% (Fenzke *et al.*, 1984). In practice, even shorter pulses are usually applied to alleviate this effect ($<\frac{\pi}{6\left(I+\frac{1}{2}\right)}$).

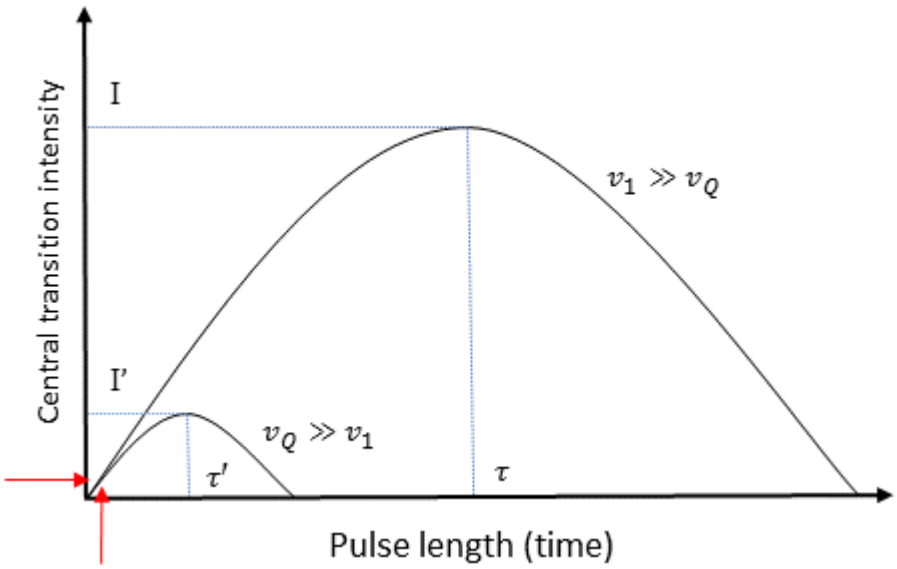

Figure 2-5 Excitation profile of quadrupole nuclei central transitions for selective and non-selective excitation scenarios. For the reasons stated in the texts, $\tau' = \tau/(I+1/2)$ and $I = (I+1/2)I'$.

2.3.3.2. Quadrupole linewidth

For I = ½ nuclei, the linewidth due to inhomogeneous broadening is invariant of the magnetic field in ppm terms because it is scaled to the reference in the same magnetic field. This is not the case for quadrupole nuclei where second-order broadening is pronounced. Equation 2-22 shows that the additional contribution to the frequency shift from second-order quadrupole interaction is inversely proportional to the nuclei's Larmor frequency. When presented in ppm, the shift in frequency is further divided by the absolute frequency of the same nuclei in the reference, which is usually very close to that of the Larmor frequency. Therefore, the quadrupole linewidths in ppm terms are approximately inversely proportional to the square of the nuclei's Larmor frequency. When spectra collected at different magnetic fields are compared, the narrowing due to this effect should be isolated from structural information. For resolution purposes[§§], it means that it is always advantageous to go for the highest possible magnetic field when dealing with quadrupole nuclei of large quadrupole interaction, to increase the *S*/*N* ratio and mitigate overlapping. As an example, the effect is clearly demonstrated in Figure 2-6 (Stebbins *et al.*, 2000) where resonances due to Al in different coordination environments are obscured due to overlapping 2nd-order broadened lines at low fields and are only resolved at 18.8 Tesla when this broadening is reduced by the higher field. Further, a high magnetic field could also increase the sensitivity by increasing the population difference between energy levels and the electrical response of the RF coil.

[§§] However, in cases where the experimental purpose is to extract structural information, too high a magnetic field would smear the line features which is the embodiment of interactions that results from the structures.

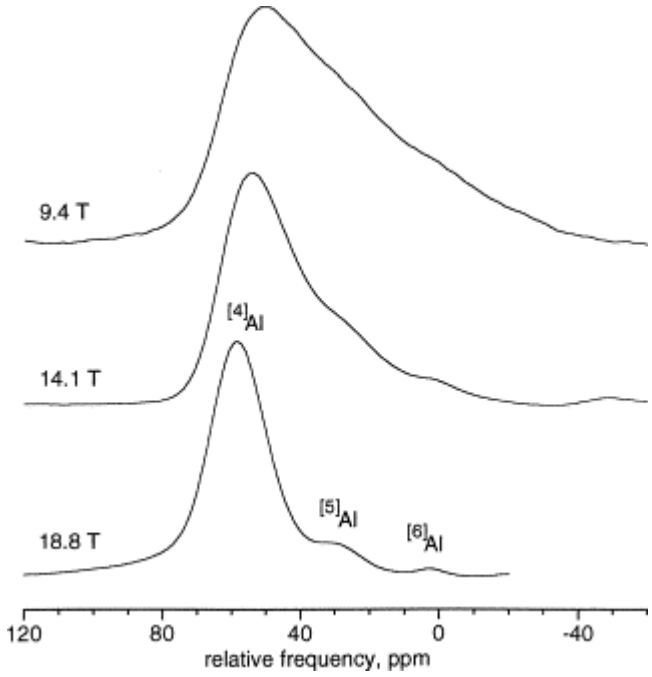

Figure 2-6 ^{27}Al MAS NMR spectra of a calcium aluminosilicate glass containing fluoride in magnetic fields of 9.4, 14.1 and 18.8 Tesla (adapted from (Stebbins et al., 2000)).

2.4. Other solid-state NMR techniques

Another important technique often used in solid-state NMR is the so-called cross-polarisation (CP) experiment. It involves the polarisation (magnetisation) transfer from one nucleus to another via dipolar coupling and the subsequent observation of the signal from the latter. Usually, CP is used to increase the sensitivity of dilute and insensitive spins, e.g. ^{13}C and ^{17}O, by using magnetisation from abundant and sensitive spins, e.g. ^{19}F and ^{1}H. In other cases, it is useful to edit the spectra by detecting only the signal arising from the transfer process.

2.4.1. Cross-polarisation

2.4.1.1. Theory

CP techniques make use of the principle of conservation of the spin system magnetisation (energy) in a doubly rotating frame during the transfer process so that the build-up of one magnetisation in the X-Y plane is at the expense of another's decay. As shown in Figure 2-7 (not to scale) in its simplest form, after creating the ^{1}H magnetisation in the X-Y plane by an initial 90° pulse on the proton channel, a so-called contact pulse is turned on in both channels for a period of time called contact time, usually in the range of tens of microseconds to milliseconds. The RF field strengths, $B_1^{\mathrm{H}}$and B_1^{X}, satisfy the Hartmann-Hahn matching condition (Hartmann and Hahn, 1962):

$$\alpha_H \gamma_H B_1^H = \alpha_X \gamma_X B_1^X$$

Equation 2-24

where α is a coefficient as a function of *I* and the transition between *m* and (*m-1*) follows:

$$\alpha = [I(I + 1) - m(m\text{-}1)]^{1/2}$$

Equation 2-25

Here, γ and B_1 have their usual meanings. For central transitions, α reduces to its familiar form $(I + \frac{1}{2})$. For one-half spins, α = 1 when $I = \frac{1}{2}$. In other words, when the nutation frequency ω_1 of both nuclei are adjust to the same magnitude, the magnetisations (energy gaps) along the new quantised direction (along B_1) in each rotating frame are the same for both spin systems. Under such a condition, the dipolar coupling between ^{1}H and X cannot change the total magnetisation (energy) of the spin system (Duer, 2001). The weak spin-locking provided by B_1^H in the rotating frame compared with B_0 in the Z direction leads to the leak of ^{1}H magnetisation, which is compensated by the build-up of X magnetisation in the B_1^X direction in its rotating frame, as required by preserving the total magnetisation. The subsequent oscillations and decay of X magnetisation can be recorded as an FID, as in a single-pulse experiment. In reality, the creation of X magnetisation is also limited by other factors, as outlined in 2.4.1.3.

Since ^{1}H has a much higher gyromagnetic ratio than most other nuclei the magnetisation of the less abundant or lower frequency nuclei is enhanced. In principle, the theoretical enhancement considering the numbers of nuclei compared with a single-pulse acquisition is given by a factor of $\frac{\gamma_H}{\gamma_X} \cdot \frac{1}{1+\varepsilon}$ [***] ($\epsilon = \frac{N_X}{(I+\frac{1}{2})N_H}$, where N_H and N_X are the number of spins of proton and X) (Vega, 1981).

[***] For central transition only.

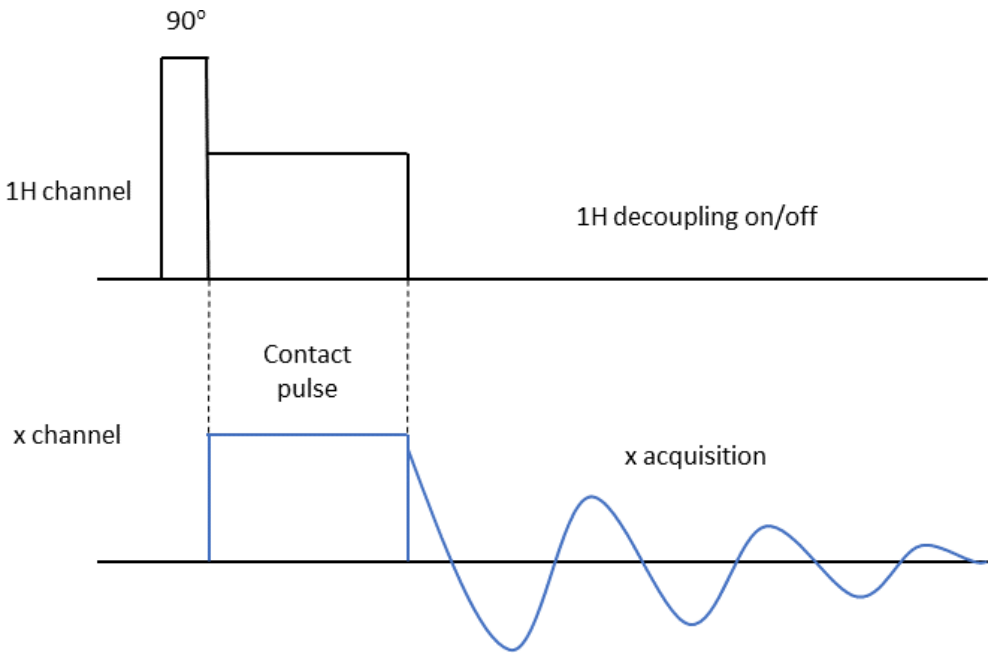

Figure 2-7 Illustration of CP pulse sequence in its simplest form involving both ^{1}H and X channels i.e. double resonance (not to scale).

2.4.1.2. Magnetisation transfer to quadrupole nuclei and CPMAS

Since the experiments herein are focused on the CP between ^{1}H and the central transition of half-integer quadrupole nuclei, the following is limited to this scenario only. There are two major complications when one is trying to practise CP between ^{1}H and quadrupole nuclei under MAS condition. First, as shown in Equation 2-24, when only transferring the magnetisation to the central transition of half-integer nuclei, the matching condition should be adjusted to equalise the effective nutation frequency because of the large quadrupole coupling, as pointed out in 2.3.3.1. Secondly, MAS complicates the spin dynamics during magnetisation transfer, hence the experimental matching conditions. Based on numerical simulations and experimental evidences, Vega (1992) established an experimental parameter α that describes the nature of the spin dynamics as a function of the RF field strengths, quadrupolar coupling and spinning speed:

$$\alpha = \frac{\nu_{1Q}^2}{\nu_Q^{PAF}\nu_R}$$

Equation 2-26

where ν_1 is magnitude of the RF power represented as the 'solution' nutation frequency and ν_R is the spinning speed. In the extreme cases where $\alpha \ll 1$ or $\alpha \gg 1$, the transfer process is efficient in either case, although the total magnetisation participating in the transfer for the former (fast spinning) is half of the latter (slow spinning). The optimum matching condition for the fast

spinning regime is changed from the Hartmann-Hahn condition to $\alpha_H\gamma_H B_1^H = \alpha_X\gamma_X B_1^X \pm n\nu_R$ (n = 1, 2), the so-called sideband matching conditions, whilst the static condition holds for the slow spinning situation. The implications are discussed alongside the CP spectra in 6.2.1.4. In essence, CP processes are mediated between nuclei through dipolar couplings. Therefore, MAS, as an experimental method to average out the dipolar couplings and improve spectral resolution, would inherently weaken the polarisation transfer efficiency in comparison to static cases.

2.4.1.3. Usefulness of CP in the NMR context

Despite the complexities involved in setting up CP experiments compared with single-pulse excitation, it is worth the effort in many applications because of the benefits that it could provide. From an experimental point of view, as mentioned above, CP has been proven to be valuable for enhancing the sensitivity of nuclei with low gyromagnetic ratio and/or natural abundance and hence increase the *S*/*N* ratio in a given time. For example, detecting the ^{17}O NMR signal from naturally occurring minerals can be a painstaking process when large EFG is present at the oxygen sites because of the low natural abundance of ^{17}O and enrichment being unfeasible. Yet, oxygen bears unparalleled structural information in solid inorganic systems, as with carbon for solid organic systems. However, since many of natural occurring minerals also contain protons in different forms, CP could provide the magnetisation source from protons to dramatically enhance the experimental sensitivity (Ashbrook and Farnan, 2004). In the meantime, in favourable cases where $T_{1\rho}$ (see below) of protons is relatively short[†††], the increase in the *S*/*N* is also assisted by faster repetitions when the nuclei of interest are of long T_1 (Pines, Gibby and Waugh, 1973).

It is the CP's ability to edit NMR spectra that extends its applications to many more solid-state systems. Aside from the build-up of X magnetisation during the contact pulse, the rate of which is determined by a time constant T_{XH}, the spin-locked ^1H magnetisation would relax simultaneously in the rotating frame to restore its thermal equilibrium. The latter process is similar to the 'free' spin-lattice relaxation, hence conventionally characterised by a time constant $T_{1\rho}$. Since T_{XH} is dependent on the strength of the dipolar coupling between proton and X and, hence, their inter-atomic distance (Mehring, 1983), the signal intensities at different contact times can be monitored to probe proton proximity, for example, to distinguish protonated and non-protonated oxygen species and achieve signal selectivity. This effect is convoluted with the rotating frame spin-lattice relaxation in the sense that efficient relaxation,

[†††] Not too short to jeopardise magnetisation transfer.

mainly of protons (Walter, Turner and Oldfield, 1988), would impair the magnetisation transfer process.

However, as already pointed out, despite the benefits associated with CP experiments, indirect excitation and structural dependent excitation efficiency usually compromises the quantitative aspect of NMR.

2.4.2. Spin-echo

Spin-echo is another commonly used multi-pulse sequence (Hahn, 1950), which is schematically illustrated in Figure 2-8. Because of the inevitable ringing of the probe and deadtime of the instrument (pre-amplifier) immediately after turning off the RF pulses, there have to be pre-acquisition delays (usually tens of microseconds) prior to acquiring the signal. The huge ringing effect, relative to the delicate RF responses from the sample, would occupy the beginning of the FID and, hence, convolute with or corrupt the true signal after Fourier transform. On the other hand, broad lines in solid-state NMR mean rapidly decaying FIDs so that the delays at the beginning would significantly reduce the signal intensities as well as distort the overall lineshape, causing a frequency dependent (first-order) phasing effect.

The spin-echo works by refocusing the spins dephasing after the first 90°pulse during a delay, τ_1, a second pulse is then applied so that the spins re-phase, causing an echo to form at a time τ_2 and replicate the initial FID thereafter. The second pulse length can vary, depending on the nature of the interactions that broaden the line. For interactions proportional to spin operator $I_{z,}$ including chemical shift anisotropy and heteronuclear dipolar coupling, a 180° pulse could reverse the magnetisations and cause them to be accurately refocused. The same holds true for selective excitation of the central transition of the second-order quadrupole interaction (Freude and Haase, 1993). Because the echo top is now away from the RF pulse, the issues mentioned above due to ringing and deadtime effects are avoided and the replicated FID can be Fourier transformed from the echo top with no phase distortions.

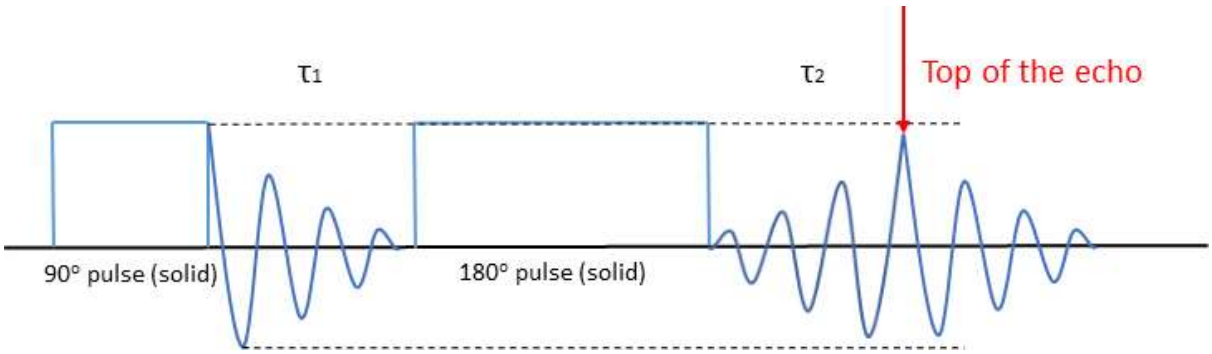

Figure 2-8 An 90°-180° spin-echo pulse sequence for forming and echo after the 180° pulse and echo delay time τ_1 (not to scale).

As with CP, the spin-echo involves multiple excitations and other delays prior to the acquisition. For example, different species with different T_2 would recover different levels of their initial magnetisation (dashed line in Figure 2-8), so that any quantitative interpretation of the echo spectra needs extra care.

2.4.3. MQMAS

2.4.3.1. Brief background

Two-dimensional (2D) multiple-quantum (MQ) MAS was firstly introduced by Frydman and Harwood (1995) as a technique to improve the resolution of one-dimensional (1D) solid-state MAS NMR spectra of half-integer quadrupole nuclei, where second-order quadrupole broadening leads to signals of chemically inequivalent sites being heavily overlapped. Similar to the time-averaged anisotropy associated with the central transition frequency (see Equation 2-22), the anisotropy associated with all symmetrical transitions between nuclear spin energy levels e.g. $-^3/_2 \leftrightarrow {}^3/_2$, even if not directly observable, can be formulated in the same manner but with different coefficients $C^I_{i=0,2,4}(m)$. Furthermore, the 4th-rank terms associated with different symmetrical transitions, which could not be averaged out completely under MAS, are proportional to each other with the proportionality determined only by the ratio between $C^I_4(m=$ $^1/_2, {}^3/_2, \ldots, I)$ values. This insight provided the theoretical possibility to eliminate the second-order anisotropy by forming an echo, as with the spin-echo experiment (see 2.4.2), where the second-order anisotropy can be refocused leaving only the isotropic terms.

The evolution of MQ and SQ (single-quantum) coherences ($-m \leftrightarrow m$) generated by RF excitation pulses can be described by an expansion of its phase Φ similar to Equation 2-22 as (Lefebvre *et al.*, 1987)

$$\Phi(m, \beta, t) = \nu_{CS}^{iso} 2mt + \nu_{Q}^{iso} C_0^I(m)t + \nu_2^Q(\theta, \varphi) C_2^I(m) t P_2(\cos\beta)t + \nu_4^Q(\theta, \varphi) C_4^I(m)t\, P_4(\cos\beta)t$$

Equation 2-27

where the common terms shared with Equation 2-22 also share the same physical meanings. ν_{CS}^{iso} and ν_{Q}^{iso} are the isotropic chemical shift and isotropic quadrupole shift, respectively. ν_2^Q and ν_4^Q are the second- and fourth-rank angular-dependent terms which give rise to the overall quadrupole broadening. While the second-rank term, as discussed previously, can be readily eliminated under MAS conditions, the fourth-rank term needs further manipulations and could be cancelled out by combining the phase evolution of two different coherences orders. Experimentally, this is achieved by appropriate phase cycling of the excitation RF pulses to select the evolving coherence order (Frydman and Harwood, 1995). In its simplest form, a two-pulse 3QMAS pulse sequence for $I=^5/_2$ nuclei is shown in Figure 2-9. According to Equation 2-27, the echo top that is devoid of second-order anisotropy would form at $t_2 = \left|\frac{C_4^2\left(\frac{3}{2}\right)}{C_4^2\left(-\frac{1}{2}\right)}\right| t_1$ and the resultant single-quantum (-1Q) coherence can be observed. By varying the MQ evolution time t_1, a second temporal dimension (t_2) can be constructed in which the isotropic echo tops form a new data series to be Fourier transformed to yield the corresponding isotropic spectrum in F_1 dimension whilst the F_2 dimension is retained to yield the same MAS spectrum as would be observed in 1D MAS experiments.

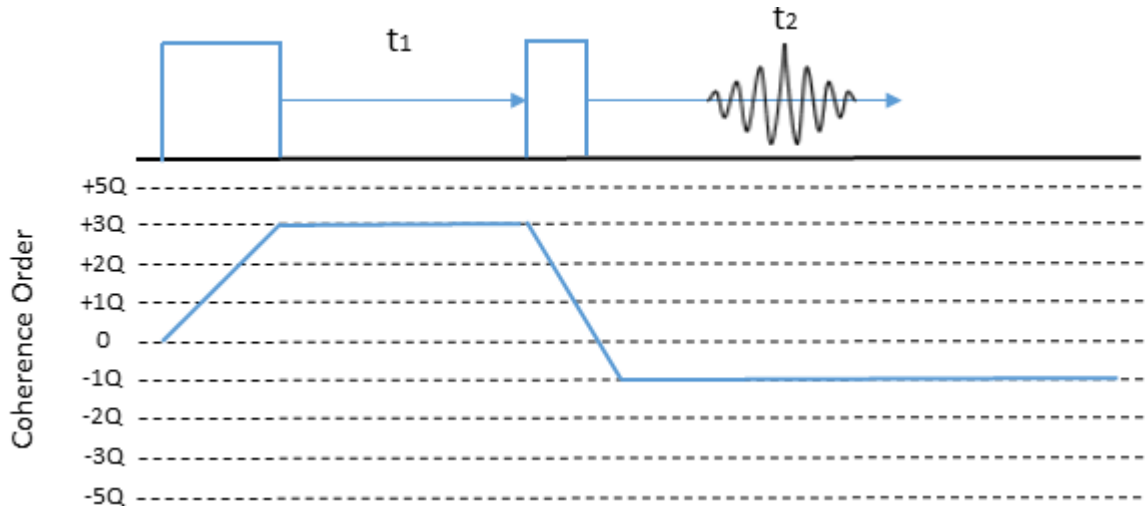

Figure 2-9 The two-pulse MQMAS sequence to achieve the coherence transfer pathway 0→-3Q→-1Q for $I=^5/_2$ nuclei. The echo top formed at $t_2 = \left|\frac{C_4^2\left(\frac{3}{2}\right)}{C_2^2\left(-\frac{1}{2}\right)}\right| t_1$ is, therefore, devoid of second-order quadrupole anisotropy.

2.4.3.2. Experimental aspects

Z-filter MQMAS

While MQMAS provides advantages over 1D MAS experiments in terms of resolution improvement, it suffers from a few experimental limitations including: 1. Loss of quantification due to C_Q-dependent excitation (conversion) efficiency; 2. Low efficiency associated with MQ coherence excitation and conversion to SQ coherence; 3. Distortion of the lineshape due to dispersive contributions to the signal (A. Medek, J.S. Harwood and L. Frydman, 1995). While the first drawback is intrinsic, a lot of work has been done since the introduction of MQMAS to improve the experimental efficiency and lineshape. Only one MQ coherence ($C_4^I(m$ or $-m)$ with the opposite sign of $C_4^I\left(-\frac{1}{2}\right)$) can be correlated with a SQ coherence to generate the observable echo, acquiring both $\pm m$ coherences i.e. echo and anti-echo is needed to produce 2D MQMAS spectra free of dispersive distortions (Fernandez and Amoureux, 1996). Moreover, pure absorptive lineshapes can only be obtained if equally strong signals from both pathways are acquired (Amoureux, Fernandez and Steuernagel, 1996). Z-filter MQMAS (triple-quantum in this case) pulse sequence, as schematically shown in Figure 2-10, satisfies these two conditions simultaneously where not only both $\pm$3Q pathways are selected but also with equal contribution. A third 90° selective pulse, which excites the central transition only, converts the unobservable zero-quantum coherence to the observable -1Q. Because of its relatively straightforward setup, a z-filter pulse sequence was used for the ^{17}O 3QMAS experiments presented in this thesis.

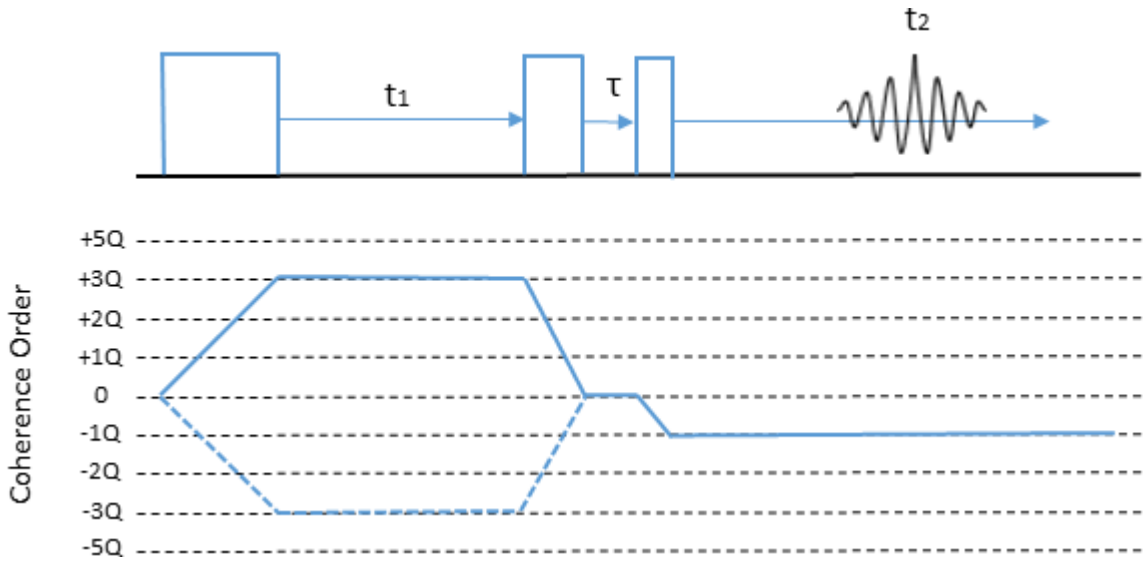

Figure 2-10 Z-filter 3QMAS pulse sequence with both coherence transfer pathways 0→ ±3Q→0→-1Q for $I=5/2$ nuclei.

Scaling and labelling of 3QMAS spectra

At each t_1 increment, since the echo would always form at $t_2 = \left|\frac{c_4^I(m)}{c_4^I\left(-\frac{1}{2}\right)}\right| t_1 = kt_1$, the echo train would align at a gradient of $1/k$ with respect to the t_2 dimension. Therefore, a shearing process is needed to align the tilted echo train perpendicular to the t_2 dimension i.e. parallel to the t_1 dimension before Fourier transform with respect to t_1, to obtain a high-resolution spectrum in the F_1 dimension. However, the procedure for the scaling and subsequent labelling of the sheared 2D spectra depends on how the evolution and acquisition periods are defined in the pulse sequence. The so-called C_z convention, firstly used by A. Medek, J.S. Harwood and L. Frydman (1995) has been adopted here where t_1 was regarded as the evolution period and the start of the acquisition is effectively at the top of the echo i.e. t_2 after shearing. There are other definitions of these two periods and hence conventions in the literature, the details of which were thoroughly summarised by Millot and Man (2002). No scaling factor is needed for labelling the F_1 dimension as the spectrum width is simply the inverse of the t_1 increment in hertz. However, the frequency hence ppm offset from the external reference for C_z convention is shifted by a factor of (k-2m). After the corresponding scaling and labelling procedures, the δ_{iso} and $\delta_Q^{iso\ddagger\ddagger\ddagger}$ could be calculated according to the equations below (Man, 1998):

$$\delta_{CS}^{iso} = \frac{k+\lambda}{2m+\lambda}\delta_{CoM}^{MAS} - \frac{1}{2m+\lambda}\delta_{CoM}^{MQMAS}$$

$$\delta_{Q}^{iso} = -\frac{k-2m}{2m+\lambda}\delta_{CoM}^{MAS} + \frac{1}{2m+\lambda}\delta_{CoM}^{MQMAS}$$

Equation 2-28

where $\lambda = \frac{C_0^I(m)}{C_0^I(-\frac{1}{2})}$ and δ_{CoM}^{MAS} (F_2) and δ_{CoM}^{MQMAS} (F_1) are the CoM of the projection(s) on each dimension of the 2D spectra. The values of k and λ of 3QMAS for $I = {}^5/_2$ nuclei e.g. ^{17}O are $^{19}/_{12}$ and $-{}^3/_4$, respectively.

‡‡‡ It is not possible to compute the C_Q directly from Equation 2-28. Instead, the so-called quadrupole product P_Q ($C_Q\sqrt{1+\frac{\eta^2}{3}}$) can be computed exactly (see Equation 2-23).

2.5. NMR parameters calculation

2.5.1. DFT code CASTEP

CASTEP is a first-principles quantum mechanical code for calculating electronic structure related materials properties, designed on DFT plane-wave pseudopotential methods (Segall and Probert, 2002). As a first-principle method, CASTEP does not depend on any empirical data, but calculates the electronic structure solely from the fundamental assumptions of quantum mechanics. That being said, it is still impossible to exactly solve many-body Schrödinger equations without making sensible approximations. Since its new modular redevelopment in 1999, the CASTEP code is now capable of calculating a series of physical properties of materials including total energy, electronic charge density, phonons, NMR parameter etc. and performing geometry optimisation and molecular dynamics tasks (Clark *et al.*, 2005).

2.5.2. DFT and plane-wave pseudopotentials

First of all, CASTEP adopts the Born-Oppenheimer (BO) approximation (Kohn and Sham, 1965) such that nuclei and electrons in a system could be treated separately because of the drastically different mass of these two kinds of particles. Since nuclei are massive and slow relative to electrons, the necessity of solving time-dependent Schrödinger equations for electrons is reduced to a time-independent problem in nuclear coordinates. Even with this simplification, solving many-electron time-independent Schrödinger equations is still an unfeasible undertaking. The idea of DFT is to deviate from solving the many-electron Schrödinger equation directly by building up a model in which each single electron can be feasibly treated by solving a single-particle Schrödinger equation. The real situation thus can be well simulated by integration/summation of each individual state, providing that good approximations are made.

In the Kohn-Sham scheme, at ground state, an interacting many-electron system can be equivalently represented by a set of non-interacting single electrons, each of which experiences an effective potential that results from the charge density ρ (ρ is a function of position r). If ρ[r] is identical to that in the true system, one only needs to solve the single-particle Schrödinger equation, even though this is needed for all the electrons in question as each one has its own energy state. This representation therefore can be explicitly described as

$$\hat{H}[\rho(\mathrm{r})] = \mathrm{V}_{\mathrm{kin}}^{\mathrm{non-int}} + \hat{V}_{\mathrm{eff}}[\rho(\mathrm{r})]$$

$$\hat{H}[\rho(\mathrm{r})]\ \psi_{\mathrm{n}}(\mathrm{r}) = \epsilon_{\mathrm{n}}\psi_{\mathrm{n}}(\mathrm{r})$$

Equation 2-29

where $\hat{H}[\rho(\mathrm{r})]$ is the Hamiltonian, $\mathrm{V}_{\mathrm{kin}}^{\mathrm{non-int}}$ is the kinetic potential that arises from the non-interacting electrons that create the charge density and the effective potential being denoted as $\hat{V}_{\mathrm{eff}}[\rho(\mathrm{r})]$. ϵ_{n} and $\varphi_{\mathrm{n}}(\mathrm{r})$ are the total energy and wavefunction of the n-th 'non-interacting' electron. The key is to figure out the exact form of $\hat{V}_{\mathrm{eff}}[\rho(\mathrm{r})]$ as $\mathrm{V}_{\mathrm{kin}}^{\mathrm{non-int}}$ (or the non-interacting kinetic energy) can be computed exactly (Segall and Probert, 2002). For the electronic states, which are what we aim to obtain using CASTEP code, the effective potential can be further divided into a few contributors as

$$\hat{V}_{\mathrm{eff}}[\rho(\mathrm{r})] = \hat{V}_{e-e}^{non-int}[\rho(\mathrm{r})] + \hat{V}_{\mathrm{e\text{-}n}}[\rho(\mathrm{r})] + \hat{V}_{\mathrm{xc}}[\rho(\mathrm{r})]$$

Equation 2-30

where $\hat{V}_{e-e}^{non-int}[\rho(\mathrm{r})]$ is the charge density potential from the other 'non-interacting' electrons, $\hat{V}_{\mathrm{e\text{-}n}}[\rho(\mathrm{r})]$ is the nuclei potential and $\hat{V}_{\mathrm{xc}}[\rho(\mathrm{r})]$ is the so-called exchange-correlation potential. We can rewrite the more familiar form of the total ground state energy E_0 in DFT frame as

$$E_0[\rho(\mathrm{r})] = \mathrm{E}_{\mathrm{kin}}^{\mathrm{non-int}} + \mathrm{E}_{\mathrm{e\text{-}n}}[\rho(\mathrm{r})] + \mathrm{E}_{\mathrm{e-e}}^{\mathrm{non-int}}[\rho(\mathrm{r})] + \mathrm{E}_{\mathrm{xc}}[\rho(\mathrm{r})]$$

Equation 2-31

So far, we can explicitly compute every term on the right-hand side of Equation 2-31 except for the exchange-correlation functional $\mathrm{E}_{\mathrm{xc}}[\rho(\mathrm{r})]$. The whole problem now is directed to figuring out the exact form of $\mathrm{E}_{\mathrm{xc}}[\rho(\mathrm{r})]$ but unfortunately this is not known and approximations have to come into place.

The fact that atoms and charge density are periodically arranged in most solids is exploited so that Bloch's theorem applies. According to Bloch's theorem, the wavefunction can be represented as

$$\psi_{\mathbf{k}}(\mathbf{r}) = e^{\mathrm{i}\mathbf{k}\mathrm{r}}\, u_{\mathbf{k}}(\mathbf{r})$$

Equation 2-32

where $u_{\mathbf{k}}$ is a periodic function that is commensurate with the lattice periodicity i.e. $u_{\mathbf{k}}(\mathbf{r}) = u_{\mathbf{k}}(\mathbf{r} + \mathbf{R})$ with $\mathbf{R}$ being an arbitrary lattice vector. $e^{\mathrm{i}\mathbf{k}\mathrm{r}}$ a phase factor because only magnitude of the wavefunction is truly periodic not their phases.

A basis set of plane-waves is adopted in CASTEP and the choice for the periodic function $u_{\mathbf{k}}$ has the form

$$u_{\mathbf{k}}(\mathbf{r}) = \sum_{\boldsymbol{G}} c_k(\boldsymbol{G}) e^{i\boldsymbol{G}r}$$

Equation 2-33

Therefore, we have

$$\psi_{\mathbf{k}}(\mathbf{r}) = \sum_{\boldsymbol{G}} c_{\mathrm{k}}(\boldsymbol{G}) e^{i(\boldsymbol{k}+\boldsymbol{G})r}$$

Equation 2-34

where c_k's are the Fourier coefficients and the exponential term is the plane-wave of wavenumber $\boldsymbol{k}$, while $\boldsymbol{G}$ is the reciprocal lattice vectors ($\boldsymbol{G}$-vectors). The quality of electronic state calculations then depends on the number/density of $\boldsymbol{k}$ sampled in the first Brillouin zone (k-points sampling) and the number of $\boldsymbol{G}$-vectors included for representing the plane-wave functions (Moran, Dawson and Ashbrook, 2017). Therefore, all calculated results must be convergence tested against these two parameters[§§§] to achieve accuracy and, hence, reliable results.

One of the disadvantages of using plane-waves is that the number of plane-waves, hence the number of $\boldsymbol{G}$-vectors, needed is determined by the greatest curvature of the wavefunction (Segall and Probert, 2002). Very large $\boldsymbol{G}$ components are required for the area close to nuclei where there are strong Coulomb potentials. Two approximations have been made in order to increase calculation efficiency with very little loss in accuracy (Kohanoff, 2006). Firstly, 'core' electrons within a defined atomic region close to nucleus are 'frozen' so that only valence electrons are explicitly calculated. Secondly, the rapid oscillations of valence electron waves close to nucleus are 'smoothed' out. Both simplifications are valid because tightly bonded 'core' electrons are largely unaffected in different chemical environments and electron waves in the near-nucleus region are not directly relevant to chemical bonding. Therefore, a smooth effective potential can be defined in the near-nucleus region to achieve these two goals at the same time: 1. To replace the strong nuclear Coulomb potential and 2. To provide the same screening effects of 'core' electrons on the valence ones. Such a potential is called a pseudopotential and this methodology is adopted in the CASTEP code.

[§§§] In setting up a CASTEP calculation, the exact number and grid of k points can be specified; the number of G-vectors is manifested in the cut-off energy *E*cut which sets the highest kinetic energy of the plane-waves in the basis set.

2.5.3. Calculating NMR parameters using CASTEP

Despite the success in increasing calculation efficiency by adopting pseudopotentials, the high sensitivity of NMR parameters, especially chemical shielding, to the near-nucleus electrons requires a full treatment of all electrons. The so-called Projector Augmented Wave (PAW) method (Van De Walle and Blöchl, 1993) treats this inconvenience explicitly by applying a linear transformation operator on the pseudised wave functions, the functionality of which is to map it onto the corresponding all-electron wave functions so that the latter is reconstructed. The breakthrough in the calculation of the magnetic response of all-electron wave functions reconstructed from PAW came about with the integration of a field-dependent transformation operator to account for the gauge origin problem, such as the Gauge Including PAW (GIPAW) method (Pickard and Mauri, 2001). The 'pseudopotential + GIPAW' method is adopted in CASTEP magres (magnetic resonance) modules for calculating NMR parameters including isotropic chemical shift, chemical shielding, J-coupling and electric field gradient (EFG) tensors. In some cases, it has provided exceptionally good agreement with experimental results, including ^{17}O NMR parameters (Profeta *et al.*, 2002; Ashbrook *et al.*, 2007). An example from the latter author(s) is shown in Figure 2-11.

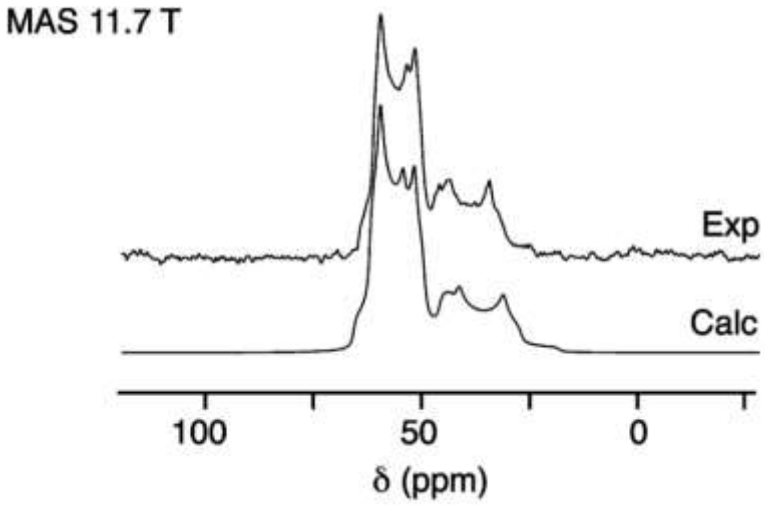

Figure 2-11 Comparison of experimental and simulated ^{17}O MASNMR spectrum (11.7 Tesla) of forsterite (α-Mg_2SiO_4). The simulated spectrum was composed of three sub-spectra corresponding to three oxygen sites, and was based on the calculation using DFT CASTEP code which employs GIPAW algorithm (adapted from (Ashbrook *et al.*, 2007)**).**

2.6. Dissolution data treatment

2.6.1. Product Consistency Test Method B protocol

The Product Consistency Test (PCT) is a designated protocol by ASTM International for determining the chemical durability of nuclear, hazardous and mixed waste glasses and

multiphase glass ceramics by measuring the concentration of chemical species released into solutions. Its Method B (PCT-B) allows flexibility in terms of test durations, temperatures, particle sizes and masses of sample as well as leachant volumes and compositions (ASTM C1285-02, 2002). This protocol has been utilised worldwide in nuclear waste glass community and is adopted here as well. In addition to the rigorous requirements for setting up the dissolution experiments in accordance with PCT-B, it also explicitly lays out the methods for treating the dissolution data. By following the protocol, it maximises the comparability between the results obtained from different experimental setups across different laboratories.

Instead of presenting the concentration data in standard chemical concentration units i.e. mol per unit volume, for example, mol/L or g/L, it is recommended in the protocol to convert the absolute concentrations C_i into normalised release (NL_i) by taking the surface area to volume ratio (SA/V) and the mass fraction (f_i) of the chemical species i in the glass originally into account. The NL_i values can then be compared between different glass compositions to determine their relative durability over the time considered. The relations between these two terms are

$$NL_i = \frac{C_i}{f_i * (SA/V)} \text{ [****]}.$$

Equation 2-35

By applying the units g/L, m^2/L for C_i and SA/V, respectively, NL_i is given in g/m^2, which translates into amount of glass (in mass) dissolved per surface area exposed to dissolution agent. Geometrically, the total surface area in cm^2 is determined by the median diameter d (cm), the glass density ρ (g/cm^3), the total mass m (g) and assuming a spherical shape of the particles[††††], thus

$$SA = \frac{6m}{\rho d}.$$

Equation 2-36

2.6.2. Equivalent dissolved thickness

The SA/V ratio in Equation 2-35 is not a constant throughout the course of the dissolution processes, especially for long-term dissolution. The ratio decreases with time as greater fractions of the pristine glass are altered/dissolved and, hence, should be corrected for the NL_i

[****] The concentrations are corrected from the raw values for the loss of leachant and blanks.
[††††] Other methods are also used to determine the (specific) surface area experimentally.

calculations between sampling points. Jégou, Gin and Larché (2000) introduced the shrinking core model which corrects for the decreasing *SA*/*V* ratio by assuming a spherical shape of the glass particles and a uniform distribution of the altered glass. The resultant altered glass thickness (T) is calculated as follows:

$$R_p = (1\text{-}LF_B)^{1/3}R_0$$

$$T = R_0 - R_p$$

where R_0 and R_P are the original mean radius of the glass particles and the corresponding mean radius of the underlying pristine glass. LF_B is the leached fraction of boron calculated from the boron concentration in the leachate and the original boron content in the glass.

Chapter 3

3. Experimental Methods and Materials

3.1. Introduction

Apart from the MW25 full-component glass introduced in Chapter 1, the other glass samples were synthesized in our laboratory. The absence of crystallinity was checked by powder X-ray diffraction (XRD) and compositions were measured by various analytical techniques. These glasses were then leached in powder form at 90℃ in deionised water but with slightly different setups for different purposes and experimental constraints, which are discussed later. Elemental concentrations of post-leaching solutions were measured by ICP-MS (Inductively Coupled Plasma Mass Spectrometry). Altered glass powders were examined using XRD, SEM (scanning electron microscopy) and various multinuclear solid-state NMR techniques with the focus on the surface structures. Before the leaching experiments, glass samples were also characterised using NMR to obtain insights into the pristine glass structures. In order to characterise the precipitates on the glass surface, resulting from glass dissolution, theoretical NMR calculations were also carried out using the DFT-based ab initio code CASTEP version 17.21 and 18.1.

3.2. Glassmaking

All the glass samples were prepared using a laboratory chamber furnace (Lenton UAF 16/10). Based on their ^{25}Mg enrichment level, they can be divided into two categories: 1. Simplified series of MW25 with Mg/Ca substitution (natural abundance); 2. Simplified MW25 glass with ^{25}Mg enrichment.

3.2.1. Synthesis of the simplified Magnox waste glasses (see 1.4.2)

The simplified glass was prepared in an attempt to mimic the composition and microstructure of its full-component counterpart as closely as practically possible. The molar ratios between cations Si, B, Na, Al and Mg were fixed to be the same as in MW25 while all the rare-earth element (REE) load was represented by La on a charge-for-charge basis, including cerium, which was attributed its fully oxidised charge of 4^+. Other elements were neglected. In particular, paramagnetic metals such as Fe and Ni were omitted from the composition mapping

to facilitate the examination of the resulting glass structures with NMR spectroscopy[*]. The nominal composition is listed in Table 3-1. For the separate effect study described in Chapter 4, Mg was then systematically substituted by Ca on a molar basis to produce 0, 25, 50, 75 and 100 mol% Ca substituted simplified glasses. These are termed MgEM, Mg75Ca25, Mg50Ca50, Mg25Ca75 and CaEM, respectively. The precursors making up the glass include SiO_2 (Sigma Aldrich, 99.995%), $Na_2B_4O_7$ (Alfa Aesar, 99.5%), Al_2O_3 (Alfa Aesar, 99.997%), Na_2CO_3 (Alfa Aesar, 99.5%), MgO (Alfa Aesar Puratronic®, 99.997%)/$CaCO_3$ (Alfa Aesar, 99.5%) and La_2O_3 (Alfa Aesar, Reacton®, 99.999%) powders. The pre-mixed precursors were heated up in a controlled manner (10℃/min) in a 100 mL platinum90/rhodium10 crucible to 1500℃. Once the temperature was reached, the melt was poured onto a steel block and allowed to cool to room temperature to solidify. This solidified material was then broken up into pieces and re-melted, following the same procedure to reach 1500℃[†]. The second melt was then poured onto a heated steel block at 250℃ and left cooled to room temperature. Finally, the glassy products were annealed at 550℃ for 2 hrs and subsequently cooled slowly in the furnace over a period of 16 hrs to room temperature. The yield of each composition was between 20.0 and 22.0 g.

Table 3-1 The nominal composition of simplified MW25 glasses in cation mol%.

MgEM	Al_2O_3/Al	B_2O_3/B	La_2O_3/La	MgO/Mg	Na_2O/Na	SiO_2/Si
Oxide wt%	5.10	18.79	5.76	5.42	9.97	54.20
Cation mol%	4.87	27.58	1.72	6.54	15.38	43.91

3.2.2. Synthesis of the simplified ^{25}Mg-enriched MgEM

To facilitate ^{25}Mg NMR experiments, an isotopically enriched MgEM glass was also made using 96.9%[‡] ^{25}Mg-enriched MgO powder (Eur-isotop). Due to the limited amount of enriched material available (~120 mg), the preparation procedure for the ^{25}Mg-enriched MgEM glass was different to the big batches stated above: the mixed precursors, including the ^{25}Mg-enriched MgO, were transferred to a 10 mL platinum90/rhodium10 crucible and heat-treated in the same way as with the big batches. At the end of the first heating step, the melt was cooled in air in an uncontrolled manner to room temperature instead of being poured due to the fast solidification in a small crucible (i.e. large surface area to volume ratio). In order to minimise material loss,

[*] The unpaired electrons in Fe and Ni ions would impose significant broadening on the spectra of neighbouring nuclei i.e. paramagnetic coupling.
[†] The second melt was intended to increase the homogeneity of the final glass product.
[‡] The natural abundance of ^{25}Mg is ~10.0%.

a second melting was not performed. Finally, the vitrified product was annealed at 550℃ without being broken up for 2 hrs, before being slowly cooled in the furnace to room temperature. The total yield was about 2.0 g. The same procedure was followed as closely as possible to produce a corresponding non-enriched small batch for which composition of the enriched glass was determined without consumption of the precious enriched sample.

3.3. Pre-leaching characterisation

3.3.1. Glass amorphism

As a precautionary procedure, the glassy products described above were subjected to powder XRD scans[§] in order to check for the absence of crystallinity. The experiments were run on a D8 Advance Bruker powder diffractometer (θ/2θ), using Cu $K\alpha_1$ radiation, equipped with a monochromator and a solid-state detector. The powder samples were evenly dispersed on a low background sample holder using methanol. For the big batch, Brigden and Farnan (2014) conducted the experiments with the 2θ range set to be 10°~65° with a step size of 0.05° and a dwell time of 15 s. For the ^{25}Mg-enriched MgEM glasses, the 2θ range was set to be 10°~60° at a step size of 0.08° and a dwell time of 160 s.

3.3.2. Glass composition measurements

Glass compositions from the big batches were determined by a combination of solution-source ICP-MS after digesting the samples, LA (laser ablation)-ICP-MS and EPMA (Electron Probe Microanalysis). The details are available in (Brigden and Farnan, 2014). For determining composition of the ^{25}Mg-enriched MgEM glass composition[**] only solid methods were adopted, since lessons were learnt that acute volatilisation of Si and B takes place during acid digestion using 1:3 nitric acid (69% v/v):hydrofluoric acid (40% v/v). A Cameca SX 100 electron microprobe was used to obtain the concentration of all elements (cations) but B (light element) with an acceleration voltage of 15 keV, a beam current of 20 nA and a beam diameter of 10 μm. Standards used for sodium, silicon, magnesium, aluminium and lanthanum were jadeite, diopside, periclase, corundrum and lanthanum hexaboride, respectively. Fifteen analysing points were randomly selected on a single polised (μm) glass chip. LA-ICP-MS was further used to determine the accurate concentration of B and Na in the same sample, with the results internally normalised to the Si concentration measured with EPMA. A laser ablation system

[§] Glass products were crushed into powder form for PCT-B leaching experiments (see 3.4).
[**] The ^{25}Mg-enriched small batch of MgEM was used for the composition measurements.

(ESI NWR193UC) connected to an ICP-MS (Perkin-Elmer NexION 350D) was equipped with an 193 nm Excimer laser source using NeF gas. NIST 614, 612, 610 and BCR-2G standard glasses were used for calibration. 10 randomly selected 50 µm squares were ablated with a fluence of 10 $J \cdot m^{-2}$, an interrogation time of 5 s and a dwell time of 10 ms.

3.3.3. Glass density measurements

The density of all the simplified glasses including the ^{25}Mg-enriched MgEM glass were determined by Archimedes principle using room temperature deionised water as the immersion liquid. The actual temperatures at which the measurements took place were between 22.0 and 23.0℃. Accordingly, the water density was assumed to be 0.998 g/cm^3 (NIST, 2018) for glass density calculations. Two pieces of each glass were weighed using an analytical balance (Ohaus, Pioneer) in air twice and in water three times to get the average readings. The final density was determined by averaging the results from the two pieces.

3.3.4. SEM imaging

SEM images were collected from washed and dried glass particles on a FEI QEMSCAM 650F SEM instrument using secondary electron (SE) and backscattered electron (BSE) collectors. Due to the non-conducting nature of the glass samples, instead of coating the glass surface with conducting agents, the images were taken in low vacuum mode to minimise charging effects. Other minimisation measures included low operating voltages (typically 3 keV) and large working distances (typically 10.0 mm), without compromising the image qualities.

3.3.5. Probing the structure of simplified pristine glasses by NMR

For the separate effect study described in Chapter 4, it is crucial to understand the structural changes at an atomistic scale in the simplified glass series. The solid-state NMR experiments were mainly performed on two instruments: Varian Infinity Plus spectrometer equipped with an 11.7 Tesla (500 MHz[††]) magnet and Chemagnetics Infinity spectrometer equipped with a 9.4 Tesla (400 MHz) magnet. Both magnets are wide bore (89 mm diameter), compatible with a series of Chemagnetics solid-state MAS double-resonance (DR) probes ranging from 2.5 mm to 7.5 mm as well as a DR Bruker Ultrafast spinning 1.3 mm probe. The different sizes refer to the external diameter of the zirconia rotors (sample container) that are compatible with and situated in the coil in the corresponding probe head, where a sample receives amplified and

[††] It is customary to use the ^1H Larmor frequency in the magnet to specify the strength of the magnetic field.

phase controlled RF radiations generated from the spectrometer. The assortment of rotors used for experiments performed on these two systems is shown in Figure 3-1.

Figure 3-1 Rotors of different sizes (1.3, 2.5, 3.2, 4.0 and 7.5 mm from right to left) used for NMR experiments performed on the 500 MHz and 400 MHz systems.

For the pristine glass structures, a multinuclear approach was adopted to focus on the local environments of B, Na, Al and La. Furthermore, the Mg environments in the MgEM (including the ^{25}Mg-enriched glass) and MW25 glasses were investigated using an 850 MHz widebore solid-state system at the National NMR Facility, University of Warwick. The enrichment in ^{25}Mg also enabled the ^{25}Mg NMR experiments to be conducted using the 500 MHz system.

3.3.5.1. ^{11}B NMR

^{11}B MAS NMR spectra were collected on the Varian InfinityPlus system operating at a Larmor frequency of ~160.3 MHz using a 3.2 mm MAS probe. Particles of the simplified glasses (size fraction 75~150 μm) were packed into 3.2 mm rotors and spun at 20 kHz. Single-pulse excitations were applied with small pulse angle of $\frac{\pi}{20}$ (0.7 μs) at an RF power of ~35.8 kHz and a recycle delay of 5 s with 40 repetitions. In addition, acquisitions with the same setup for the simplified glasses but with 800 repetitions were also applied for the pristine MW25 glass. The Fourier transformed spectra were referenced to $BF_3{\cdot}OEt_2$ in $CDCl_3$ as 0 ppm (via a secondary reference of -42.05 ppm for ^{11}B in a $NaBH_4$ compound).

3.3.5.2. ^{23}Na NMR

^{23}Na MAS NMR spectra were collected on the Chemagnetics Infinity system at 9.4 Tesla operating at a Larmor frequency of ~105.8 MHz using a 4.0 mm MAS probe. Fine particles

(<75 μm) of MgEM and CaEM glasses were packed into 4.0 mm rotors and spun at 12 kHz for single-pulse acquisitions. 1024 repetitions were made with a pulse angle of $\frac{\pi}{18}$ (0.75 μs) at an RF power of ~37.0 kHz. The recycle delay between each repetition was 1.0 s. The Fourier tranformed spectra were referenced to ^{23}Na in 1M $NaNO_3$ solution as 0 ppm.

3.3.5.3. ^{27}Al NMR

^{27}Al MAS NMR spectra were collected on the Varian InfinityPlus system operating at a Larmor frequency of ~130.2 MHz using a 2.5 mm MAS probe. Fine particles (<75 μm) of MgEM, Mg50Ca50 and CaEM glasses were packed into 2.5 mm rotors and spun at 15 kHz. Single-pulse acquisitions were applied with small pulse angle of $\frac{\pi}{18}$ (1.33 μs) at an RF power of ~20.8 kHz and a recycle delay of 0.3 s for 8192 repetitions. The Fourier transformed spectra were referenced to ^{27}Al in 1M $Al(NO_3)_3$ solution as 0 ppm.

3.3.5.4. ^{139}La NMR

Due to the efficient spin-spin relaxation (short T_2) and the limited spinning speed (up to 25 kHz for the 2.5 mm rotors) achievable, static Hahn echo experiments on the Varian InfinityPlus system were performed and operated at 79.6 MHz to obtain ^{139}La NMR spectra. Because the total La cation concentration was below 2 mol% for the simplified glasses, a 7.5 mm probe was used to maximise the signal intensity at reasonably high pulse powers. Fine particles (<75 μm) of MgEM, Mg50Ca50 and CaEM glasses were packed in 7.5 mm rotors for static acquisition. The pulse power was set to the maximum at ~40.0 kHz so that the solid 90° pulse was 1.6 μs. The nominal tau time between the 90° and 180° pulses was practically determined to be 12 μs to recover a decent amount of signal, as the echo forms without exceeding the spectrometer limits[‡‡]. The recycle delay was set at 0.2 s with 335550, 403288 and 407472 repetitions for CaEM, Mg50Ca50 and MgEM glass, respectively. All Fourier transformed spectra were referenced to ^{139}La in 1M $LaCl_3$ solution as 0 ppm.

3.3.5.5. ^{25}Mg NMR

Three glass samples were subjected to ^{25}Mg MAS NMR examination, including natural abundant and ^{25}Mg-enriched MgEM as well as MW25. ^{25}Mg has a very low NMR sensitivity due to its low natural abundance (~10.0%), large quadrupole moment (199.4 mbarn) and in particular, extremely low Larmor frequency (~30.6 MHz at 11.7 Tesla). Combined with the low

[‡‡] tau is limited by the 90° and 180° pulse lengths and was experimentally determined/set to be 12 μs.

concentration (~6.5 mol%) of Mg in the glass, acquiring the ^{25}Mg signal at natural abundance and 11.7 Tesla magnetic field is impractical. Therefore, both the unenriched and enriched samples were examined using the 850 MHz National Solid-State NMR Facility at the University of Warwick to increase the experimental sensitivity (the operating frequency was accordingly ~52.0 MHz). Further, double-frequency sweep (DFS) (Kentgens and Verhagen, 1999) was applied prior to excitation of the central transition in rotor-synchronised Hahn echo[§§] pulse sequence to increase the spin population difference between $\frac{1}{2}$ and $-\frac{1}{2}$ levels, hence the sensitivity, further. The spectra were referenced to ^{25}Mg in either 1M $MgCl_2$ solution as 0 ppm or in MgO oxide as a secondary reference at 26 ppm from 1M $MgCl_2$ (Mackenzie and Meinhold, 1994).

3.3.5.6. DMFIT

DMFIT (Massiot *et al.*, 2002) is a lab-developed programme for fitting and simulating 1D- and 2D-NMR solid-state spectra. It was used to fit the ^{11}B and ^{27}Al spectra and simulate the ^{17}O and ^{25}Mg[***] spectra to obtain quantitative information regarding inequivalent sites. The choice of a specific model for fitting depends on the specific spectrum in question, which will be specified where needed. It should be borne in mind that the computed models include non-linear dependencies on the fitting parameters. Therefore, the fitting solutions might not be unique and depend on the starting parameters.

3.4. Leaching experiments

3.4.1. Glass crushing, sieving and washing

All the glasses made as outlined in 3.2 were crushed and ground then sieved to the size range of 75~150 μm (U.S. Standard Screen Size 200 and 100). After the sieving procedure, the sized glass particles were washed in a controlled manner with Type I deionised water and absolute ethanol according to the PCT-B (Product Consistency Test-Type B) protocol (ASTM C1285-02, 2002) in order to remove adhering fines and contaminants from crushing and grinding. After rinsing, the washed glass particles were dried in a laboratory box oven at 90℃ for 24 hrs and stored in glass vials prior to leaching experiments. In the meantime, SEM (secondary electron)

[§§] Probe ringing is a problem particularly at low operating frequencies.
[***] The latter two refer to the spectra obtained from post-leaching experiments.

images in Figure 6-1 show that, by following this protocol, the objective of washing the glass, to remove fine adhering particles, had been achieved.

3.4.2. Leaching of the simplified glasses

3.4.2.1. Short-term leaching

Short-term leaching experiments were designed to measure the initial dissolution rates of the simplified glasses. A sized glass sample of each composition ranging from 0.5 to1.0 g was leached in a sealed PFA (perfluoroalkoxy alkane) vessel in 100 mL 18.2 MΩ deionised water at 90 $\pm$ 1℃. The whole system was agitated with a magnetic stirrer. This setup results in the *SA*/*V* ratios being no greater than 22 m^{-1} to ensure that the dissolution takes place in very dilute conditions, i.e. forward hydrolysis reactions are not hindered and the formation of barrier layers is precluded (Gin, Jollivet, Fournier, Berthon, *et al.*, 2015b). This should be the maximum dissolution rate (r_0) of the glasses under these conditions of temperature and leaching agent.

The values of r_0 were determined from the change in normalised release of Si (NL_{Si}) within the first 7.2 hrs of experiments. The shrinking core model was applied to correct for the change in *SA*/*V* ratio over time as dissolution proceeds as follows (Jégou, Gin and Larché, 2000):

$$\mathrm{AG}\,(t) = \mathrm{AG}\,(t\text{-}1) + \left[\frac{(C\mathrm{i}(t) - C\mathrm{i}(t-1)) * V}{m_0 * X\mathrm{i}}\right] \times 10^{-6}$$

$$\mathrm{ET}\,(t) = \frac{3}{\rho * SA} \times \left[1 - (1 - \mathrm{AG}(t))^{\frac{1}{3}}\right] \times 10^{3}$$

$$\mathrm{r}_0 = \frac{\mathrm{d}NL\mathrm{i}}{\mathrm{d}t} = \rho \times \frac{\mathrm{dET}\,(t)}{\mathrm{d}t} \times 10^{-3}$$

Equation 3-1

(AG – altered glass fraction; C_i– concentration of element i in leachate (mg/L); V – solution volume (mL); m_0 – initial mass of glass sample (g); X_i– mass fraction of element i in glass; *ET* – equivalent thickness of dissolved glass (nm); *SA* – initial specific surface area (geometric in m^2/g); ρ – glass density (g/cm^3); r_0 – initial dissolution rate ($g/m^2/d$); NL_i – normalised release of element *i* (g/m^2); *t* – time interval (d)). The rationale of using Si concentration rather than that of Na or B is to bypass the initial ion-exchange stage and reflect the direct dissolution of the glass network by hydrolysis.

3.4.2.2. Long-term leaching (see 1.4.2)

For long-term leaching experiments up to 112 days (16 weeks), a static batch of each duration including 7, 14, 28 and 112 days was set up to study the dissolution behaviour over these durations. A glass sample of each composition of 0.22~0.23 g was leached in 4.0 mL 18.2 Ω deionised water at 90 ± 1℃ in triplicate, with two blanks containing deionised water only for each batch. The glass-solution system was placed in a 5 mL PTFE (polytetrafluoroethylene) liner which was further sealed inside a stainless vessel to create a closed system without pH control. The vessels were then placed in customised aluminium blocks and heated to the target temperature in thermostatically controlled and calibrated heaters (Grant Instruments) and held for the corresponding durations. The system is shown in Figure 3-2. Based on the geometric surface area, a *SA*/*V* ratio of 1200 m^{-1} was targeted and applied in the analyses of the leaching data. In addition, leaching experiments on CaEM and MgEM glasses using ^{17}O-enriched (45%) water were also performed for the longest 112-day period to facilitate the ^{17}O NMR experiments for characterisation of the altered glass and precipitates. These experiments targeted the same *SA*/*V* ratio based on the geometric surface area as the other tests but on a smaller scale using PTFE liners of reduced volume (1 mL) because of the limited amount of ^{17}O-enriched (45%) water.

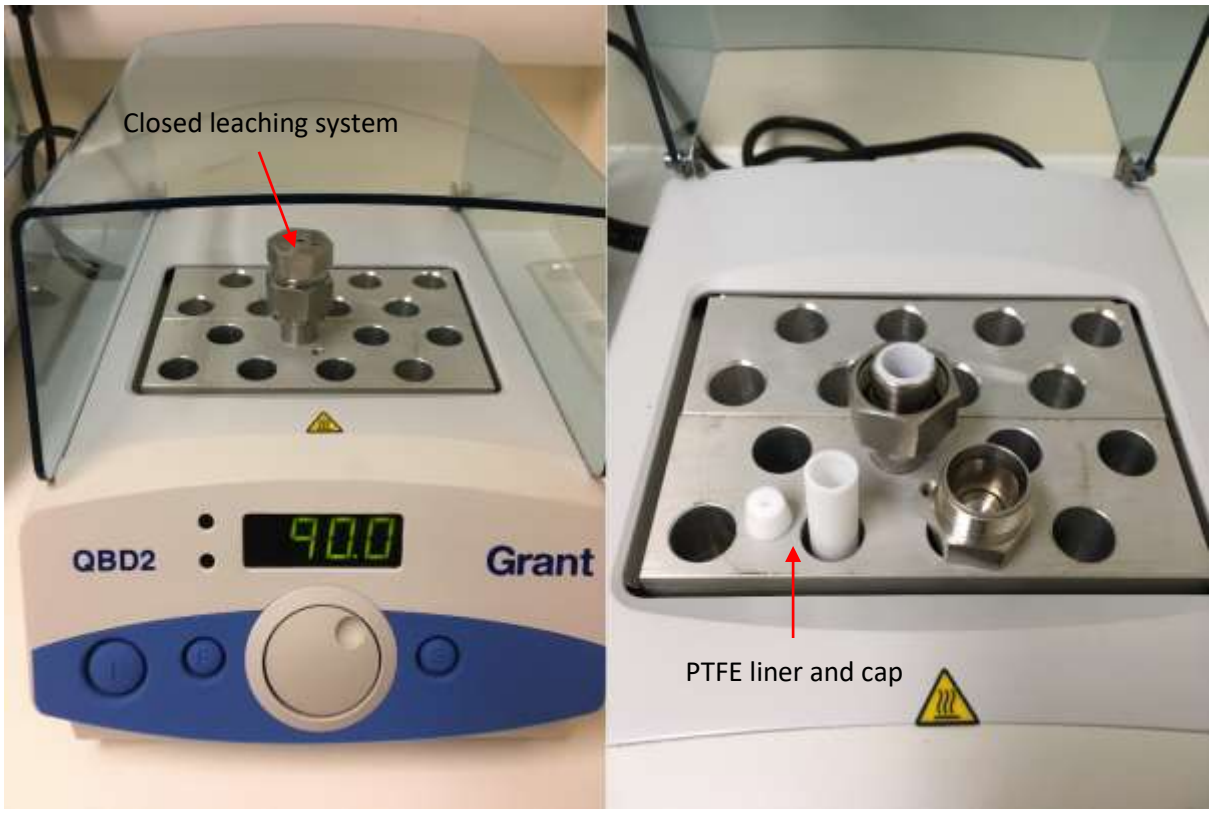

Figure 3-2 The PTFE liner and steel vessel system for conducting the long-term static batch leaching experiments.

After the leaching experiments were finalised for each batch, the system was allowed to cool to room temperature passively before removing the steel vessel and liner cap. Each leachate sample was then extracted using PVC (polyvinyl chloride) pump tubing attached to a 10 mL BD Plastipak™ Concentric Luer-lock syringe and filtered through a Whatman® Puradisc PVDF (Polyvinylidene fluoride) 0.45 micron pore-size filter to remove any entrained solid phase. The collected solutions were then subjected to elemental analysis (ICP-MS) and pH measurements.

3.4.3. Leaching of ^{25}Mg-enriched MgEM glass

Leaching of ^{25}Mg-enriched MgEM glass followed the same procedure as for the non-enriched simplified glasses, in accordance with the PCT-B protocol, as well as for the pH measurements and elemental analyses. However, because of the limited amount of enriched sample, there were two changes made to the leaching setup. First, the amount of glass sample in each leaching vessel was reduced to 0.16 g and only two durations (triplicate batches) were set up: 4-week and 16-week, with one blank for each batch. Second, the volume of deionised water as the leaching agent was 3 mL instead of 4 mL to target the *SA*/*V* of 1200 m^{-1} based on geometric surface area. The theoretical median diameter of the sized fraction of glass particles should be 112.5 µm. However, in order to measure the real median size and verify this approximation, ~50 mg of the sized glass particle was used to measure the glass particle diameter distribution using a Malvern Instruments Mastersizer E. The results are schematically illustrated in Figure 3-3, with the median diameter determined to be 145.86 µm. Therefore, the total surface area used in calculating the normalised release of ^{25}Mg-enriched MgEM was based on the measured instead of theoretical values.

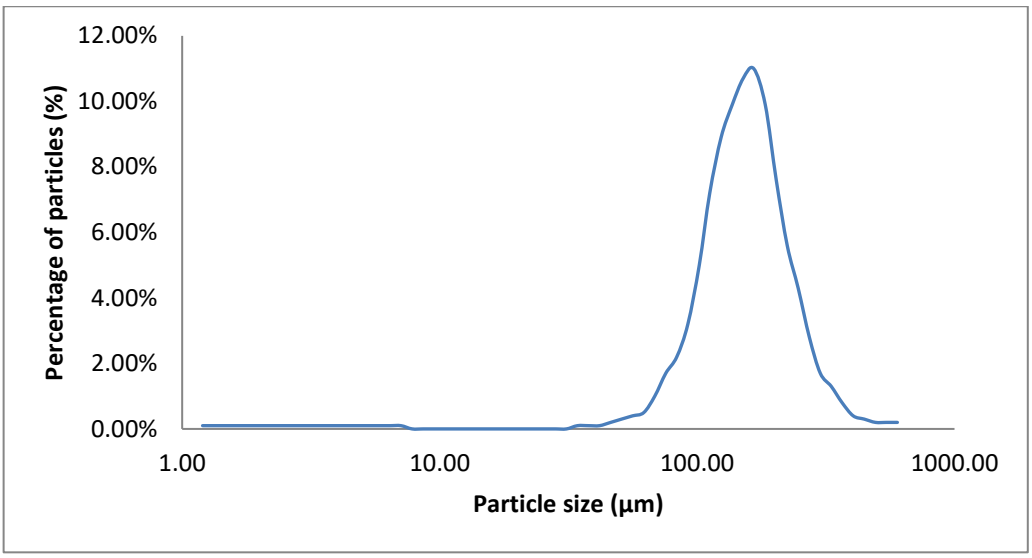

Figure 3-3 Particle size distribution of sized ^{25}Mg-enriched MgEM glass measured by using ~50 mg sample dispersed in industrial spirits in an enclosed cell on a Malvern Instruments Mastersizer E.

3.5. Post-leaching characterisation

3.5.1. pH measurements and elemental concentration analysis

The pH measurements and element/ion concentration analysis of the ^{25}Mg-enriched MgEM glass followed the methodology described in the previous study (Brigden and Farnan, 2014).

pH measurements were carried out as soon as practically possible after opening the reactor vessel, i.e. within 30 s. An aliquot of 1.1~1.2 mL filtered leachate of each sample was dispensed into a 5 mL PTFE beaker in order to cover the electrode tip of the pH meter (Mettler Toledo®). The probe was calibrated at room temperature using the NIST Traceable Liquid buffer of pH 7.00 and pH 10.00 prior to the measurements.

The remainder of the filtered leachates were dispensed into leak-proof 4 mL Kartell PE (polyethylene) scintillation vials and acidified by a dilution factor of 100 (volume) by adding ultra-clean quartz distilled 1% nitric acid (HNO_3) prior to ICP-MS analysis. The external standards were prepared using serial dilution from blank to 10 ng/mL from single element high purity standards (CPI International, California, USA) in 1% HNO_3. Two independently prepared quality control standards (SPS-SW2, LGC Standards and SCP Verification Mix, SCP Science) were repeatedly analysed throughout the run to check for calibration accuracy (~5 %) with a similar precision. Instrumental drift was less than 10 %, as measured for the raw intensity of the internal standards during the entire run (100 ppb Rh, In and Re in 1% HNO_3). The solutions were analysed using a Micromist FM05 micro-concentric nebuliser at a pump flow rate of 80 µL/min and a quartz cyclonic baffled spray chamber with nickel samplers and

skimmer cones. ICP-MS sensitivity in this configuration was 4.5 x 10^5 cps/ppb In with CeO/Ce ratios = 2.8%. Concentration results were calculated using the Syngistix 1.1 software with a simple linear calibration line and intercept set to zero. The raw intensities were blank subtracted and internal standard normalised before calibration calculations were performed. All results were also corrected for the dilution factors (i.e 100).

3.5.2. SEM and XRD

The same SEM imaging and XRD scans procedures were followed, as described in 3.3.1 and 3.3.4, to observe the surface features and detect the alteration products of the post-leaching MgEM glass.

3.5.3. Probing the altered glass structures by NMR

The leached glasses were subject to extensive multinuclear NMR characterisations that focused on the altered layer on the glass surface. Especially, a large amount of effort was devoted to elucidate the oxygen environments using the samples leached in ^{17}O-enriched water. With the ability to spin the 1.3 mm rotors above 60 kHz, ^{1}H MAS NMR experiments were conducted at different spinning speeds to give more insights into the hydrogen species inside the altered layers. In addition, ^{25}Mg NMR signals from the altered glass on the surface were selectively detected by using CP pulse sequences on the 850 MHz system.

3.5.3.1. ^{1}H NMR

^{1}H MAS NMR experiments were performed on a Bruker Avance III console equipped with a 200 MHz magnet using the 1.3 mm ultrafast spinning probe. Both single-pulse excitation and Hahn echo experiments at 20 and 60 kHz spinning speed were applied to collect ^{1}H spectra of samples, including 4-week leached MgEM, 16-week leached MgEM and CaEM as well as the full-component MW25 and SON68. The operating frequency was ~200.1 MHz with a pulse power of ~111.1 kHz and 90° pulse of 2.25 μs. Recycle delay for the simplified glasses was 2.0 s while that for MW25 and SON68 glasses was 1.0 s. The rotors were also weighed as packed and unpacked to determine semi-quantitatively the hydrogen content in different samples. Besides, because of the ubiquitous presence of hydrogen, sample preparations were handled with care to reduce sources of contamination. However, the background signals were not specifically measured by running the same scans on empty rotors. Instead, they were selectively suppressed in Hahn echo experiments.

3.5.3.2. ^{29}Si NMR

^{29}Si CPMAS NMR spectra were collected using the 400 MHz systems with a ^{29}Si operating frequency of ~79.5 MHz using the 3.2 mm probe, on three samples, including talc (Fluka®, analytical specification of BP, Ph. Eur.), a magnesium-containing smectite (secondary precipitates recovered from leaching of AVM (Atelier Vitrification Marcoule) 10 glass (Thien *et al.*, 2010)) and 16-week leached MgEM glass. The matching power in all cases was adjusted to ~55 kHz after optimisations and the MAS rate was set at 5 kHz [†††]. The signal intensity and lineshape were monitored as a function of contact time from short, 0.5 ms, to long, 80.0 ms. Individual CP spectra for each sample were then obtained by applying the contact time that brought about the highest intensity and recycle delay at 1.5 s. Despite the fact that ^{29}Si can have notoriously long T_1's in rigid solid materials that do not contain paramagnetics, in the altered structure where protons are present the relaxation should be enhanced. The lineshapes at longer recycle delays were shown to be similar to those at 1.5 s even though with slight increase in intensity (<5 %, not shown). All spectra were secondary referenced to ^{29}Si in RTV rubber as -22.3 ppm (Hayashi and Hayamizu, 1991).

3.5.3.3. ^{25}Mg NMR

^{25}Mg MAS NMR spectra of the 112-day leached ^{25}Mg-enriched MgEM glass were collected on the 850 MHz National solid-state NMR Facility (operating frequency for ^{25}Mg of ~52.0 MHz). In addition, the same two 'known' hydrous Mg silicate samples investigated in the ^{29}Si experiments were also investigated. ^{25}Mg MAS rotor-synchronised and DFS assisted spin echo experiments were performed on the Mg-smectite, talc and 16-week leached ^{25}Mg-enriched MgEM glass using the same setup, with a recycle delay of 1.0 s (3.0 s for talc), and spun at 14 kHz. In addition, standard ^{1}H-^{25}Mg CP experiments were also performed under static condition on talc and the leached glass. The talc spectrum was collected after optimisation with respect to the matching condition, contact time (43 ms) and recycle delay (3.0 s) to achieve highest intensity without exploration of its effect on the lineshape. For the glass sample, a large number of repetitions (65536) with a recycle delay of 1.5 s were necessary to obtain a spectrum of acceptable *S*/*N*, hence no optimisation with respect to contact time was carried out. This was set to be 20 ms, due to time restraints. In addition, the enrichment enabled the 500 MHz system to be used to collect ^{25}Mg signal from the glass in pristine and leached conditions operating at ~30.6 MHz. For all three samples, a rotor-synchronised Hahn echo pulse sequence was used

[†††] ^{1}H decoupling during acquisition was not applied because of the corruption of the FID (the reasons were unknown).

with a pulse power of ~31 kHz. The spinning speed was set to 20 kHz, with a recycle delay of 0.5 s and 409600 scans.

3.5.3.4. ^{17}O NMR

^{17}O NMR sensitivity suffers from a combination of low natural abundance (0.037%) and relatively low frequency (~67.8 MHz at 500 MHz ^{1}H). Moreover, oxygen usually sits in asymmetrical (disordered) sites in silicate materials (glasses) leading to reasonably large EFGs, and thus broad lines, which renders the acquisition very difficult. Therefore, isotopic enrichment of the samples is usually required prior to solid-state ^{17}O NMR experiments. In this case, simplified glasses, including CaEM and MgEM, that had been leached in ^{17}O enriched water were investigated, which is not stochastic isotopic enrichment as usually employed for ^{17}O NMR studies of glasses. Rather ^{17}O water is used as a forensic leaching agent that reports signal from materials that have re-precipitated onto the glass surface from the leachate. These experiments were carried out using the 500 MHz system and 2.5 mm double-resonance probe. Single-pulse excitations were employed under both MAS (20 kHz) and static conditions. The pulse power was set to be ~71.5 kHz giving a $\frac{\pi}{18}$ pulse length of ~0.4 µs. Recycle delays of 0.5 s and 5.0 s were tested to find a faster acquisition approach without a noticeable compromise of lineshape and intensity. For static acquisitions, spin-echo spectra with and without ^{1}H decoupling and different echo delay times were obtained in an effort to differentiate oxygen of different bonding environments and relaxation efficiencies. The pulse power was chosen to be ~52.0 kHz, giving a 90° solid pulse length of 1.6 µs. ^{17}O NMR spectra of ^{17}O-enriched SiO_2 glass were also obtained as the reference for Si-O-Si type bridging oxygens. However, the spectra were acquired with a recycle delay of 5.0 s to compare with the corresponding spectra of the sample. A large proportion of the experiment time was spent on optimising and performing ^{1}H-^{17}O CP experiments to provide extra resolution and structural information, which is not available otherwise. The recycle delay was set to be 0.75 s after tests against longer values yielded the same lineshape and intensity. More details are provided and discussed in Chapter 6.

In addition, 3QMAS experiments were also trialled in an effort to increase the 1D spectral resolution. A z-filter 3QMAS pulse sequence was applied using the hypercomplex approach to create echo and anti-echo signals, by combining the signals from two consecutive acquisitions with a phase shift of $\frac{90^{\circ}}{2m}$ of the first pulse and further combining them to yield 2D pure absorption lines (Massiot *et al.*, 1996). The first and second pulses were applied at relatively

high RF power (~85.0 kHz) with a flip angle of 180° and 60°, respectively, based on the work by Amoureux and Fernandez (1998), which give the highest excitation and conversion efficiencies for triple-quantum coherences of $I = {}^5/_2$ nuclei. The 90° pulse was applied at a very low power (10.0 kHz), hence relatively long length, to selectively excite the central transition only. In addition, the t_1 increment was synchronised to the MAS rate (20 kHz) with one rotor period, i.e. 50 μs, to correctly form the echo and hence improve MQMAS experimental sensitivity and processed lineshape (Massiot, 1996). A total number of 128 increments were accumulated to ensure enough data points were collected to avoid truncation in the t_1 dimension.

3.6. CASTEP calculation setup

A few magnesium silicate structures obtained from American Mineralogist Crystal Structural Database (AMCSD) and Inorganic Crystal Structural Database (ICSD) were used as the starting structures. The choice of structures on which calculations were performed was based on the thermodynamic calculations using the available leaching data by PHREEQC code (Guo, 2015). The original .cif files were converted by using the cif2cell package (Björkman, 2011) to .cell files as the adopted structural format in CASTEP calculations. The jobs to run are defined by .param files that contain the keywords, identifiers and the corresponding values specifying the job including the type of calculation, cut-off energy, correlation functional etc. Finally, the jobs were submitted to a local cluster computer that composed of 2 nodes, each of which contains 12 Intel Xeon® X5650 CPUs for calculations. These were run in parallel mode using OpenVPN v2, and the parallelism was achieved using shared memory across cores on the same physical processor. Despite the limited capability locally, all the computational jobs were run in the CamGrid (*CamGrid — IT Help & Support*, 2018), which is made up of a number of Linux clusters including this one, each running a Condor middleware (*HTCondor - Home*, 2018). This provides the job scheduling and transparent workload distribution across the grid.

Since the crystallographic data were all obtained from open sources and given that NMR parameters are extremely sensitive to its short-range surroundings, calculations for as-obtained and geometry-optimised structures were both carried out for comparison. It has been well accepted that, for structures containing hydrogen atoms, geometry optimisation is mandatory to yield accurate calculation results (Bonhomme *et al.*, 2012) because of the limits in the accuracy of determining the hydrogen position within a crystal structure by XRD techniques. For each structure, convergence tests with respect to the cut-off energy and number of k points were carried out in order to obtain reliable calculation results. The cut-off energy was taken care of by setting the BASIS_PRECISION in the .param files to specify the precision of the

basis set, from the least precise level, COARSE, to the most precise level, EXTREME. The CUT_OFF_ENERGY, which would be specified otherwise, will then equal the highest cut-off energy associated with the level of precision for the pseudopotentials used in the calculation (Materials Studio, 2014). The number of k points was systematically increased in ‘single point’ calculations by specifying the mp_kpoints_grid dimensions (Monkhorst and Pack, 1976) until a satisfactory convergence was reached for both the total energy and stress of the system.

Chapter 4

4. Simplified glass structures and their effects on initial dissolution

Most of the work presented in this chapter has been published in the Journal of Non-crystalline Solids (Guo *et al.*, 2018), which was further modified to form this chapter.

4.1. Introduction

As introduced in Chapter 1, Mg is present in Magnox waste glasses and is suspected to be the main cause of the inferior long-term aqueous durability of the vitrified wasteform compared with Ca-based glasses e.g. SON68. However, the effect Mg would have on the pristine glass structure when substituted for its alkaline earth counterpart Ca is unclear. Furthermore, it is not known whether the compositional and any resultant structural change would have a significant impact on the long-term glass dissolution. The aim of this chapter is to look at these aspects by conducting a separate effect study of Mg and Ca on glass structure and initial dissolution rate with all other parameters being equal. This is achieved by investigating a series of simplified 6/7-component glasses based on the full-component simulant MW25 composition (see Table 1-1) and varying only in Mg/Ca content. The simplified glass that contains no Ca is named Mg endmember (MgEM) and its nominal composition is listed in Table 3-1. Based on the MgEM glass composition, a series of simplified glasses was made by substituting Ca for Mg, on an atom-for-atom basis, to produce 25, 50, 75 and 100 mol% Ca-substituted simplified glasses.

4.2. Pristine glass characterisation

4.2.1. Vitreous state of the glasses

The state of the ^{25}Mg-enriched MgEM glass was examined visually to be transparent and vitreous. Two pieces of as annealed products are shown in Figure 4-1. Further, the crushed glass powders, as prepared for NMR and leaching experiments, were examined using powder XRD to check for any devitrification of the glass. The results are shown in Figure 4-2, which shows a typical pattern of amorphous materials. The highly vitreous state of other simplified glasses from CaEM to MgEM from previous work was confirmed by Brigden and Farnan (2014).

Figure 4-1 Two pieces of the non-enriched analogue of ^{25}Mg-enriched MgEM glasses as made in small batch.

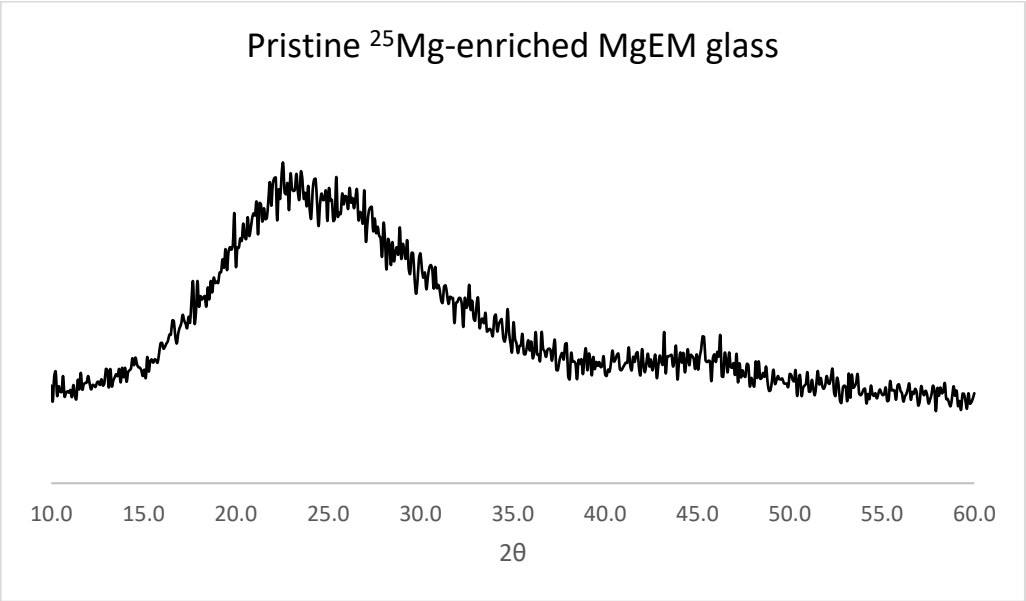

Figure 4-2 Powder XRD spectrum of the ^{25}Mg-enriched MgEM glass from 10.0 to 60.0° 2θ angle.

4.2.2. Nominal and measured glass composition

The nominal composition of the MgEM glass was chosen such that the cation molar ratios between Si, B, Na, Al and Mg were the same as in MW25, while the rare-earth load was represented by La^{3+} on a charge-for-charge basis. The other constituents in MW25 were then discarded in the simplified version. Although the glasses were synthesised aiming at the targeted composition, errors in weighing of the precursors and loss during mixing as well as volatilisation during the melting procedures were inevitable. Therefore, a combination of acid digestion/solution ICP-MS, LA-ICP-MS and EPMA techniques was used in order to fully

measure the compositions. For the ^{25}Mg-enriched MgEM glass, only the latter two techniques were utilised, as detailed in 3.3.2. The combined results are listed in Table 4-1.

Table 4-1 Nominal composition of the simplified MW25 glass (MgEM) and analysed compositions of the simplified glass series (cation mol%). Errors denote ±σ.

Cation (mol%)	Al	B	La	Mg	Ca	Na	Si
MgEM (Nominal)	4.87	27.58	1.72	6.54	-	15.38	43.91
MgEM	4.81±0.20	28.26±3.56	1.68±0.16	6.54±0.30	-	15.08±0.81	43.63±3.02
^{25}Mg-enriched MgEM	4.92±0.32	25.75±0.77	1.72±0.05	6.51±0.10	-	15.47±0.32	45.63±1.35
Mg75Ca25	4.82±0.35	28.32±6.64	1.66±0.17	4.24±0.32	1.57±0.11	14.80±1.20	44.61±5.59
Mg50Ca50	4.89±0.21	26.46±2.06	1.73±0.15	3.08±0.12	3.15±0.14	14.72±0.71	45.98±3.61
Mg25Ca75	4.93±0.24	26.24±2.40	2.01±0.42	1.57±0.07	4.78±0.23	15.28±0.82	45.18±4.33
CaEM	4.71±0.19	26.44±2.97	1.69±0.10	-	6.11±0.22	14.92±0.58	46.13±2.75

4.2.3. Measured glass density and simple substitution models

Since Mg/Ca is the only compositional variable, despite the deviations from the targeted compositions, changes in glass density are expected with changes in the Mg/Ca ratio. Table 4-2 lists the measured densities across the simplified glass compositions. On top of that, the predicted densities based on isomorphous and volumetric substitution of Ca for Mg are shown in Figure 4-3. For ease of illustration and discussion, the data is presented in a way that CaEM glass acts as the starting composition, as highlighted in Figure 4-3. The density shows a monotonic decrease from 2.56 g/cm^3 for CaEM to 2.49 g/cm^3 for MgEM glass, showing a lower density than predicted by either of these simple substitution models (see 4.4.1) and indicating a substantive structural change associated with the substitution of Mg for Ca.

Table 4-2 The measured density of the simplified glass series by Archimedes principle. Errors denote the upper and lower bound of the two measurements.

	CaEM	Mg25Ca75	Mg50Ca50	Mg75Ca25	MgEM

Density g/cm^3	2.560±0.005	2.550±0.001	2.531±0.001	2.510±0.002	2.486±0.002

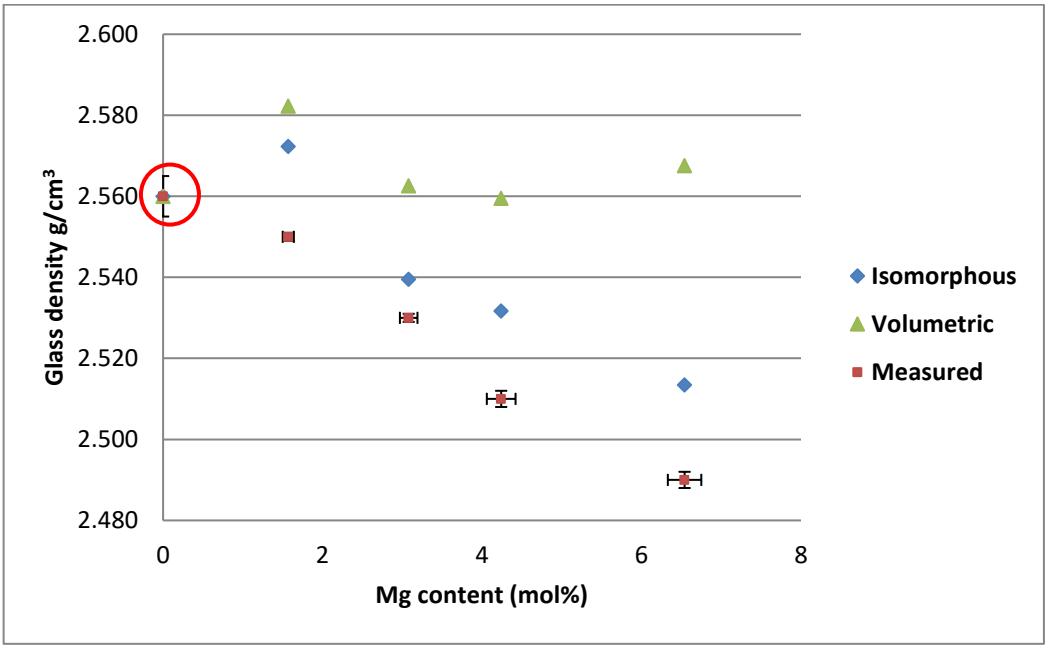

Figure 4-3 The measured glass densities as a function of Mg content and predicted densities based on: (i) an isomorphous substitution of Ca for Mg according to the molar mass of CaO and MgO; and (ii) a volumetric substitution which also takes the molar volumes of CaO and MgO into account.

4.2.4. Glass microstructure

4.2.4.1. Boron local environments

A stack plot of ^{11}B MAS NMR central transition spectra of three of the simplified glasses is shown in Figure 4-4 (a). Each spectrum consists of a narrow Gaussian-like peak centred at around 0 ppm which is attributed to B in 4-fold coordination ($^{[4]}$B) and a broadened quadrupole doublet centred at around 10 ppm which is attributed to B in 3-fold coordination ($^{[3]}$B) (MacKenzie and Smith, 2002). The broader $^{[3]}$B peaks arise from the anisotropic trigonal configuration of BO_3 units, which have larger EFGs compared with more symmetric BO_4 units with tetrahedral configuration. Each $^{[3]}$B peak is made up of contributions from ring and non-ring BO_3 structures, both of which contain a distribution of δ_{iso} as well as EFGs. The spectra are shown normalised to $^{[4]}$B intensities in order to compare the relative $^{[3]}$B intensity. The intensity of the $^{[3]}$B peak, which is directly proportional to the $^{[3]}$B fraction of total B in the glass, increases as more Mg is present. The intermediate glasses Mg75Ca25 and Mg25Ca75 are consistent with this trend but are omitted from the figure for clarity.

As shown, the central transition peaks of $^{[3]}$B and $^{[4]}$B signals are slightly overlapped. Additionally, due to the small EFGs associated with BO_4 units, the first-order satellite transition sidebands are present in the full spectrum as shown in Figure 4-4 (b). Quantification of either species therefore needs to take into account these two factors. It was achieved by curve fitting using DMFIT software by incorporating a quadrupole first-order spinning sideband manifold. An example of the fitting for MgEM glass is shown in Figure 4-5 for MgEM glass and the remainder are displayed in Appendix I. In Figure 4-5 (b), the QUAD 1st line (blue) is the isotropic part of the satellite transition manifold. Table 4-3 shows the full fitting results reported as the relative percentage of B in 3- and 4-fold coordination. Excess $^{[3]}$B stands for the excess cation mole percentage of $^{[3]}$B above that found in the CaEM glass.

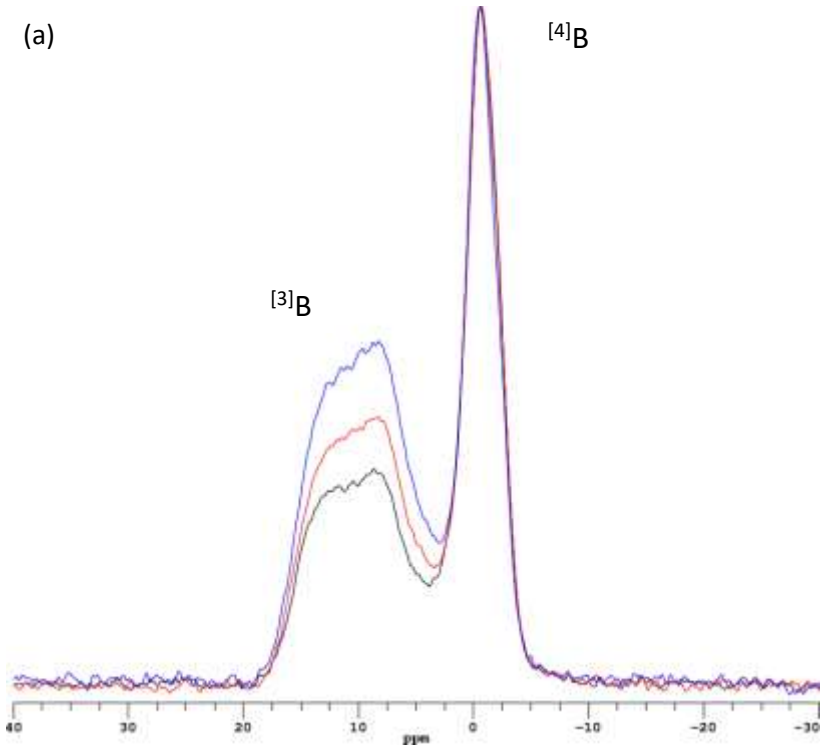

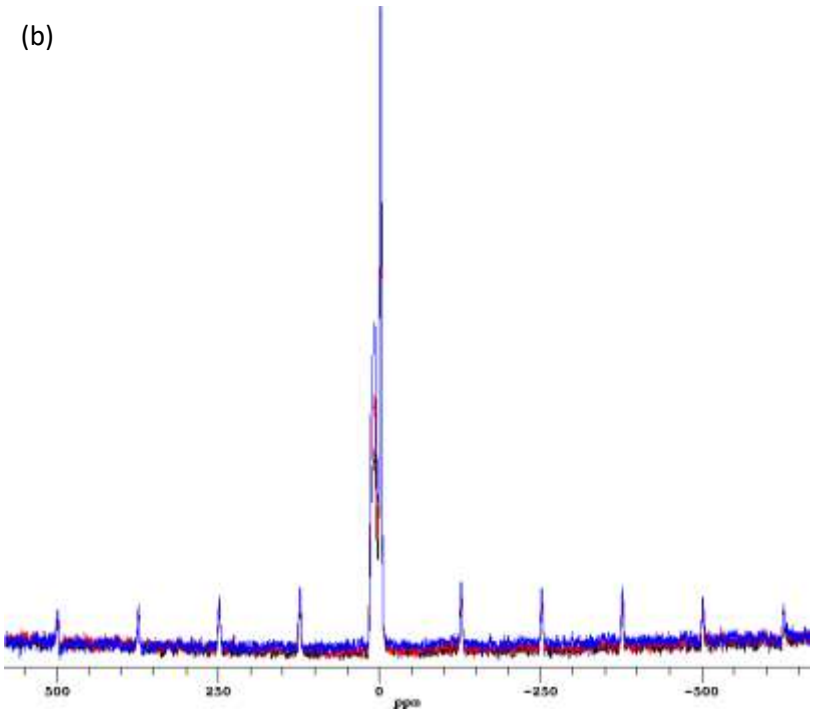

Figure 4-4 ^{11}B MAS NMR spectra of the simplified glasses CaEM (black), Mg50Ca50 (red) and MgEM (blue) obtained at 160.34 MHz with a MAS rate of 20 kHz. (a) The central transition lineshape of $^{[4]}$B and $^{[3]}$B peaks; (b) The full spectra that manifest the sideband manifold of ^{11}B satellite transitions. The intensities of the $^{[4]}$B peaks are normalised for comparison of the relative proportion of trigonal $^{[3]}$B.

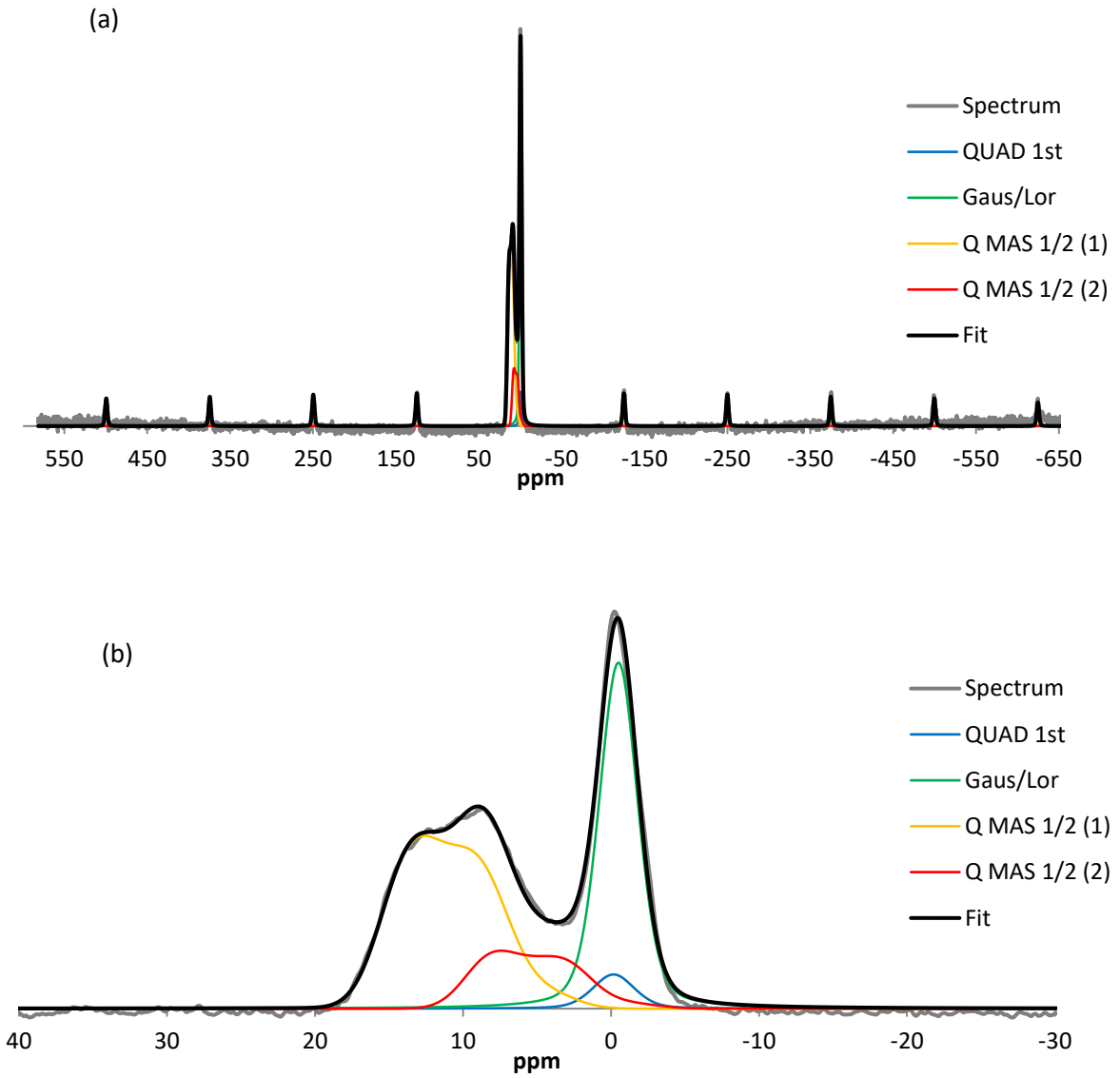

Figure 4-5 (a) ^{11}B MAS NMR spectrum of MgEM glass with its fit and sub-components. The fit is composed of four sub-components including one Quad 1st line, one Gaus/Lor line and two Q mas 1/2 lines; (b) Expansion of the centreband in (a) showing the 4 subcomponents.

Table 4-3 $^{[3]}$B and $^{[4]}$B proportions in the simplified glass series: 'fraction'-the proportion of $^{[3]}$B or $^{[4]}$B with respect to the total amount of boron; 'mole'-the molar amount of $^{[3]}$B or $^{[4]}$B with respect to 100 moles of cations in the glass as presented in Table 4-1 (analysed composition)

	CaEM	Mg25Ca75	Mg50Ca50	Mg75Ca25	MgEM
$^{[3]}$B fraction	48.3%	50.0%	55.0%	57.8%	61.7%
$^{[3]}$B mole	12.8	13.1	14.6	16.4	17.4
$^{[4]}$B fraction	51.7%	50.0%	45.0%	42.2%	38.3%
$^{[4]}$B mole	13.7	13.1	11.9	11.9	10.8

Excess $^{[3]}$B mole	0	0.3	1.8	3.8	4.6

Figure 4-6 illustrates the ^{11}B MAS NMR spectra of unleached and 112-day leached MgEM as well as MW25 glass. Drawn on an absolute scale adjusted for sample mass and number of acquisitions in Figure 4-6 (a), it is clear that the total spectral intensity drops for both B species after leaching, which highlights the fact that B was indeed lost from the glass*. On the other hand, the spectra as shown in Figure 4-6 (b) and (c) are normalised to make the $^{[4]}$B intensities equal. The ^{11}B spectra of both MgEM and MW25 glasses each show identical relative intensity before and after leaching. The much broader, and hence, poorly resolved lines of the MW25 spectra are due to the presence of paramagnetic ions in the full-component glass.

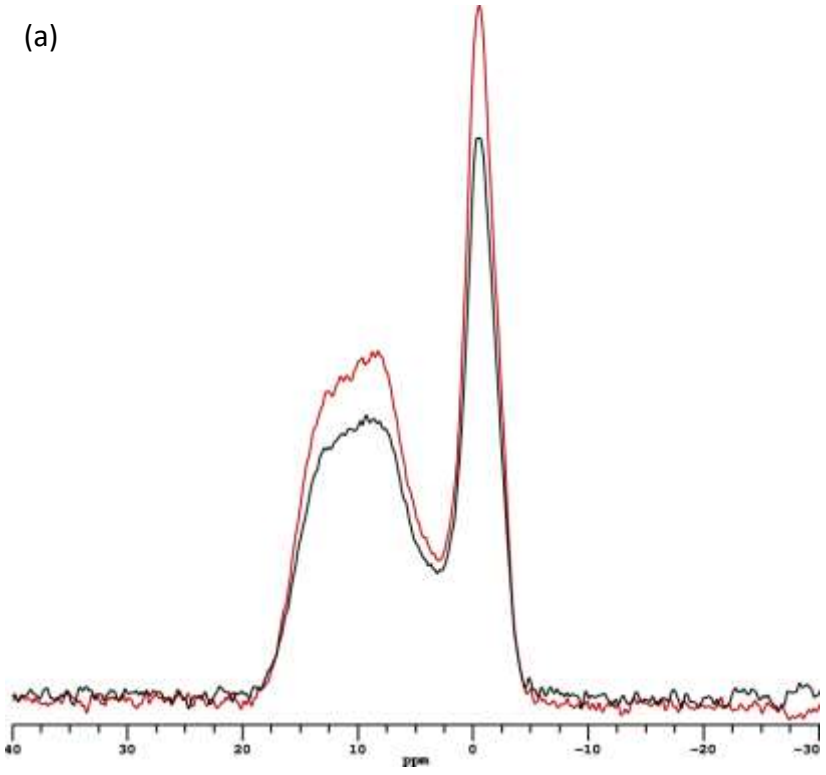

* Without the knowledge of alteration layer density which depends on its exact composition and structure, the exact difference in intensity cannot be quantitatively related to the concentration of leached boron. However, this comparison based on mass is validated in Chapter 5 by calculating the total alteration layer thickness.

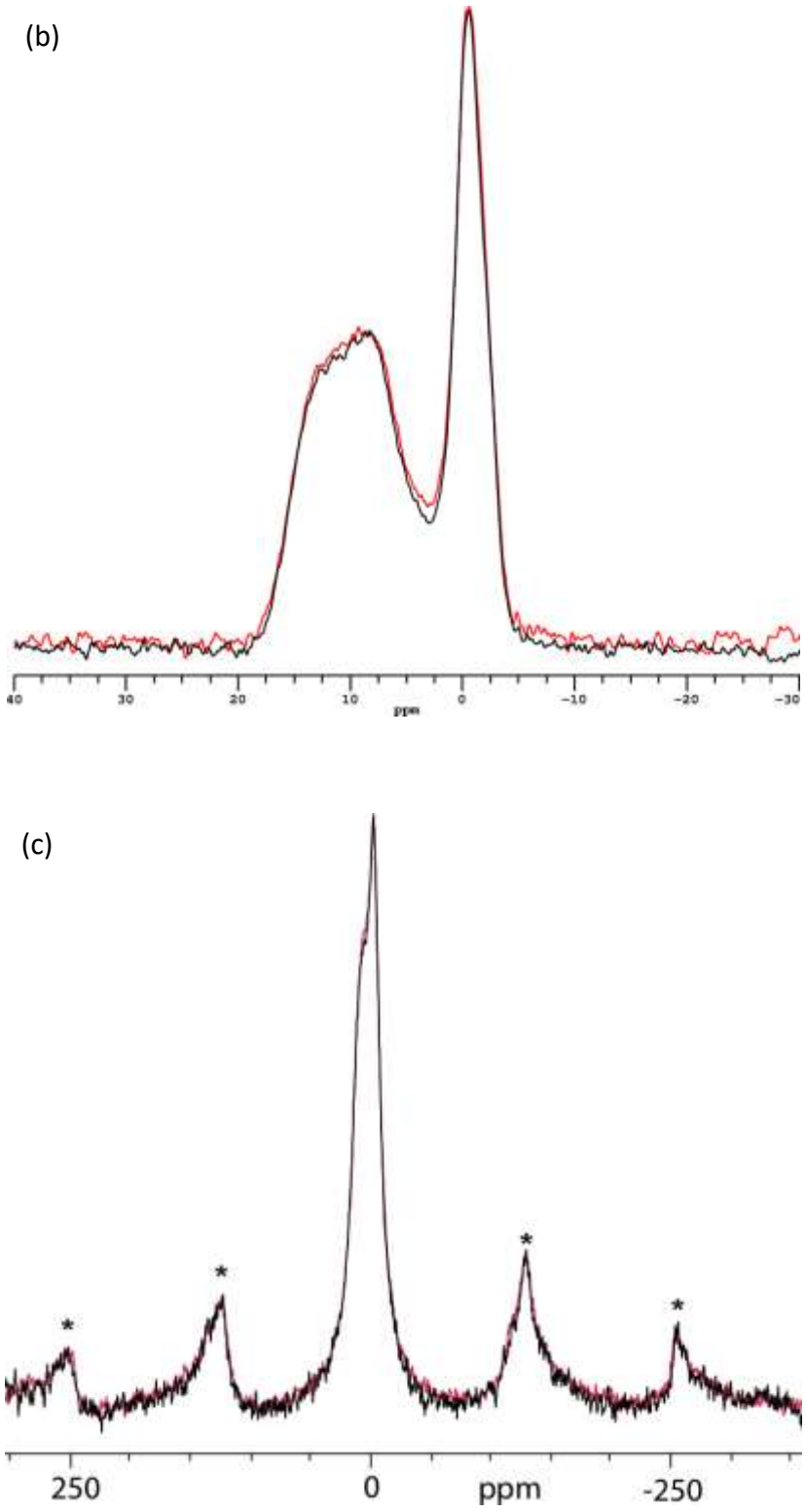

Figure 4-6 ^{11}B MAS NMR spectra of MgEM glass before (red) and after (black) the 112-day leaching experiments presented in (a) on an absolute scale and (b) normalised to make the $^{[4]}$B peak intensities equal, obtained with the same experiment setup as in Figure 4-4; (c) ^{11}B MAS NMR spectra of MW25 glass before (red) and after (black) the 112-day leaching experiments normalised to make the $^{[4]}$B intensities equal, spinning sidebands are denoted by asterisks.

4.2.4.2. Sodium local environments

Figure 4-7 shows the overlaid plot of 23Na MAS NMR spectra of CaEM and MgEM glasses. The centre peaks are coincident and centre at around -20 ppm, while δ_{iso} is estimated likely to be ~10.0 ppm[†]. A distribution of both δ_{iso} and EFGs, i.e. δ_{Qiso}, contributes to the total linewidth, as expected in glass structures. The spectra of intermediate compositions are identical to the two endmembers shown here, but have been omitted for clarity. Despite the distribution of interaction parameters that would affect the line appearance, the identical peak position, linewidth as well as lineshape clearly suggest that the local environments around Na are unchanged within the Mg/Ca compositional series of simplified glasses.

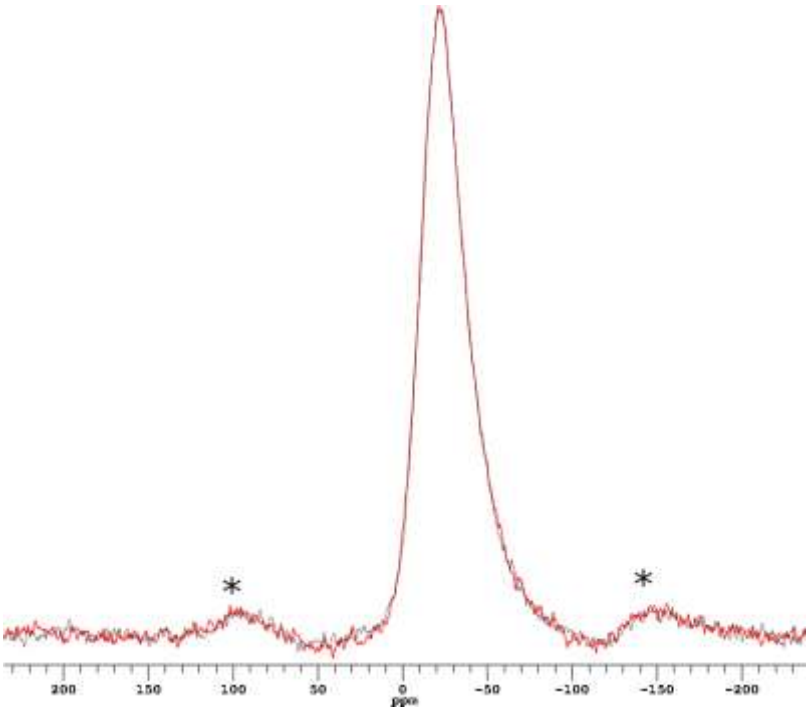

Figure 4-7 ^{23}Na MAS NMR spectra of simplified CaEM (red) and MgEM (black) glasses obtained at 105.82 MHz with 8192 π/18 pulse and 1.0 s pulse delay. Spinning speed was 12 kHz in both cases and the spinning sidebands are denoted by asterisks. Spectra are referenced to 1M $NaNO_3$ solution.

4.2.4.3. Aluminium local environments

^{27}Al MAS NMR spectra of Mg50Ca50 and the two endmember glasses are shown in Figure 4-8. Each spectrum consists of a predominant, well-defined 4-fold coordinated ($^{[4]}$Al) and much smaller 6-fold coordinated ($^{[6]}$Al) peaks, judged by their shift positions (MacKenzie and Smith, 2002). The presence of 5-fold coordinated Al ($^{[5]}$Al) is not evident but this could be due to the resolution limitations at a magnetic field of 11.7 Tesla. The spectra are presented on a scale

[†] The exact position is not important for comparison purposes.

with $^{[4]}$Al peaks normalised to the same height, to compare the minor changes in the concentration of the higher coordinated $^{[6]}$Al. The predominant Al species is $^{[4]}$Al, with δ_{iso} estimated to be ~70 ppm and a tiny fraction of $^{[6]}$Al with δ_{iso} of ~5 ppm‡. The shift position of $^{[5]}$Al, if there is any, should lie between these two boundaries. The coordination change for Al is observed as the Mg/Ca ratio changes: the relative fraction of $^{[6]}$Al in these three glasses ranks as CaEM > MgEM > Mg50Ca50 whilst the difference between the latter two is almost negligible (see the inset). Because the $^{[4]}$Al and $^{[6]}$Al peaks are not completely resolved, with a slight degree of overlapping at the low frequency end of the former, and from the appearance of the lineshape, there is a distribution of both δ_{iso} and EFG. The CzSimple model, which implements a Gaussian Isotropic Model to account for the probability and, hence, distribution of a (C_Q, η_Q) pair and uncoupled distribution of δ_{iso} (Neuville, Cormier and Massiot, 2004; d'Espinose de Lacaillerie, Fretigny and Massiot, 2008) in DMFIT was used to obtain the relative fractions of these two species§. The results for the three glasses are summarised in Table 4-4. The amount of $^{[6]}$Al decreases from 4.8% of total Al, or 0.2% of the total cations in the CaEM glass, to 1.6% and 0.7% or 0.08% and 0.03% in the MgEM and Mg50Ca50 glass, respectively. An example of the fit for CaEM glass is shown in Figure 4-9 and the total fitting results are listed in Appendix II.

‡ The exact positions are not important for comparison purposes. Besides, they are also dependent on NNN species.
§ The possibility and significance of $^{[5]}$Al being present in the glass is small, as discussed in 4.4.2.2.

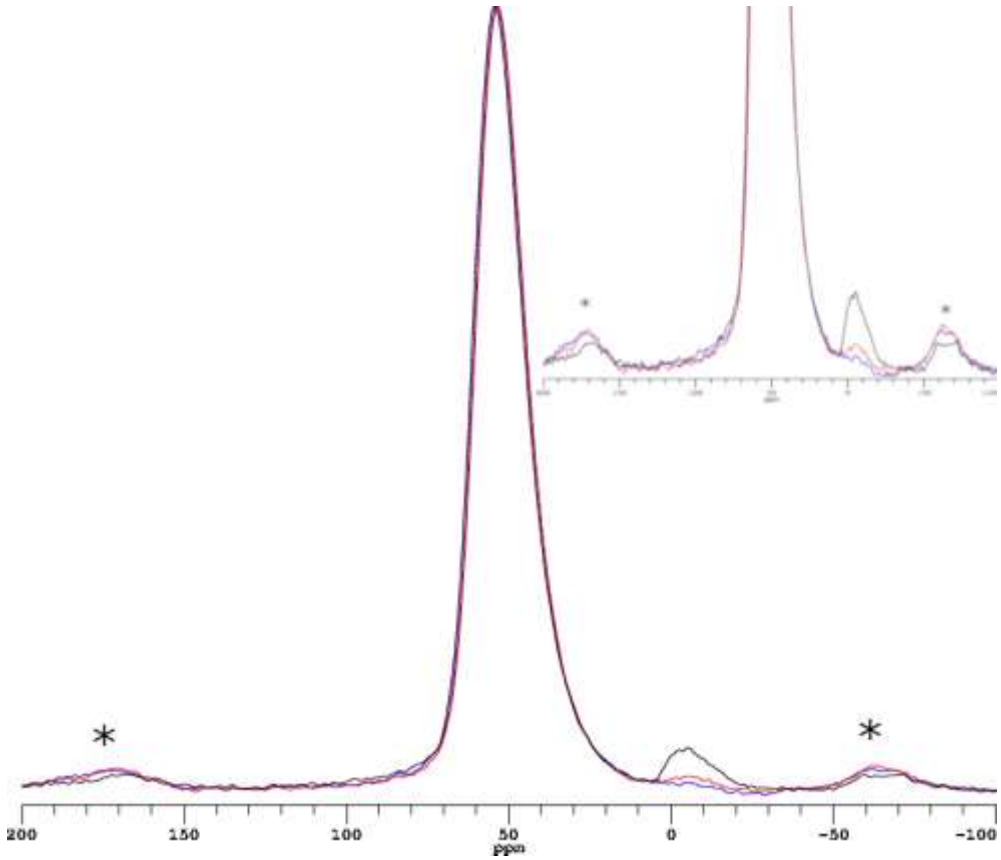

Figure 4-8 ^{27}Al MAS NMR spectra of simplified CaEM (black), Mg50Ca50 (blue) and MgEM (red) glasses obtained at 130.22 MHz with 8192 π/18 solid pulse and 0.3 s pulse delay. The four-coordinated Al peaks are normalised for comparison of the relative proportion of six-coordinated Al. Spinning speed is 15 kHz in all cases and the spinning sidebands are denoted by asterisks. Spectra are referenced to 1M $Al(NO_3)_3$ solution.

Table 4-4 The relative fraction and cation concentration of $^{[4]}$Al and $^{[6]}$Al in the MgEM, Mg50Ca50 and CaEM glassess

	$^{[4]}$Al/($^{[4]}$Al + $^{[6]}$Al)	$^{[4]}$Al/cation	$^{[6]}$Al/($^{[4]}$Al + $^{[6]}$Al)	$^{[6]}$Al/cation
CaEM	95.2%	4.5%	4.8%	0.2%
MgEM	98.4%	4.7%	1.6%	0.03%
Mg50Ca50	99.3%	4.9%	0.7%	0.08%

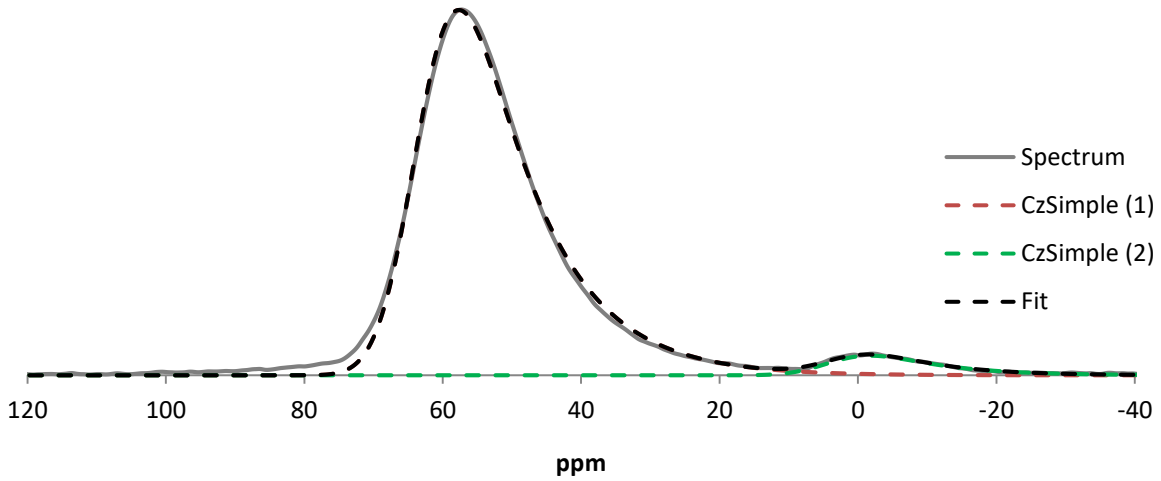

Figure 4-9 Curve fitting of the CaEM ^{27}Al MAS NMR spectrum with 2 CzSimple lines using DMFIT: $^{[4]}$Al in dashed red and $^{[6]}$Al in dashed green. The grey line is the experimental spectrum while the superimposed overall fit is displayed in dashed black.

4.2.4.4. Magnesium local environments

The similarity of Mg local environments in both simplified and full-component glasses is confirmed by the ^{25}Mg MAS NMR spectra shown in Figure 4-10. Within the *S*/*N* level, the overlaid spectra show similar position and linewidths which are consistent with a similar distribution of δ_{iso} and EFG and further indicate a similar coordination for Mg in both glasses. This confirms that MgEM is a good representation of MW25 from the Mg perspective. In addition, the shape of both lines, i.e. a sharp edge at the high frequency end and tails towards the low frequency end, is characteristic of a distribution of EFGs and η with rather similar δ_{iso} values. Despite both samples being spun at the same speed (14 kHz), spinning sidebands are just observable in the MgEM glass spectrum while absent for MW25. The appearance of the centre line and presence of spinning sidebands in the MgEM spectrum was confirmed by the ^{25}Mg-enriched MgEM spectrum[**], which clearly shows the benefit of isotope enrichment. In fact, in this case, an enrichment level of ~10 (96.9% vs 10.9%) for ^{25}Mg effectively increased the sensitivity by a factor of ~100, i.e. the same *S*/*N* level could be achieved by using the enriched sample in 1/100 of the time.

[**] The spectra acquired on the enriched glass samples were collected in a separate session at the University of Warwick 850 MHz facility. Nevertheless, the same DFS setup, rotor size and spinning speed were applied.

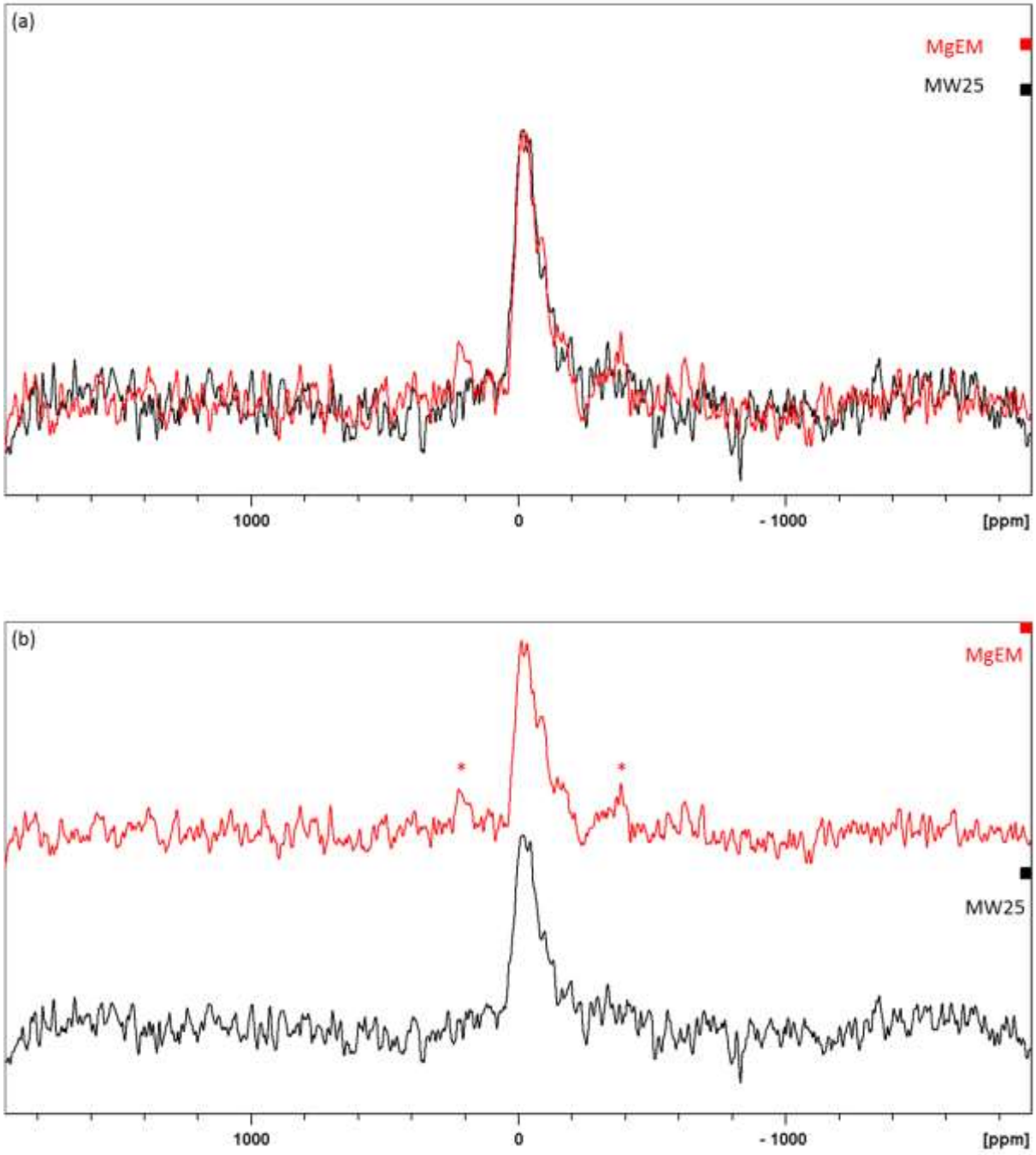

Figure 4-10 (a) Overlaid ^{25}Mg MAS NMR spectra of pristine MW25 and MgEM glasses obtained at 52.05 MHz with 54200 π/18 pulse and 0.1 s pulse delay and 102400 π/18 pulses and 1.5 s pulse delay, respectively. The spinning speed was the same at 14 kHz. Spectra are referenced to 1M $MgCl_2$ solution as 0 ppm; (b) The same spectra as shown in (a) stacked so that the spinning sidebands on the MgEM spectrum can be seen (denoted by asterisks).

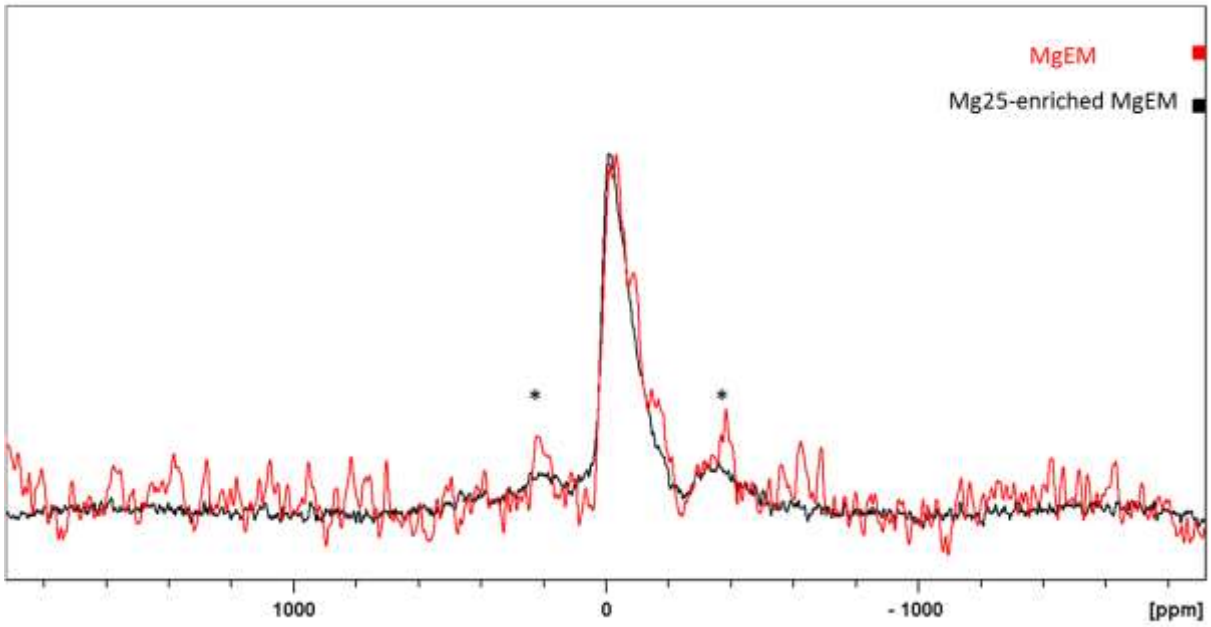

Figure 4-11 Overlaid ^{25}Mg MAS NMR spectra of pristine ^{25}Mg-enriched MgEM obtained at 52.05 MHz with 61440 π/18 pulse and 1.0 s pulse delay and natural abundant MgEM (as in Figure 4-10) glasses. The spinning speed was the same at 14 kHz. The spectrum of enriched glass was referenced to MgO oxide as 26 ppm.

4.2.4.5. Lanthanum local environments

The quadrupole moment of ^{139}La is comparable to that of ^{25}Mg but with 99.9% natural abundance and greater gyromagnetic ratio (i.e. higher operating frequency). However, the large number of electrons leads to a dual effect of large chemical shift anisotropy and an accentuation of the EFG generated from the surrounding nuclear charges due to polarisation of core electrons and, hence, large effective quadrupole interactions (Sternheimer, 1950). Therefore, NMR spectra of ^{139}La in disordered environments like glasses are expected to be very broad, which will severely hinder the resolution of different sites in a sample, even under fast MAS conditions. Hence the ^{139}La NMR acquisitions were performed under static conditions. The spectra shown in Figure 4-12 are, as expected, featureless and broad (FWHM: ~130kHz for CaEM and Mg50Ca50; ~170 kHz for MgEM). However, a clear shift to higher frequencies of the MgEM spectrum (peaked at ~1400 ppm) as opposed to the CaEM and Mg50Ca50 (peaked at 100~150 ppm) is observed, with the latter two being very similar.

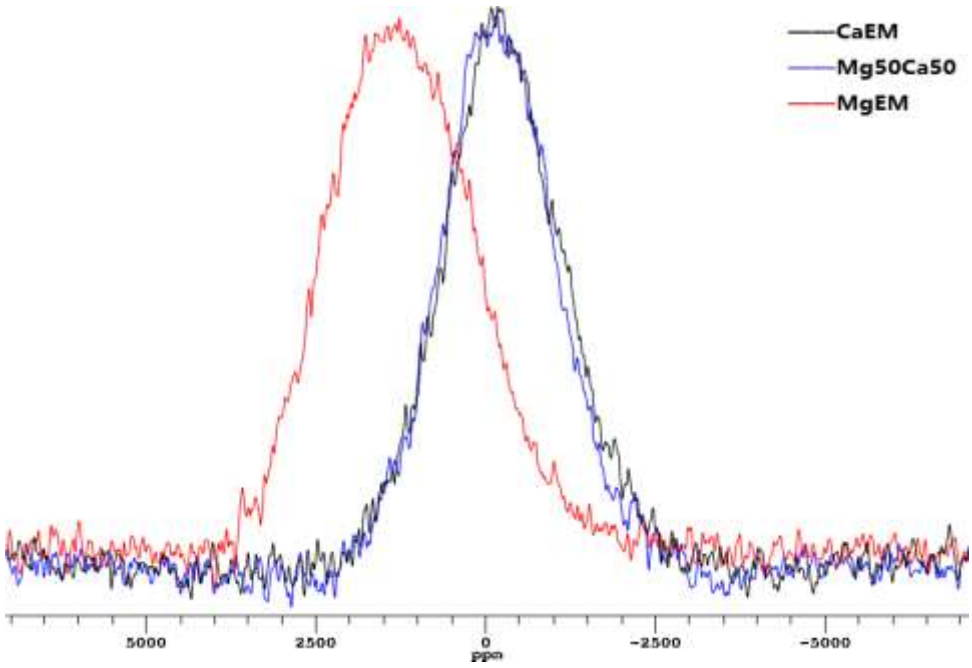

Figure 4-12 ^{139}La static Hahn echo NMR spectra of CaEM, Mg50Ca50 and MgEM glasses obtained at 79.59 MHz for 335550 & 403288 & 407472 repetitions respectively with a recycle delay of 0.2 s. All three spectra were referenced to ^{139}La in 1M $LaCl_3$ as 0 ppm.

4.3. Initial dissolution rates

As shown in Figure 4-6, there is no selective leaching of B with regard to its coordination. However, it is not clear whether the ratio of $^{[3]}$B/$^{[4]}$B would affect the dissolution rate. To probe this effect on glass solubility, initial dissolution rates were measured for all five simplified glasses via short duration leaching experiments with very low *SA*/*V* ratios (< 22 m^{-1}), i.e. under very dilute conditions where dissolution of individual elements will not be inhibited by their concentrations in the leachate. Given the same leaching conditions, the rates are dependent on the glasses to be leached, their chemical compositions and structures.

The full results are illustrated in Figure 4-13: linear fits of the ET (effective thickness) of dissolved glass evolution with time yield the dissolution rate r_0 (see Equation 3-1). The rates based on Si concentration in the leachate all lie between 2.22~2.60 g/m^2/d with no clear dependence on composition. The uncertainty of r_0 values measured in the way is at the level of 10%, as calculated by uncertainty propagation methods (Gin *et al.*, 2012). Therefore, r_0 values for all the simplified glasses are effectively the same within error. However, a more recent work (Fournier *et al.*, 2016) suggested that the actual uncertainty in r_0 is expected to be greater by taking additional uncertainties associated with the estimated glass surface area into account. This was demonstrated to be as high as 25%, depending on the exact experimental conditions

deployed. The complete initial dissolution result is listed in Table 4-5. On either basis, no difference in the initial dissolution rates of the glasses with composition could be discerned.

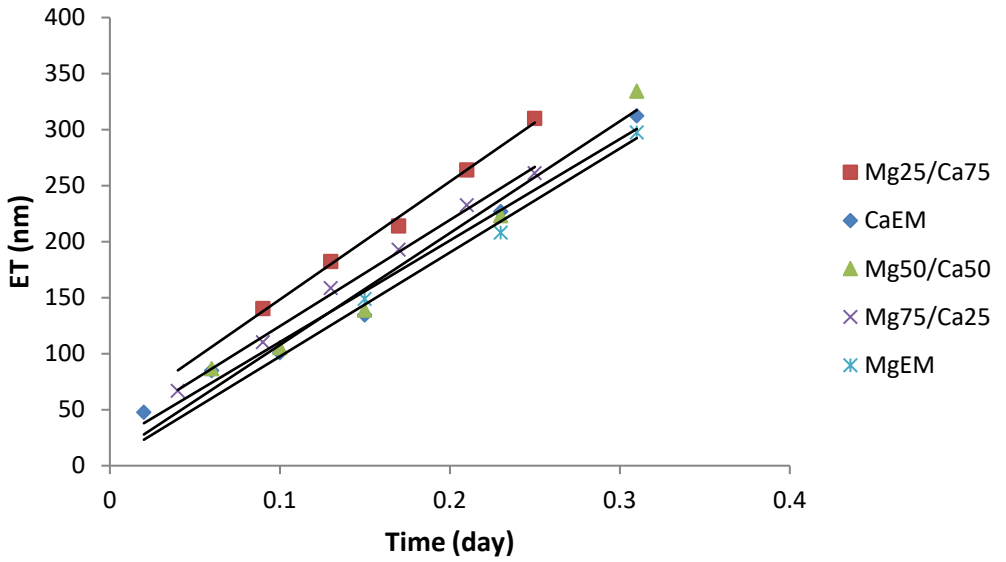

Figure 4-13 Effective thickness (ET) of simplified glasses being dissolved as a function of time in the initial dissolution rate experiments based on Si concentration in the leachate.

Table 4-5 Initial dissolution rates of the simplified glass series as determined from the rate of change in the effective thickness of dissolved glass based on Si concentration.

	CaEM	Mg25Ca75	Mg50Ca50	Mg75Ca25	MgEM
Initial dissolution rate ($g/m^2/d$)	2.33±0.23	2.60±0.26	2.54±0.25	2.42±0.24	2.22±0.22

4.4. Discussion

4.4.1. Glass density and boron coordination

As a macroscopic property, density variations accompany compositional and/or structural changes in glasses. Despite the lower atomic mass of Mg compared with Ca, explaining the monotonic density decrease following molar substitution of Ca by Mg is not trivial. A simple isomorphous model could be tested: one Ca in the glass is substituted by one Mg without

causing any structural change, which would result in a density reduction due to the lower atomic mass of Mg (24.305 g/mol) compared with Ca (40.078 g/mol). On the other hand, because the substitution is on a molar basis and glasses are made from oxide precursors, another substitution model incorporating the molar volume of oxides was also considered. In this case, MgO has a lower molar volume of 11.196 cm^3/mol compared with that of CaO (16.790 cm^3/mol) (Rumble, 2018). Therefore, the density reduction would be moderated depending on the relative degree of change in mass and volume associated with Ca/Mg substitution in the volumetric model. The prediction of glass density variations based on these two simple substitution models, together with the measurements, is depicted in Figure 4-3. Neither of the models fully describes the reduction in density caused by Mg substituting Ca, particularly for Mg75Ca25 and MgEM, which suggests that other local structural changes took place.

Due to the high concentration of B in the glasses, its local structural changes could notably change the glass density. Since one of the effects of converting tetrahedral B to trigonal B is a reduction in the packing efficiency: trigonal B tends to form open ring-like structures, i.e. boroxol rings (Bray *et al.*, 1982), a higher proportion of $^{[3]}$B would reduce the glass density provided that other factors are minor. As the measured density reduces more significantly with increasing Mg content than the simple models predict, the results are consistent with the fundamental structural change observed in B coordination.

4.4.2. Glass local structures

4.4.2.1. Insights into Mg sites in the glasses

The main purpose of making simplified glasses is to use them as the surrogate for studying the full-component glasses without losing the key structural and compositional features. In comparison to other inactive benchmark nuclear waste glasses such as SON68 and ISG, the presence of Mg in MW25 is the major compositional difference and is suspected to reduce the aqueous durability. A fundamental requirement for studying the effect of Mg on dissolution mechanisms with a simplified glass is to ensure a similar Mg environment as in MW25 glass to start with. Due to the difficulties in acquiring solid-state ^{25}Mg NMR signal in general, as outlined in 3.3.5.5, obtaining spectra of sufficient *S*/*N* and resolution is very challenging. Indeed, as can be noticed from Figure 4-10, the spectra are still quite noisy even with acquisitions being carried out using a 20.0 Tesla magnetic field and using a large number of acquisitions. In addition, it was impractical to obtain spectra with enough quality to distinguish between Mg of different coordination number across the simplified glasses (the experimental setup and length

of acquisition were limited by the access to the national facility). Nevertheless, the broadly similar ^{25}Mg spectra of MgEM and MW25 indicate that the simplified glass provides a good representation of the full-component glass in terms of the Mg local environment. This indicates that the local structural effects, which contribute to the average values and distributions of δ_{iso} and EFGs at the Mg sites, are reasonably similar. However, it is difficult to determine the exact position without applying higher resolution 2D methods. The positions of average δ_{iso} of Mg in 4-fold and 6-fold coordination regimes have been demonstrated in other studies on well-defined crystalline Mg-containing silicates and glasses. The typical δ_{iso} of 6-fold coordinated Mg is in the range of 1.0~15.0 ppm whereas that of 4-fold coordinated Mg were found to be above 30.0 ppm. In the meantime, there has been no clear record of 5-fold coordinated Mg positions but likely to be intermediate between that of tetrahedral and octahedral sites (Kroeker and Stebbins, 2000; Shimoda *et al.*, 2007; Shimoda, Nemoto and Saito, 2008). The recorded δ_{iso} for 4-fold to 6-fold coordinated ^{25}Mg are indicated by the highlighted zone in Figure 4-14 from ~10.0 ppm to ~40.0 ppm. The average isotropic shift position could well lie within the zone, depending on the exact distribution of EFG and η_Q. Therefore, Mg could be in tetrahedral and/or octahedral sites in the glass and acts as either network former and/or charge compensator or modifying the network. The role of Mg in MgEM is further discussed in 4.4.2.2. It is worth noting that spinning sidebands are only present in the MgEM spectrum and not the MW25 spectrum. This either indicates that the average EFGs are much greater at Mg sites due to higher distortion in the MgEM glass than in MW25 glass or the paramagnetic ions in MW25 are preventing them from being observed. The latter explanation is more likely because the central lines appear similar: a big difference in the local EFGs would reflect on the width and shape of the central line.

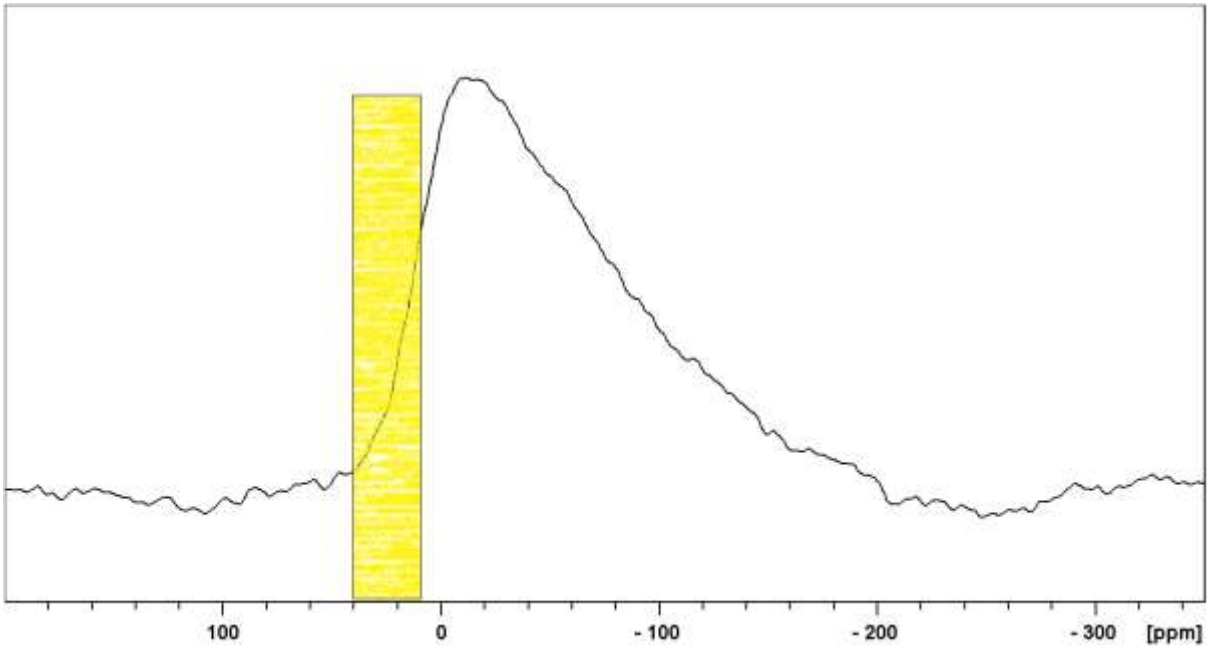

Figure 4-14 Expansion of the ^{25}Mg-enriched MgEM spectrum as shown in Figure 4-11. The highlighted range denotes the δ_{iso} range recorded in the literature from 4-fold to 6-fold coordination.

4.4.2.2. Inferring charge balance in the glasses

The local bonding requirements of Mg could influence the local structure of other network-forming cations. Figure 4-4 illustrates that the $^{[3]}$B/$^{[4]}$B ratio increases as the Mg content of glass increases. This monotonic increase in the fraction of $^{[3]}$B is consistent with other studies on aluminoborosilicate glasses where B coordination was shown to be affected by the field strength of network modifiers: $^{[4]}$B fraction decreases as the field strength of the added modifier increases (field strength is defined as the formal charge of a cation, Z, over the square of average M-O distance, d, in its first coordination shell i.e. $\frac{Z}{d^2}$ (Shannon and Prewitt, 1969)). In this case, Mg has a higher field strength than Ca because the ionic radius of Mg is smaller than Ca (e.g. 86.0 pm compared with 114.0 in 6-fold coordination (Shannon, 1976)).

For singly charged Na ions, one Na^+ is needed to charge compensate one $^{[4]}$B to achieve local charge neutrality. Such a charge-compensating Na ion must be released into other structural roles, primarily as a network modifier linked to non-bridging oxygen (NBO), once a $^{[4]}$B converts to $^{[3]}$B. It has been demonstrated that such a structural role change would be reflected as a noticeable shift in the ^{23}Na MAS NMR spectrum even for peaks that are profoundly broadened due to local structural distributions in glasses (Bunker *et al.*, 1990; Xue and Stebbins, 1993). In contrast, in the case of Mg/Ca substitution in this series of glasses, no such changes are evident from the spectra shown in Figure 4-7. Clearly, $^{[4]}$B charge compensated by Na^+ is not

converted to $^{[3]}$B by the addition of Mg. In other words, Na ions are not the sole charge compensator for $^{[4]}$B. Ca ions in the CaEM glass and Mg in the MgEM glass, and both in intermediate compositions, contribute to this charge compensation role. On the other hand, given that the Mg/Ca ratio alters the $^{[3]}$B/$^{[4]}$B ratio and the role of Na stays invariant, the relative structural role between Mg and Ca ions should differ. Figure 4-15 shows the excess 3-fold coordinated B (Table 4-3) as a function of the Mg content in the glass. The linear fit gives a gradient of approximately 0.8. The large uncertainties are propagated from the associated errors in B concentration measurements. This should not be confused with the clear increase in $^{[3]}$B fraction of total B. If all Ca was charge compensating $^{[4]}$B and Mg was replacing Ca but not its structural role, we would expect the gradient in Figure 4-15 to be approximately 2, i.e. 1 mol of $^{[4]}$B is converted to $^{[3]}$B per unit of charge. Unfortunately, the exact amount of Ca that compensates the charge deficits at $^{[4]}$B sites is unknown since there is a surfeit of charge (see column 1 of Table 4-6). Nevertheless, together with the higher fraction of $^{[3]}$B, this suggests a poorer charge compensating capability of Mg compared with Ca to compete for lower coordination configurations, probably owing to its higher field strength. Therefore, Mg is likely to be in both 4- and 6-fold coordination, which corroborates the observations from the ^{25}Mg MAS NMR spectra of MgEM and MW25 glasses that Mg exists in multiple-coordination with oxygen.

In inorganic Al-O environments, tetrahedral and octahedral sites of Al can be well resolved by MAS NMR at 11.7 T thanks to the noticeable difference in δ_{iso} as an indicator of coordination. Typically, the former and latter locate in the range of 50~80 ppm and -10~15 ppm respectively, whilst that of pentahedral sites is 30~40 ppm, as found in well-defined crystalline compounds (MacKenzie and Smith, 2002). Using the fitted CaEM ^{27}Al spectrum as an example (Figure 4-9), the fact that the tentatively assigned $^{[4]}$Al peak can be fitted reasonably well with only one CzSimple line suggests that 5-fold coordinated Al must either be absent or in very low concentration in the glass (Cochran *et al.*, 1988). Further, using two separate CzSimple lines does not improve the fit. To resolve any $^{[5]}$Al, a significantly higher magnetic field (e.g. 14.1 Tesla) is required to narrow the lines due to second-order quadrupole broadening. It was reported that when modifiers with higher field strength are added to aluminosilicate glasses, a higher fraction of 5-/6-fold coordinated Al would be present from the conversion of $^{[4]}$Al. The results here show a reversed trend. However, it should be kept in mind that Al constitutes less than 5 mol% of the total cations and $^{[6]}$Al accounts for only ~4.8% and ~1.6% of the total Al (~0.23% and ~0.08% of the total cation) in CaEM and MgEM, respectively. Unlike the coordination changes observed for B, such a subtle change can easily be attributed to other

factors such as compositional uncertainties and thermal history of the glasses (Morin, Wu and Stebbins, 2014). Therefore, the subtle changes in Al coordination and its low concentration do not contribute noticeably to the charge balancing scheme of network formers (predominantly $^{[4]}$Al) when compared with the effects that are evident from the ^{11}B NMR results.

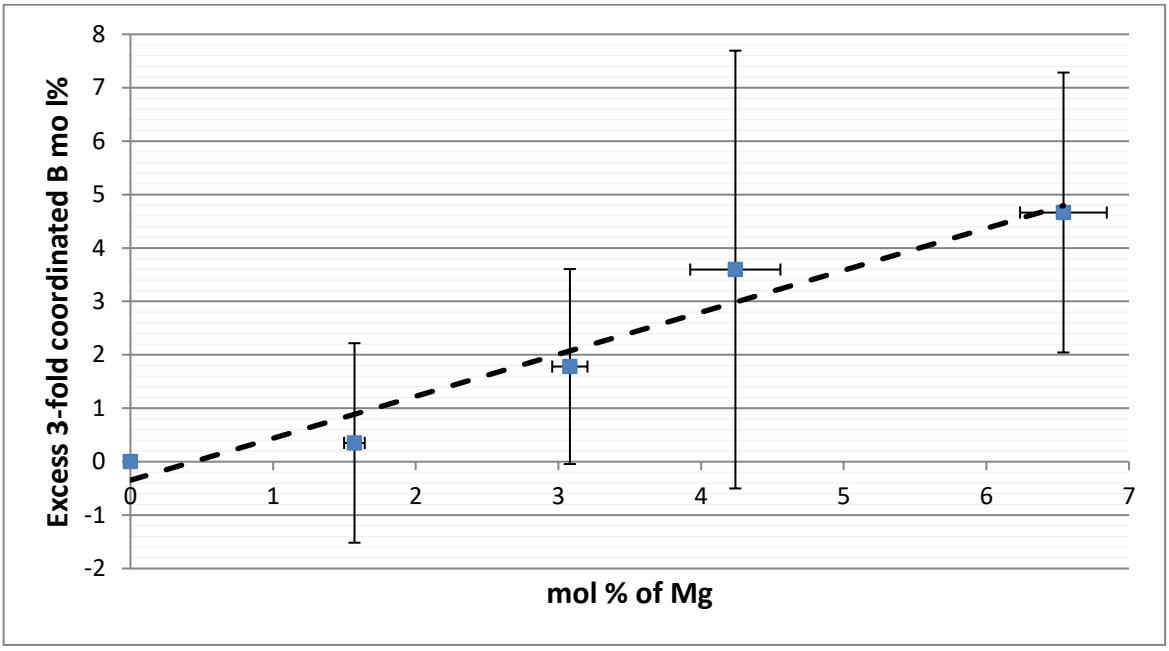

Figure 4-15 The linear fit (dashed line) of the amount of boron that transform from four-fold coordination to three-fold coordination on substitution of Mg for Ca per 100 moles of cations (filled square).

Table 4-6 lists the network formers that need to be charge compensated and the available charge compensators or network modifiers. As an intermediate oxide (MgO) in terms of glass forming ability, the structural role of Mg in MgEM and MW25 is important in determining the holistic charge balancing scheme of the glasses since it could be either providing or consuming the charge (Pedone *et al.*, 2008; Kuryaeva, 2009). However, as mentioned above, the exact ratio of $^{[4]}$Mg to higher coordinated Mg is unknown. Nevertheless, the similar composition and density of the simplified glasses indicate a similar degree of network connectivity in spite of the local structural changes such as B coordination. It has been noted that an excess of network formers (e.g. 4-fold coordinated Al and B) could be charge compensated by REEs acting as charge compensators (Cormier, Capobianco and Monteil, 1993; Du and Cormack, 2005). Therefore, La^{3+} ions are able to charge compensate when there is a lack of charge provided by usual charge compensators such as Na^{+} and Ca^{2+}. On the other hand, REEs in aluminosilicate and aluminoborosilicate glasses normally have a coordination number of 6-8 and they are assumed to be charge compensated by Na^{+} and Ca^{2+} through sharing of NBOs with the latter due to over-

coordination (Schaller and Stebbins, 1998; Molières *et al.*, 2014). In the absence of Mg, it is likely that La in the CaEM glass needs to be charge compensated due to a surfeit in available charge. This leads to an excess of potential charge compensators of 3.8 mol per 100 mol cations assuming 6-fold coordination of La (0.4 mol per 100 mol if 8-fold coordination is assumed). In the case of MgEM, there would be a charge deficit of 4.5 mol per 100 mol cations even if all La^{3+} is in charge compensating role if all Mg acts as network former in 4-fold coordination. Since excessive positive charge lowers glass network connectivity by creating NBOs, this would lower the glass density in the opposite way from that observed for this series of glasses, i.e. from MgEM to CaEM. The contrast in the charge balance between CaEM and MgEM suggests that some of the Mg does the charge compensating. In addition, the clear difference in ^{139}La spectrum between CaEM and MgEM reflects not only the different structural role of La in the two glasses but also between Mg and Ca. These findings are consistent with the ^{25}Mg and ^{11}B NMR results.

Table 4-6 Total charge balancing scheme for the simplified glass series. Note: $^{[4]}$Al data is only available for CaEM, MgEM and Mg50Ca50 glasses.

Species (mol%)	CaEM	Mg25Ca75	Mg50Ca50	Mg75Ca25	MgEM
Four-coordinated network former					
$^{[4]}$B	13.7	13.1	11.9	11.9	10.8
$^{[4]}$Al	4.5	-	4.9	-	4.7
Charge compensator/network modifier					
Na^{+}	14.9	15.3	14.7	14.8	15.1
Ca^{2+}	6.1	4.8	3.2	1.6	-
La^{3+}	1.7	2.0	1.7	1.7	1.7
Four-coordinated network former and/or charge compensator/network modifier					
Mg	-	1.6	3.1	4.2	6.5
Excessive positive charges	0.4~3.8[i]	-	-	-	'-4.5'[ii]

i. 0.4 for La in 8-fold coordination and 3.8 for La in 6-fold coordination;

ii.This assumes all the Mg in the MgEM glass acts as network former.

4.4.3. Initial dissolution rate and B coordination

Iwalewa, Qu and Farnan (2017) measured the initial dissolution rate of full-component simulant MW25 glass in deionised water at 90℃ in SPFT (Single-Pass-Flow-Through) mode and found it to be 1.84 $\pm$ 0.35 g/m^2/d. This agrees, within measurement uncertainty, with that measured on MgEM glass (see Table 4-5), which again indicates a good representation of the simplified glass for the full-component complex glass. Furthermore, the initial dissolution rates as a function of Mg content in these simplified glasses are the same within error. This is in contrast to the data reported in the literature for experiments conducted at much longer time scales of up to 12.2 years (Curti *et al.*, 2006) and in the previous work for experiments conducted for relatively long periods of up to 112 days (Brigden and Farnan, 2014). In the former case, it was found that the long-term (residual) dissolution rates, which are generally 3~4 orders of magnitude lower than the initial dissolution rates for these glasses, differ by about one order of magnitude. In the latter case, after 112 days of leaching, the normalised release of MgEM was determined to be 7.960 g/m^2 and that of CaEM to be 0.928 g/m^2 (see Chapter 5). Despite other compositional differences between the full-component glasses, the separate effects as observed for the simplified glasses highlighted that the key factor that leads to the inferior aqueous durability of Magnox waste glasses in long-term is the presence of Mg in a comparable concentration to Ca in SON68.

The residual dissolution rates in the long-term situations are generally attributed to a combination of kinetic and thermodynamic effects. The transport of glass species and water becomes hindered by the presence of an altered layer of in-situ re-constructed and resorbed materials on the glass surface and the thermodynamic driving force for dissolution is inhibited by solution chemistry due to Si saturation (Gin, Abdelouas, *et al.*, 2013; Gin, Jollivet, Fournier, Berthon, *et al.*, 2015b). In leaching experiments where fresh SON68 glass was placed into a Si saturated leachate, a similar dissolution rate was observed as with fresh glass in fresh water (Vernaz *et al.*, 2001). Therefore, the dissolution rate differences associated with the presence of Mg are primarily determined by secondary effects related to the effectiveness of the altered layer in hindering transport of reactive species. Any fundamental change in the pristine glass, such as B coordination induced by the addition of Mg, appears to have no effect on the glass aqueous durability.

4.5. Summary

The key questions for this chapter to address were, what are the structural changes arising from the substitution of Ca/Mg in simplified MW25 glass and are these the reason for the drastically

different behaviour in long-term dissolution? On balance, the primary effect of substituting Mg is to produce glasses of lower density with more 3-fold coordinated B. This change, however, is not a result of competition for Na, the dominant charge balancing cation, but a result of the poor charge compensating capability of Mg. Some Mg is in 4-fold coordination (network-forming), but the amount of $^{[4]}$B to $^{[3]}$B conversion and overall charge balancing scheme are consistent with Mg also being present in higher coordination. These compositional and structural changes do not impose a noticeable change on the initial dissolution rate of the glasses. Therefore, the drastically different long-term dissolution behaviour between Mg and Ca based radioactive waste glasses, based on this separate effect study, should be attributed to secondary effects related to the efficacy of surface altered layer in retarding dissolution.

Chapter 5

5. Long-term dissolution of simplified MW25 glasses

5.1. Introduction

The deleterious effects of Mg, as opposed to Ca, on long-term nuclear waste glass aqueous durability were reported in studies on the full-component surrogates SON68 and MW25 as well as AVM10 glasses (Frugier *et al.*, 2005; Curti *et al.*, 2006). Despite being compositionally similar in the primary glass constituents, including SiO_2, B_2O_3, Al_2O_3 and Na_2O and their relative amount, especially for the former two glasses, there are noticeable differences in the presence/absence of other minor constituents, mainly transition metals and REEs, the effects of which on dissolution are unknown (see Table 1-1). In Chapter 4, the simplified glasses provided a separate effect route to specifically investigate the effect of Mg on the glass density, glass local structures and initial dissolution rates. The long-term dissolution behaviour can also be studied on this basis.

The long-term (up to 16 weeks) dissolution experiments on the simplified glasses were described and the results presented in the previous study by Brigden and Farnan (2014). Some experimental and results are highlighted in 5.2. Here, the results of the dissolution experiments on ^{25}Mg-enriched MgEM glass are also presented but only for two durations: 4 and 16 weeks, due to the limited amount of enriched sample available.

5.2. Dissolution of MgEM and CaEM glasses

The leaching experiments were conducted in batches with each batch being composed of three reaction vessels for each composition and two blank vessels, run for the targeted durations: one, two, four and sixteen weeks. After the sample preparation and analysis procedures described in 3.4.2.2 and following the data processing steps laid out in 2.6, results for the normalised release $NL_{B,\ Na,\ Si,\ Ca\ \&\ Mg}$ of MgEM and CaEM glasses, as well as the corresponding leachate pH values (room temperature), are schematically shown in Figure 5-1. The normalised release of B and Na, both of which are regarded as dissolution indicators, are significantly higher for MgEM than that for CaEM, across the different durations of the leaching experiments. The differences are highlighted for the longest leaching duration (112-day) and is about one order of magnitude higher for MgEM glass (7.960 vs 0.928 g/m^2). This is in contrast to the same (within error) initial dissolution rates between these two endmembers. Since the only nominal difference, in

terms of composition, between these two glasses is the ~6.54 mol% (cation) constituent of Mg or Ca and the resultant leachate pH are very similar throughout, the presence of Mg must have played an important role in keeping the long-term dissolution rates relatively high compared with if it is absent.

While the concentrations of Si in the leachate were much lower than those of B and Na, the evolution profile shows the opposite trend for the two endmember glasses despite the NL_{Si} values being similar at the end of the leaching experiment (Figure 5-1 (b)). On the other hand, the temporal evolution of NL_{Ca} and NL_{Mg} also follows the same trend as a function of glass composition whilst the latter is about two orders of magnitude lower than that of the former after 16 weeks. The decrease in release suggests that the dissolved Si and Mg had been continually re-incorporated into the MgEM glass alteration products. This phenomenon could be considered in parallel comparison with the extensive secondary precipitations that are thought to be responsible for the resumption of dissolution after the residual rate regime has been reached and sustained, where certain constituents in the leachate and altered layers are consumed to form the large amount of precipitates. However, the key difference is that the incorporation processes seem to be continual and at the very early stage of the dissolution, where kinetic processes were thought to be dominant, compared with the thermodynamic steady states at much later stages. Therefore, this continual incorporation, which was only observed here for the Mg-containing glass, might have modified the supposedly dense 'protective' gel structure during its formation and, hence, influenced the underlying glass dissolution as measured by the leached boron, at later stages of glass-water interaction.

Based on the average boron concentration, hence NL_B, values at the end of the leaching experiments, i.e. 112 days, and by applying the shrinking core model as described in 2.6.2, the effective thicknesses of the glass that has been altered in MgEM and CaEM are 3.402 and 0.364 μm, respectively.

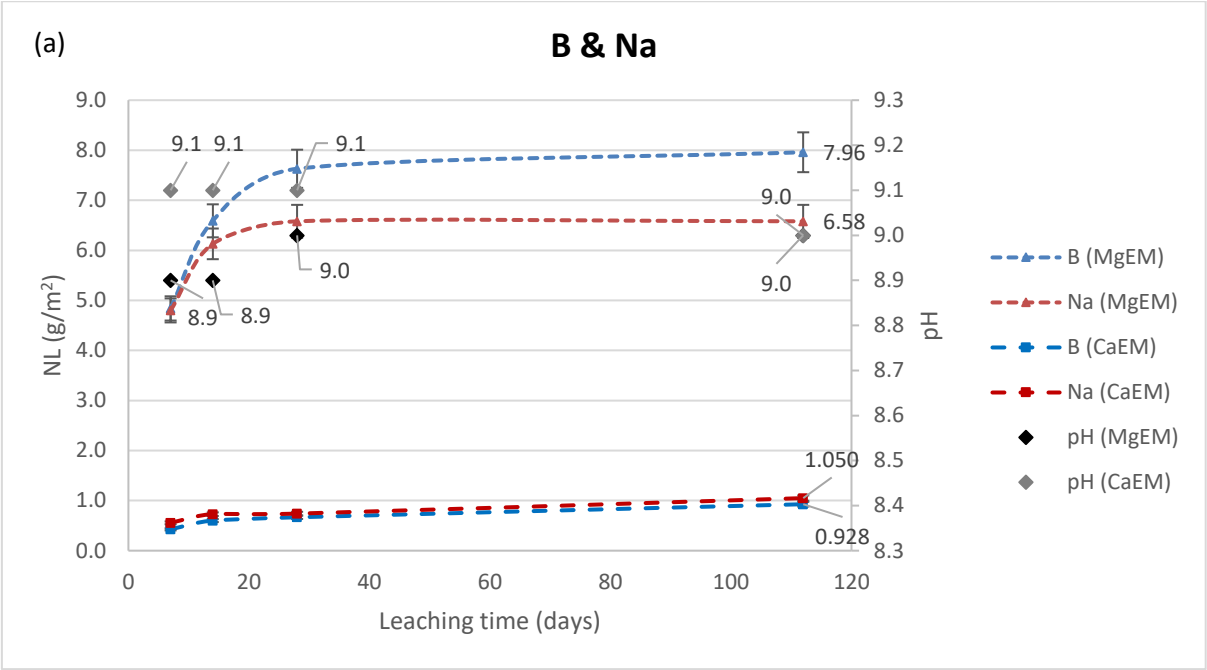
(a)
B & Na
NL (g/m²)
pH
Leaching time (days)
9.1
9.1
9.1
7.96
9.0
6.58
9.0
9.0
8.9
8.9
1.050
0.928
B (MgEM)
Na (MgEM)
B (CaEM)
Na (CaEM)
pH (MgEM)
pH (CaEM)

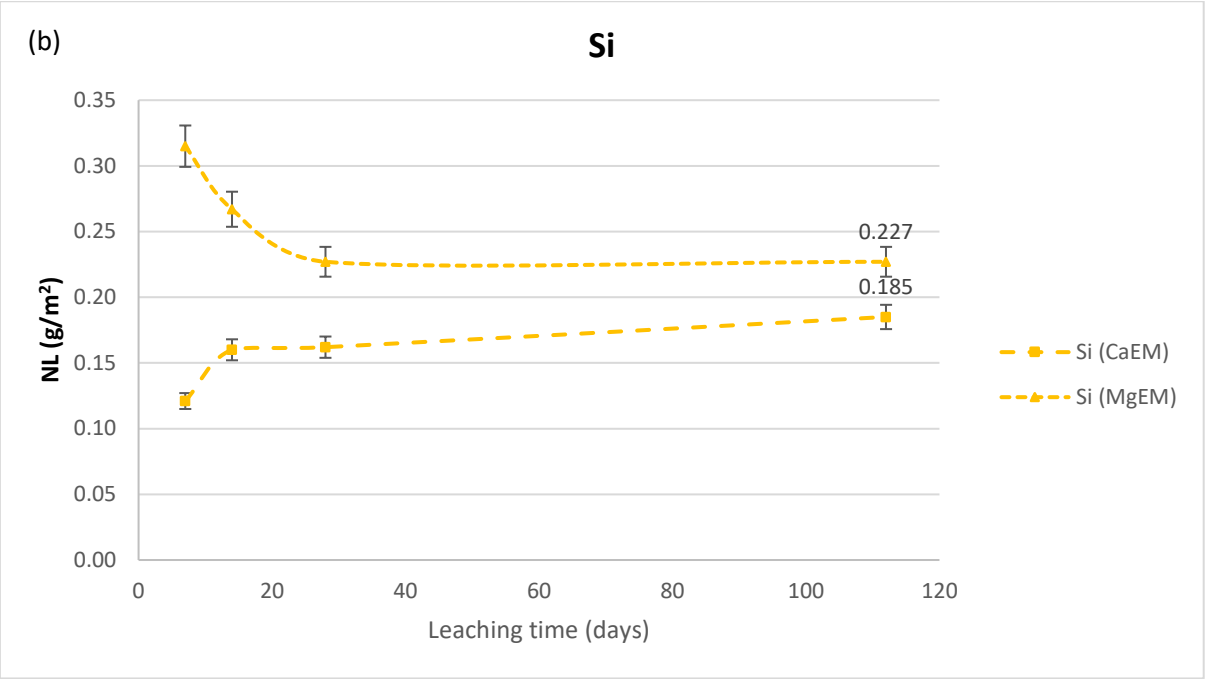

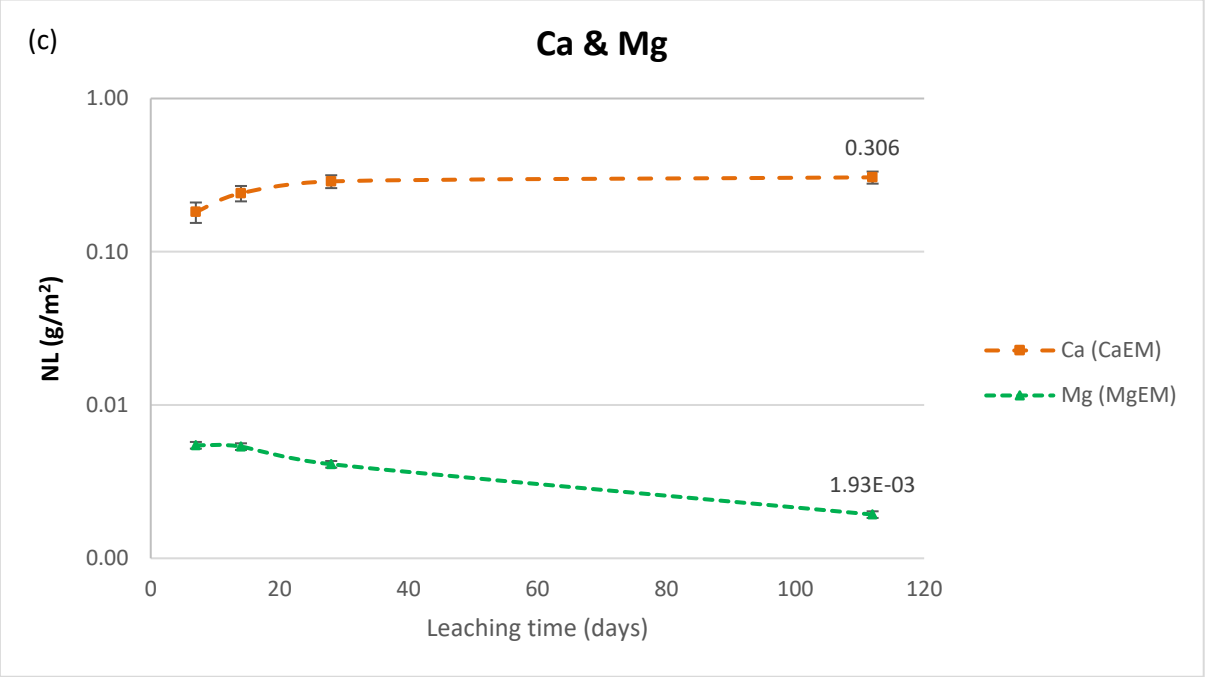

Figure 5-1 Normalised release in g/m² of B, Na, Si, Ca and Mg as well as the pH values (room temperature) of the simplified MW25 glass MgEM (Mg) and its counterpart CaEM, as a function of leaching time up to 112 days. Only the average values are presented with the error bars, denoting an intrinsic 10% uncertainty of the measurements. The leaching experiments were conducted in deionised water at 90℃.

5.3. Dissolution of ^{25}Mg-enriched MgEM glass

The limited amount of sized ^{25}Mg-enriched MgEM glass led to some deviations from the leaching setup for the non-enriched simplified glass series. Specifically, although the targeted *SA*/*V* ratio was set to remain 1200 m^{-1}, the sample mass and leachant volume were scaled down.

In addition, the batch leaching experiments of only two durations i.e. 28- and 112-day were conducted. Further, the calculations for normalised release were based upon the measured median radius (145.86 µm) instead of the nominal geometric value (112.5 µm), the latter of which, however, was adopted for the results presented in 5.2.

Figure 5-2 (a) shows the $NL_{B,\ Na,\ Si,\ \&\ Mg}$* values of the ^{25}Mg-enriched MgEM glass being leached for 28 and 112 days with the abovementioned experimental setups. Since there is only data available for two leaching durations, it is irrational to postulate a trend in *NL* variation. In addition, the results should not be drawn in direct parallel comparison with those presented in Figure 5-1 because of the different ways in calculating the surface area. Nevertheless, the absolute and relative magnitudes are in good agreement between these two sets of experiments. In Figure 5-2 (b), the *NL* values (y-axis) are presented in logarithm scale where the variations and values of $NL_{Si\ \&\ Mg}$ are better illustrated. Despite the relatively big measurement uncertainty of the 4-week Mg data, a decreasing Mg normalised release from 4-week to 16-week observes a similar trend as in Figure 5-1 (c). In the meantime, the similar Si normalised release between 4-week and 16-week is also consistent with the previous results. Therefore, the resultant leached ^{25}Mg-enriched glass samples were regarded going through similar, if not the same, alteration processes as with the MgEM glass from the previous study and subsequently used for ^{25}Mg NMR experiments for alteration surface characterisation.

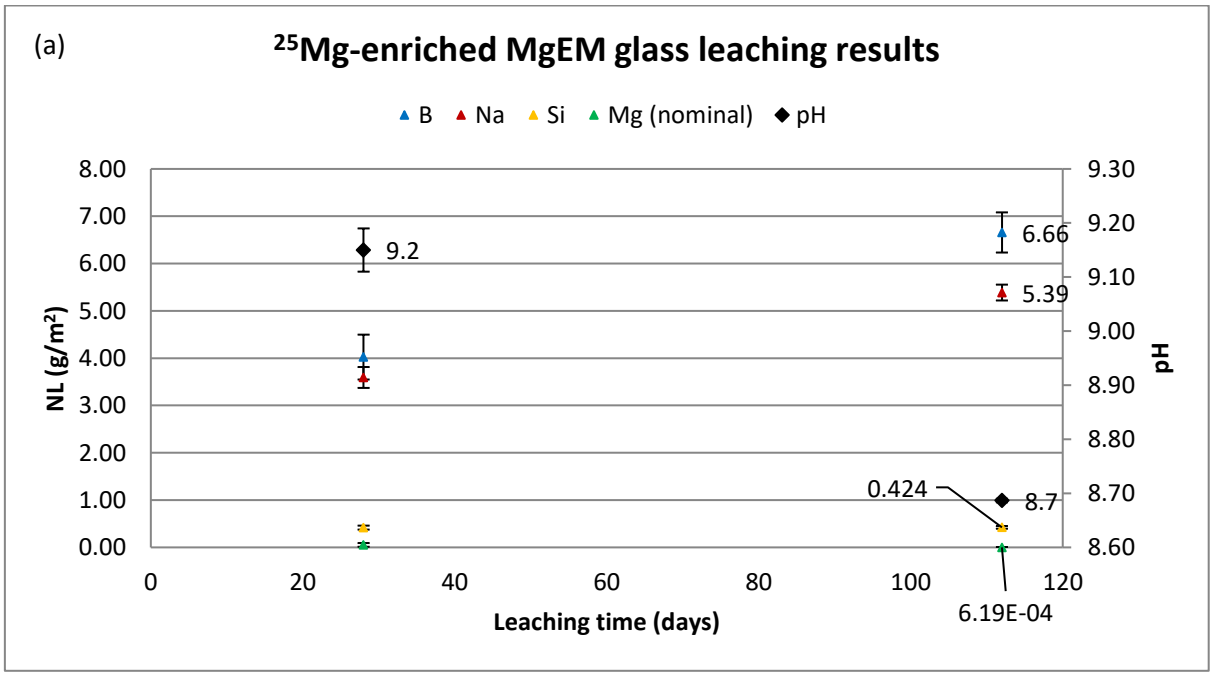

* The calculation of Mg concentration hence normalised release was based upon the Mg isotopic ratio of the enriched MgO precursor i.e. 96.9% ^{25}Mg.

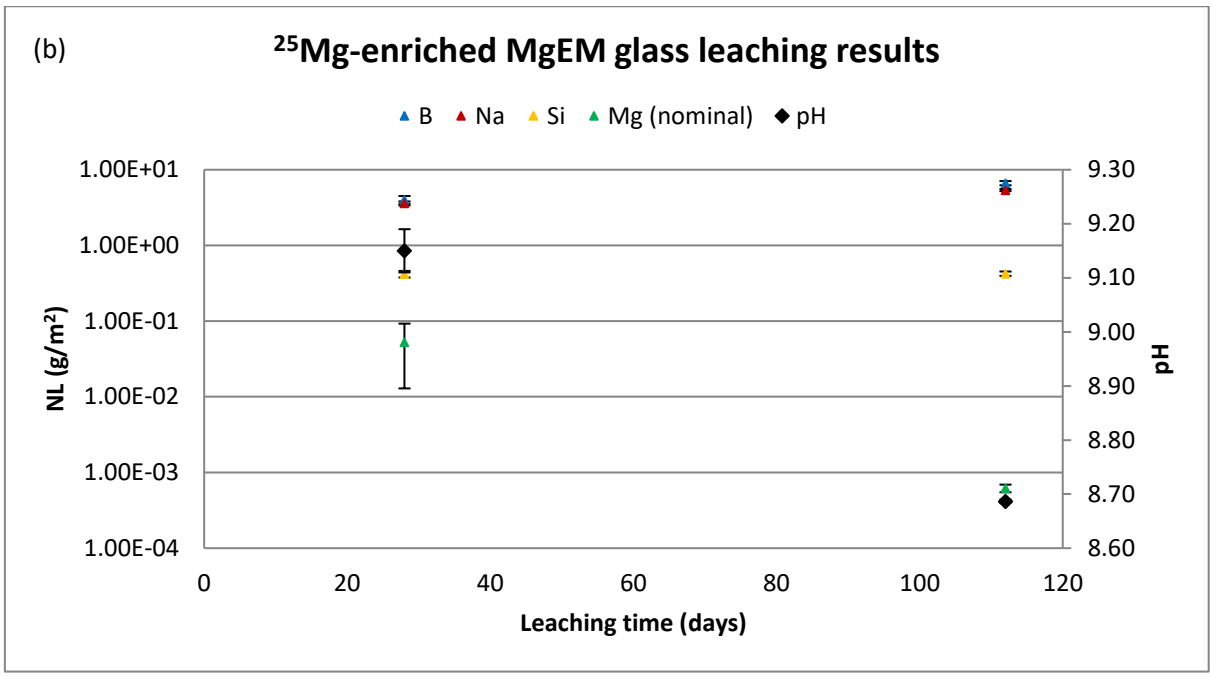

Figure 5-2 Normalised release in g/m² presented in (a) linear and (b) logarithm scale of B, Na, Si and Mg as well as the pH values (room temperature) of 28- and 112-day leached ^{25}Mg-enriched MgEM glass. The error bars denote the maximum and minimum among the triplicate measurements. The leaching experiments were conducted in deionised water at 90℃.

5.4. Summary

The simplified MW25 glass, i.e. MgEM, showed a much higher normalised release of B (and Na), which has been widely regarded as the borosilicate glass dissolution indicator, than its Ca counterpart throughout the leaching period from 7 to 112 days. The difference was the greatest for the longest duration, i.e. 112 days, with approximately one order of magnitude higher for the former, i.e. 7.960 vs 0.968 g/m^2. This is in contrast to the initial dissolution rate as measured on the same set of samples (see 4.3) where the two endmembers exhibit effectively the same dissolution rates within the first 7.2 hrs of leaching. The secondary effects that might lead to the difference in dissolution kinetics in long-term were manifested by the temporal evolution of NL_{Mg} as opposed to NL_{Ca}, where continual re-incorporation of Mg was observed. This had necessitated the extensive characterisation for the MgEM glass surface post-leaching (Chapter 6). ^{25}Mg-enriched MgEM glass exhibited similar dissolution characteristics despite the leaching experiments being run with slightly different experimental setups, where Mg concentration significantly reduced (more than one order of magnitude) after 16-week leaching relative to 4-week. The leached sample was then used for ^{25}Mg NMR experiments as part of the multinuclear approach to characterise the alteration layers.

Chapter 6

6. Characterisation of the glass alteration layers

6.1. Introduction

Unlike the Mg in the Magnox waste glasses, which originates from the magnesium-based cladding alloy material used in the first-generation Magnox reactors, Mg was one of the frit components added during the vitrification processes in the French AVM waste glasses (Sombret, 1993). A few studies have been devoted to investigating the long-term dissolution behaviour of AVM glasses as opposed to R7T7 glass in various solution environments and comparing the results. They all reached similar conclusions that Mg plays a key role in the glass dissolution behaviour in terms of modifying the altered glass surface structure and, in long-term, Mg-containing AVM glasses show inferior aqueous durability. However, the mechanism was not fully understood and mainly attributed to the secondary precipitation of Mg-smectite, more generally phyllosilicates, that were observed on the glass surface at the end of the dissolution experiments, which usually took more than a year (Frugier *et al.*, 2005; Thien *et al.*, 2012; Thien *et al.*, 2010). Indeed, formation of secondary phases would consume the elements that are needed to form the protective gel layer and disrupt the established structure, hence changing the chemistry at the reaction front as well as in the solution. In this chapter, the post-leaching MgEM glass surface is examined and characterised in great detail to provide more insights into the exact structure of the alteration layers formed during its dissolution.

6.1. Preliminary characterisations of the alteration layers

6.1.1. Surface features of altered glasses

Before looking at the post-leaching features of the glass surface, it is necessary to look at what it was like pre-leaching. Figure 6-1 shows the relatively smooth and featureless appearance of the pristine ^{25}Mg-enriched MgEM glass surface. Some fines can still be spotted after the glass particles went through the washing procedure. At the same magnification as Figure 6-1 (b), some distinctive surface features can already be observed on the 4-week leached glass surface, as highlighted in Figure 6-2 (a). Besides, the glass surface is shown to be corroded, as embodied by the spread of the darker areas, which is absent from the pristine glass surface. Since these

are secondary electron SEM images, the darker features reflect morphology rather than elemental mass information. An expansion into the highlighted area (Figure 6-2 (b) & (c)) shows traces of bead-like secondary phases formed and exposes the underlying eroded surface. After 16 weeks, the glass surface was fully covered in the secondary phases (Figure 6-3 (a)). Moreover, the underlying surface, as shown closely in Figure 6-3 (b) and (c), is completely different from that of the 4-week sample (Figure 6-2 (c)) under the same level of magnification. While the surface of the 4-week leached glass is still quite even, the 16-week leached glass surface shows rough features of porous and of flower-like structures, which is consistent with a higher degree of alteration at longer dissolution durations.

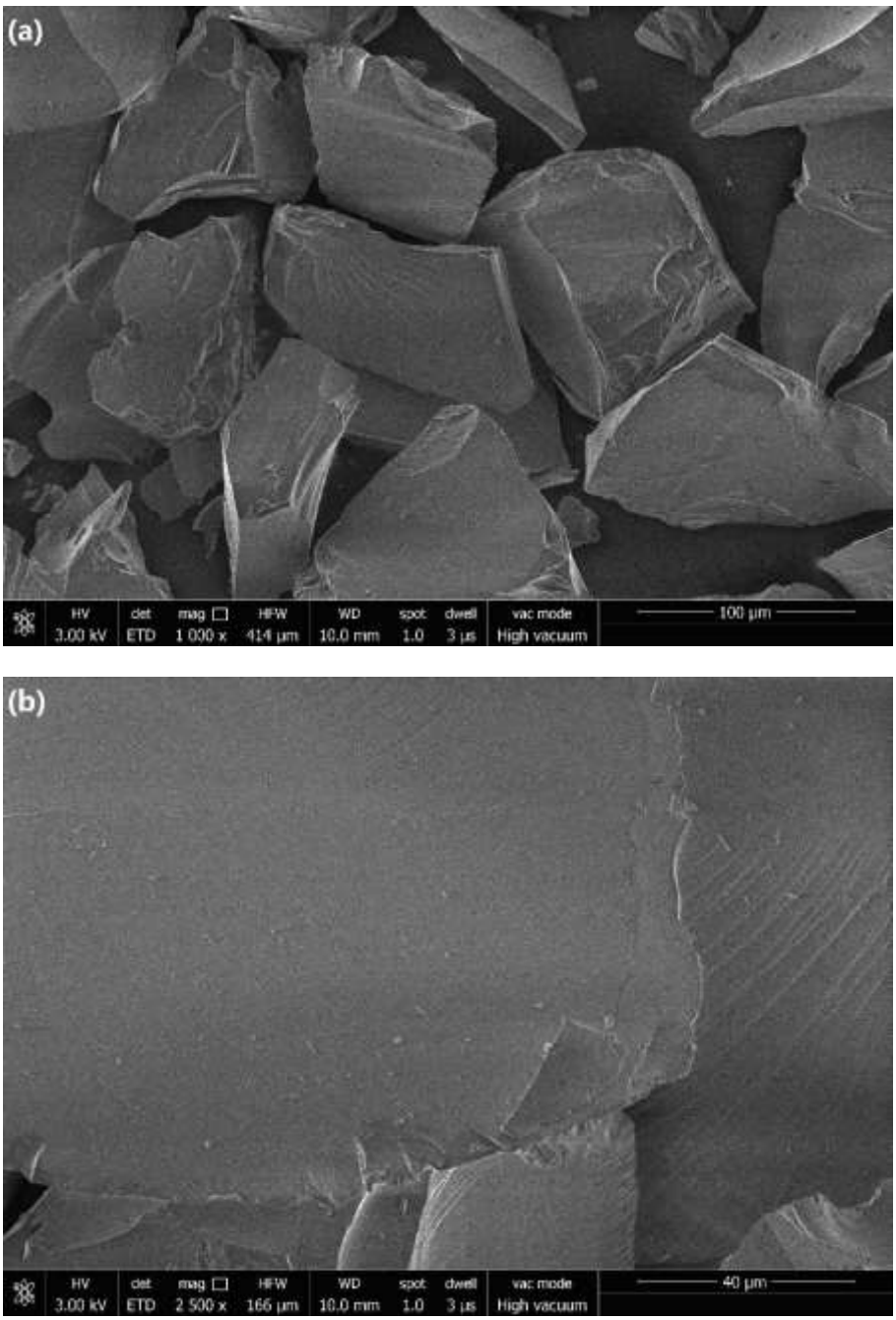

Figure 6-1 SEM (SE) images of pristine ^{25}Mg-enriched MgEM glass prior to leaching experiments at (a) 1000x and (b) at 2500x magnification.

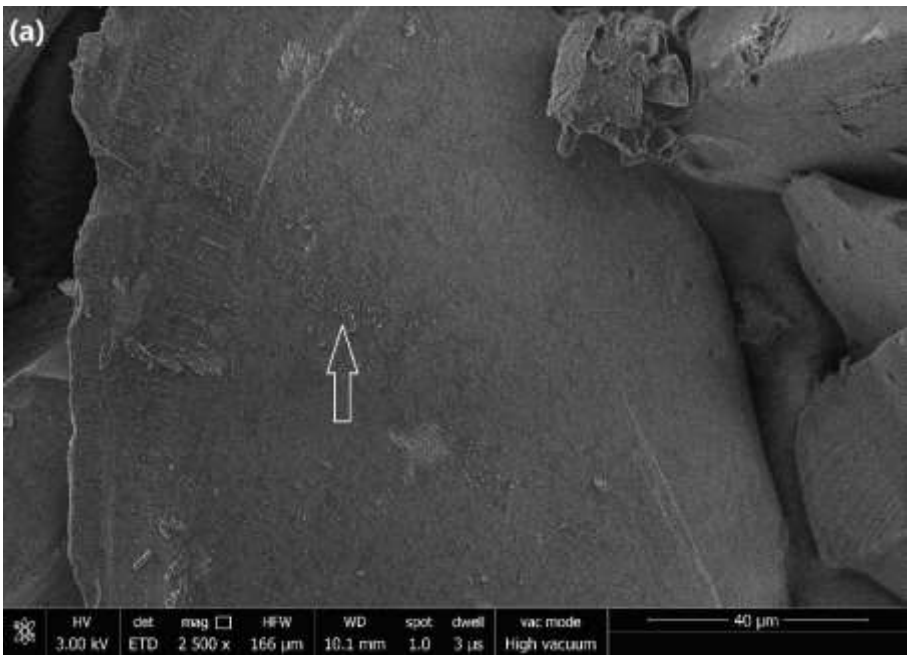
(a)
HV
3.00 kV
det
ETD
mag
2 500 x
HFW
166 µm
WD
10.1 mm
spot
1.0
dwell
3 µs
vac mode
High vacuum
40 µm

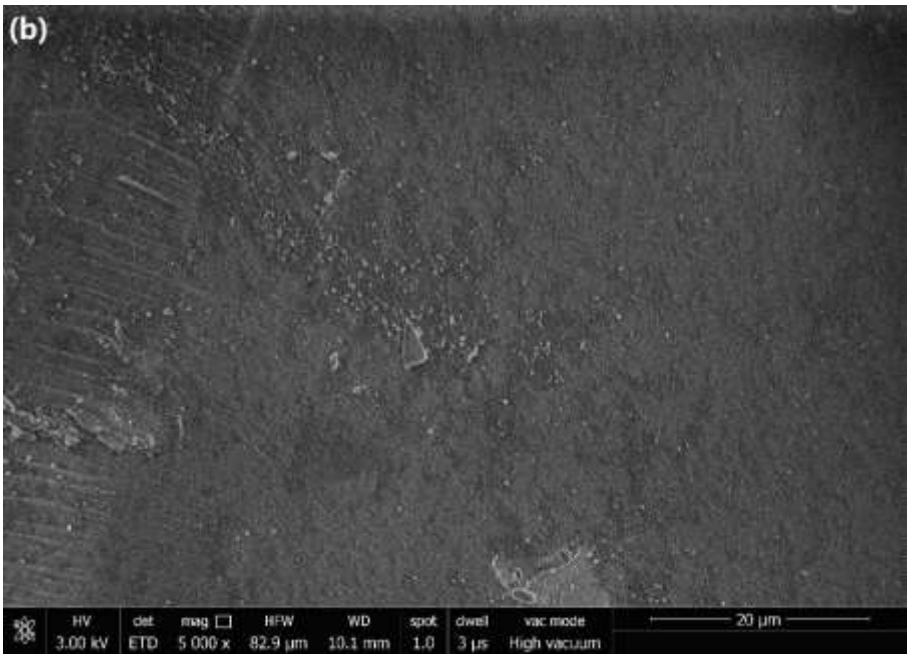
(b)
HV
3.00 kV
det
ETD
mag
5 000 x
HFW
82.9 µm
WD
10.1 mm
spot
1.0
dwell
3 µs
vac mode
High vacuum
20 µm

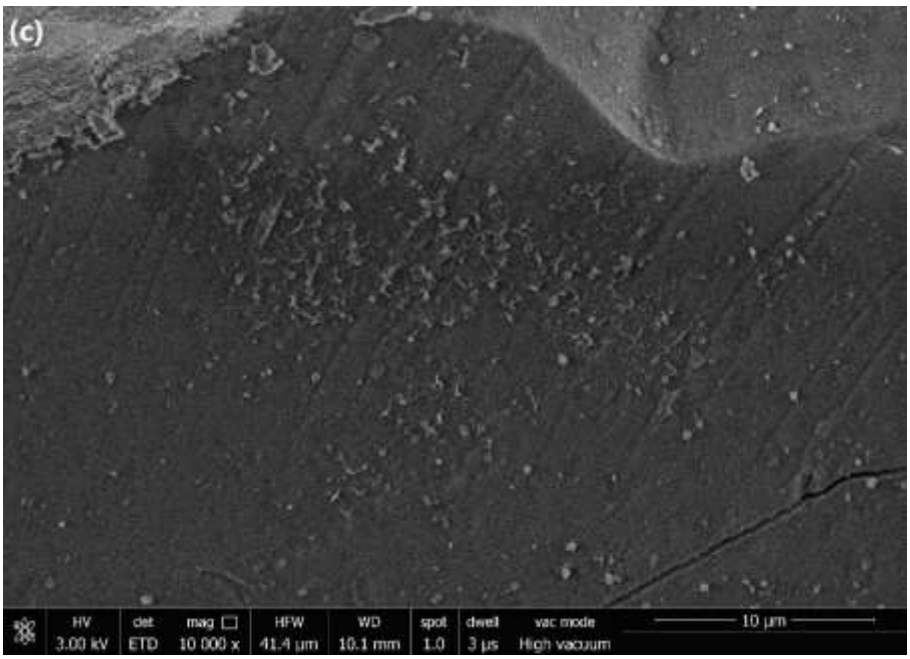

Figure 6-2 SEM (SE) images of 4-week leached ^{25}Mg-enriched MgEM glass at (a) 2500x; (b) 5000x and (c) 10000x magnification. (b) shows the highlighted area in (a).

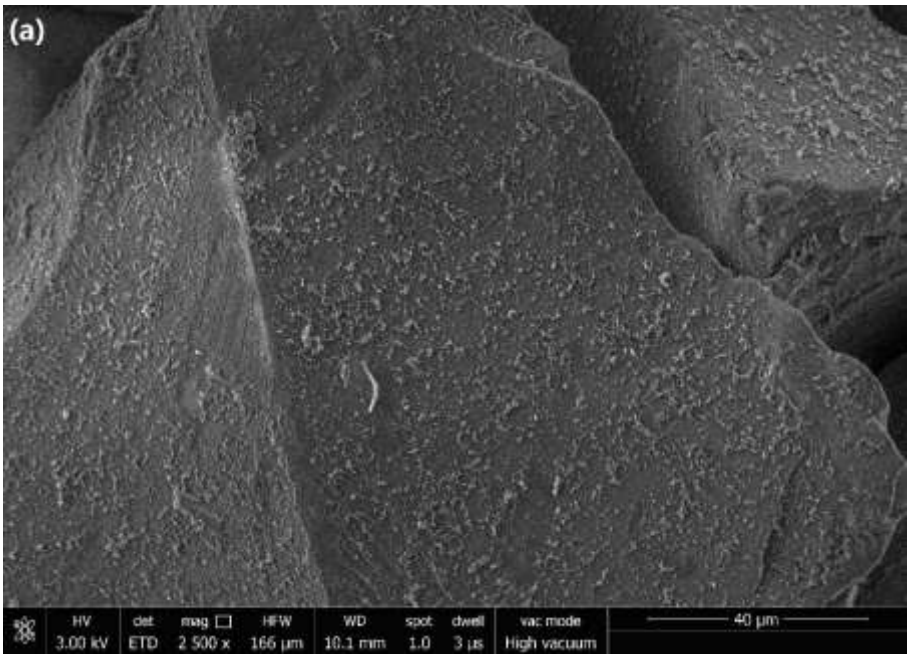

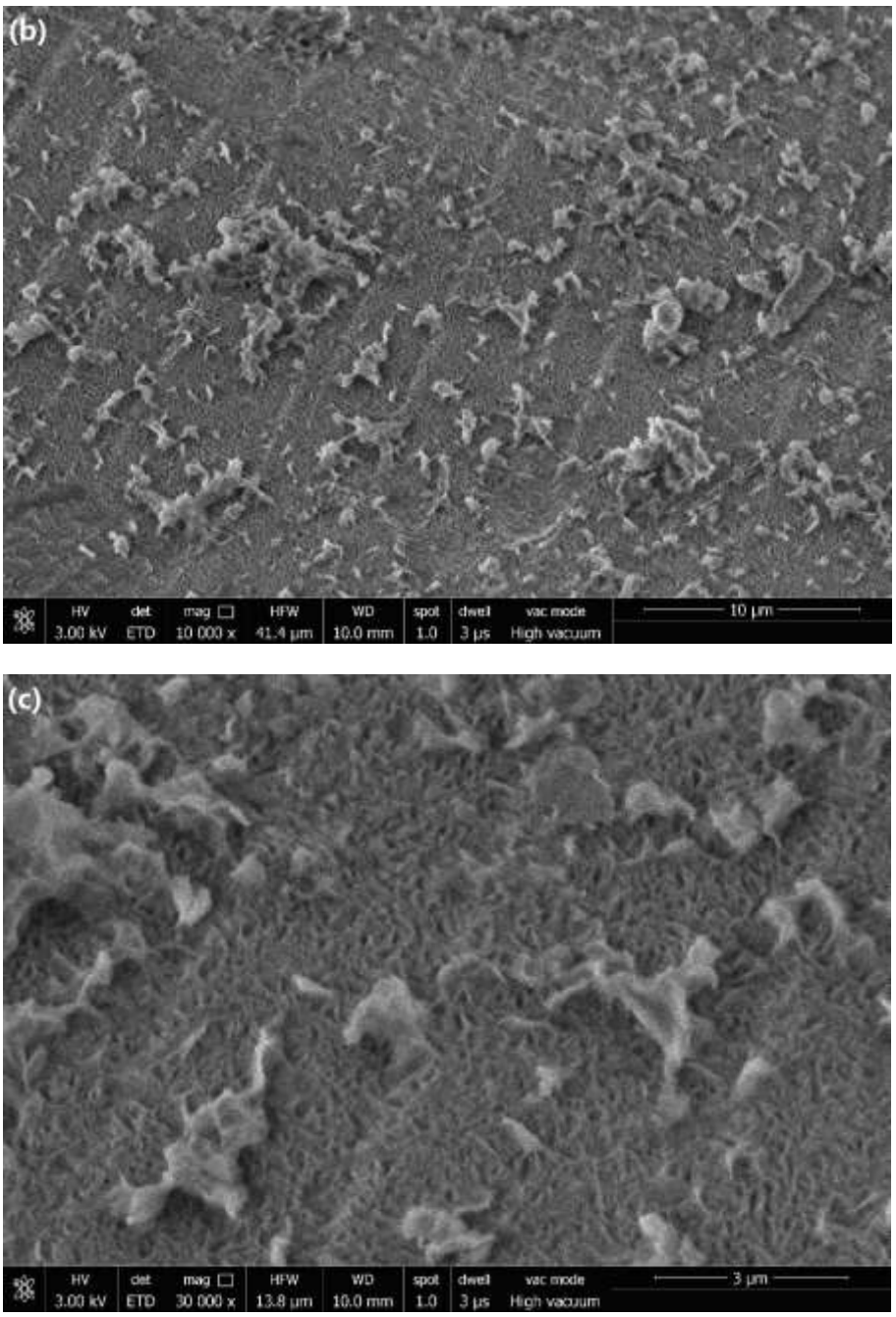

Figure 6-3 SEM (SE) images of 16-week leached ^{25}Mg-enriched MgEM glass at (a) 2500x; (b) 10000x and (c) 30000x magnification. (c) is a closer view of the area shown in (a).

6.1.2. 'Non-crystalline' state of the alteration products

In the first instance, XRD scans were carried out on the leached glass samples in an effort to identify the secondary phases that formed on the glass surface. Figure 6-4 shows the powder XRD patterns of the 4-week and 16-week leached 25Mg-enriched MgEM glass, which are characteristic of materials in their amorphous state and essentially the same as what is shown in Figure 4-2 of the pristine glass. However, it should be noted that the amount of the precipitated secondary phases, as a fraction of the total amount of glass samples being investigated, is small (see Chapter 5) and XRD scans were not set up to detect the surface

selectively. Further, unlike the widely reported extensive secondary precipitation reactions that could potentially lead to glass dissolution resumption, the products of which showed XRD detectable crystallinity, crystallisation and growth of the early-stage precipitates are likely to could be in a 'proto-crystalline' state where long-range order is still absent. Both factors could contribute to the characteristic 'amorphous' powder XRD pattern.

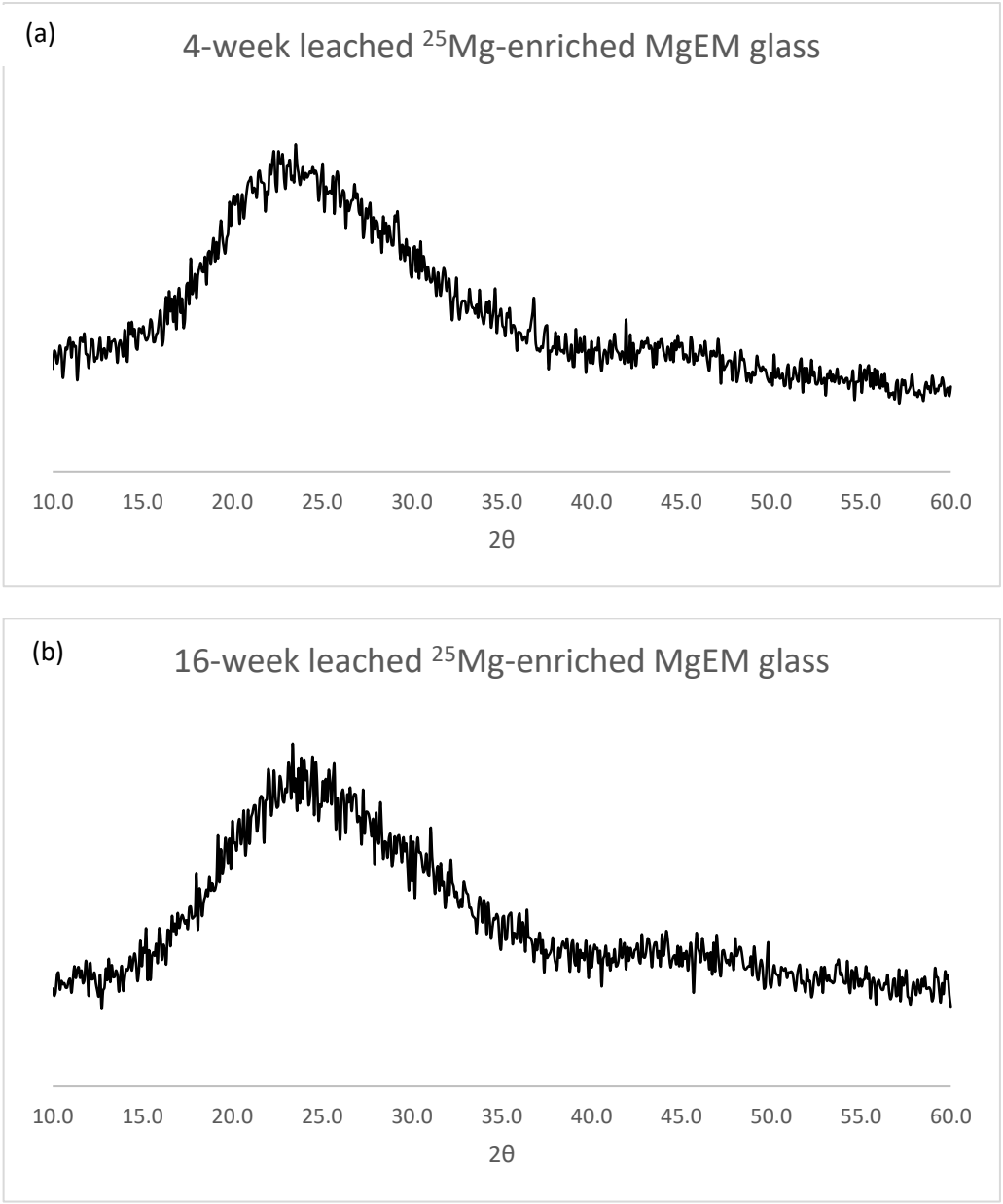

Figure 6-4 The powder XRD pattern of 25Mg-enriched MgEM glass that has been leached for (a) 4 weeks and (b) 16 weeks from the 2θ angle of 10.0 to 60.0° degrees.

6.2. In-depth characterisations by multinuclear NMR

The much higher dissolution degree/rate of the MgEM glass relative to the CaEM glass in the long-term (up to 112 days) was attributed to secondary effects (see Chapter 4). Given the null result from the XRD experiments, the focus was switched to multinuclear solid-state NMR

techniques to identify the degree and nature of the secondary reactions taking place during the dissolution.

6.2.1.1. Magnesium local environments

Enrichment of the MgEM glass to 96.9% ^{25}Mg made it possible to obtain ^{25}Mg MAS NMR spectra at relatively low magnetic field of 11.7 Tesla (Larmor frequency for ^{25}Mg of ~30.6 MHz). The spectra of pristine and 4-week leached ^{25}Mg-enriched MgEM glass are shown in Figure 6-5. While the centre band of the 4-week leached glass spectrum resembles the total linewidth and shape of the pristine glass counterpart, which is expected, there is a slight shift of the signal to higher frequencies, which may be due to the Mg species on the surface as a result of alteration and/or precipitation. More clearly, the fraction of the higher frequency signal increases for the 16-week leached sample, where a higher degree of dissolution took place, as shown in Figure 6-6. In Figure 6-6 (b), the pristine glass spectrum has been scaled and can be seen to represent part of that of the 16-week leached glass. A more quantitative illustration of the signal intensities between pristine and leached glass is discussed in the following paragraph. It is clear that Mg is present in different chemical environments than those in the pristine glass as a result of glass dissolution. However, it is difficult to uniquely identify them due to the rather small difference in NMR shifts for different Mg coordination and distribution induced broadening at such a low *S*/*N* level.

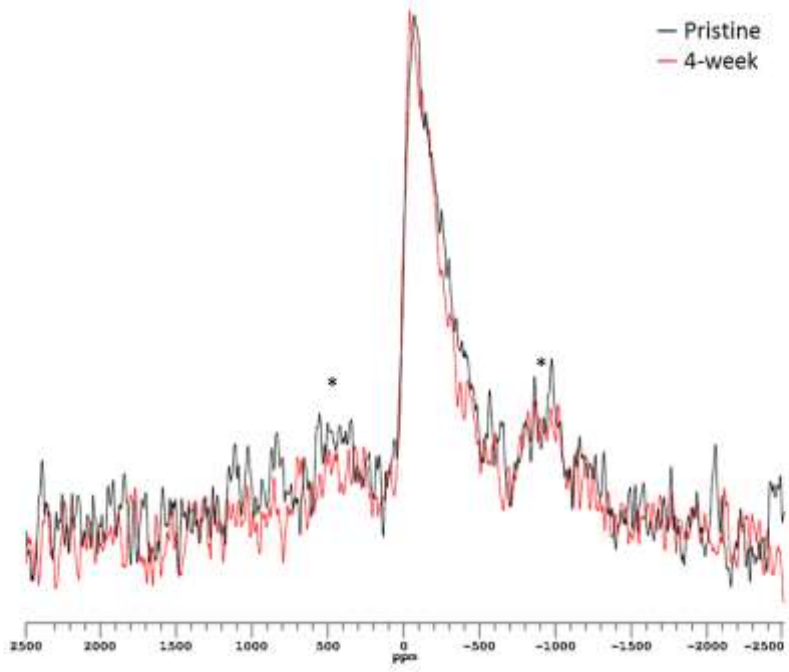

Figure 6-5 ^{25}Mg MAS NMR spectra of ^{25}Mg-enriched MgEM glass in pristine condition and after 4-week leaching. Spectra were acquired using a rotor-synchronised Hahn echo with a 20 kHz MAS rate at ~30.6 MHz. Asterisks denote spinning sidebands.

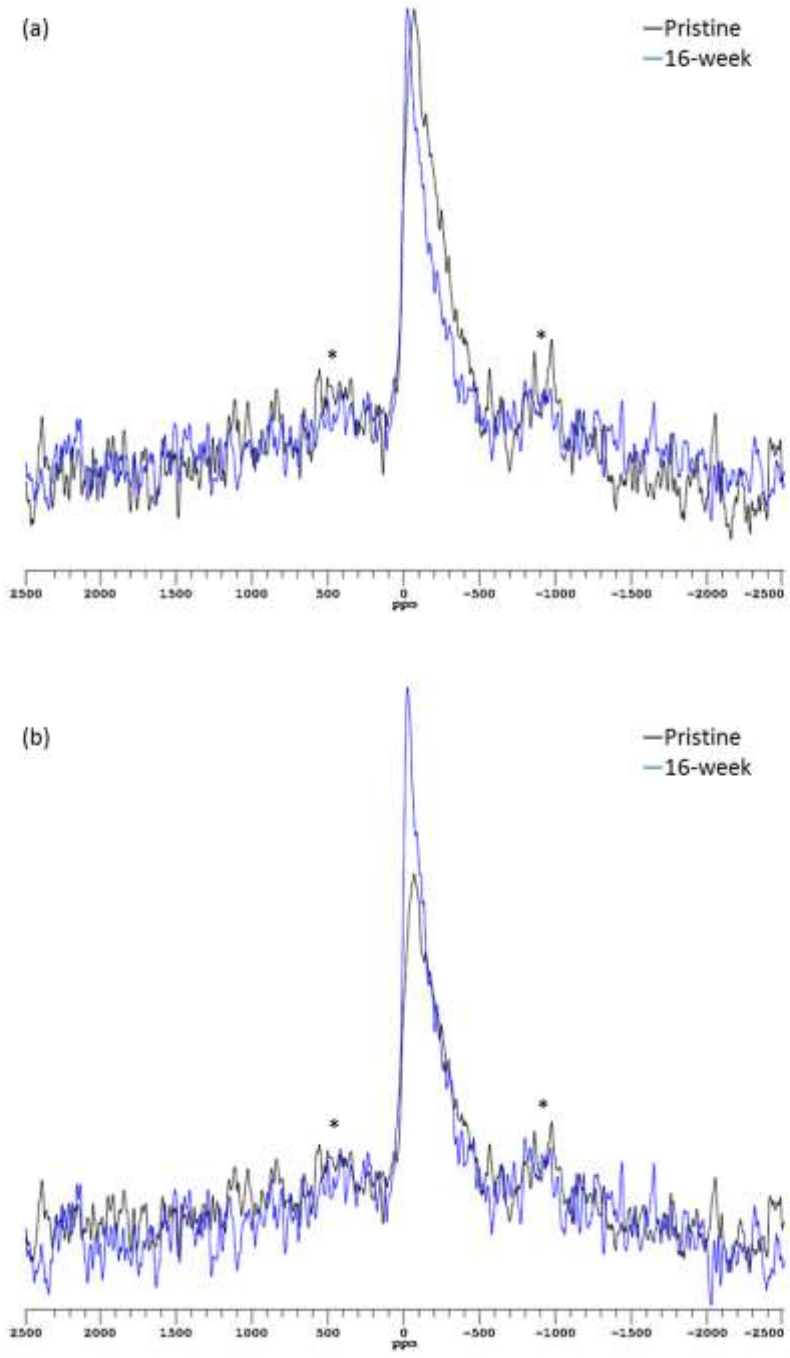

Figure 6-6 ^{25}Mg MAS NMR spectra of ^{25}Mg-enriched MgEM glass in pristine condition and after 16-week leaching acquired using rotor-synchronised Hahn echo at ~30.6 MHz with a 20 kHz MAS rate shown in (a) a similar amplitude manner; (b) signal of pristine glass as part of 16-week leached glass signal. Asterisks denote spinning sidebands.

A better *S*/*N* and higher resolution were achieved by going up to a higher magnetic field (850 MHz) with the assistance of DFS prior to the excitation as well as a CP pulse sequence. Figure 6-7 (a) compares the spectra between pristine and 16-week leached ^{25}Mg-enriched MgEM glass, as with Figure 6-6 (a). Similarly, there is clearly a fraction of signal to higher frequencies of that observed for the pristine glass. In Figure 6-6 (b), the same spectra were presented as normalised to the number of acquisitions and the sample mass so that the two spectra could be

quantitatively compared on a mass basis*. It is clear that the reduction of signal in the pristine glass regime is compensated by the additional signal of the surface Mg species (the absolute quantification is hindered by the baseline). The ^{25}Mg MAS NMR spectra of talc and the Mg-containing trioctahedral smectite (see 3.5.3.3) with a composition and structure intermediate between Mg-saponite and –hectorite were also obtained under similar conditions (except that the recycle delay for the talc experiment was 3.0 s whereas 1.0 s was applied to both the glass and smectite samples†). Figure 6-8 shows that the chemical environments of Mg in the smectite seems to well resemble that of the leached glass. However, the leached glass sample bears Mg in both the pristine part of the glass and in the alteration layers, which are not completely resolved in the 1D spectrum shown‡. Moreover, the lineshape of the smectite spectrum also indicates that the phase is of poor crystallinity and there is a distribution of EFGs at the Mg sites (see 4.2.4.4). Nevertheless, the similar high frequency end position suggests that the Mg local environments in the altered products are, broadly, chemically similar to those in the smectite if the linewidth (unresolved) of the former are shown to be similar, too. On the other hand, although there are two distinct Mg sites in talc, it consists of a more ordered structure hence EFGs and their distributions at Mg sites are much smaller. Either way, comparing Figure 6-7 and Figure 6-8 it is clear that the shift and widths of ^{25}Mg signal of talc corresponds well to the fraction of signal that is deduced to be originated from the alteration products.

* However, the altered product on the surface tend to have a lower density than the glass.
† Shorter delays were justified by the presence of Fe in the smectite and tested for the glass sample.
‡ 2D MQMAS (multiple quantum MAS) trials on the leached glass sample were not successful within the time available at the Warwick 850 MHz national facility.

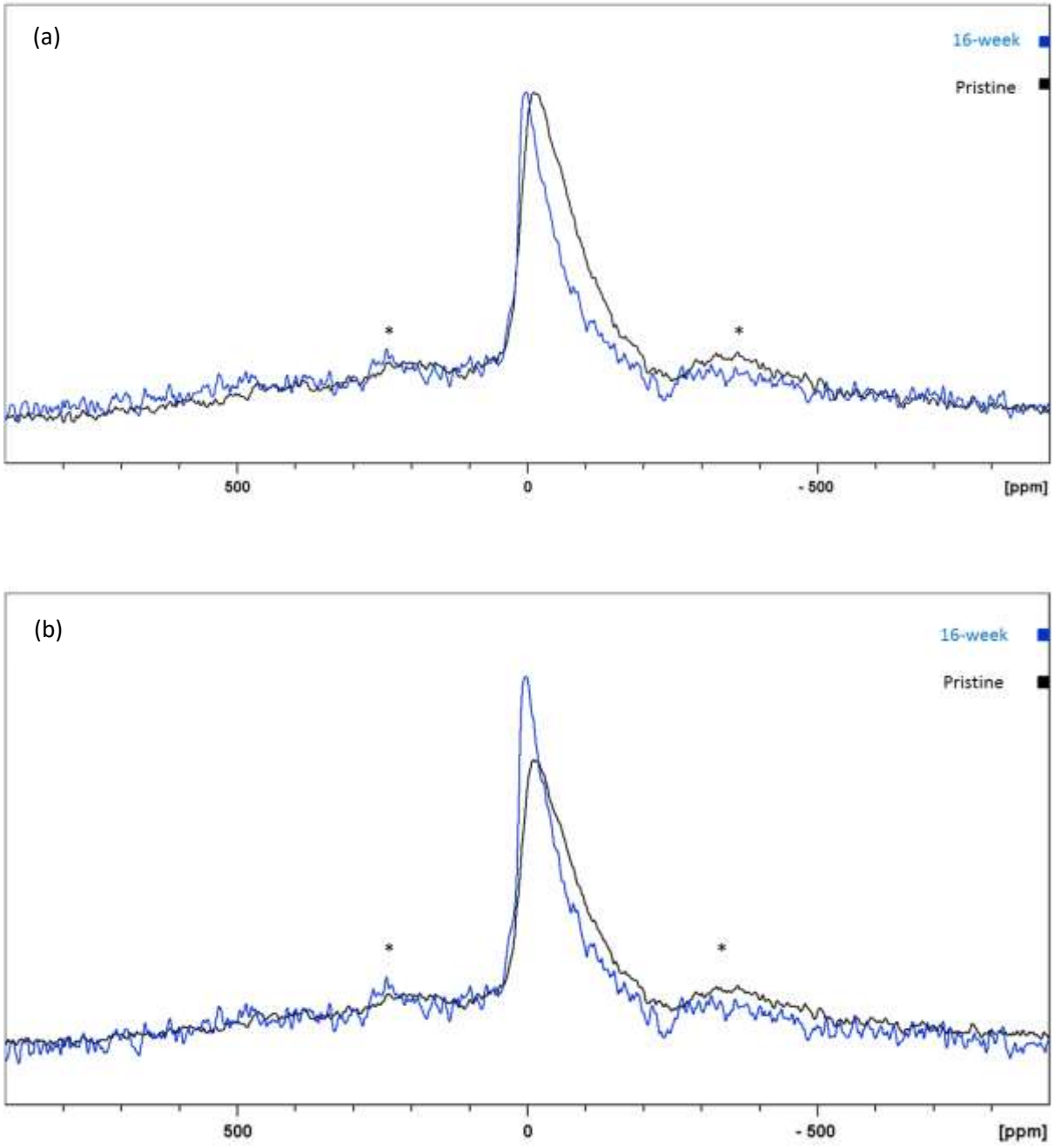

Figure 6-7 ^{25}Mg MAS NMR spectra of ^{25}Mg-enriched MgEM glass in pristine condition and after 16-week leaching : (a) with the same amplitude and (b) normalised to the sample mass and number of acquisitions, acquired using DFS assisted rotor-synchronised Hahn echo at ~52.04 MHz with a 14 kHz MAS rate. Asterisks denote spinning sidebands.

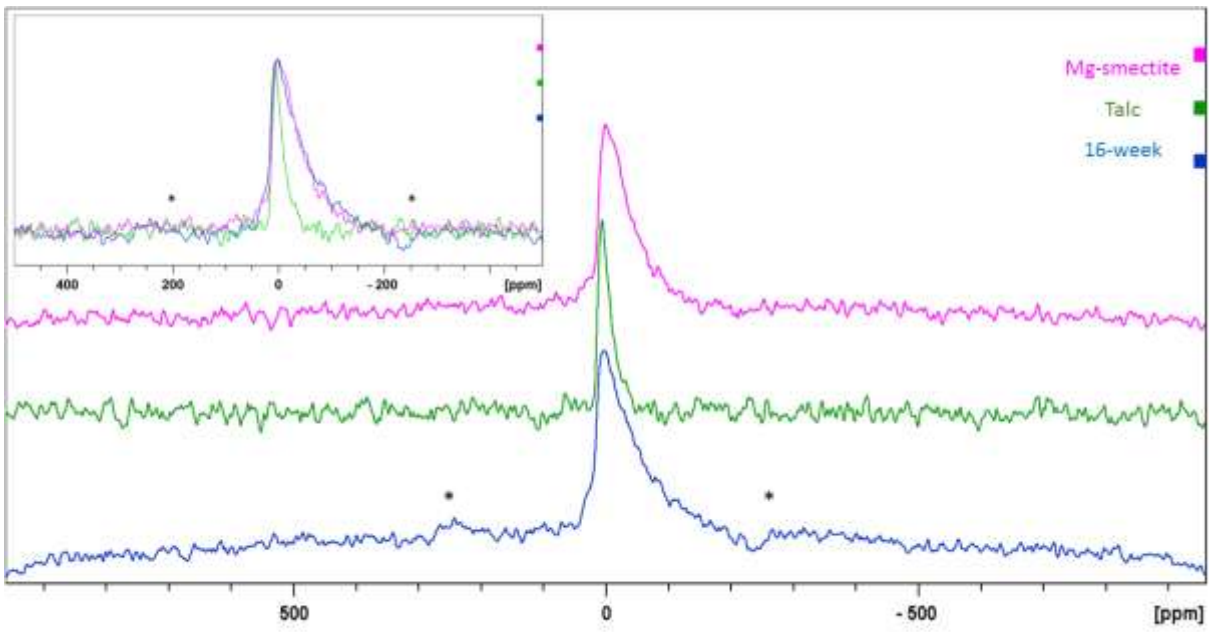

Figure 6-8 ^{25}Mg MAS NMR spectra of ^{25}Mg-enriched MgEM glass after 16-week leaching, talc and Mg-smectite acquired using DFS assisted rotor-synchronised Hahn echo at ~52.04 MHz with a 14 kHz MAS rate. The inset is the expansion of the same spectra overlaid. Asterisks denote spinning sidebands.

In order to selectively detect the NMR signal of ^{25}Mg from the alteration layers, static CP experiments were performed on the same 16-week leached ^{25}Mg-enriched MgEM glass sample as well as on the talc and smectite samples. While the ^{1}H-polarised ^{25}Mg signal was seen from the former two samples, there was no success with the smectite[§]. Unfortunately, the CPMAS experiments, which could potentially provide better resolution, were not successful either using the static contact and matching conditions. The similarities between the static CP spectra of talc and 16-week leached glass are shown in Figure 6-9 in terms of shift position, line width and lineshape. As mentioned, the limited time and sensitivity did not allow the exploration of lineshape and intensity as a function of the contact time, hence the line features could well change if a different contact time was used. However, the implications from the MAS spectra between these two samples (Figure 6-8) corroborate the claim that the alteration products and talc possess Mg in similar chemical environments.

[§] There are many reasons CP did not work on the smectite, please refer to 2.4.1.3.

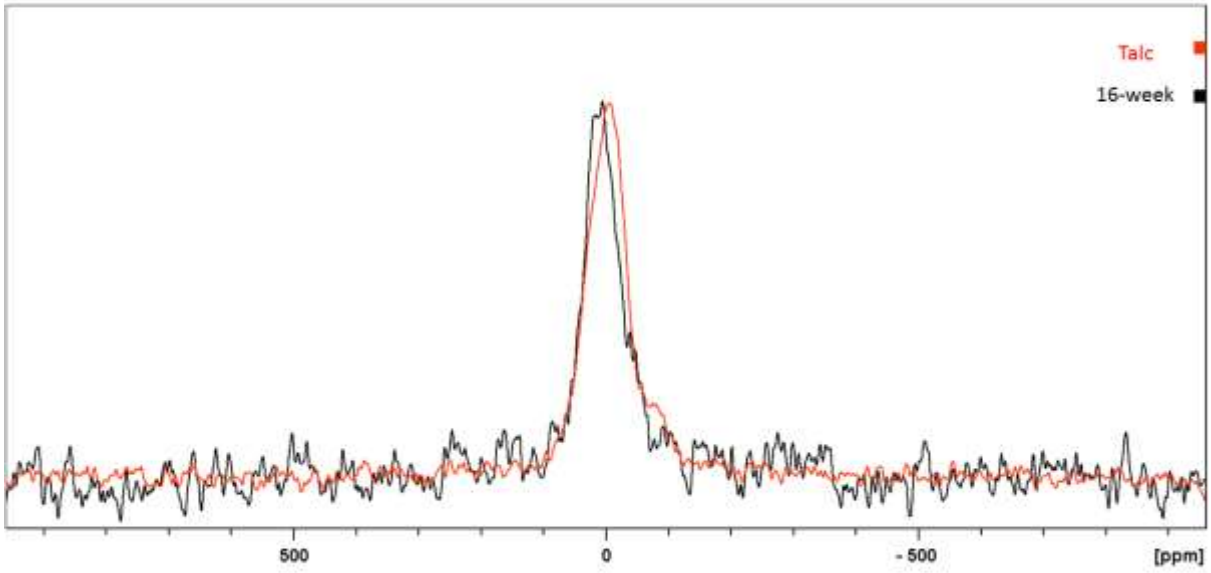

Figure 6-9 Static ^{1}H-^{25}Mg CP spectra of talc (ct=43 ms) and ^{25}Mg-enriched MgEM glass leached for 16 weeks (ct=20 ms).

While the static ^{1}H-^{25}Mg CP experiment successfully detected the signal from the alteration layers selectively, the spectrum lacks resolution. Therefore, it is unclear, from Figure 6-9, how many Mg sites actually give rise to the signal (note: the two magnesium sites in talc are not resolved statically, either). Nevertheless, the linewidth and shape is characteristic of Mg sites coupled with modest EFGs (considering the large quadrupole moment of ^{25}Mg) and a high η_Q. Assuming there is only one type of Mg or two very similar ones (like in talc), the lineshape can be simulated. Figure 6-10 shows the 'best' fit of the spectrum using one static central transition quadrupole lineshape. The corresponding NMR parameters are: $\delta_{iso} \sim 15.0$ ppm, $C_Q \sim 2.4$ MHz and $\eta_Q \sim 0.72$. The result of this fit can be compared with CASTEP calculations of chemical shift and EFG parameters for several Mg silicates to approximate the chemical environment of Mg in the alteration layers of the leached glass (see Chapter 7).

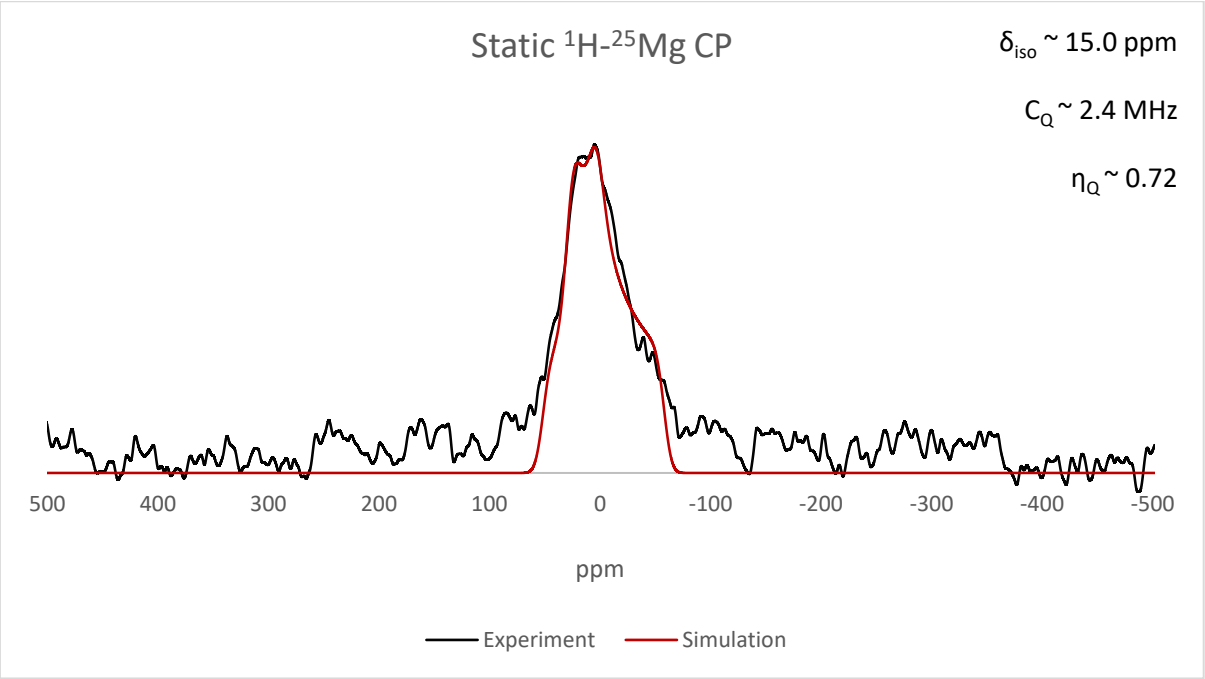

Figure 6-10 Static ^{1}H-^{25}Mg CP spectrum of ^{25}Mg-enriched MgEM glass leached for 16 weeks and simulation of the spectrum using the Q stat ½ model (1 line) in dmfit. The NMR parameters extracted from the fitting are also listed.

6.2.1.2. Silicon local environments

^{29}Si NMR is very sensitive to the local coordination environment in silicates (e.g. number of coordinated oxygen, the type of NNN, such as the presence or not of bridging oxygens, and Q^n speciation). In contrast to ^{25}Mg and ^{17}O NMR, it is not subject to quadrupole broadening effects due to its I = ½ spin number. Thus, ^{29}Si MAS NMR spectra can usually differentiate between bonding environments and provide mid-range connectivity information (MacKenzie and Smith, 2002). Furthermore, ^{1}H-^{29}Si CPMAS experiments have been used to study the hydration at the surface of some silicates and silica where distinctive surface Si sites were identified (Maciel and Sindorf, 1980; Schmelz and Stebbins, 1993; Davis *et al.*, 2009). However, disorder in glassy silicates tends to result in featureless ^{29}Si MAS NMR lines due to distributions in δ_{iso}, especially when the bonding environments give rise to overlapping chemical shift ranges. Figure 6-11 shows the single-pulse, MAS spectra of MgEM glass in pristine and post 16-week leaching conditions as well as the CPMAS spectrum (5 ms contact time) of the latter, normalised to the same amplitude. The single-pulse spectra of pristine and leached glass both show a featureless line centred at ~-99.2 ppm (CoM), typical of Q^3 for 4-fold coordinated Si in silicates, and cover the shift ranging from Q^2 to Q^4 (Mägi *et al.*, 1984). The two spectra are also almost entirely overlapping (the same recycle delay of 240.0 s) and the signal from the alteration layers was not resolved from the pristine glass, within the *S*/*N*. The spectrum obtained by CP, which arises from silicon adjacent to protons does show a narrower line but the CoM remains at ~99.0 ppm, consistent with an average of Q^3 species within the alteration layers as well (the

line is highly asymmetrical, though). Both observations are in contrast to what was observed for ISG where the surface passivation layer has a noticeably higher degree of polymerisation, as indicated by a more shielded ^{29}Si shift position by ~6.0 ppm (Gin, Jollivet, Fournier, Angeli, *et al.*, 2015). This is highlighted in Figure 6-12 where both the MAS NMR spectra in Figure 6-11 are replicated but expanded to the same chemical shift range as presented in the literature, to capture any delicate changes.

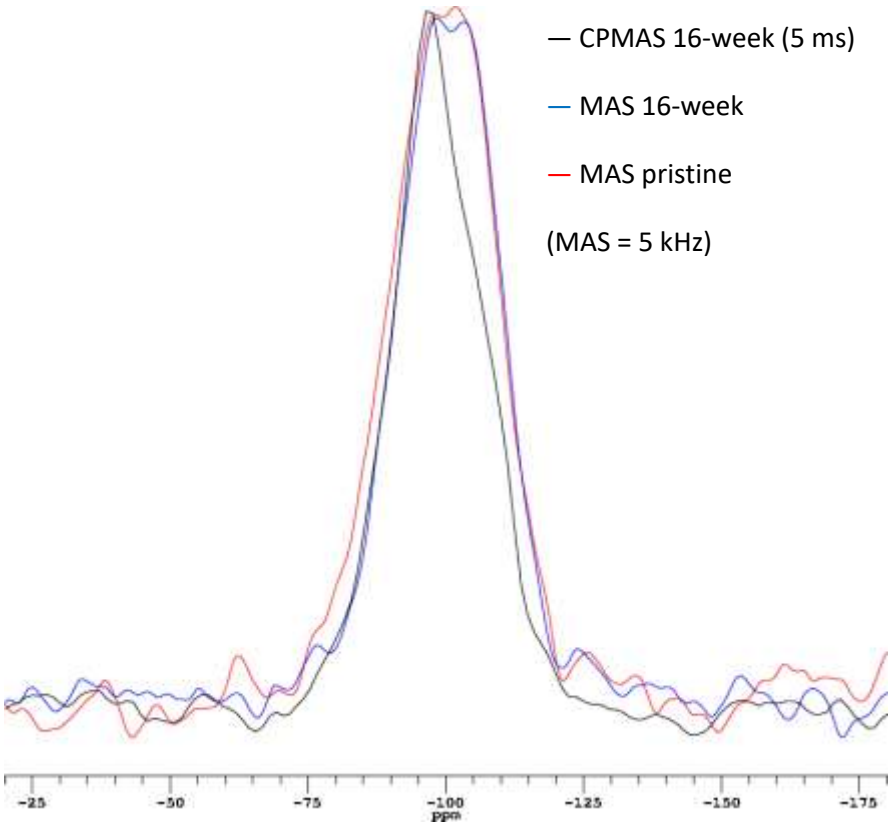

Figure 6-11 Single-pulse ^{29}Si MAS NMR spectrum of pristine and 16-week leached MgEM glass as well as the ^{1}H-^{25}Si CPMAS spectrum (contact time = 5 ms), presented with the same amplitude. The MAS rates in all cases were 5 kHz.

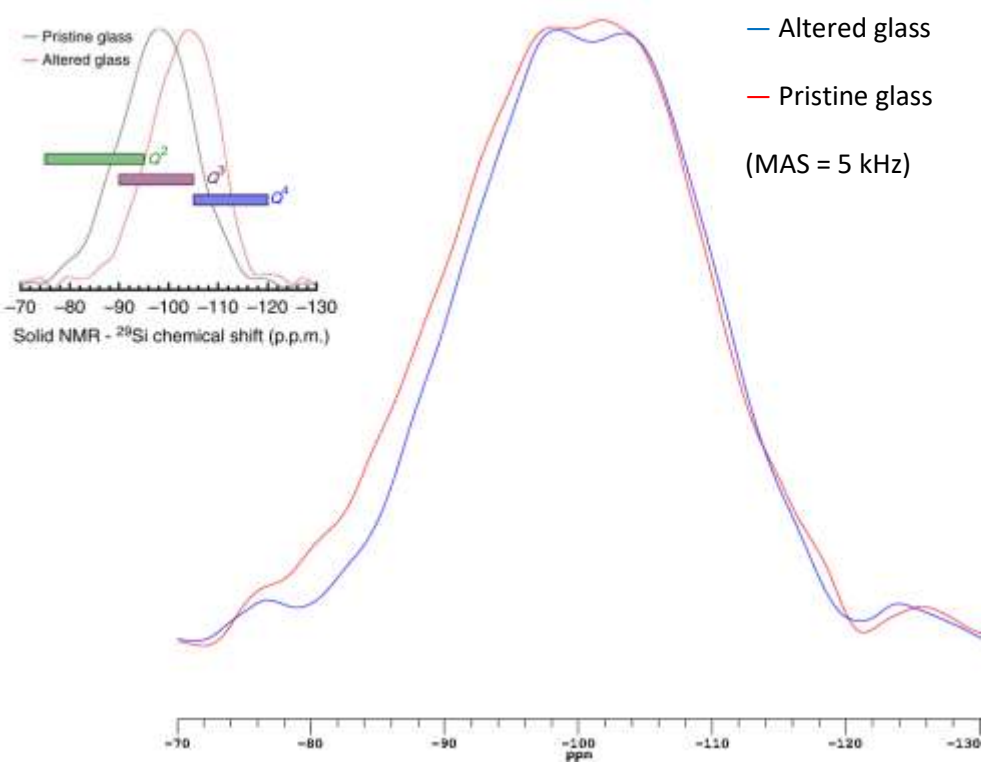

Figure 6-12 Single-pulse ^{29}Si MAS NMR spectra of pristine and 16-week leached MgEM glass as in Figure 6-11 with an expanded view from -70 to -130 ppm in order to compare with the results of ISG in the literature (inset) (Gin, Jollivet, Fournier, Angeli, *et al.*, 2015).

The effect of contact time on CP signal intensity and lineshape is shown in Figure 6-13 for the 16-week leached sample. The CP signal intensity peaked at 5.0 ms and more or less plateaued and diminished after 40.0 ms. The intensity profile exhibits the typical shape that results from the two simultaneous and competing processes: 1. magnetisation transfer from ^{1}H to ^{29}Si (T_{Si-H}) and 2. ^{1}H spin-lattice relaxation in the rotating frame ($T_{1\rho}$) (see 2.4.1). As the contact time was increased, a higher proportion of more shielded Si Q^4 species was observed as they are located further away from protons when compared with 'Si-OH' type structures. This is confirmed in Figure 6-13 (b) where the signal at ~-110 ppm is clearly seen at contact times longer than 20.0 ms (pure silica glass has a shift of -111~-112 ppm and a width of 11~12 ppm (Kirkpatrick *et al.*, 1986)), even though the total intensity is diminished in the meantime. Therefore, it can be concluded that Q^4 units are also present in the alteration layers. They could arise from either a relic of the glass network, from the re-construction of the hydrated glass (see 6.3) or from within the precipitates as structural units. However, the overall very convoluted and broad signal, and possibly very similar shift positions, do not provide sufficient resolution to differentiate between different Si species within the alteration layers.

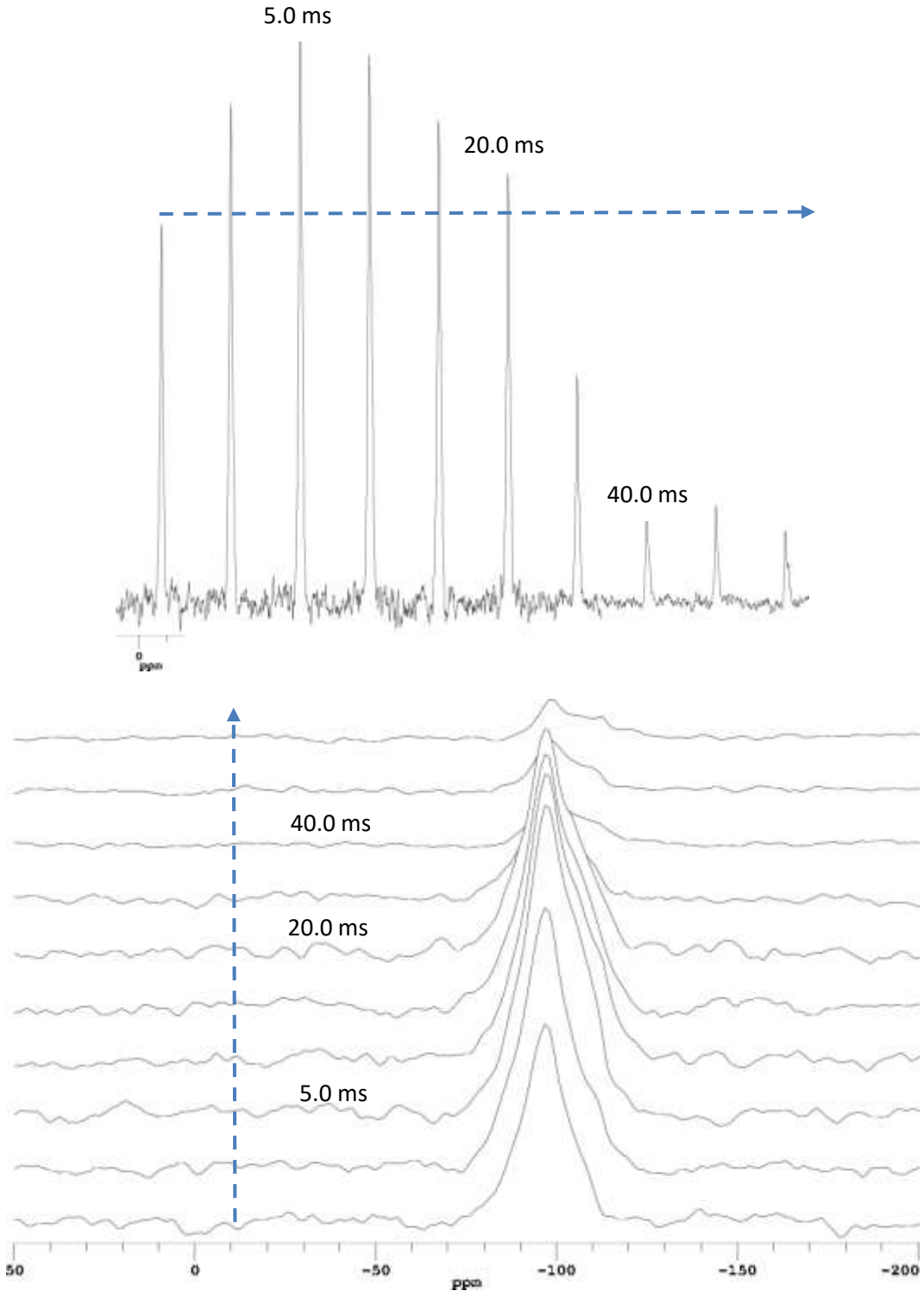

Figure 6-13 ^{1}H-^{29}Si CPMAS signal (a) intensity and (b) lineshape as a function of contact time ranging from 0.5 to 80 ms. The time increment is in the direction noted by the dotted arrows.

However, comparisons could be made between the leached glass sample and other hydrous Mg silicates. The CPMAS spectra of the same Mg-smectite (see 6.2.1.1) and talc, together with that in Figure 6-11, were shown in Figure 6-14. It is clear that silicon environments, as manifested by the average shift position, in the alteration layers resemble those in talc (CoM ~98.3 ppm) more than in the Mg-smectite (CoM ~ -92.0). Nevertheless, the alteration layers do show a high degree of positional disorder manifested in its much broader linewidth compared with talc. The

comparable linewidth between Mg-smectite and the leached glass, on the other hand, suggests a similar degree of disorder and reconciles with the fact that the Mg-smectite was also a precipitation product from glass (Mg-containing) dissolution. Because AVM 10 glass is much more complex (31-component) than MgEM (6-component), the precipitation products are supposed to have very different chemistry hence the ^{29}Si shift position could drift even with the same local structure but different chemistry e.g. NNN effect. The findings from ^{29}Si NMR spectra of these three materials are consistent with the ^{25}Mg NMR results.

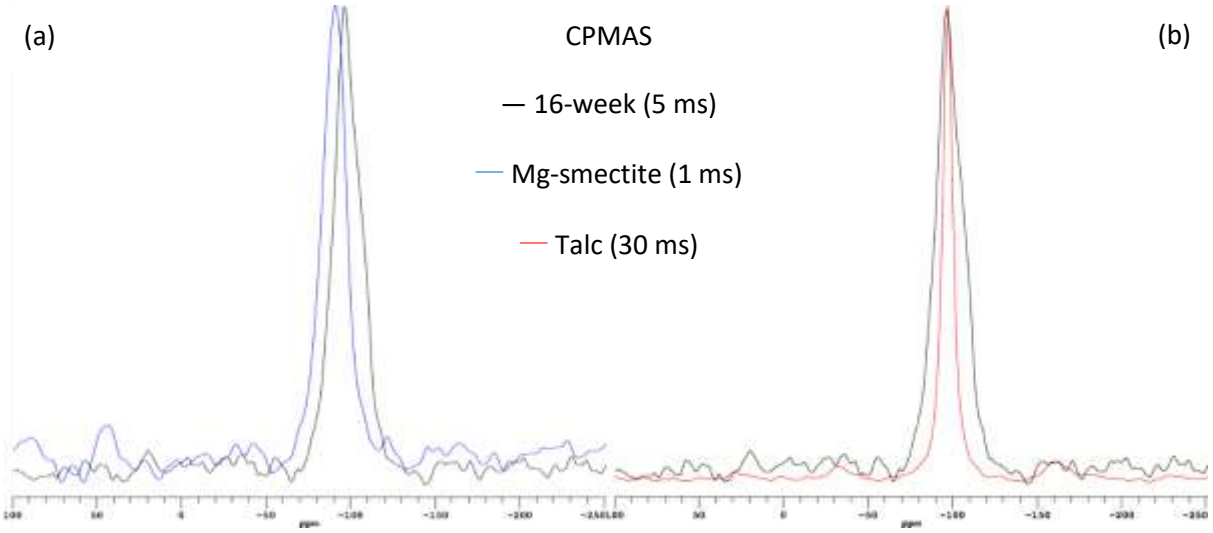

Figure 6-14 CPMAS (5 kHz) spectra of (b) 16-week leached MgEM glass and Mg-smectite and (b) 16-week leached MgEM glass and talc. The contact time at which the each spectrum was obtained was noted.

6.2.1.3. Proton local environments

As the most NMR sensitive isotope with I = ½, it is usually relatively easy, quick and straightforward to achieve high S/N ratio in ^{1}H solid-state experiments. However, its high sensitivity also means that the homonuclear coupling could be very strong relative to other nuclei so that the residual line width of ^{1}H signal is often primarily rendered by this mechanism, which could not necessarily be narrowed under MAS (see below). In inorganic solids, the chemical shift of proton has been well linked with the strength of hydrogen bond, which in turn reflects the O-H···O distance (Berglund and Vaughan, 1980). While ^{1}H solid-state NMR could potentially provide insightful structural information for hydrous inorganic solid materials[**], the ubiquitous nature of proton is usually a nuisance, appearing as background signals in the spectra, for example from the probehead outside the coil, which could severely interfere with the signal from the sample, especially when the sample's proton content is low.

[**] The ^{1}H NMR topic is restricted to inorganic solids in this thesis whilst it finds its applications far beyond e.g. pharmaceutical and protein characterisations.

Figure 6-15 (a) shows the difference in intensity of ^{1}H signal arising from CaEM and MgEM glasses leached for 16 weeks. They are presented on a scale normalised to the mass of the sample so that the intensities reflect the relative hydrogen content as well as the speciation in the alteration layers. The overall proton signal per mass unit was determined by spectral integration, and thus, the hydrogen content in the MgEM glass alteration layers is ~6.5 times that of the CaEM. The greater hydrogen content is qualitatively consistent with the greater degree of dissolution of the former, as determined by B concentration in the respective leachant (see 5.2), and there are more than one hydrogen species present in the alteration layers of both glasses. A similar phenomenon is also observed between 16-week leached SON68 and MW25 glasses (Figure 6-15 (b)).

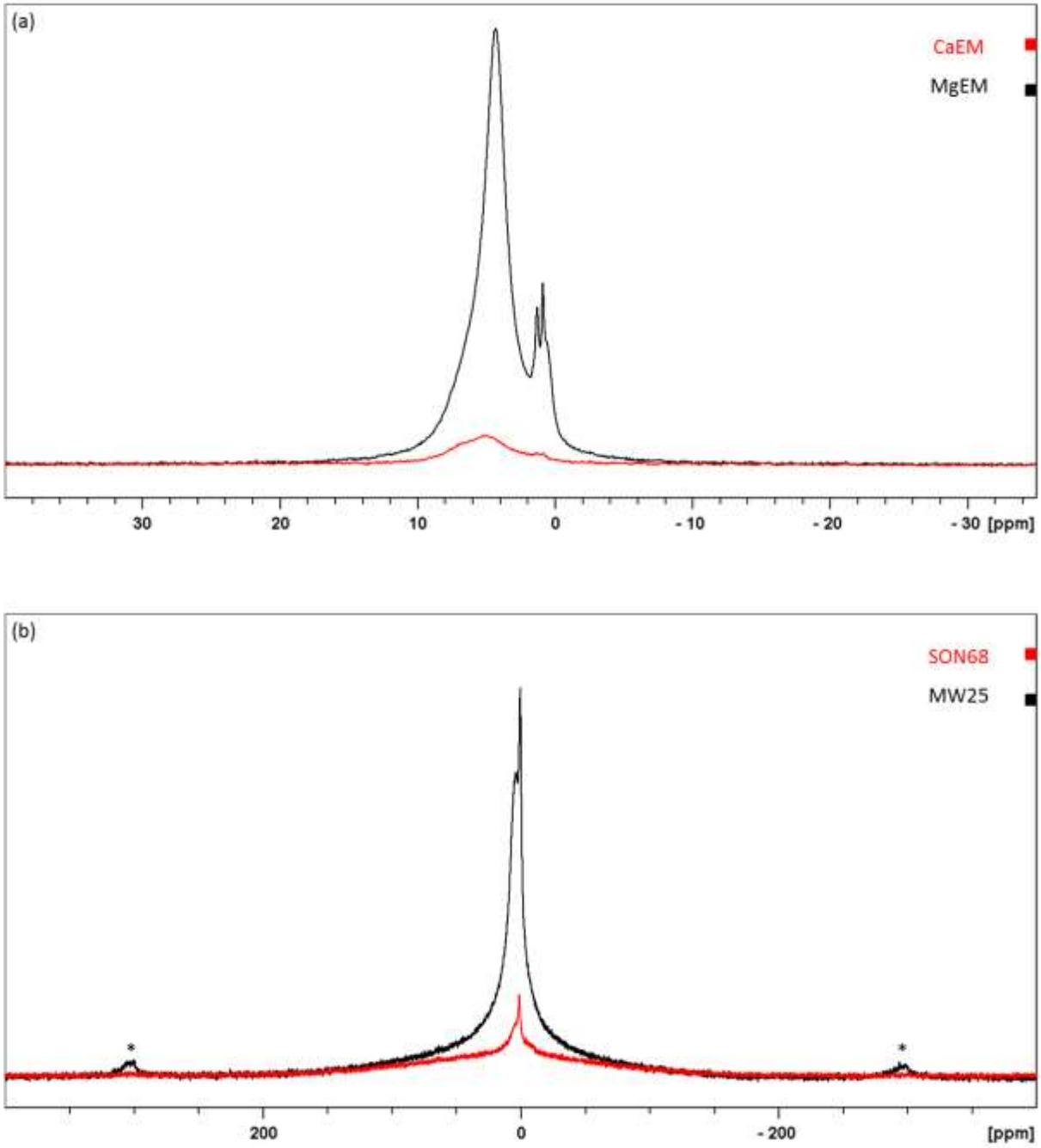

Figure 6-15 ^{1}H MAS NMR spectra of (a) 16-week leached CaEM and MgEM glasses and (b) 16-week leached SON68 and MW25 glasses acquired at 200.21 MHz using a rotor-synchronised (60 kHz) Hahn echo pulse sequence. The intensities are normalised to the mass of the sample. Asterisks denote spinning sidebands.

It should be recalled that the thickness of the altered glass determined by B concentration is 3.402 and 0.364 µm for MgEM and CaEM, respectively. For a median glass particle diameter of 112.5 µm, these thicknesses represent a small fraction of the total sample being investigated and, thus, the proton signal will be relatively weak despite its high NMR sensitivity. In this case, the background ^{1}H signal of the probe and rotor must be taken into account. The application of a rotor-synchronised Hahn echo pulse sequence to acquire spectra places phases and amplitude constraints on the refocused signal and this results in primarily the signal from inside the rotor

forming the echo. This is to say that signal from outside the rotor, detected in signal pulse experiments, will not be refocused hence will not be detected in the echo. This is demonstrated in Figure 6-16 where the ^{1}H MAS NMR spectra obtained from MgEM glass leached for 16 weeks by both single-pulse and synchronised Hahn echo are compared. Figure 6-16 (a) demonstrates that the background signal was clearly suppressed by applying Hahn echo pulse sequence due to its poor refocusing. Similar background signals were seen across the acquisitions while the real signal differs from one another. A major advantage of very rapid sample rotation speed (60 kHz) is that the delay in the synchronised echo is very short, leading to negligible loss of signal due to T_2 effect between excitations. An expansion of the central resonances is shown in Figure 6-16(b): three peak maxima are resolved at ~4.3, ~1.3 and ~0.9 ppm, respectively, and there is a low frequency shoulder to the 0.9 ppm peak. In addition, the signal that appeared as a high frequency shoulder to the 4.3 ppm peak in the single-pulse spectrum was suppressed by Hahn echo. However, it is unclear whether this signal arises from the background or the sample itself. On the other hand, spectra obtained at different spinning speeds show a different picture. Single-pulse spectra[††] of 16-week leached MgEM in Figure 6-17 (a) show that a higher spinning speed (60 kHz) increases the amplitude of the 4.3 ppm peak. On the contrary, the intensity in a wider region was increased at a lower spinning speed (20 kHz), as indicated. Further, spinning sidebands appeared at both speeds.

It is also interesting to observe the changes, if there are any, in hydrogen species between 4-week and 16-week leached MgEM glass because of the observed differences in solution chemistry and surface features. Figure 6-18 (a) highlights the similarities and differences between the ^{1}H NMR signals from MgEM glass leached for these two durations. The primary line features are similar with the group of peaks seen from the 16-week leached sample all present in the 4-week sample. However, for the latter, the low frequency peaks are less well resolved and of lower intensity. In addition, the higher frequency 'shoulder' to the 4.3 ppm peak is much more pronounced and an additional signal is observed at between 14.0 and 15.0 ppm (similar features are observed when the single-pulse spectra are compared (not shown)). Moreover, as shown by Figure 6-18 (b), the additional signal vanished when the sample was spun at a lower MAS rate (20 kHz). A similar trend in signal amplitude and intensity as a function of spinning speed as shown in Figure 6-17 (a), is also seen for the 4-week sample except

[††] Hahn echo spectra would selectively suppress/accentuate certain signals depending on their lattice-lattice relaxation rates.

that the amplitude of the 'shoulder' also decreases at 20 kHz compared with 60 kHz spinning (detailed analysis in 6.3).

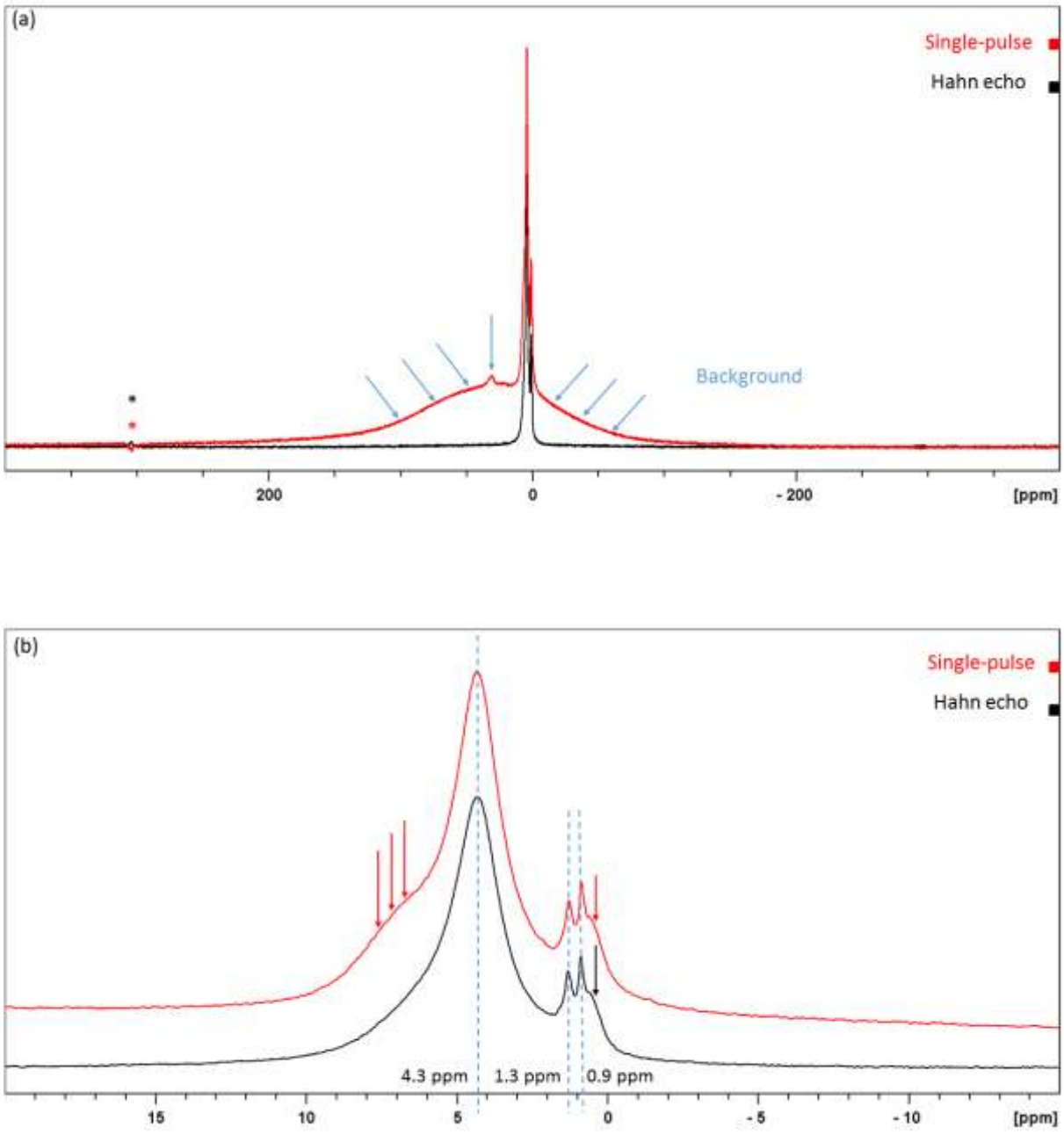

Figure 6-16 (a) ^{1}H MAS NMR spectra of 16-week leached MgEM glass acquired using single-pulse excitation and Hahn echo; (b) Expansion of (a) highlighting the three peak positions and a shoulder in the single-pulse spectrum. For both acquisitions, the spinning speed was 60 kHz. 96 scans were accumulated for Hahn echo acquisition while 64 scans for single-pulse excitation, but the spectra were normalised to the number of acquisitions. Asterisks denote spinning sidebands.

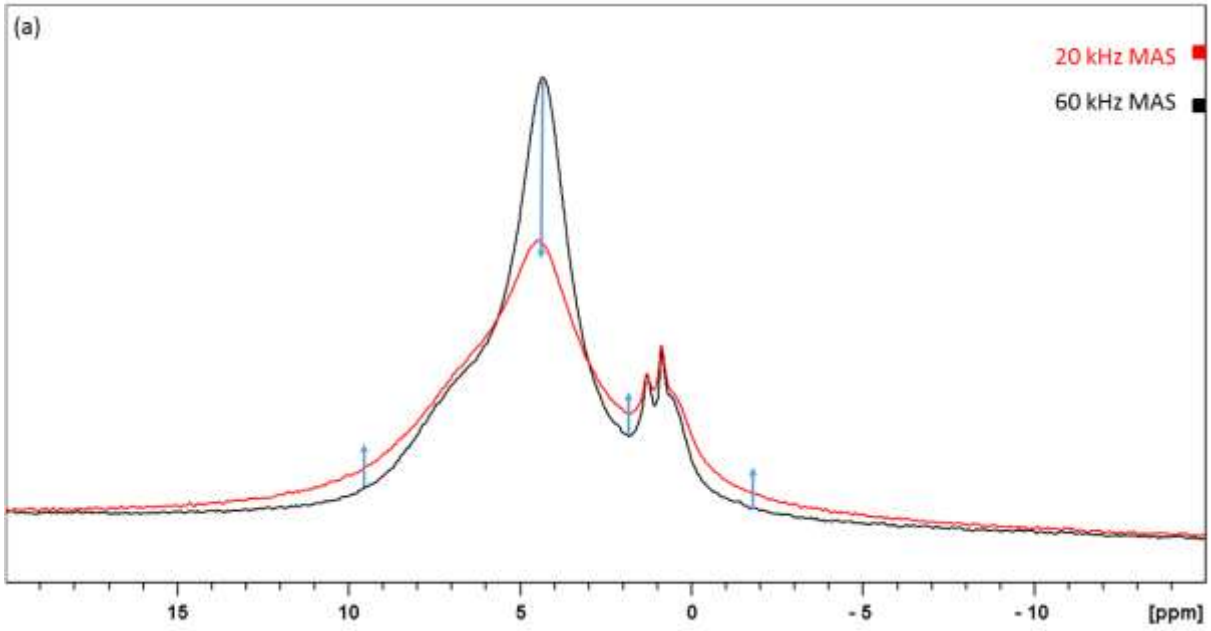
(a)
20 kHz MAS
60 kHz MAS
15
10
5
0
- 5
- 10
[ppm]

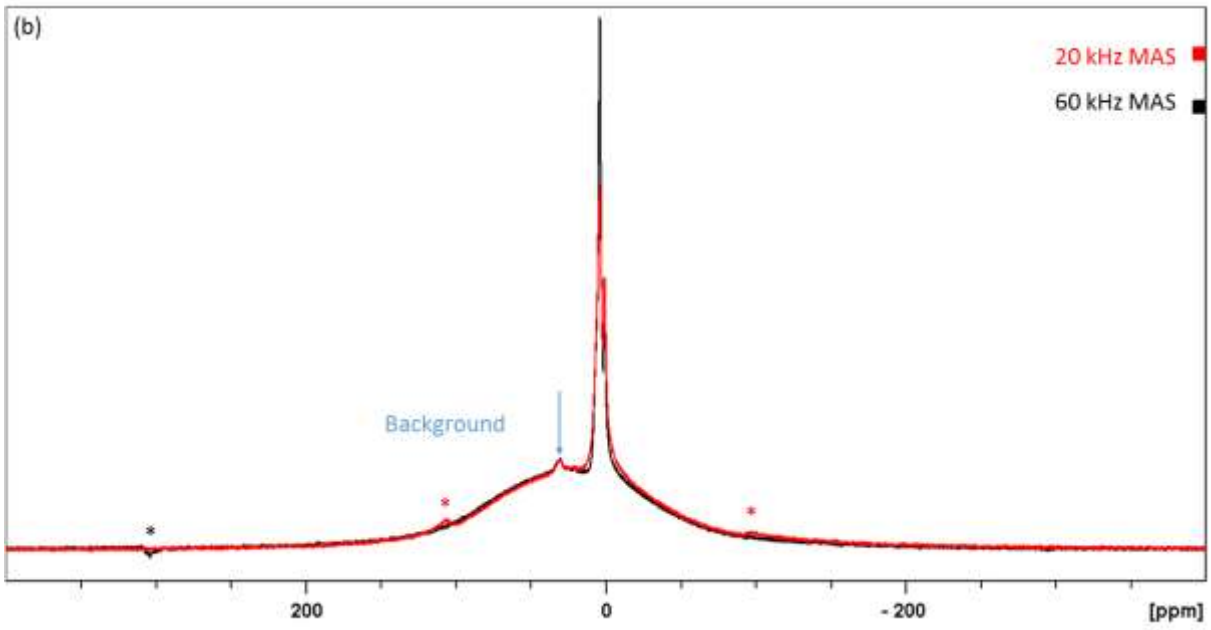
(b)
20 kHz MAS
60 kHz MAS
Background
*
*
*
200
0
- 200
[ppm]

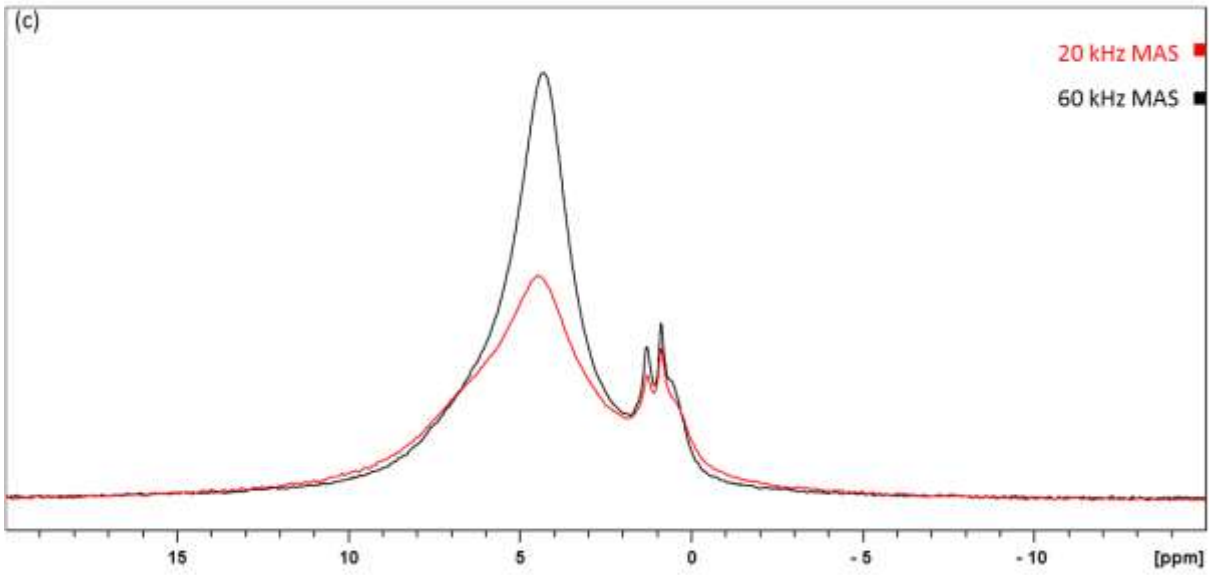

Figure 6-17 (a) ^{1}H MAS NMR spectra of 16-week leached MgEM glass acquired using (a) single-pulse excitation at 20 and 60 kHz spinning speed; (b) Full range of (a) showing the spinning sidebands (asterisks); (c) Hahn echo pulse sequence.

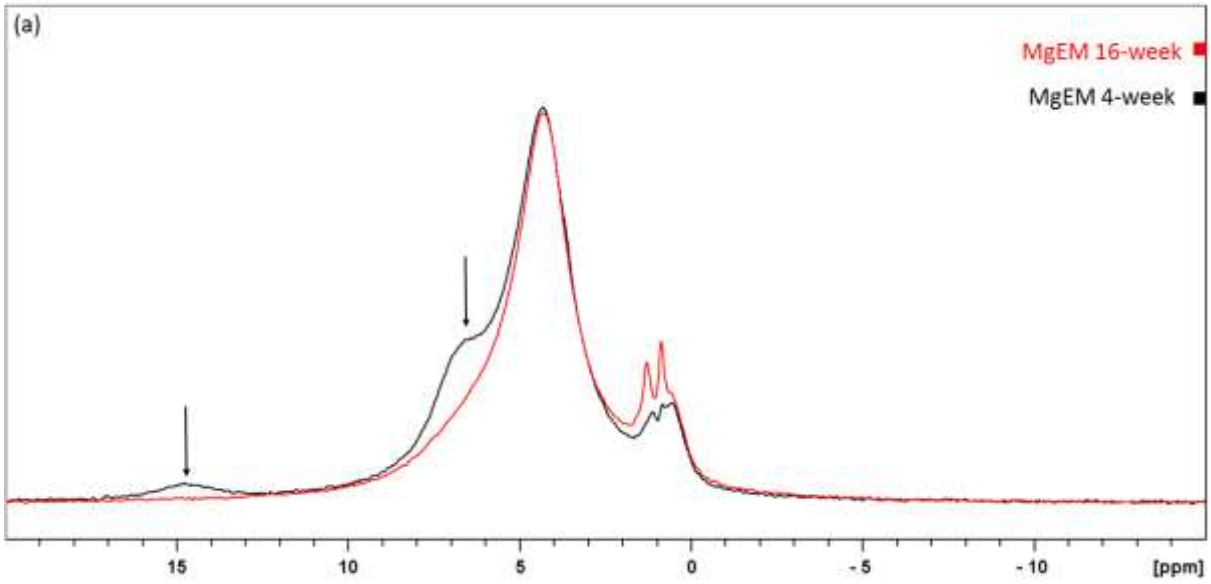

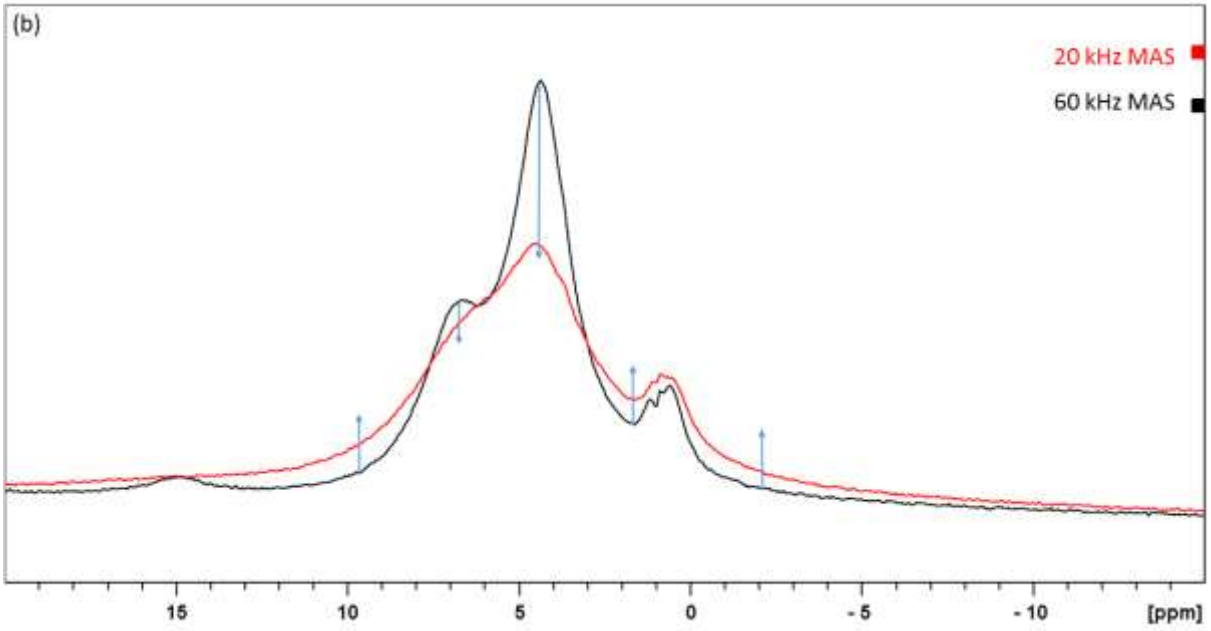

Figure 6-18 (a) Comparison between 60 kHz Hahn echo ^{1}H MAS NMR spectrum of 4-week and 16-week leached MgEM glass normalised to the sample mass; (b)) ^{1}H MAS NMR spectra of 4-week leached MgEM glass acquired using single-pulse excitation at 20 and 60 kHz spinning speed.

6.2.1.4. Oxygen local environments

While oxygen is the most important element in crystalline silicates and glasses, and holds unique information about the network connectivity as well as intermediate-range order/disorder for the latter, isotopic enrichment is usually needed for solid-state ^{17}O NMR experiments because of its extremely low natural abundance. Ashbrook and Farnan (2004) demonstrated the power of ^{1}H-^{17}O CP for obtaining high quality ^{17}O spectra for brucite without ^{17}O enrichment. However, it was a static acquisition using a full 7.5 mm rotor on a material with every oxygen being hydroxyl, with an attached proton available for magnetisation transfer. In a leached glass sample, CP signals can only be acquired from an alteration layer of a few microns, on the surface of a particle with a 112.5 µm median diameter. Based on the measured concentration of leached boron, even for the most altered MgEM glass that was leached for 112 days, the estimated thickness of the alteration layer is ~3.4 µm which means that any ^{1}H-^{17}O CP signal acquired would be only from this layer of material whilst the remainder unaltered glass simply fills the rotor space without contributing to any signal. Therefore, ^{17}O NMR experiments were performed on CaEM and MgEM glasses that were leached in ^{17}O-enriched (45%) water for 112 days as described in the previous study (Brigden and Farnan, 2014) and 3.4.2.2.

Figure 6-19 shows the drastic difference in ^{17}O NMR signal intensity between that of the CaEM and MgEM glasses, with the spectra normalised to the number of scans and sample mass and

acquired using the same recycle delay time (5.0 s[‡‡]). Since the observed ^{17}O signal would primarily originate from the enriched water, the intensities basically illustrate the degree of glass-water interaction. Qualitatively, this is consistent with the proton content between these two endmembers (see Figure 6-15), both of which denote a much higher degree of alteration for MgEM compared with CaEM. In addition, some features in the MgEM lineshape could be seen but not resolved, probably owing to multiple oxygen sites of similar shift positions and the broadening of each component due to the distributions in both δ_{iso} and EFG, given the non-crystalline nature of the alteration products.

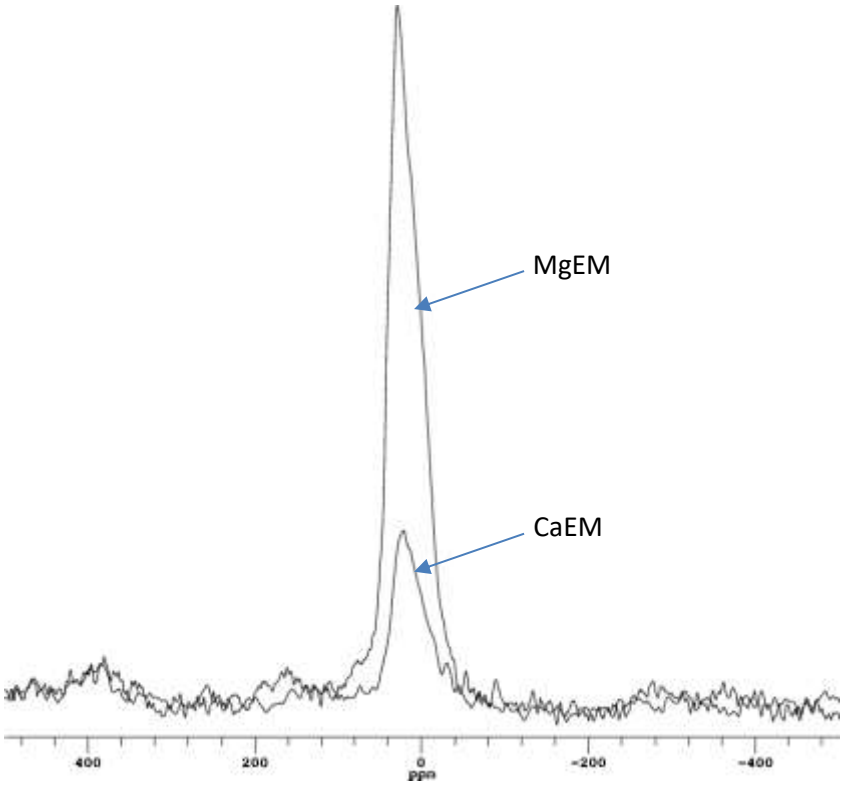

Figure 6-19 ^{17}O MAS NMR single-pulse spectra of MgEM and CaEM glasses leached in ^{17}O-enriched water for 112 days. The MAS rate was 20 kHz and spectra were acquired at ~67.8 MHz using a π/18 pulse every 5.0 s. The intensities are normalised to the number of scans and sample mass. However, the spectra were obtained ~2 years after the samples were prepared. Therefore, strict quantitative comparisons are not made.

A Z-filter 3QMAS experiment was performed on the same MgEM sample in an effort to improve the resolution of the ^{17}O MAS spectrum with the same spinning speed 20 kHz. The isotropic 3QMAS dimension (F_1) is presented vertically and the anisotropic MAS dimension (F_2) is horizontal. Both axes are referenced to H_2O as 0 ppm and scaled and labelled as described in 2.4.3.2. The 2D signals (peaks) are plotted as contours from 20% to 100% intensity of a linear spacing of 10% and lighter colours denoting higher intensities and vice versa. Evidently, two separate peaks, (a) and (b), are clearly resolved. In order to determine the δ_{CS}^{iso} and P_Q of

[‡‡] Single-pulse excitation MAS spectra collected with a recycle delay of 0.5 s and 5.0 s exhibit (not shown) the same lineshape and almost the same intensity (slightly i.e. < 5 % higher) for the latter.

each peak, Equation 2-23 and Equation 2-28 were applied after determining the CoMs of the projections of each peak on both axes as shown in Appendix III, and the results are shown in Table 6-1.

For 3QMAS spectra of $I = {}^5/_2$ nuclei following the C_z convention, according to Equation 2-28, there are two special lines in the sheared 2D spectra. Line CS with a gradient of -17/12 reflects a distribution of δ_{CS}^{iso} values in the case of a fixed δ_{Q}^{iso} whilst line QIS denotes the opposite with a gradient of ${}^5/_6$. While peak (b) shows its isotropic characteristics with its alignment almost parallel to the F2 dimension, peak (a) shows distributions in both parameters especially the isotropic chemical shifts. The relatively poor *S*/*N* ratio, as seen in Appendix III, does not allow a very accurate determination of the NMR interaction parameters. Nevertheless, the δ_{CS}^{iso} and δ_{Q}^{iso} values reported in Table 6-1 for site (b) are consistent with bridging Si-O-Si type oxygens, as in silica polymorphs including quartz (~38 ppm; ~5.3 MHz) and cristobalite (~40 ppm; ~5.3 MHz) (Spearing, Farnan and Stebbins, 1992; Van Eck, Smith and Kohn, 1999; MacKenzie and Smith, 2002) despite the apparently higher chemical shifts computed here. This issue and the identity of site (a) are further discussed below with ^{1}H-^{17}O CP results.

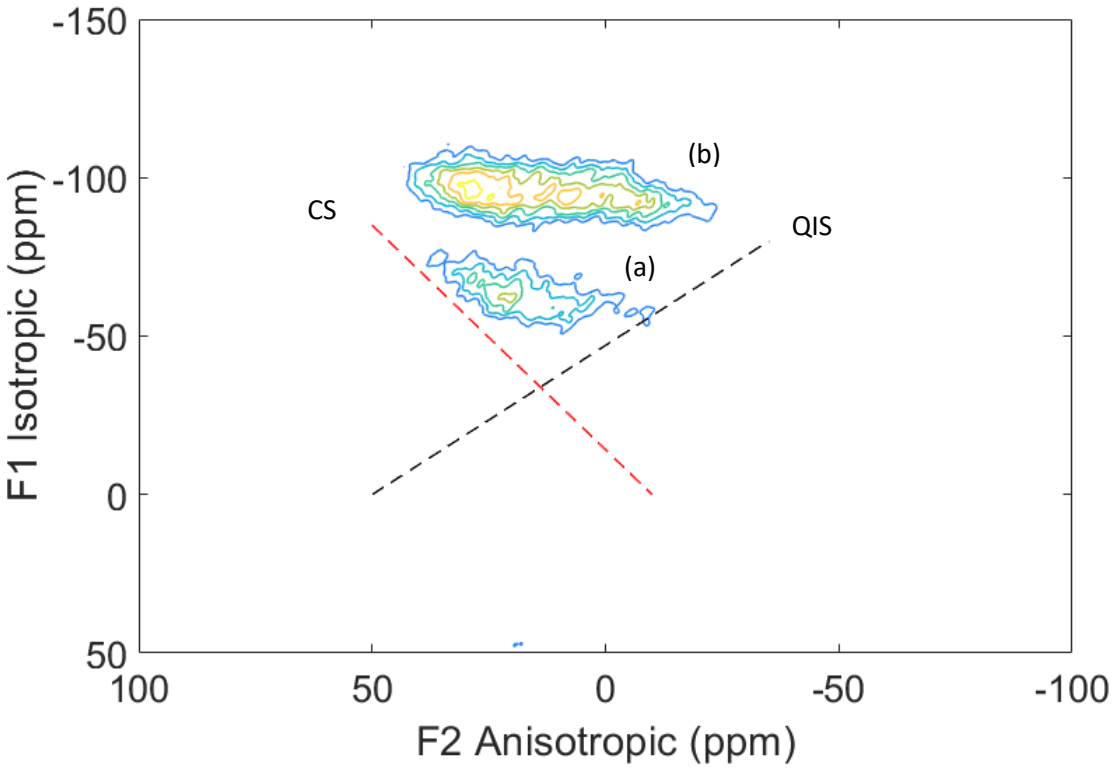

Figure 6-20 3QMAS ^{17}O spectra of MgEM glass leached in ^{17}O-enriched water for 16 weeks (MAS rate = 20 kHz).

Table 6-1 Computed isotropic chemical shift and quadrupole shift for site (a) and (b) as resolved in Figure 6-20 in the 2D ^{17}O 3QMAS spectra.

	δ_{CS}^{iso} (ppm)	P_Q (MHz)

Site (a)	~34	~4.0
Site (b)	~ 50	~ 5.1

In these cases, static spectra could potentially yield more line features that could help identify signals of different origins. Hydroxyl oxygen, because of its proximity to a proton, tends to relax faster both transversely and longitudinally and have low quadrupole coupling constant, if the protons in question have high mobility (Van Eck, Smith and Kohn, 1999). This is attributed to the fluctuation of the interactions with the associated protons, which leads to a dynamic averaging effect. Therefore, the static echo spectra were acquired at various recycle delay and echo delay times in an attempt to exploit the potential differences in relaxation rates between multiple oxygen sites. Figure 6-21 shows the effect of both delays on the intensity and lineshape of the signal. Firstly, compared with the MAS spectra, there are clear line features being 'spread out' due to a wider distribution of resonance frequencies under static condition. However, despite the changes in intensity, the lines seem to adopt a similar shape, suggesting very similar relaxation rates of the signal shown, at least within the time range of the varying delays. If the proton mobility was not high then the lineshape and/or linewidth (hence amplitude) of the strongly ^{1}H-coupled hydroxyl oxygen signal would be expected to change upon ^{1}H-decoupling. Figure 6-22 illustrates the effect of ^{1}H-decoupling on the ^{17}O signal. Since the two spectra are presented on the same scale with the same recycle delay (1.5 s), ^{1}H-decoupling 'pulls up' the signal and sharpens the features due to the narrowing effect despite the total linewidth is not reduced. Because the spectra are still overlapped and not all parts of the signal are affected by ^{1}H-decoupling, it is impossible to quantitatively evaluate the effect and differentiate the hydroxyl oxygen signal.

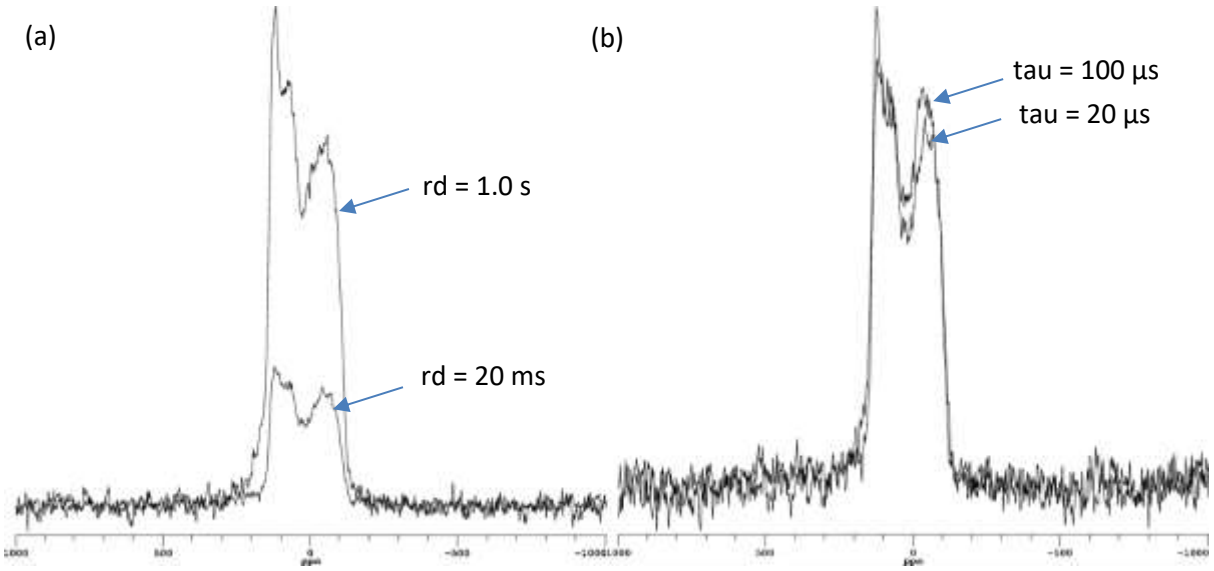

Figure 6-21 ^{17}O static NMR Hahn echo spectra of MgEM glass leached in ^{17}O-enriched water for 112 days: (a) recycle delay of 1.0 s and ~20 ms with an echo delay of 100 µs; (b) echo delay of 100 and 20 µs with a recycle delay of ~20 ms.

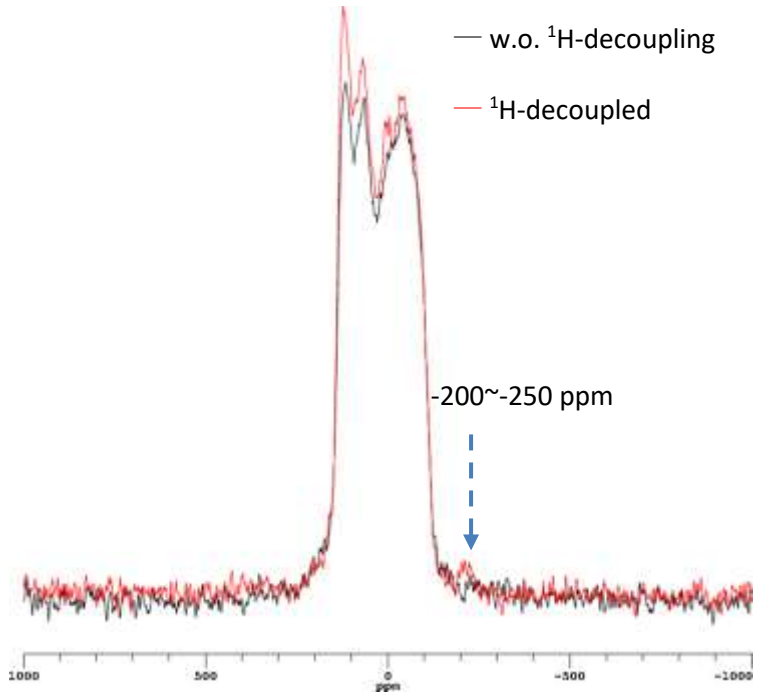

Figure 6-22 ^{17}O static NMR Hahn echo spectra of MgEM glass leached in ^{17}O-enriched water for 112 days, with and without ^{1}H-decoupling during acquisition. The ^{1}H channel decoupling power was ~41.7 kHz.

The relatively fruitless results from direct excitation experiments above led to the application of CP pulse sequence (indirect) in an effort to provide extra resolution to the ^{17}O spectra. Firstly, CP was trialled under static condition and the spectrum is shown in Figure 6-23 alongside the static echo spectrum (Figure 6-21 (a)). Clearly, an extra singularity centred at ~-260.0 ppm is resolved in the CP spectrum whilst the remaining part, more or less, resembles the static echo spectrum with similar shape and width. This is consistent with Figure 6-22 where some part of the signal is shown to be affected by ^{1}H-decoupling hence the corresponding oxygen species can also be ^{1}H cross-polarised. Furthermore, a small line feature also appears at -200~-250 ppm when compared with the spectrum obtained without ^{1}H-decoupling in Figure 6-22. This corresponds to the singularity position and further implies that the extra signal resolved in CP spectrum is from hydroxyl oxygen(s). It is highly unlikely, however, that the singularity alone stands as a Gaussian-like peak, considering its position and the fact that the experiment was static. More likely, it is a line feature of a static second-order quadrupole central transition spectrum with low η_Q values: the static ^{1}H-^{17}O CP spectrum of brucite (Ashbrook and Farnan, 2004), the oxygen site in which has a C_Q of 6.8 MHz and a η_Q of 0.0, and that of the leached glass sample (Figure 6-23) are compared in Figure 6-24. Although EFG and/or δ_{iso} do not exactly match between the hydroxyl oxygen sites in brucite and the CP excited oxygen(s) in the leached glass sample, as judged by the position of the low frequency singularity, the latter does share the line features of characteristic low η_Q central 2nd-order quadrupole static lines.

Having demonstrated that CP could uncover additional signals, the contact time was then varied to investigate its effect on the total lineshape and intensity and the results are shown in Figure 6-25. Apart from the spectrum acquired at 10 μs contact time, which shows no characteristic lines and the lowest signal intensity, the other spectra have similar features but also embedded with systematic changes in the relative intensities of different components as well as the total intensity. The singularity intensity, hence the signal associated with it, increases as the contact time was reduced whilst the primary part of the signal that coincides with the static echo spectrum (see Figure 6-23) shows the reverse trend. This observation alone suggests that the former has closer proximities to protons and the latter's polarisation build-up was interrupted by short contact time due to larger distances (see 2.4.1.3). Moreover, a closer look at the spectra of contact time 0.1 ms and 50 μs (Figure 6-26) highlights that not only the intensity of the apparent singularity increases at shorter contact times but also the part of signal at 90~120 ppm, both of which could be the boundaries of the underlying static quadrupole line. Since hydroxyl oxygen sites usually occupy sites of large EFGs and, hence, large C_Q typically between 6~8 MHz (Van Eck, Smith and Kohn, 1999; Ashbrook and Smith, 2006), Figure 6-23 also indicates that the C_Q, based on the postulated line boundaries, is within the range of hydroxyl oxygen. The evidence shown from Figure 6-23 to Figure 6-26 together hints that the CP signal is from structural hydroxyl oxygen species. The simulations of static quadrupole centre line of hydroxyl oxygen(s), based on the CASTEP calculations of a few hydrous Mg silicates, are compared with these experimental results in Chapter 7.

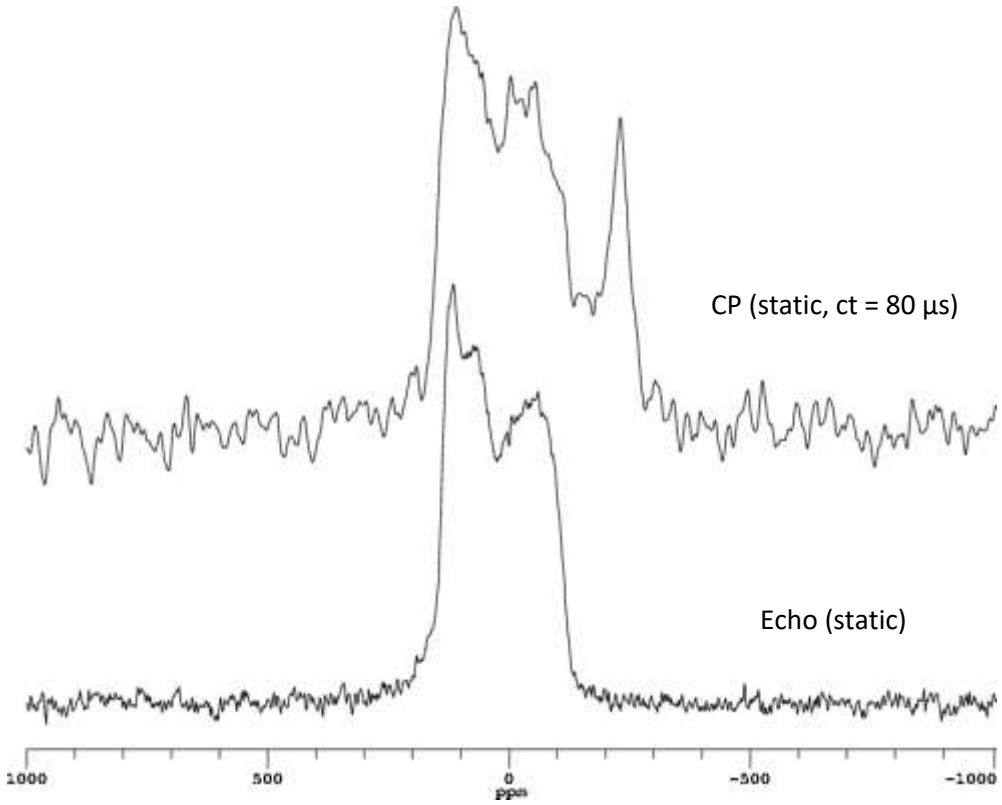

Figure 6-23 Static CP and Hahn echo spectra of MgEM glass leached in ^{17}O-enriched water for 16 weeks. The contact time was 80 µs and ^{1}H-decoupling (~75.0 kHz) was applied during acquisition. Recycle delay in both cases was 1.0 s.

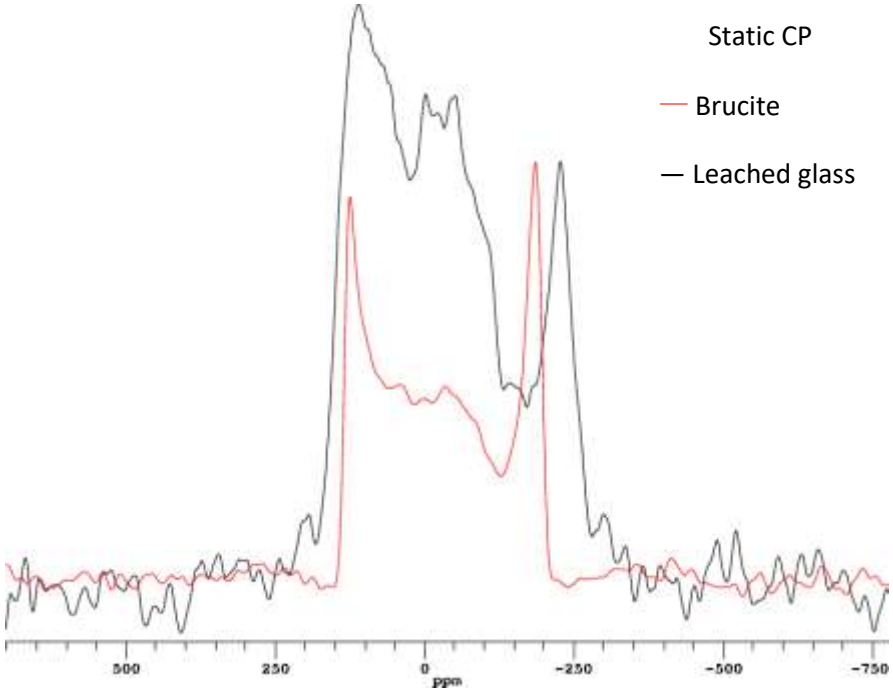

Figure 6-24 Static ^{17}O CP spectra of brucite (ct = 0.5 ms) and MgEM glass leached in ^{17}O-enriched water for 16 weeks (ct = 80 µs).

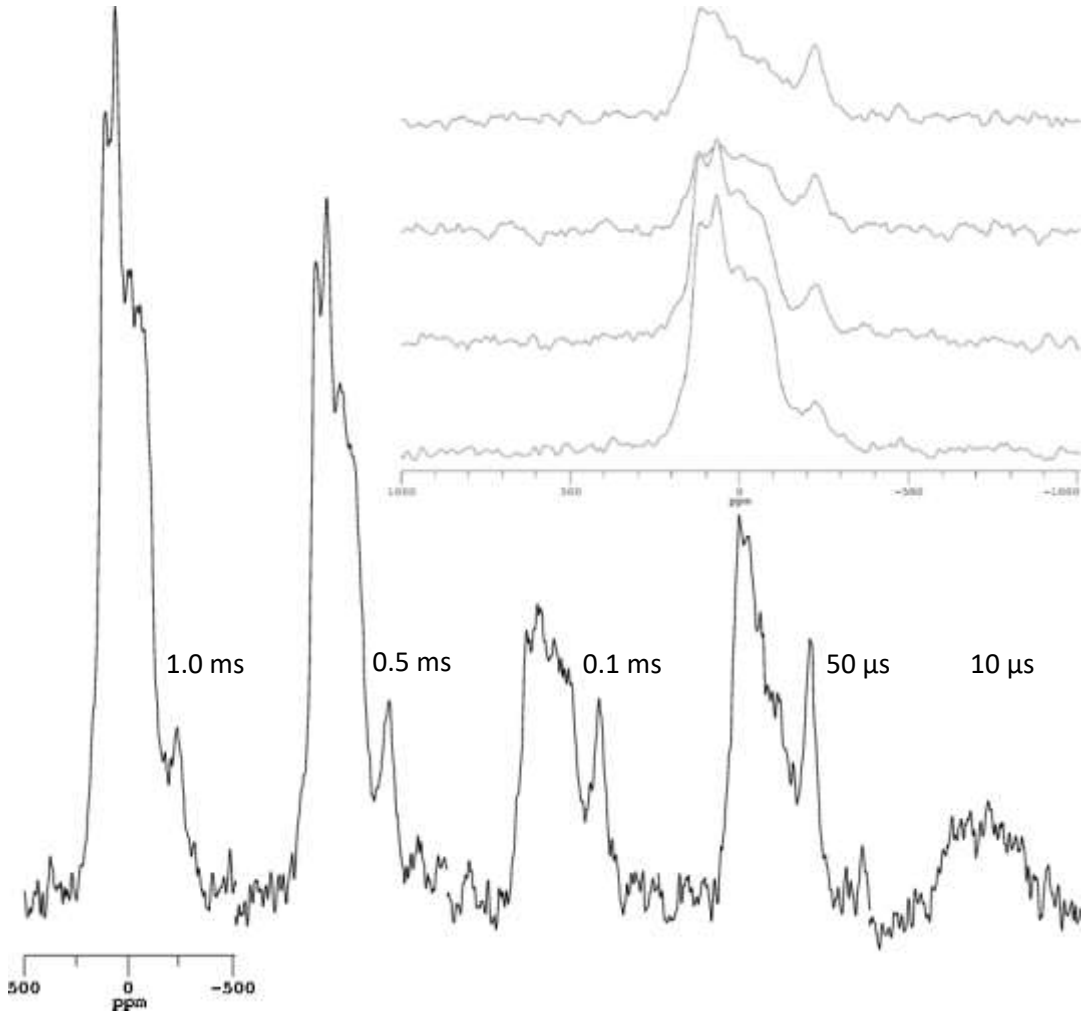

Figure 6-25 Static CP spectra of MgEM glass leached in ^{17}O-enriched water for 16 weeks, as a function of contact time: 1000, 500, 100, 50 and 10 µs from left to right. The other experimental parameters were set to be the same for comparison. The inset displays the first four spectra in a stacked view to show the similar positions and line features.

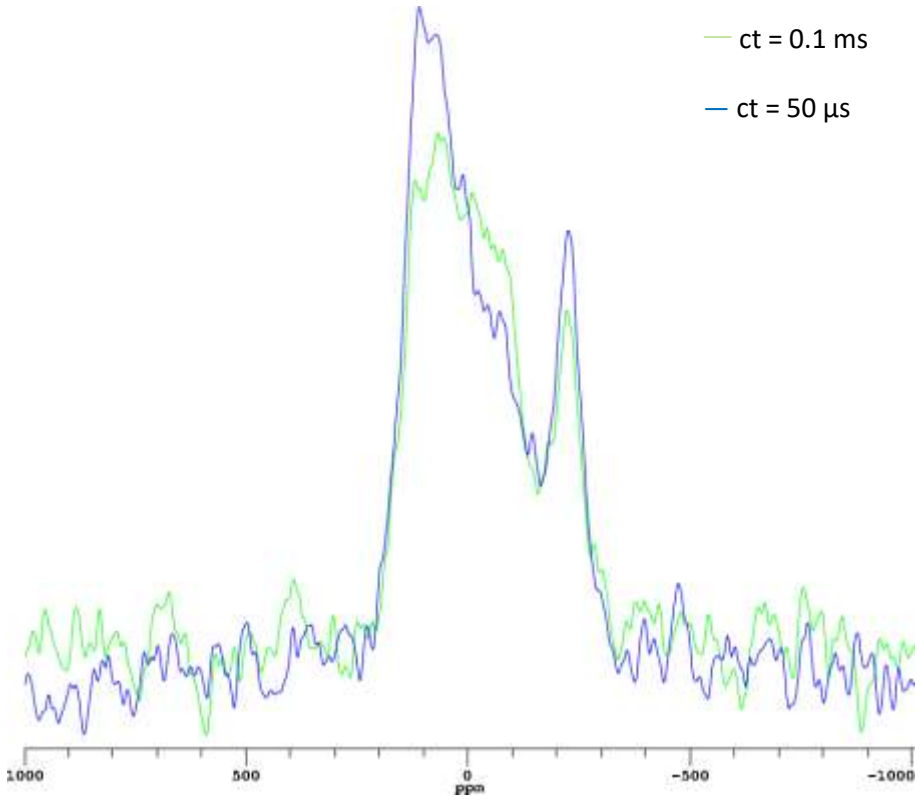

Figure 6-26 Static CP spectra with contact time of 0.1 ms and 50 µs of those shown in Figure 6-25. The spectra are normalised to the number of acquisitions for comparison purposes.

Having established the static CP conditions and identified hydroxyl oxygen(s) in the alteration products, the next step was to try to improve the resolution. CPMAS would benefit from the selective capability of CP while averaging out the CSA, which usually results in an improved resolution from overlapped static lines. However, as outlined in 2.4.1.2, the polarisation transfer efficiency is lowered for higher MAS rates and depends on the magnitude of the quadrupole coupling and the power of the RF irradiation. For characterisation purposes, an experimental, rather than theoretical, optimisation approach was adopted i.e. the MAS rate and pulse power were adjusted by trial and error to find the optimum intensity. Exploration of the effects of contact time lengths on signal intensity and lineshape was also conducted under the optimised conditions. In contrast to the static matching condition, where the standard Hartmann-Hahn matching condition was met, the overall intensities were found (not shown) to be higher at the sideband matching condition at 18 kHz MAS rate, which suggests that the CP process was in the fast spinning regime (see 2.4.1.2). Figure 6-27 (a) shows the spectra obtained at 0.1, 1.0 and 5.0 ms contact time, with the other conditions the same. Clearly, both the intensity and lineshape are significantly changed as a function of the contact time. The relative positions of the different components across the three spectra are illustrated in Figure 6-27 (b). Broadly speaking, the signal can be separated into two parts and both are evident in the medium (ct = 1.0 ms) spectrum. At shorter contact times, more line features are uncovered for the lower frequency part.

Specifically, the centre band seems to be composed of two components, with a narrower peak sitting on top of a broader one. The width of the line reflects the magnitude of EFG at each site. This observation is consistent with the presence of the second-order spinning sidebands of the broader central line. When the contact time is longer, the higher frequency part is accentuated while the previously observed signal disappears. These observations imply that the two types of oxygen sites that give rise to the former signal are located closer to protons than the latter.

To further identify these oxygen species, the CPMAS spectra are compared with the single-pulse spectrum as in Figure 6-19. Figure 6-27 (c) shows that the signal observed in the single-pulse experiment corresponds only to the higher frequency part whilst the lower frequency signals that are only observed at short contact times, i.e. < 1.0 ms, are completely absent when direct excitations are applied. While there might be multiple reasons behind this, it is important to recognise that the CPMAS signal at short contact time, e.g. 0.1 ms, typically correspond to hydroxyl oxygens (Van Eck, Smith and Kohn, 1999) as in the static CP spectra shown in Figure 6-26. At least two hydroxyl species are uncovered by MAS. Hence, the CPMAS spectrum at 5.0 ms contact time (as well as the higher frequency part in the medium spectrum) should be explicitly excluded from being hydroxyl oxygen(s). This is shown in Figure 6-28, where the shift positions and linewidth are compared with that of the ^{17}O in pure silica glass (^{17}O-enriched), in which all oxygen sites are supposedly bridging i.e. Si-O-Si. Despite the small mismatch in the average shift position, their distinction from the hydroxyl oxygens is clearly illustrated. The bridging oxygen NMR shift positions of Si-O-Si have been found to be within the range of 30~100 ppm (Ashbrook and Smith, 2006) from pure silica (e.g. cristobalite: ~40 ppm) to ternary silicates (e.g. $MgSiO_3$: 61~62 ppm) and more complex aluminosilicates (e.g. albite: ~50 ppm) (Timken *et al.*, 1987; Spearing, Farnan and Stebbins, 1992; MacKenzie and Smith, 2002). This trend is consistent with the mismatch observed. Moreover, the higher computed δ_{CS}^{iso} value of peak (b), supposedly bridging oxygen signal, compared with that of silica polymorphs quartz and cristoballite is also manifested in Figure 6-28 given that the oxygen environments are very similar to their amorphous counterparts (Geissberger and Bray, 1983; Jäger *et al.*, 1993).

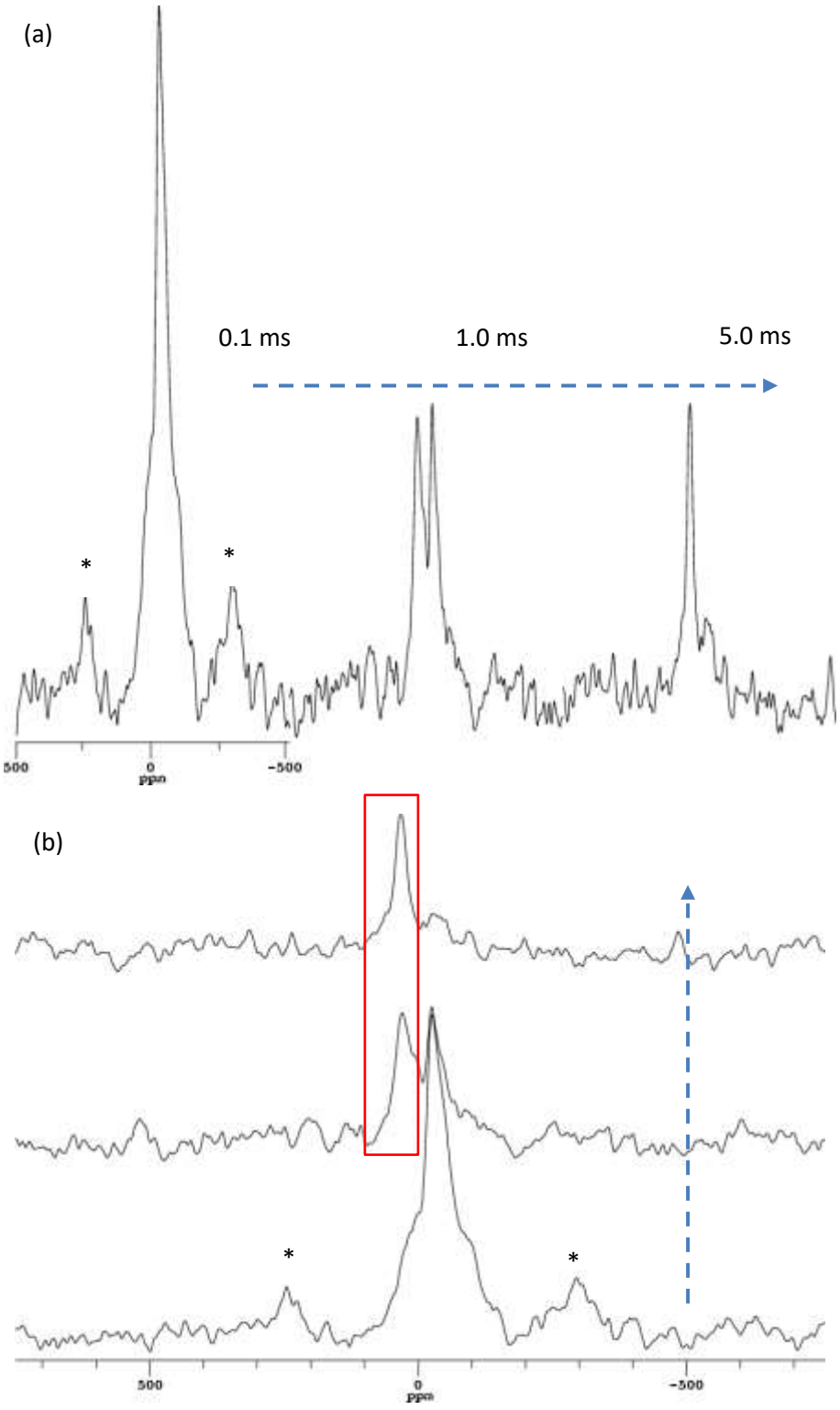
(a)
0.1 ms
1.0 ms
5.0 ms
*
*
500
0
PPm
-500
(b)
*
*
500
0
PPm
-500

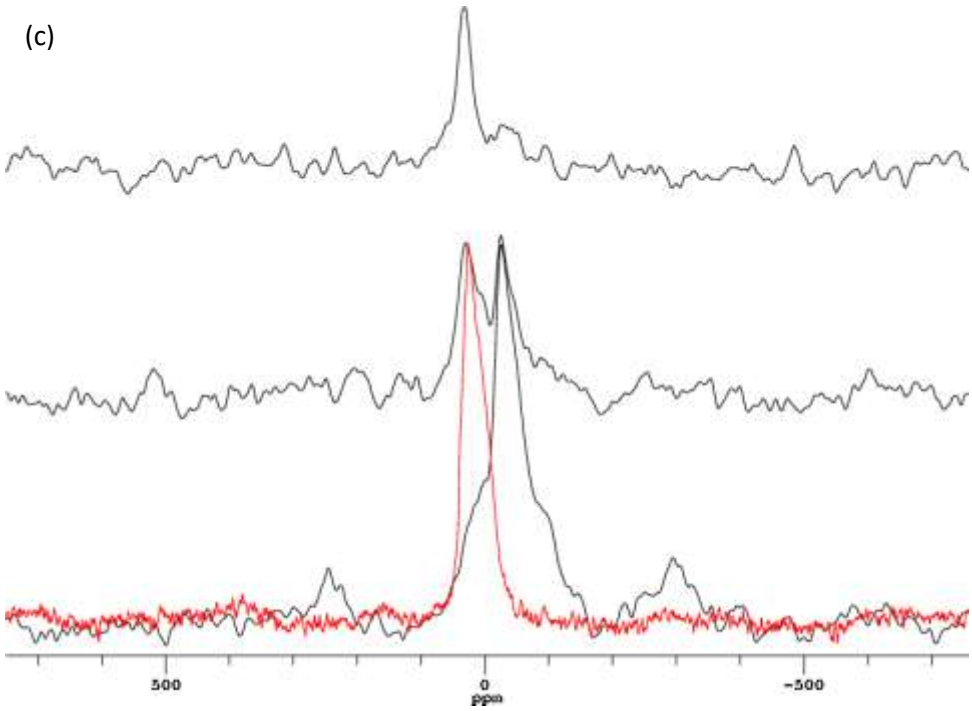

Figure 6-27 CPMAS spectra of MgEM glass leached in ^{17}O-enriched water for 16 weeks with the contact time of 0.1, 1.0 and 5.0 ms (a) in series (left to right), (b) stacked (bottom to top) and (c) with the single-pulse MAS spectrum as in Figure 6-19. The matching was adjusted to be the first spinning sideband condition with the ^{1}H channel power lower by 18 kHz (MAS rate) than the ^{17}O channel. The recycle delay was set to be 0.75 s in all cases.

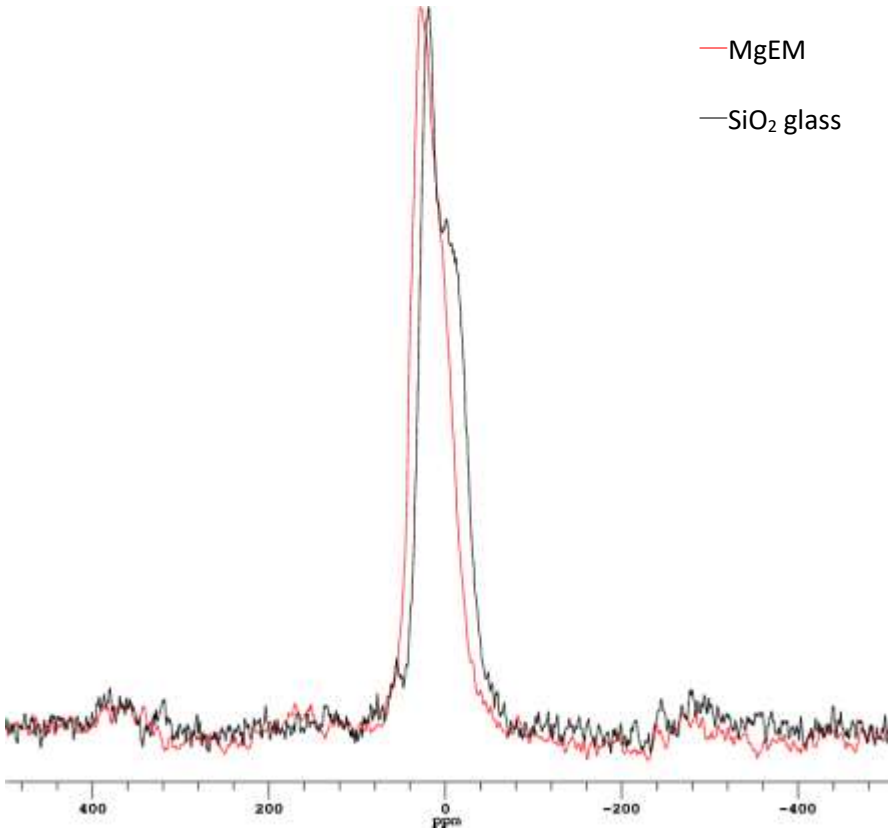

Figure 6-28 ^{17}O MAS NMR spectra of MgEM glass leached in ^{17}O-enriched water for 16 weeks and ^{17}O-enriched SiO_2 glass. They are presented in an arbitrary scale to show the similarities in terms of shift positions and linewidth.

Now, it is worth evaluating the two signals resolved in the 3QMAS spectra. Figure 6-29 shows the projection[§§] of the 2D spectra in the anisotropic F2 dimension. Because the F2 dimension projection should replicate the normal 1D MAS spectrum, it is clear that peak (a) in Figure 6-20 does not correspond to the hydroxyl oxygen(s) observed in the CPMAS experiments, as judged by its position (refer to Figure 6-27 (c)). Instead, even the MAS spectrum, which shows relatively fewer features than the CPMAS spectra, is a superposition of at least two types of ^{17}O signals: peak (a) could be Si-O-Al type bridging oxygens as they usually exhibit both lower δ_{CS}^{iso} and δ_{Q}^{iso} values compared with their Si-O-Si counterparts within the same aluminosilicate framework, as summarised by MacKenzie and Smith (2002).

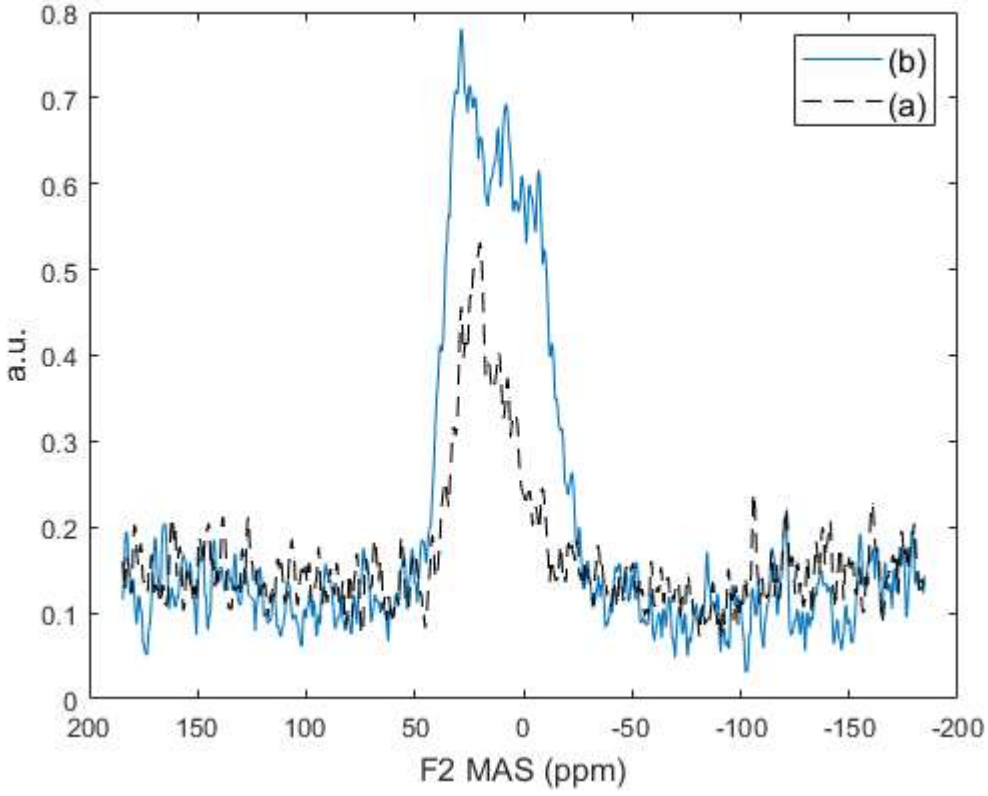

Figure 6-29 The overall anisotropic projection of the 2D 3QMAS 17O spectra shown in Figure 6-20 showing also the overshadowed peak (a) as dashed lines.

6.3. Discussion

6.3.1. Hydrogen species in the alteration layers

Since the glass surface was hydrated and precipitation reactions took place during dissolution, different ^{1}H species could be present in the alteration layers. Depending on the exact mechanism

[§§] The projection is not the superimposed spectrum as in the 1D MAS experiments.

of water reacting with the glass, these might include: 1. restrained molecular water, resulting from diffusion within the glass network or free water in the altered glass pore structure (Gin, Jollivet, Fournier, Angeli, *et al.*, 2015; Gin *et al.*, 2017); 2. hydroxyl groups that are bonded to different network cations owing to hydrolysis rupturing the glass network (e.g. Si-OH) (Eckert *et al.*, 1988; Kohn, Dupree and Smith, 1989); 3. other forms of –OH groups in the precipitates as stoichiometric structural units. ^{1}H species that result from the dissolution of ISG were identified by Collin *et al.* (2018) attributing hydrogens in the form of molecular water, isolated and hydrogen-bonded hydroxyl groups.

In spite of there only being one electron, the δ_{iso} range of oxygen-bonded hydrogen is as large as 20 ppm and the shifts are correlated with the strength of hydrogen bonding (Berglund and Vaughan, 1980). Attempts were made to deconvolute the single-pulse spectra shown in Figure 6-17 (a) of the 16-weeked leached sample. Compared with Hahn echo spectra, single-pulse spectra are inherently more quantitative because of the direct acquisition after excitation (except for necessary instrument delays). The drawback is the inclusion of excessive background signal. In Figure 6-30 (a) and (c), the broad underlying peak and the ~30.0 ppm peak, both of which are from the background, are shown as well. The range to be deconvoluted is indicated by the red bar from 100.0 to -40.0 ppm centred at the broad background. The corresponding expansion from 30.0 to -25.0 ppm is shown in Figure 6-30 (b) and (d). Such a deconvolution scenario is composed of 7 Voigt lines (2 for the background), as judged by the number of line features seen in the spectra. The values of isotropic chemical shift and FWHM for peak (1) 4.3 ppm, (2) 5.0 ppm and (3) 0.5~0.6 ppm extracted from this deconvolution scenario are listed in Table 6-2. Despite both peak (1) and (2) being somewhat broader at 20 kHz, it is obvious that the intensity increment seen in Figure 6-17 (a) at 20 kHz is due to the wider dispersed peak (2) even though its own intensity remains more or less the same at both speeds (by spectral integration, not shown). Both observations suggest that the protons giving rise to this signal are predominantly broadened by multiple ^{1}H-^{1}H homonuclear dipolar couplings, which results in a homogeneous broadened line. Unlike inhomogeneous broadening, spinning speeds comparable to the strengths of the homogeneous coupling are required to yield sidebands and even higher spinning speeds are required to obtain narrow central peaks, although insufficient MAS could reduce the linewidth somewhat. Therefore, the peak (2) signal is possibly arising from a hydrogen cluster such as hydronium ions (H_3O^+) retained in the structure as physically close H_2O and OH species. Usually, stronger ^{1}H-^{1}H dipolar couplings lead to more efficient transverse relaxations and this effect was clearly demonstrated in other ^{1}H NMR studies of hydrous silicate glasses (Angeli *et al.*, 2006; Collin *et al.*, 2018). Figure 6-16 (b) shows that the high frequency shoulder (allegedly

peak (2)) decreases in intensity in the Hahn echo spectrum relative to the 4.3 ppm signal, despite being spun at 60 kHz i.e. short echo delay.

On the other hand, for molecular water structures (i.e. isolated two-spin systems), proton NMR signals have been shown to have significant inhomogeneous features so that the isotropic linewidth is more or less independent of the spinning speed and sidebands appear (depending on the spinning speed) under MAS. The intensity of peak (1) at 4.3 ppm increases upon faster spinning, with small changes in the linewidth. The presence of sidebands is also consistent with MAS splitting up the inhomogeneous broadened signal and focusing more intensity into the isotropic line at higher spinning speed. Molecular water shifts have been found to be spanning quite a wide range in silicate glasses, e.g. from 2.7 to 4.8 ppm in albite glass, depending on the nearest cations to the water molecule. Higher shifts could also result if a higher degree of hydrogen bonding between ^{1}H nuclei and glass network exists (Zeng, Nekvasil and Grey, 1999). Moreover, the shift of water molecules of high mobility in fluid inclusions usually appears at ca. 4.7 ppm as a very sharp line regardless of the spinning speed (Yesinowski, Rossman and Eckert, 1988), which is not observed here. This suggests a relatively open alteration layer structure which allows evaporation of the physically adsorbed water during the drying process. Consequently, the water species observed here (4.3 ppm) is more likely to be structurally bonded within the altered glass, with limited mobility. Indeed, peak (2) could also be a molecular water signal that originates from the region where hydrogen density is high enough to induce some extent of homogeneous broadening. The difference in transverse relaxation behaviour is more clearly observed in Figure 6-17 (c), where the longer echo delays at 20 kHz spinning reduce the peak (1) and (2) intensities noticeably whilst the intensity of the peaks at lower frequencies show limited reduction[***].

Table 6-2 Isotropic chemical shifts and FWHM of peak (1), (2) and (3) in ppm to 1 decimal place extracted from deconvolution as shown in Figure 6-30.

δ_{iso} (fwhm) ppm	(1)	(2)	(3)	(4)	(5)
20 kHz	4.3 (1.5)	5.0 (6.1)	0.6 (1.4)	1.3	0.8
60 kHz	4.3 (1.3)	5.0 (5.1)	0.5 (1.2)	1.3	0.9

[***] The apparent reduction is mainly from underlying peak (3), which shows extensive dipolar coupling as with peak (1) and (2) as discussed later.

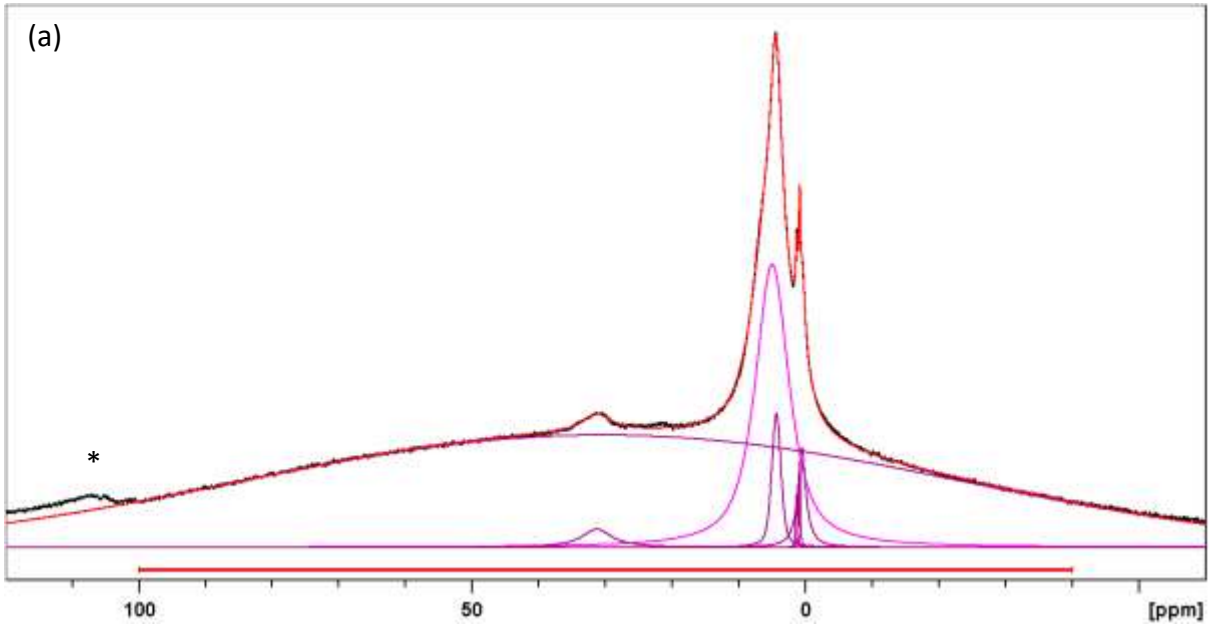
(a)
*
100
50
0
[ppm]

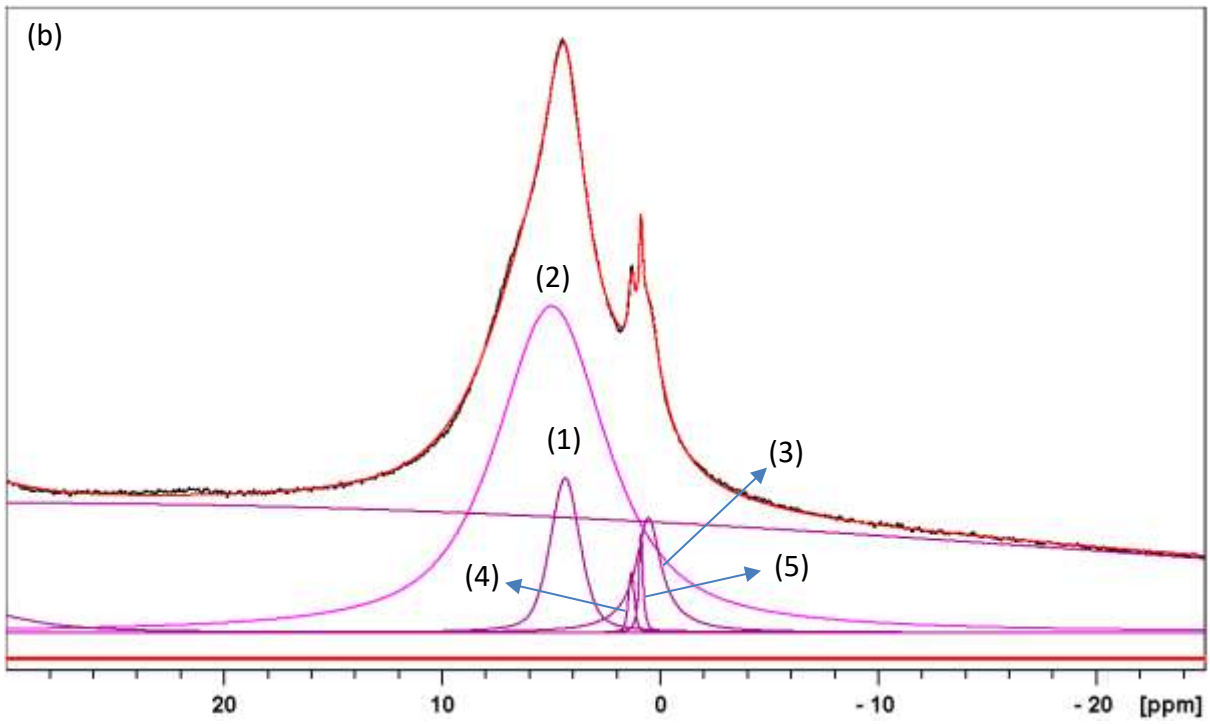
(b)
(2)
(1)
(3)
(4)
(5)
20
10
0
- 10
- 20
[ppm]

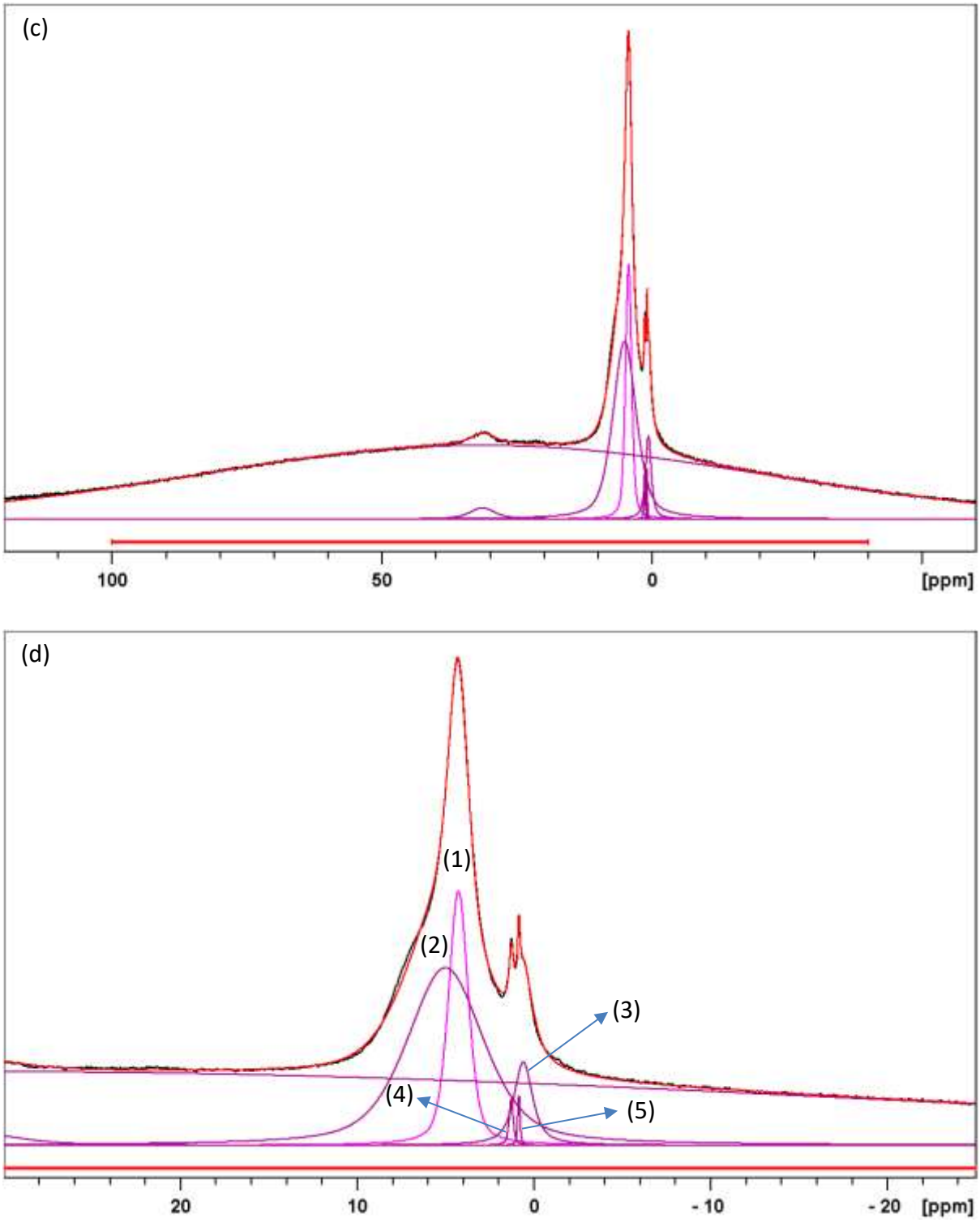

Figure 6-30 Deconvolution of the single-pulse spectra shown in Figure 6-17 (a) and Figure 6-18 (b). (a) and (b): 16-week leached MgEM at 20 kHz MAS; (c) and (d): 16-week leached MgEM at 60 kHz MAS. The simulations were composed of 7 Voigt lines with 2 of which attributed to the background signal.

In some cases, sidebands could provide extra resolution with respect to the centre band because convoluted signals in the centre band could be broadened by different mechanisms and/or

possess different broadening magnitude. Hence, certain parts of the signal could be accentuated/diminished in, especially, higher-order sidebands. At spinning rates of either 20 or 60 kHz, sideband manifold was not observed. However, based on the fact that sidebands are seen at both MAS rates, it should be that the higher-order sidebands in the 20 kHz spectra are diminished in intensity in the background noise rather than being absent. This is also corroborated by the fact that the signal intensity at 60 kHz is much higher than at 20 kHz (Figure 6-31 (a)). Despite interference of the background noise, it is seen in Figure 6-31 (b) that the overall lineshape of the centre band is echoed in the sidebands, especially at 60 kHz where the *S*/*N* ratio is higher. The presence of sidebands at such high spinning speeds is consistent with the magnitude of ^{1}H-^{1}H dipolar couplings in water molecules found in silicate glasses and minerals (Eckert *et al.*, 1988; Yesinowski, Rossman and Eckert, 1988; Zeng, Nekvasil and Grey, 1999). However, the low intensity (relative to the centre band) of the sidebands also suggests a certain degree of proton mobility, which reduces the level of ^{1}H homonuclear coupling as with an isolated water molecule (Brunet *et al.*, 2008). At this point, it is reasonable to postulate that, at 60 kHz MAS rate as compared with 20 kHz, the higher amplitude of the 4.3 ppm peak but lower intensity in a broader area (for single-pulse acquisitions) is attributed to three factors: 1. focus of the sideband intensity into the centre band of the 4.3 ppm peak (1); 2. partial narrowing of the 5.0 ppm peak (2) upon faster spinning; 3. homogeneous broadening dominant in the latter's linewidth.

Even though it is not clear whether the sidebands of the very narrow (FWHM<0.5 ppm) peaks (4) and (5) are likewise present from Figure 6-31, the 0.5~0.6 ppm, peak (3) is clearly extended into the sidebands and narrowed upon faster spinning as well. This suggests a similar degree of dipolar coupling as with the water species. The narrowness of peak (4) at 1.3 ppm and (5) at 0.8~0.9 ppm is more characteristic of hydroxyl species that are not subject to extensive ^{1}H-^{1}H dipolar couplings so that the isotropic lines are well resolved upon MAS spinning. ^{1}H δ_{iso} of the hydroxyl group in a few Mg silicates and Mg hydroxide have been shown to be in the neighbouring range: talc:1.1 ppm, brucite: 0.5 ppm, hydroxyl-chondrodite: 1.1 ppm and natural-occurring hydrous sepiolite 0.4 ppm etc. (Sears, Kaliaperumal and Manogaran, 1988; Yesinowski, Rossman and Eckert, 1988; Aramendía *et al.*, 1997; Phillips *et al.*, 1997). It is worth noting that these typical shift values are all assigned to proton in Mg-OH type stoichiometric hydroxyl groups.

On the other hand, it is shown in Figure 6-18 (a) that an additional peak at 14.0-15.0 ppm and a more pronounced higher frequency shoulder are evident in the 4-week Hahn echo spectrum but missing from its 16-week counterpart. In the meantime, the low frequency signals peak (3),

(4) and (5) are stronger and more characteristic for the longer leached sample. To obtain the exact isotropic shift values of the singularities, the ^{1}H spectrum (4-week) shown in Figure 6-18 (a) was simulated using 6 Voigt lines following the previous procedure. Since the aim was to find the position of the extra peaks, the simulation was carried out for the Hahn echo spectrum instead of the single-pulse one while fitting for the low frequency peaks was not refined. The shift values of interest are labelled in Figure 6-32. The shoulder to the 4.3 ppm, the existence of which is consistent with previous simulations, seems to have a higher isotropic shift at 6.6 ppm as object to 5.0 ppm and the high frequency extra peak has a shift value of 14.8 ppm. Both values suggest a high(er) hydrogen-bonding strength of these two types of hydrogen. The fact that the 14.8 ppm peak only appears at 60 kHz MAS rate indicates that the corresponding protons are also subject to a significant degree of homogeneous broadening.

It is worth noting that the deconvolution scenarios, upon which the discussions are based, are judged visually by the number of features seen in the spectra. The lack of structural and compositional constraints of the altered glass means that they are not necessarily correct. Therefore, there could well be more unresolved signals from the samples as well as background, so that these deconvoluted lines are not unique in a theoretical sense.

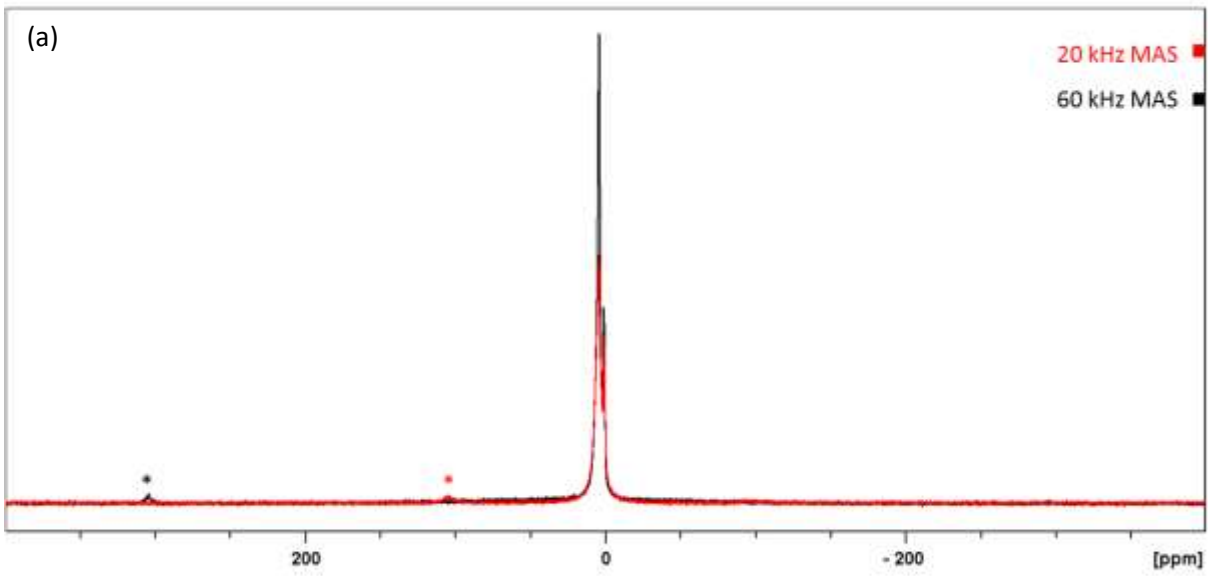

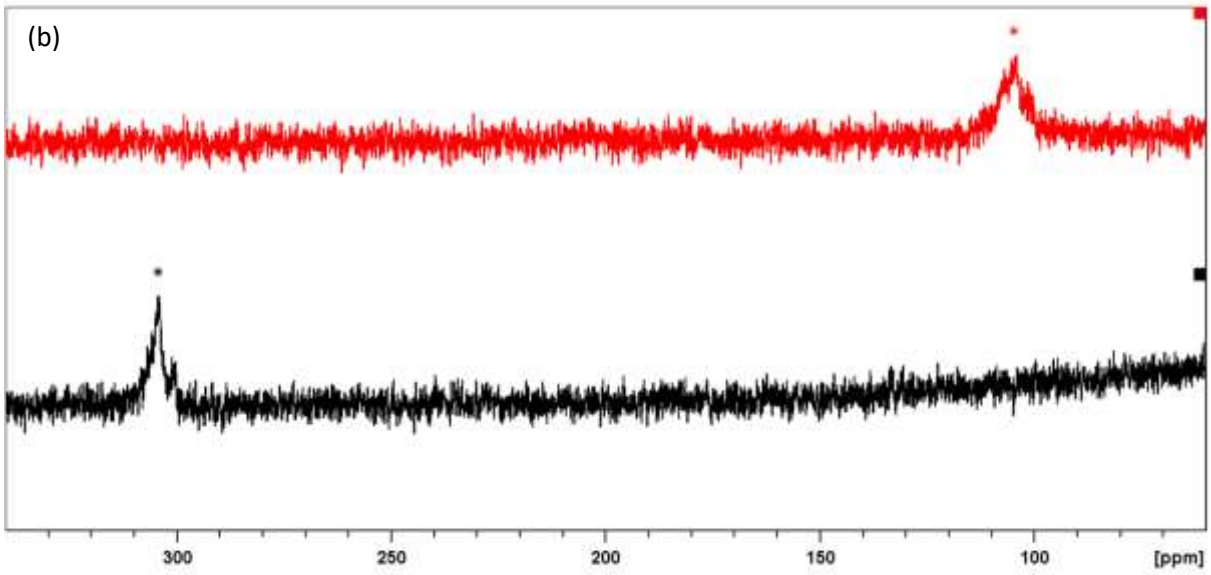

Figure 6-31 (a) ^{1}H MAS NMR Hahn echo spectra of spinning speed at 20 and 60 kHz; (b) Expansion of (a) at the noted spinning sidebands.

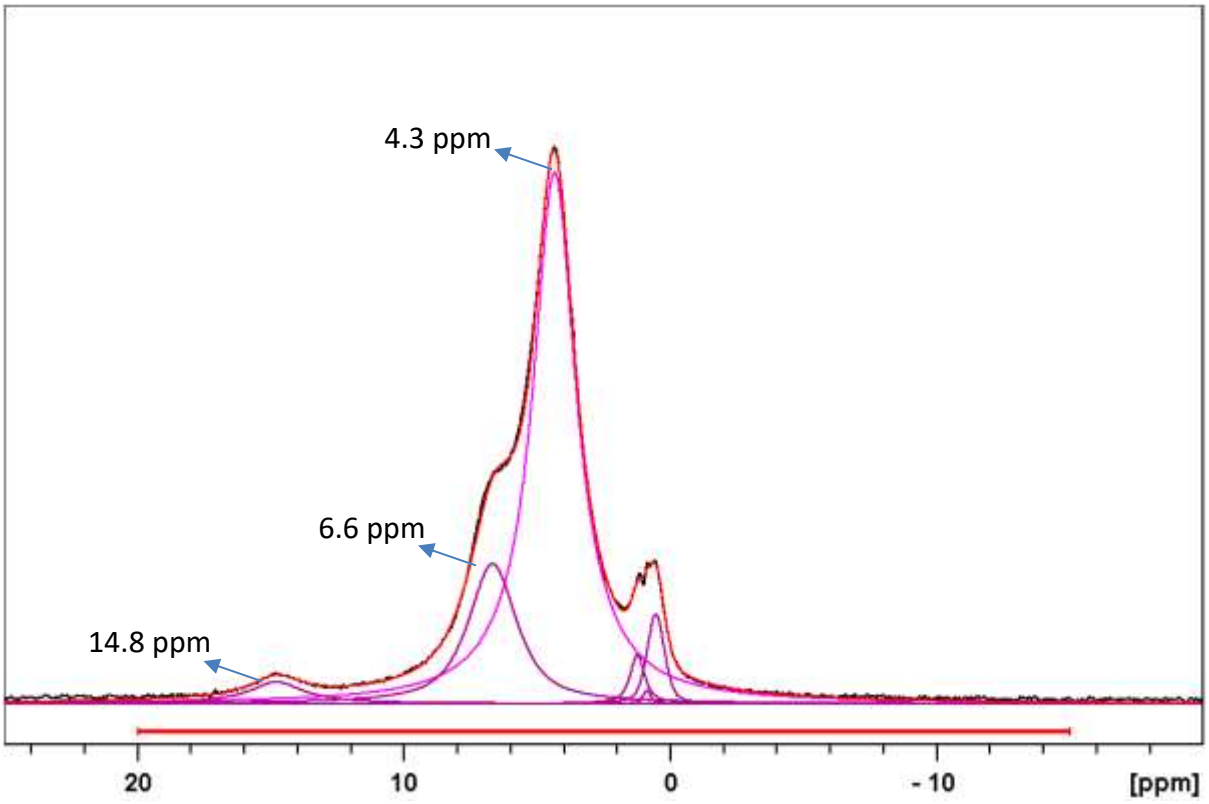

Figure 6-32 Deconvolution of the ^{1}H NMR MAS spectrum at 60 kHz of 4-week leached MgEM glass as shown in Figure 6-18 (a) using 6 Voigt lines.

6.3.2. Structural features of the alteration layers

A larger amount of secondary precipitates and more morphological features seen on the 16-week leached MgEM glass surface are relative to its 4-week counterpart (Figure 6-2 and Figure 6-3). These differences are also reflected in the ^{1}H NMR results. Specifically, the more intense and characteristic hydroxyl proton peaks in the 16-week spectrum imply a higher degree of precipitation reactions for this longer dissolution duration. More insights can be gained by comparing the overall proton signal intensity. Despite the potential inaccuracy introduced by the echo delays, it is more sensible to compare the intensity without background signals. Integration results for the normalised spectra in Figure 6-18 (a) are shown in Figure 6-33, with the intensity scale of the 16-week leached sample set as 1.0. Surprisingly, there is a similar number of protons in both leached glasses even though one was leached for 4 times longer in time than the other[†††].

It was found that the hydrogen-bonded hydroxyl groups from leaching of ISG adopt a ^{1}H shift of 6.7 ppm (refer to Figure 6-32) after heating the leached sample at 90℃ and the strong hydrogen-bonding was attributed to close proximity to trapped water molecules in the glass

[†††] Integration of the respective single-pulse spectrum over the same spectral width yielded a similar result of 1:1.0139.

network (Collin *et al.*, 2018). In addition, in-situ condensation of the ruptured glass network and the concurrent resorption of the dissociated orthosilicic acid in Si-rich solutions following hydrolysis of the glass network have long been thought to be the key processes in forming a protective gel layer, which retards further dissolution. The related reactions and mechanisms can be referred to 1.3.1. Therefore, one of the scenarios that could account for the similar normalised ^{1}H NMR intensity between 4-week and 16-week leached samples is that the re-construction and densification of the hydrolysed glass, according to Equation 1-2, up to 4 weeks were still insignificant probably owing to non-saturation of Si locally. Such processes, despite taking place between 4 and 16 weeks, were restricted and the non-binding water molecules produced were lost during sample drying. This could be further explained as the precipitates interrupting the formation and/or protectiveness of the gel layer. Meanwhile, because of the extensive precipitation that took place at the same time, the overall proton content in the altered products did not vary noticeably. It is clear from Figure 6-18 (a) that the extra proton intensity of the 16-week spectrum is exclusively from stoichiometric hydroxyl groups in the precipitates, as discussed before.

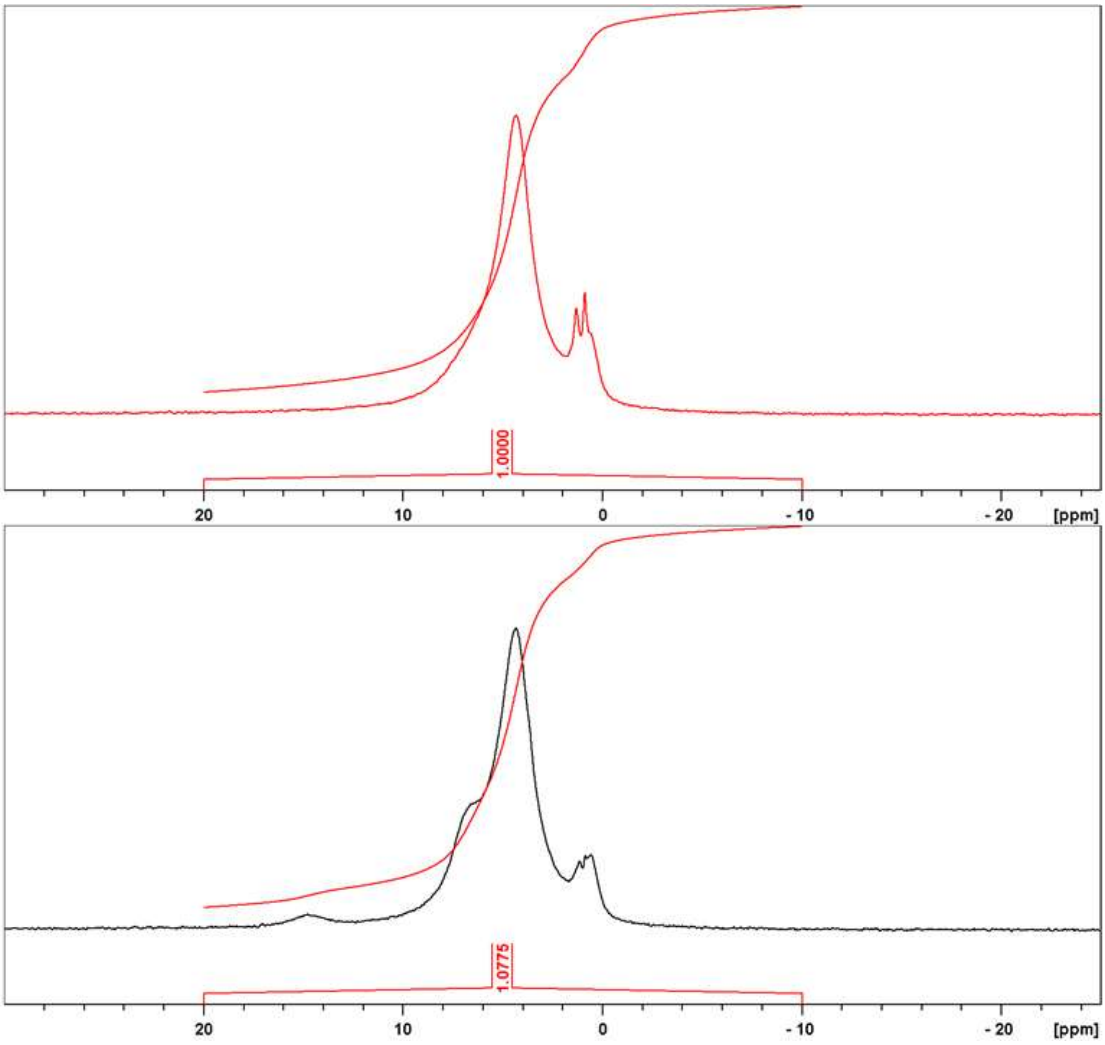

Figure 6-33 The relative proton signal intensity of 4-week (black) and 16-week (red) leached MgEM glass of Hahn echo spectra as shown in Figure 6-18 (a).

For the 16-week leached MgEM glass, the altered glass structure and precipitates are also identified as well as distinguished by the ^{17}O NMR results. 2D 3QMAS spectra resolve two types of bridging oxygens, presumably Si-O-Si and Si-O-Al, which are entirely overlapped in the 1D MAS spectrum. The re-construction process (Equation 1-2) would lead to ^{17}O atoms from the enriched water replacing some of the nearly 100% bridging ^{16}O in the glass network. Without this process, which is in principle a traditional methodology for preparing ^{17}O enriched oxide samples by creating a hydrolysed medium agent (MacKenzie and Smith, 2002), it is inconceivable that bridging oxygens signal could be detected at natural abundance level. On the other hand, the ^{1}H-^{17}O CP(MAS) spectra, as with the ^{1}H MAS spectra (see 6.3.2), of the 16-week leached MgEM glass show the existence of stoichiometric hydroxyl groups, most likely in the precipitate(s) structures because of their characteristic lineshape and singularities as well as their low mobility. In addition, although CP is a transfer process via space requiring no chemical bonding, the comparison made in Figure 6-26, which demonstrates the linewidth scale

of the CP signal, and the calculated as well as documented C_Q values (see Chapter 7) further corroborate the claim made above. ^{29}Si NMR results show a similar connectivity degree i.e. Q^3 in the altered glass relative to the pristine glass, and this observation is in disagreement with polymerisation of the altered glass structure, which was demonstrated by ^{29}Si NMR on ISG. This suggests that unlike Mg-free glasses, the precipitation reactions that involve Mg have an impact on the in-situ condensation processes of the hydrolysed glass network and re-construction of the dissolved orthosilicic acid at the surface region. This is consistent with the proton intensity data where the loss of protons (i.e. water) is related to the inferior protectiveness of the gel layer. An equally valid argument can be put forward that the average Q^3 is attributed to the Si environments in the precipitates, e.g. talc as shown in Figure 6-14. Indeed, the potential precipitated Mg silicate phases are largely phyllosilicates with each Si connected to three bridging oxygens in their SiO_4 tetrahedral sheets (see Chapter 7). In reality, it is most likely that both factors contribute to the observed Si coordination environments given the combination of proton NMR results and surface features.

Despite the low *S*/*N* ratio and resolution of the ^{25}Mg NMR spectra, the existence of Mg site(s) that differ from the pristine glass have been detected in the alteration layers even in the 1D MAS spectra, as shown in Figure 6-7. Both static ^{1}H-^{25}Mg CP and single-pulse ^{25}Mg MAS NMR results of the other two Mg silicates suggest talc as the better candidate in comparison to the Mg-smectite. Although this is also in agreement with what the ^{29}Si NMR results suggest, further validation and exploration are needed utilising Ab initio calculations and spectrum simulations. For example, the appearance of two hydroxyl ^{1}H peaks in Figure 6-18 (a) and others means that there are two distinct –OH sites, either in different structures or two sites within the same structure.

6.4. Summary

This chapter described and detailed the multinuclear NMR characterisation of the leached MgEM glass, mainly for the two leaching durations of 4 and 16 weeks, in an effort to elucidate the atomic level structures of the altered glass and precipitates, i.e. alteration layers. The morphological changes on the glass surface from 4-week to 16-week leaching clearly indicated extensive precipitation taking place between these two periods, although there were already signs of precipitates formed before 4 weeks time. Firstly, ^{1}H and ^{17}O NMR results implied that there are multiple oxygen and proton sites within the alteration layers and distributed between the altered glass and precipitates. The altered, i.e. hydrolysed, condensed and re-constructed, glass was manifested by both the similar proton NMR intensity between the 4-week and 16-

week leached sample and the two types of bridging oxygens resolved in 2D 3QMAS ^{17}O spectrum. Moreover, the characteristic Mg-OH hydroxyl proton signal and the static ^{1}H-^{17}O CP spectra linewidth (hence C_Q) corroborated the precipitates being present on the glass surface. Rather than being two non-interfering phases, the formation of precipitates seemed to interrupt the formation of the altered glass (gel) layer, hence reducing its supposedly protective efficacy. ^{29}Si and ^{25}Mg NMR results from the 16-week sample experimentally showed a greater similarity between the precipitate(s) and talc than the Mg-smectite (the secondary Mg silicates precipitate from dissolution of AVM10 glass). However, this needs further validation and comparison among more NMR datasets of other Mg silicate minerals.

Chapter 7

7. DFT (CASTEP) and GIPAW NMR calculations of Mg silicates

Glossary

Brucite	Magnesium hydroxide; chemical formula: $Mg(OH)_2$
Sepiolite	Magnesium silicate; clay; chemical formula: $Mg_4Si_6O_{15}(OH)_2{\cdot}6H_2O$
Saponite	Aluminium silicate; smectite (clay); chemical formula: $Ca_{0.25}(Mg, Fe)_3(Si, Al)_4O_{10}(OH)_2{\cdot}nH_2O$
Montmorillonite	Aluminium silicate; smectite (clay); chemical formula: $(Na, Ca)_{0.33}(Mg, Al)_2Si_4O_{10}{\cdot}nH_2O$
Talc	Magnesium silicate; clay; chemical formula: $Mg_3Si_4O_{10}(OH)_2$
Clinochlore	Aluminium silicate; chlorite (clay); chemical formula: $(Mg, Fe)_3(Si, Al)_4O_{10}(OH)_8$

7.1. Introduction

The precipitates formed during MgEM glass dissolution could hold the key to explaining the drastically different dissolution kinetics compared with Mg-free glasses. As a first step, it is crucial to identify these secondary phases, which could, in turn, uncover the chemistry of such precipitating reactions and provide a thermodynamic basis for modelling the dissolution processes. Moreover, identifying the structural features of the precipitates could potentially help explain their disruption of the passivation process that prevails in their absence.

As shown in 6.1.2, XRD yielded null result for characterising the structures of alteration products on the glass surface. Apart from the potential reason of poor crystallinity, it may also be due to the small amount of materials being present: the equivalent alteration thickness is ~3 μm for the MgEM glass after 16 weeks. On the other hand, despite being a powerful tool, the results (spectra) of solid-state NMR are not trivial to interpret especially for samples with uncertain compositions and static disorder at the same time. In this case, the exact chemistry of the precipitation reactions is unknown. Therefore, it is often useful to acquire NMR spectra on the relevant standard materials of which both the compositions and microstructures are known.

As outlined in Chapter 1 and 6, the alteration products/precipitates resulting from silicate glass dissolution usually found their mineralogical origins in various clay minerals, especially the smectite group minerals, such as Na-montmorillonite, Mg-rich saponite and hectorite (Curti *et al.*, 2006; Thien *et al.*, 2010). It is not usually practical to conduct ^{17}O and ^{25}Mg NMR experiments on these materials, because of the necessity for enrichment in most cases. In addition, the compositional disorder within these naturally occurring minerals makes it difficult to identify the exact members of the mineral groups that correspond to the composition of the glass in question. Therefore, theoretical calculations emerge as an alternative to experiments.

7.2. Selection and refinement of Mg silicate structures

7.2.1. Selection of Mg silicates for NMR calculation

The Mg silicate phases to conduct CASTEP NMR calculations on were determined by thermodynamic calculation of the leaching data obtained in the previous study (Brigden and Farnan, 2014; Guo, 2015). The methodology was to create a solution (pH fixed at 9.0) as if the dissolution was congruent, based on the boron concentrations. Then, amorphous silica and another hydrous Mg-containing phase were imposed as the equilibrium phases with the solution and the solution was allowed to reach a global thermodynamic equilibrium, to identify the corresponding resultant solution that has the closest chemistry to the experimentally analysed results across the leaching period. Finally, each mineral phase with a calculated positive saturation index was considered to be having the potential to precipitate out in such a hypothetical and simplified scenario. Despite being simplified, the whole process was rationalised by the IDP mechanism of glass dissolution and the fact the altered glass layer is mainly a silica gel (see Chapter 1). Together with brucite, which was selected as the imposed equilibrium Mg-containing phase, positively saturation indexed hydrous Mg silicates with high quality structural data available in the ICSD and AMCSD are listed in Table 7-1, for CASTEP NMR calculations. There are several prominent candidate structures missing for calculations, including sepiolite, Mg-saponite and -montmorillonite owing to the lack of information on the proton positions, which are crucial for determining the NMR parameters of the corresponding hydroxyl oxygen(s). In addition, NMR parameters of the hydroxyl oxygen(s) in a hydroxyl clinohumite sample (calculated) (Griffin *et al.*, 2009), which was identified as the secondary precipitate phase during the leached layer formation of forsterite (Mg_2SiO_4) (Davis *et al.*, 2009); and a talc sample (experimentally determined) (Walter, Turner and Oldfield, 1988) with a

different structure to the one being calculated, were also used to simulate the corresponding ^{17}O spectra.

Table 7-1 Mg silicates (structures) from the literatures that are used for CASTEP NMR calculations.

	Composition	a, b, c (Å)/α, β, γ (°)	Source
Brucite	$Mg(OH)_2$	3.14979(4), 3.14979(4), 4.7702(1)/90, 90, 120	(Catti *et al.*, 1995)
Talc	$Mg_3Si_4O_{10}(OH)_2$	5.293(2), 9.179(3), 9.469(3)/90.57(3), 98.91(3), 90.03(3)	(Rayner and Brown, 1973)
Clinochlore (monoclinic)	$(Mg_{11.148}Fe_{0.852})(Si_{4.99}Al_{3.01})O_{20}(OH)_{16}$	5.3363(9), 9.240(1), 14.37(3)/90, 96.93(5), 90	(Zanazzi *et al.*, 2007)
Clinochlore (triclinic)	$(Mg_{11.06}Fe_{0.94})(Si_{5.22}Al_{2.78})O_{20}(OH)_{16}$	5.327(4), 9.233(6), 14.381(6)/90.2(2), 97.2(2), 89.97(6)	(Zanazzi *et al.*, 2006)

However, it should be borne in mind that the thermodynamic calculations can only be as good as the database itself and the assumption of congruent dissolution in the first place is not necessarily true. Nevertheless, this approach, combined with experimental and theoretical NMR, provides a starting point for identifying the precipitates at early stages of glass dissolution. In the literature where XRD experiments were used to uncover some structural features of the alteration products, the Mg-containing glass samples were, with no exception, all leached in aqueous agents for at least 7 years and up to 20 years with the same or higher *SA*/*V* ratio to the leaching experiments described in this thesis (Curti *et al.*, 2006; Thien *et al.*, 2010). Extensive secondary phases formed during rate drop as well as residual rate stage must have largely accumulated, crystallised and grown, which could possibly lead to a resumption of the dissolution by significantly changing the solution chemistry and consuming the elements that form the underlying alteration layers. The amount and crystallinity of these precipitated secondary phases provided the basis for XRD to help with their structural identification.

As can be seen from Table 7-1, both types of the chlorite possess compositional disorder, with multiple ions occupying structurally identical sites. The best approach to simulate

compositional disorder is to construct a supercell and artificially distribute the ion population to simulate the exact ionic ratios. Usually, different spatial configurations are needed as well. It has been proven to yield excellent matches between supercell calculations and experiments based on this approach in the literature (Ashbrook *et al.*, 2015; Ashbrook and McKay, 2016). However, the approach is very computationally expensive because of the size of the supercells usually needed to re-construct the disorder and the concurrent reduced crystallographic symmetry. Due to the extent of disorder considered here and the limited available computational power, the Mg and/or Si endmember structures were adopted in the calculations. The composition(s) of the endmember clinochlore (see Table 7-1) is accordingly: $Mg_{12}Si_8O_{20}(OH)_{16}$.

7.2.2. Geometry optimisation

As outlined in 2.5.2, it is essential to use high enough cut-off energy and k-point density to ensure that the electronic wavefunctions are accurately 'enough' represented by the basis set for the pseudopotentials used in a calculation. Although computationally more expensive, the cut-off energies in all the k-point tests were set to be the highest possible for the given pseudopotentials by specifying the level of BASIS_PRECISION as EXTREME for all the structures considered here. There has been a variety of exchange-correlation functional (see 2.5.2) being supported in CASTEP. The generalised gradient approximation (GGA) family provides a good balance between accuracy and computational cost by including the gradient of the electron density, $\nabla\rho(r)$, in the exchange-correlation functional compared with the simplest localised density approximation (LDA) and usually serves as an improvement to the latter. PBE (Perdew, Burke and Ernzerhof, 1996), among other GGAs, has been the most widely used exchange-correlation functional and was adopted here as well without further exploration.

The total energy and stress of each structure were then monitored in 'single point' (the least computational cost) calculations (Studio, 2014), with increasing number of k-point in the first Brillouin zone until the trend of both identifiers 'flatten out'. Figure 7-1 shows an example of the convergence tests with the corresponding MP grid labels. In this example, the geometry optimisation and NMR calculations were performed with a kpoints_mp_grid size of '4 4 3' with 24 k-points being sampled in total in the first Brillouin zone. The convergence test results for the other structures are listed in Appendix III.

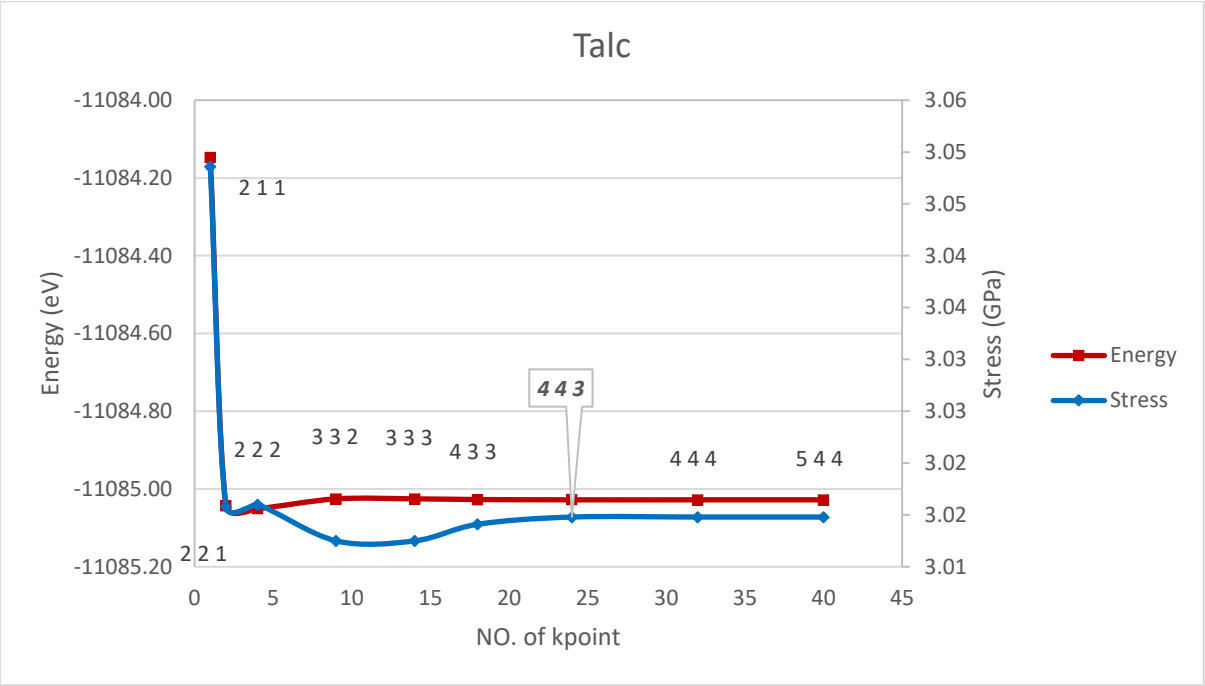

Figure 7-1 Calculated total energy and stress of talc structure as a function of the number of kpoint (mp_grid) sampled in the first Brillouin zone served as convergence tests for geometry optimisation and NMR calculations.

The as-obtained structures were then subject to geometry optimisation (GO) using the BFGS minimisation algorithm in CASTEP modules to find the structure that corresponds to the local energy minimum, i.e. ground state (Pfrommer *et al.*, 1997). It starts by minimising the electronic energy for a fixed ionic state and evaluating the forces on ions and total stress. Subsequently, the scheme uses a starting Hessian matrix and updates it recursively until the maximum force and stress are below the specified values and the internal convergence criteria are met in a specified number of iterations. In all the optimisation calculations presented herein, default criteria were applied without further refinement. The example of talc's structure* before and after the GO procedure is shown as follows:

* The structures presented herein are specifically referred to primitive unit cells, which are not necessarily the unit cell as obtained from the literature and listed in Table 7-1. The primitive unit cells are always used for computational codes because they are the most efficient, with fewer atoms and electrons, and are equivalent to the corresponding non-primitive ones for representing the crystallographic structures.

Before GO

α = 94.934°

B = 93.941°

Γ = 120.061°

a = 5.299Å

b = 5.297Å

c = 9.469Å

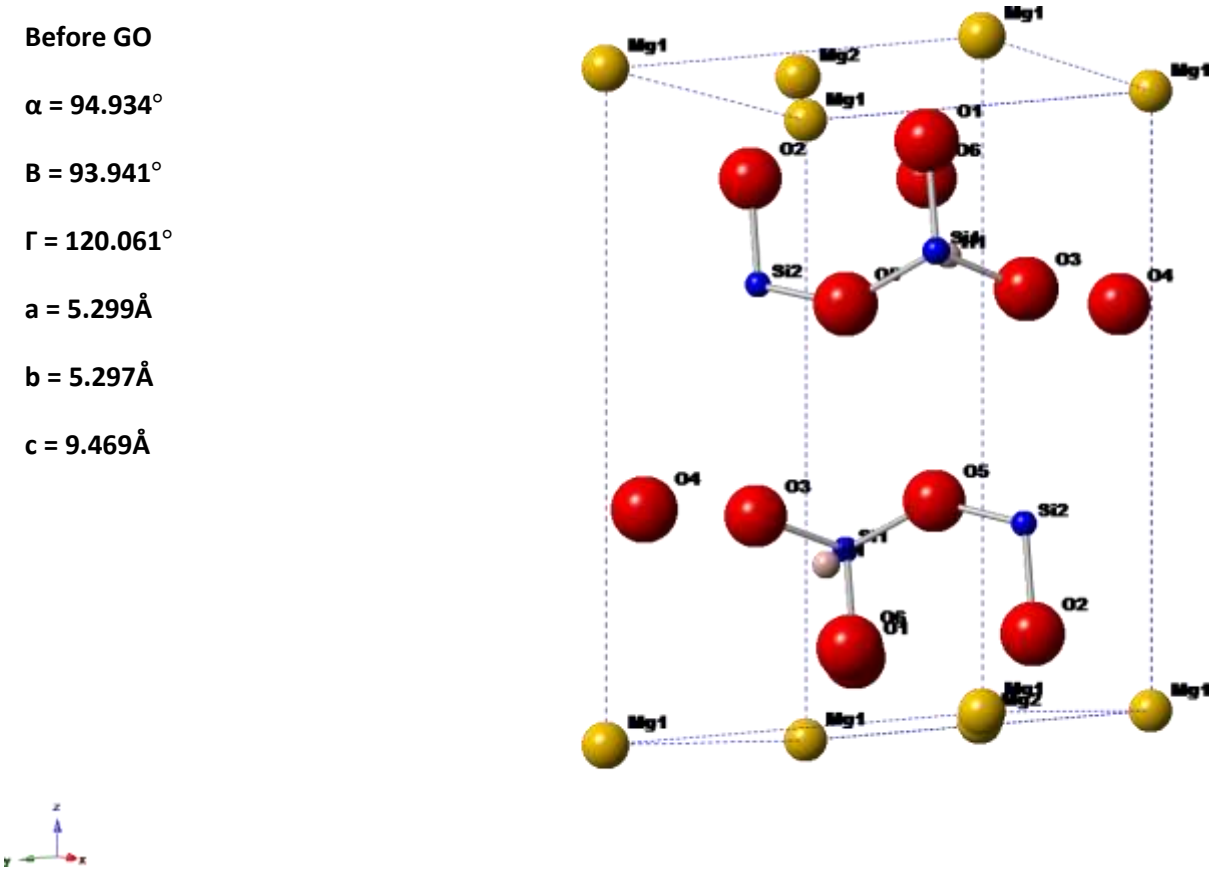

Figure 7-2 The primitive unit cell structure of talc before GO.

Table 7-2 The fractional coordinates of every atom/ion shown in the primitive cell in Figure 7-2.

Fractional coordinates (Before GO)				
Element	Label	x	y	z
H	H1	0.970000	0.570000	0.760000
H	H1	0.030000	0.430000	0.240000
Mg	Mg1	0.000000	0.000000	0.000000
Mg	Mg1	1.000000	0.000000	0.000000
Mg	Mg1	0.000000	1.000000	0.000000
Mg	Mg1	1.000000	1.000000	0.000000
Mg	Mg1	0.000000	0.000000	1.000000
Mg	Mg1	1.000000	0.000000	1.000000
Mg	Mg1	0.000000	1.000000	1.000000
Mg	Mg1	1.000000	1.000000	1.000000
Mg	Mg2	0.667100	0.333100	0.000100
Mg	Mg2	0.332900	0.666900	0.999900
O	O1	0.299300	0.296300	0.881700
O	O1	0.700700	0.703700	0.118300
O	O2	0.633300	0.960700	0.879600
O	O2	0.366700	0.039300	0.120400
O	O3	0.574600	0.913200	0.347200
O	O3	0.425400	0.086800	0.652800
O	O4	0.906700	0.050100	0.652500
O	O4	0.093300	0.949900	0.347500
O	O5	0.392000	0.567600	0.651300

O	O5	0.608000	0.432400	0.348700
O	O6	0.030300	0.365700	0.113200
O	O6	0.969700	0.634300	0.886800
Si	Si1	0.255500	0.250100	0.709000
Si	Si1	0.744500	0.749900	0.291000
Si	Si2	0.588400	0.915200	0.708000
Si	Si2	0.411600	0.084800	0.292000

After GO

α = 94.640°

B = 93.818°

Γ = 120.006°

a = 5.347Å

b = 5.346Å

c = 10.234Å

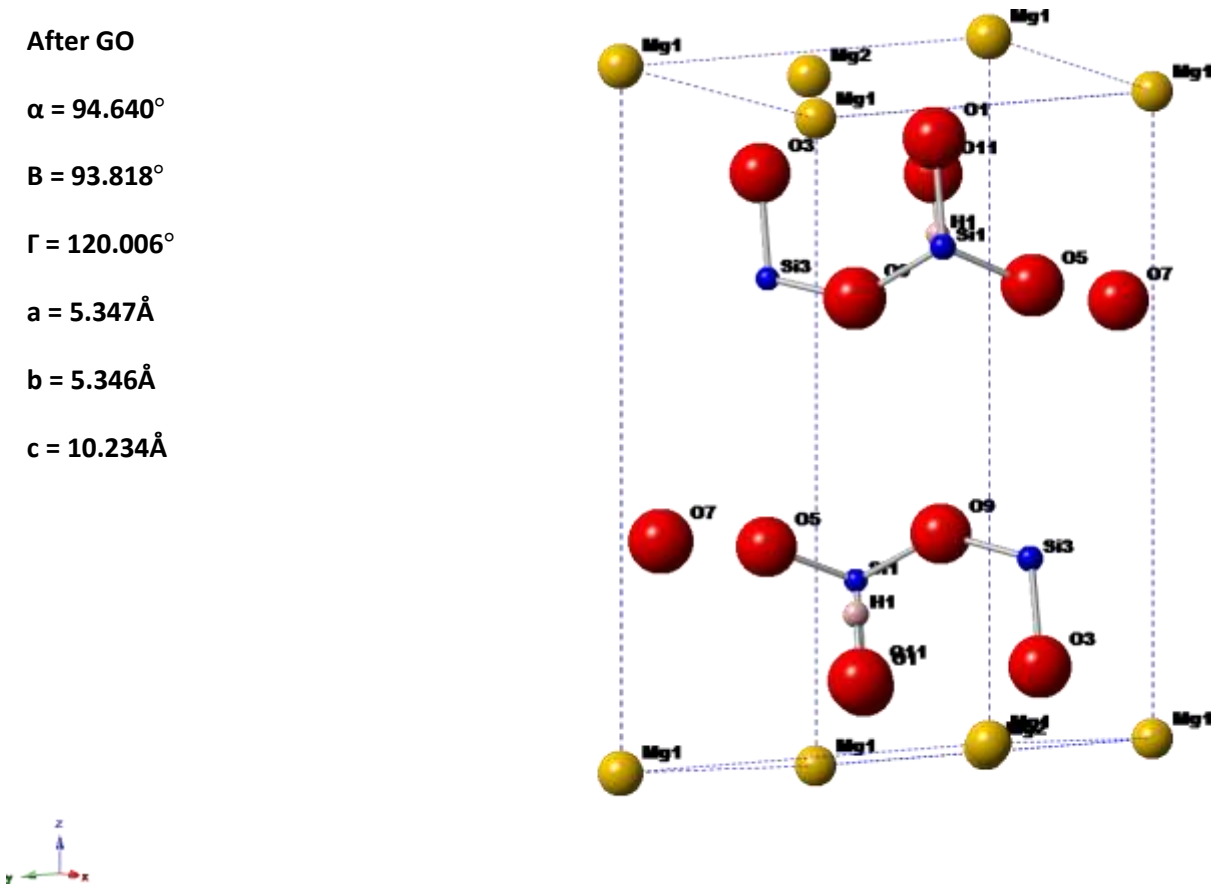

Figure 7-3 The primitive unit cell structure of talc after GO.

Table 7-3 The fractional coordinates of every atom/ion shown in the primitive cell in Figure 7-3.

Fractional Coordinates (After GO)

Element	Label	x	y	z
H	H1	0.059166	0.392414	0.198686
H	H1	0.940834	0.607586	0.801314
Mg	Mg1	0.000000	0.000000	0.000000
Mg	Mg1	1.000000	0.000000	0.000000
Mg	Mg1	0.000000	1.000000	0.000000
Mg	Mg1	1.000000	1.000000	0.000000
Mg	Mg1	0.000000	0.000000	1.000000
Mg	Mg1	1.000000	0.000000	1.000000
Mg	Mg1	0.000000	1.000000	1.000000
Mg	Mg1	1.000000	1.000000	1.000000

Mg	Mg2	0.666689	0.333277	0.000494
Mg	Mg2	0.333311	0.666723	0.999506
O	O1	0.695418	0.698791	0.109970
O	O1	0.304582	0.301209	0.890030
O	O3	0.363790	0.032535	0.109929
O	O3	0.636210	0.967465	0.890071
O	O5	0.576502	0.916909	0.327012
O	O5	0.423498	0.083091	0.672988
O	O7	0.088105	0.940212	0.326242
O	O7	0.911895	0.059788	0.673758
O	O9	0.599008	0.428668	0.326827
O	O9	0.400992	0.571332	0.673172
O	O11	0.029260	0.363532	0.103179
O	O11	0.970740	0.636468	0.896821
Si	Si1	0.739619	0.745857	0.271683
Si	Si1	0.260381	0.254143	0.728317
Si	Si3	0.406880	0.079307	0.271692
Si	Si3	0.593120	0.920694	0.728308

The most noticeable changes in the cell structure after the GO for talc is the lattice parameter c (~0.8 Å) and the proton coordinates (positions). This is not surprising because talc has a layered structure in the c direction: the leeway between the layers leads to a higher spatial flexibility in c direction for the BFGS minimizer to explore and find the local ground state. On the other hand, the real proton positions are not always accurately determined from diffraction experiments and should be optimised by minimising the total energy during GO. The effect of GO on talc structure is demonstrated in the calculated stress before and after the GO: 3.0148 and 0.0214 GPa, respectively. The structural and GO data for the other minerals are listed in Appendix IV.

7.3. Calculations vs experiments

7.3.1. Calculated ^{17}O NMR parameters

The structures before and after converged GO were then subjected to CASTEP NMR calculations using the converged k-point grid, highest possible cut-off energy and PBE to obtain the NMR parameters of all species and sites within each structure.

Since the CASTEP NMR calculation outputs report the absolute chemical shielding rather than chemical shift (both in ppm), extra steps are needed to compute the shifts from the reported shielding values. While it is not always possible to calculate the primary reference used in NMR experiments e.g. liquid water for ^{17}O as 0 ppm, it is usually the secondary references, of which the chemical shift values are known with respect to the primary reference, which are calculated.

The simulated ^{17}O spectra herein are all referenced to the ^{17}O chemical shielding values of the three oxygen sites in the secondary reference compound forsterite, the structure upon which in-depth NMR investigations have been carried out both experimentally and computationally. The experimentally determined δ_{iso} of the three oxygen sites in forsterite is 48, 64 and 61 ppm for O_1, O_2 and O_3 sites, respectively (Ashbrook *et al.*, 2005). In order to utilise the published data, NMR calculations on forsterite (Hazen, 1976; Farnan, 2017, personal communication), following the steps described in 7.2, were performed. The corresponding chemical shielding for oxygen sites O_1, O_2 and O_3 are 202.3042, 183.3078 and 191.5020 ppm, respectively. It can be recalled from Equation 2-17 that $\delta_{iso} = \sigma^{ref} - \sigma_{iso}$. One of the ways to find the shielding value that corresponds to 0 ppm shift is to plot the calculated shielding values against the correctly referenced experimental shift values and this is shown in Figure 7-4. Based on the linear fits, the σ^{ref} value should be ~260 ppm. In theory, the gradient of the linear regressed line should be -1.00. The deviation from the theoretical gradient probably reflects the inaccuracy in calculating the shielding properties. However, the limited range of the shift values and the fact that all three shielding values were obtained from one single calculation might not effectively eliminate the embedded systematic error. A simpler approach is to average both sets of values and assume a gradient of -1.00. For the geometry optimised structure, this yields a ~248 ppm shielding (σ^{ref}) for 0 ppm shift.

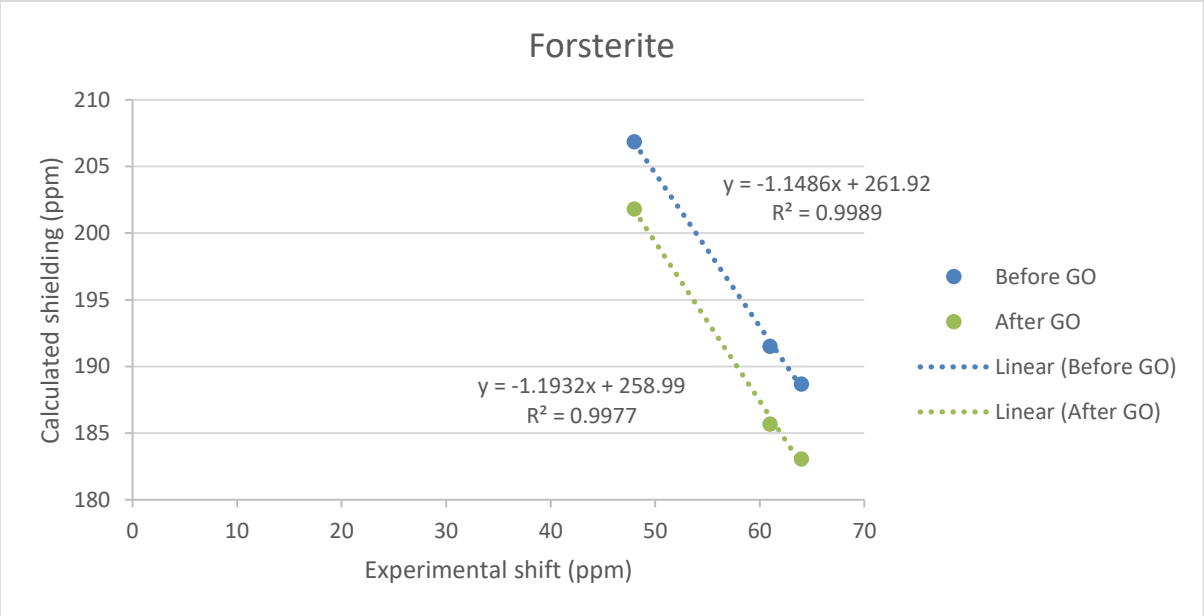

Figure 7-4 Calculated shielding vs experimental shift for forsterite (Ashbrook *et al.*, 2005).

The CASTEP NMR calculation output file (.magres) can be visualised and analysed by using a web-based programme named MagresView built upon the widely used Jmol crystal viewer (Sturniolo *et al.*, 2016). An example is shown in Figure 7-5, with an expanded view to include

all the oxygen atoms. The key calculated NMR parameters, including isotropic chemical shielding, anisotropy and asymmetry (CSA) as well as the quadrupole coupling constant and asymmetry (Q), are summarised in Table 7-4, where the results are also compared between before and after GO. Noticeably, the shift and anisotropy change by more than 100 ppm and the quadrupole coupling constant changes by more than 3 MHz for the hydroxyl oxygen(s). GO clearly modified and/or refined the hydroxyl oxygen local environments. This further justifies the necessity of GO prior to NMR calculations for proton-containing structures. The theoretical central transition MAS (infinitely fast) and static spectra at ~67.8 MHz operating frequency are simulated using DMFIT for the hydroxyl oxygen with these two sets of interactions and displayed in Figure 7-6 (260 ppm chemical shielding as 0 ppm shift). The effect of GO on the NMR spectral response for the hydroxyl oxygen in talc is clearly demonstrated. Indeed, the selective detection of surface alteration products were realised by CP experiments at relatively short contact times (tens of microseconds). Therefore, the focus will be placed on the hydroxyl groups in the case of ^{17}O results.

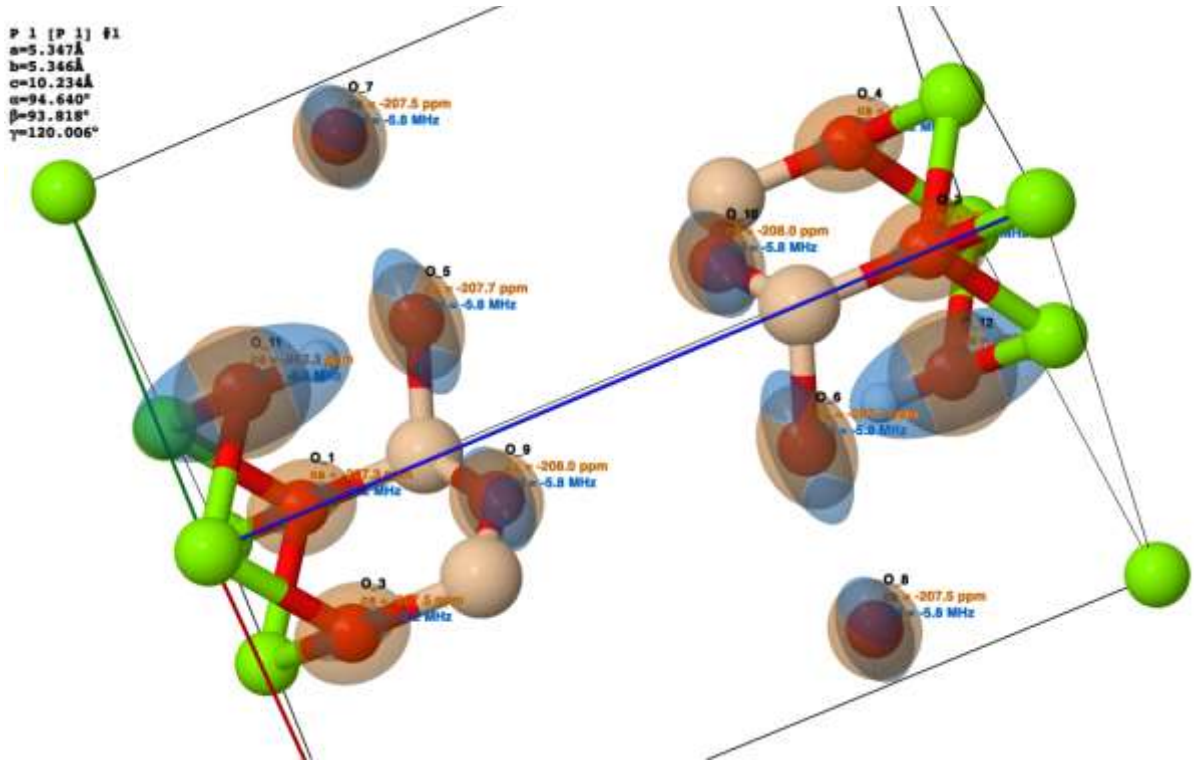

Figure 7-5 MagresView visualisation of the NMR calculation output of the geometry optimised talc structure (expanded view which include all the oxygen atoms). The isotropic shielding and quadrupole coupling constant of each atom are labelled next to it. The chemical shielding tensor and EFG tensor are presented in bronze and blue ellipsoids: the scale is the same across the same set of tensors.

Table 7-4 A summary of the CASTEP calculated key NMR parameters of oxygens in talc (a) after and (b) before geometry optimisation. O (11, 12) are the hydroxyl oxygen(s). δ_{iso1} and δ_{iso2} are the isotropic chemical shift with respect to 260 and 248 as 0 ppm, respectively.

(A)	σ_{iso} (ppm)	δ_{iso1} (ppm)	δ_{iso2} (ppm)	Anisotropy (ppm)	η_{csa}	C_Q (MHz)	η_q
O (1, 2)	207.3121	52.6879	40.6879	37.6003	0.0380	-3.1979	0.0111
O (3, 4)	207.5236	52.4764	40.4764	37.4774	0.0195	-3.2108	0.0068
O (5, 6)	207.7044	52.2956	40.2956	63.1915	0.0704	-5.7633	0.1125
O (7, 8)	207.5148	52.4852	40.4852	63.6270	0.0642	-5.7848	0.1030
O (9, 10)	207.9695	52.0305	40.0305	64.2088	0.0703	-5.7726	0.1104
O (11, 12) Hydroxyl	262.3151	-2.3151	-14.3151	8.9434	0.0175	-8.0956	0.0013
(B)							
O (1, 2)	209.5997	50.4003	38.4003	33.0118	0.2169	-3.0075	0.0629
O (3, 4)	209.8893	50.1107	38.1107	32.4188	0.1676	-2.8868	0.0475
O (5, 6)	207.5225	52.4775	40.4775	53.0375	0.1169	-5.5738	0.0693
O (7, 8)	206.3777	53.6223	41.6223	51.5392	0.0528	-5.5289	0.1298
O (9, 10)	207.5183	52.4817	40.4817	52.5710	0.3329	-5.4366	0.0301
O (11, 12) Hydroxyl	144.3004	115.6996	103.6996	170.3466	0.0298	-11.1424	0.0119

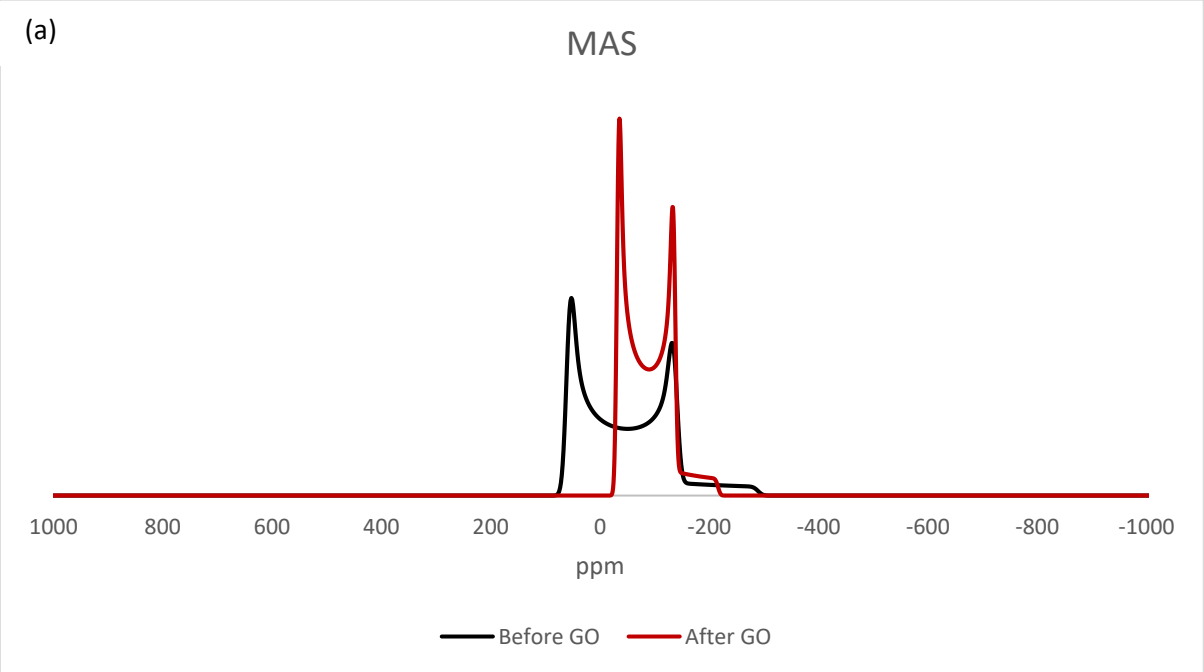

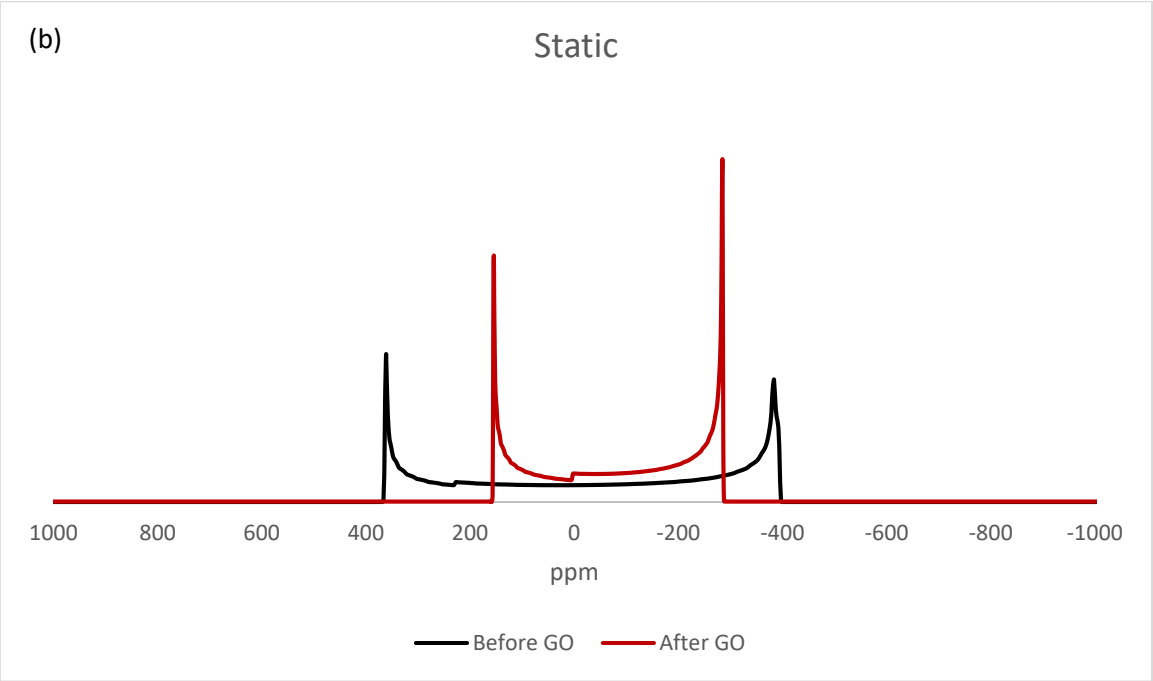

Figure 7-6 Simulated ^{17}O NMR (a) MAS and (2) static central transition spectra of the hydroxyl oxygen(s) in talc based on the corresponding calculated parameters before and after GO (the same intensity). No line broadening function is applied.

The same set of calculated NMR parameters of the hydroxyl oxygen sites in all the considered minerals (geometry optimised) and those from the literature are listed in Table 7-5[†]. Despite there being more than one hydroxyl oxygen site in some structures, e.g. oxygen sites (13-18), in both clinochlores, for solid-state experiments especially when structural disorder is present, it is highly unlikely that they can be resolved statically and most likely the superimposed spectrum would appear as a broadened single one. These simulated spectra are shown in 7.3.3.

Table 7-5 Hydroxyl oxygens NMR parameters calculated on the respective geometry optimised structures of the potential Mg silicate precipitates.

Mineral	Hydroxyl Oxygen(s)	σ_{iso} (ppm)	δ_{iso1} (ppm)	δ_{iso2} (ppm)	Anisotropy (ppm)	η_{csa}	C_Q (MHz)	η_q
Clinochlore (Triclinic)	O (11, 12)	263.4550	-3.4550	-15.4550	8.6665	0.0292	-8.0512	0.0022
	O(13, 14)	264.3775	-4.3775	-16.3775	27.1060	0.0578	-8.8313	0.0021
	O (15, 16)	264.3969	-4.3969	-16.3969	27.0186	0.0097	-8.8252	0.0016
	O (17, 18)	264.3044	-4.3044	-16.3044	27.3426	0.0331	-8.8313	0.0078
Clinoclhore (Monoclinic)	O (11, 12)	263.4230	-3.4230	-15.4230	8.8794	0.0562	-8.0501	0.0022
	O(13, 14)	263.8872	-3.8872	-15.8872	27.9899	0.0543	-8.8113	0.0030
	O (15-18)	263.8863	-3.8863	-15.8863	27.5783	0.0424	-8.8066	0.0012

	δ_{iso1} (ppm)	C_Q (MHz)	η_q	Ref.
Hydroxyl clinohumite	14.5	-7.6	0.18	(Griffin *et al.*, 2009)
Talc	0.0	7.3	0.0	(Walter, Turner and Oldfield, 1988)

[†] The NMR calculation results of brucite are not presented because of the experimentally available spectrum as shown in Figure 6-24.

7.3.2. Calculated ^{25}Mg NMR parameters

Referencing the ^{25}Mg shielding is more difficult in the sense that experimental solid-state ^{25}Mg NMR spectra with high *S*/*N* are difficult to obtain (see 3.3.5.5), hence there have not been many reliable isotropic shift values reported. Nevertheless, Pallister, Moudrakovski and Ripmeester (2009) published a comprehensive study reporting CASTEP calculated shielding and experimental shift (at 21.8 Tesla ultra-high field) of 28 Mg compounds, the majority of which have Mg coordinated by oxygen. These results, as taken from the paper, are shown in Figure 7-7[‡]. From the diagram, the shielding that corresponds to the 0 ppm shift reference is somewhere close to 566 ppm and was adopted herein for ^{25}Mg referencing. The same set of calculated NMR parameters of the Mg-OH magnesium sites in all the considered minerals (geometry optimised) are listed in Table 7-6, following the same procedures for the ^{17}O calculations as in 7.3.1. Similar to the hydroxyl oxygens, the primary differences in the NMR calculation results for Mg-OH magnesiums before and after geometry optimisation liess in δ_{CS}^{iso} and C_Q (not shown).

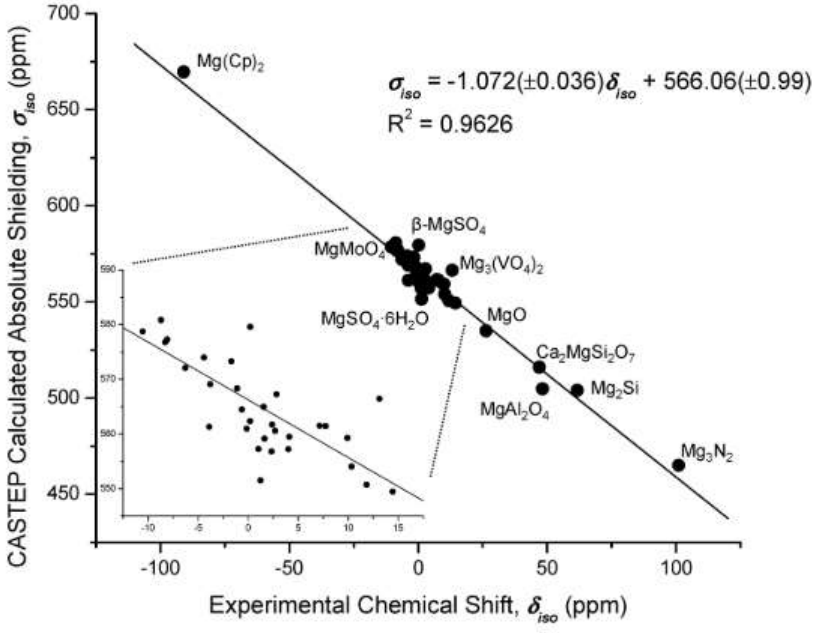

Figure 7-7 CASTEP calculated shielding against experimentally determined shift for 28 Mg compounds, taken from Pallister, Moudrakovski and Ripmeester (2009).

Table 7-6 Mg···OH magnesiums NMR parameters calculated on the respective geometry optimised structures of the potential Mg silicate precipitates.

Mineral	Mg···OH	σ_{iso} (ppm)	δ_{iso} (ppm)	Anisotropy (ppm)	η_{csa}	C_Q (MHz)	η_q

[‡] With a relatively large dataset, the expected -1.00 gradient for a shielding vs shift plot is being approached.

Brucite	Mg (1)	555.1796	10.8204	-9.7853	0	-2.9761	0
Clinochlore (Triclinic)	Mg (1)	551.3661	14.6339	-13.4495	0.6499	-3.8168	0.1395
	Mg (2, 3)	551.2201	14.7799	-11.9679	0.3218	2.0047	0.1239
	Mg (4, 5)	542.8347	23.1653	-13.4538	0.0953	-0.2680	0.9554
	Mg (6)	543.3048	22.6952	-15.3461	0.0862	-0.4579	0.6955
Clinochlore (monoclinic)	Mg (1)	551.3805	14.6195	-12.6934	0.5551	-3.2604	0.1525
	Mg (2, 3)	551.1788	14.8212	-11.9140	0.3200	2.1992	0.0143
	Mg (4, 5)	543.0235	22.9765	-13.4440	0.0651	-0.2481	0.3334
	Mg (6)	542.9738	23.0262	-14.9358	0.0970	0.6544	0.4405
Talc	Mg (1)	549.6417	16.3583	-13.0976	0.6537	-3.7857	0.1777
	Mg (2, 3)	549.4094	16.5906	-11.8331	0.3037	1.9738	0.1548

7.3.3. Simulated vs experimental spectra

The simulated ^{17}O static spectra of hydroxyl oxygen(s), according to the calculation results in Table 7-5 and the two sets of data from the literatures for a hydroxyl clinohumite and a talc sample, are compared with that of the static CP spectrum shown in Figure 6-25. Despite the characteristic low frequency singularity in each case it exhibits similar features and in close proximity to those observed of the leached glass sample, which suggests a close-to-zero η_Q, no combination of δ_{CS}^{iso} and C_Q generates a spectrum that perfectly matches the experimental results based on the calculated data in Table 7-5. It should be borne in mind that where multiple inequivalent sites were involved, the spectra were simulated according to the stoichiometry. The overall line shape, but not the position, might change if this is not experimentally achievable due to the different CP dynamics for different sites at a constant contact time. Nevertheless, none of the sub-spectra of the two forms of clinochlore corresponds to the singularity position, either. Therefore, changes in the relative intensity will not improve the match between the simulated and experimental spectra.

Interestingly, the hydroxyl ^{17}O signal based on the NMR parameters extracted from the talc sample investigated in the study by Walter, Turner and Oldfield (1988) seems to match the position of the low frequency singularity of the CP spectrum very well. In addition, the high frequency end at a shift of ~120 ppm is also in agreement with the increasing CP intensity between 90~120 ppm at shorter contact times in Figure 6-26. By comparing Table 7-4 and Table 7-5 it is clear that the main discrepancy between the calculated and experimentally determined NMR parameters lies in the C_Q value. Unfortunately, the lattice parameters and angles, as well as the exact atomic coordinates of this specific talc sample were not given, and they could well be different to the one being calculated. As shown in 7.2.2, NMR parameters of hydroxyl oxygen(s) are extremely sensitive to the exact geometry of the lattice, as well as the O···H

orientation and proton position. Therefore, the hydroxyl oxygen(s) in that specific talc structure seem to emulate, at least, one of the –OH groups within the alteration products.

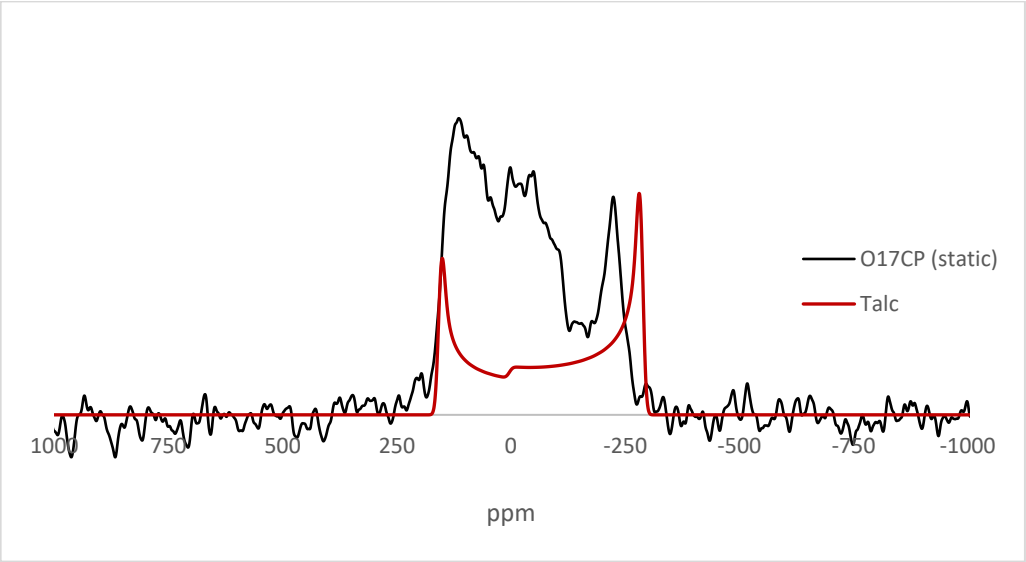

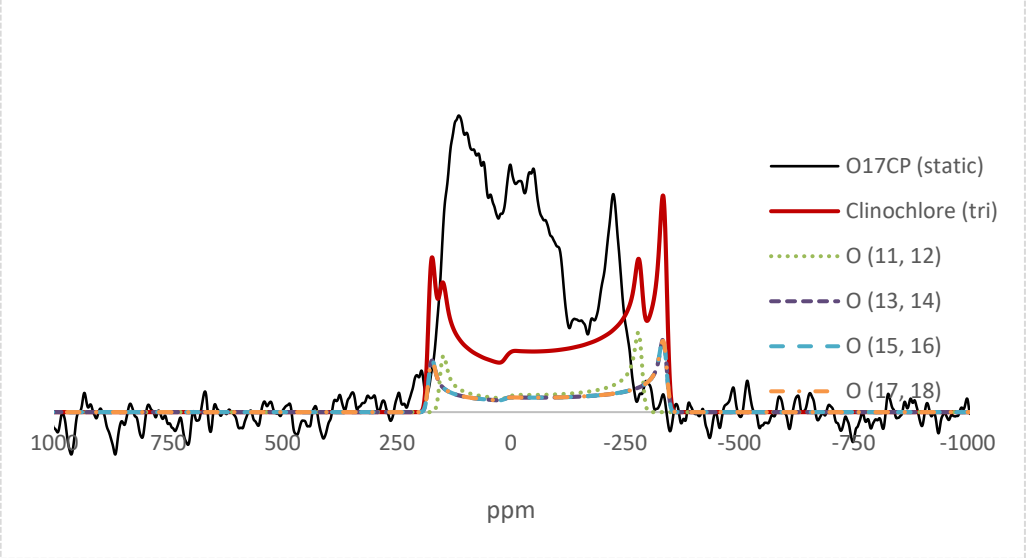

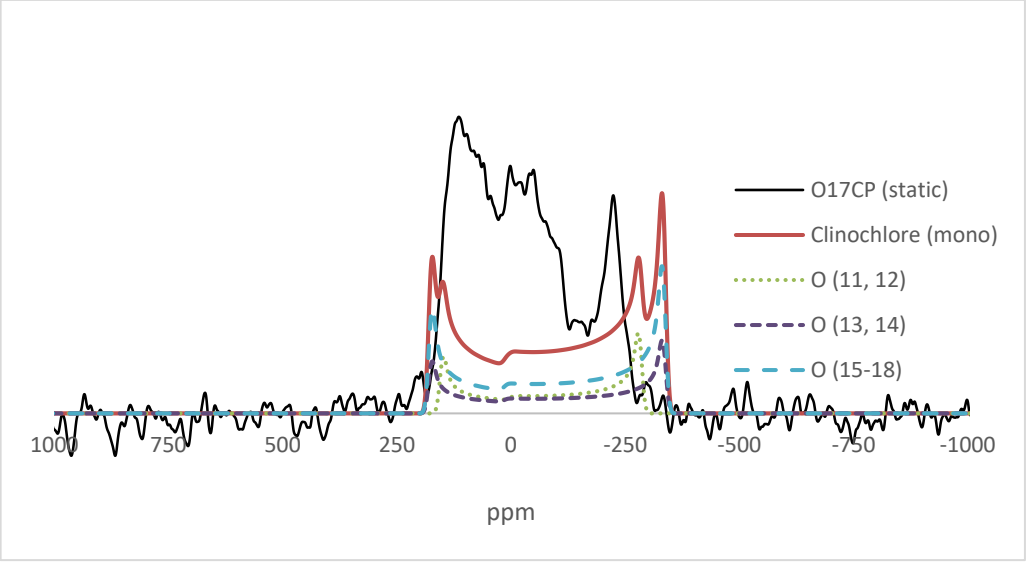

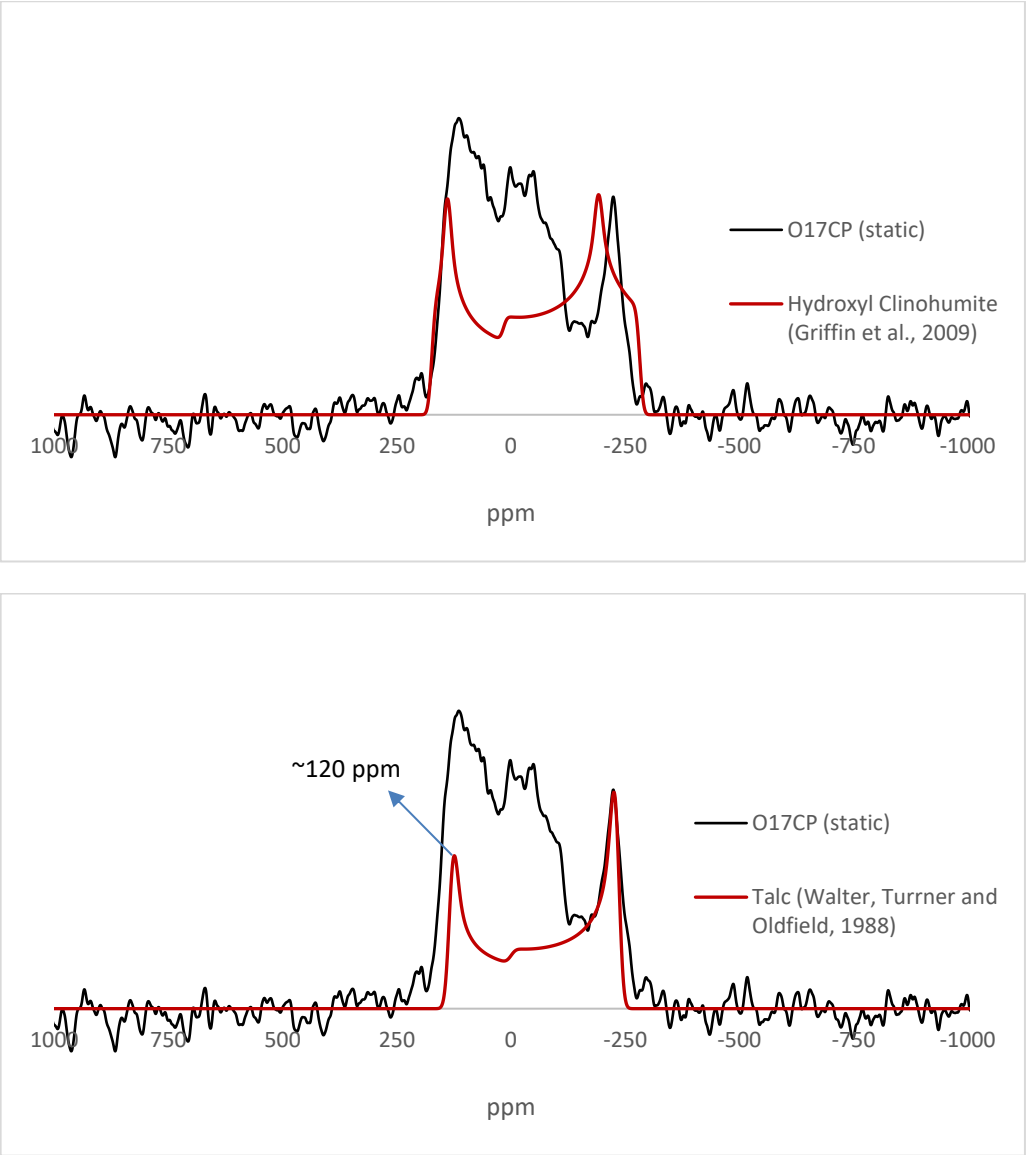

Figure 7-8 Static ^{1}H-^{17}O CP spectrum of MgEM glass leached in ^{17}O-enriched water for 16 weeks and the simulated static spectra of hydroxyl oxygens in each Mg silicate mineal. The simulations are based on the calculated NMR parameters listed in Table 7-4 and Table 7-5 using DMFIT software. ~10 Hz Gaussian line broadening was applied.

The corresponding simulated ^{25}Mg spectra are also compared with the static ^{1}H-^{25}Mg CP spectrum shown in Figure 6-9. Similarly, the relative intensity was determined by the Mg stoichiometry of each structure even though the total line is compared with a CP spectrum. While the other structures seem to adopt completely different Mg environments from those in the alteration products, the superposition of the static spectra of the two types of Mg sites in talc exhibit an overall similar lineshape and position of the experimental spectrum. This is consistent with Figure 6-9 and the corresponding static ^{1}H-^{25}Mg CP spectrum of talc obtained with a contact time of 43 ms. However, based on the sub-spectrum of each magnesium site, the overall lineshape heavily depends on the relative contributions. There is only one type of hydroxyl proton within the structure as the magnetisation source. It is measured in the geometry optimised talc structure the distances between the only proton site and the nearest neighbouring

Mg site (1) and (2, 3) are 2.683 and 2.681 Å, respectively. Moreover, the diminishing magnetisation transfer during the contact time is mainly caused by the rotating frame spin-lattice relaxation of proton(s) (see 2.4.1.3). Therefore, the 1:2 stoichiometric ratio between site (1) and site (2, 3) applied in the simulation is justified, based on this common ground, and yields a good match between the simulated and experimental spectra.

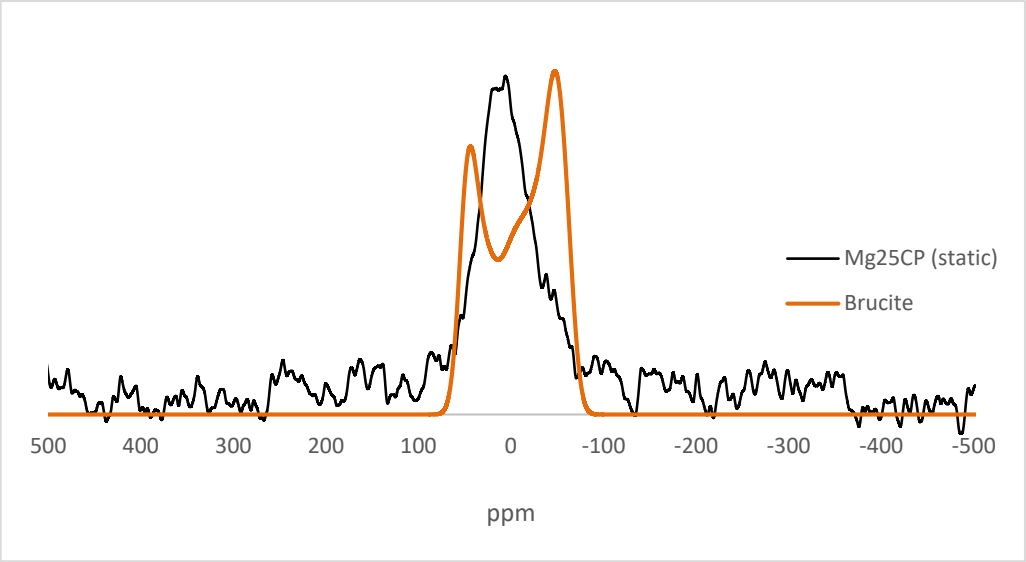

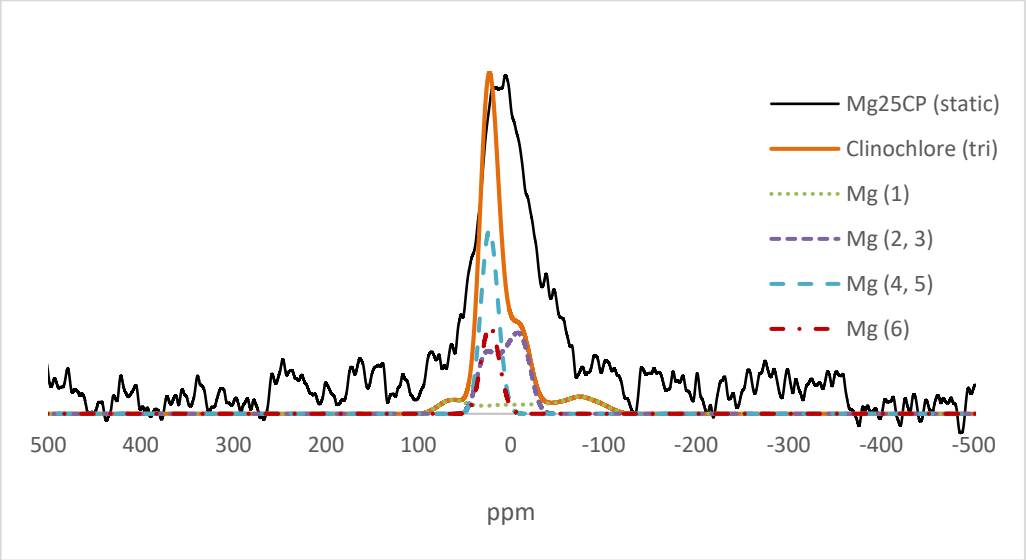

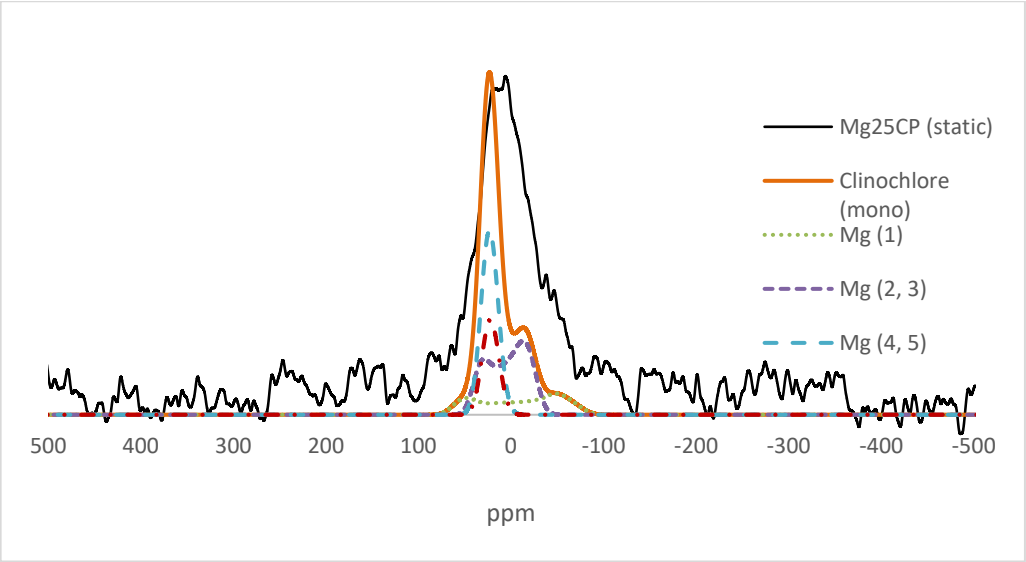

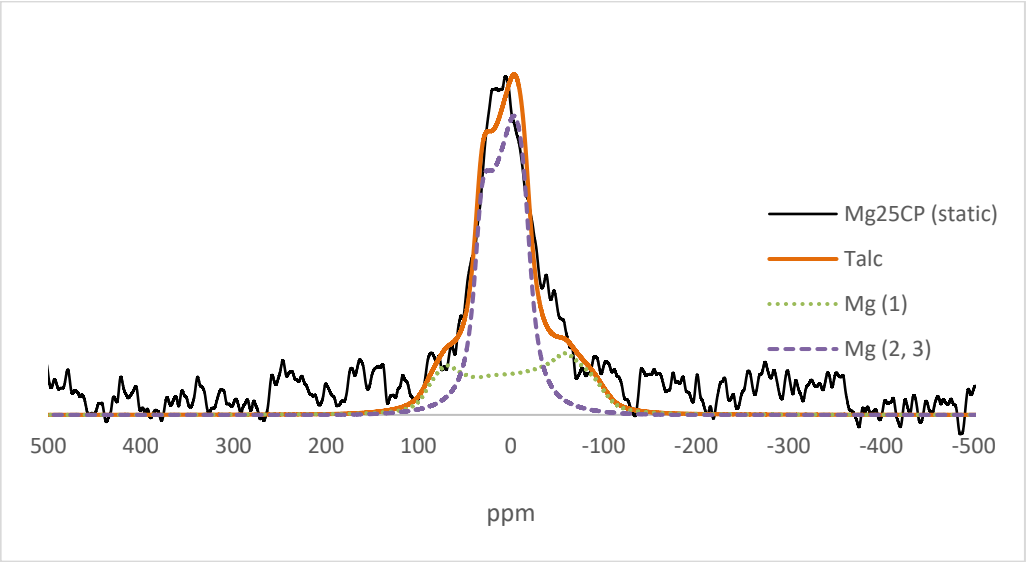

Figure 7-9 Static ^{1}H-^{25}Mg CP spectrum of MgEM glass leached for 16 weeks and the simulated static spectra of hydroxyl bonded magnesium in each Mg silicate mineal. The simulations are based on the calculated NMR parameters listed in using DMFIT software. ~20 Hz Gaussian line broadening was applied.

7.4. Summary

The calculated NMR parameters, particularly δ_{CS}^{iso} and C_Q, of hydroxyl oxygens and Mg-OH magnesiums in several Mg-containing phyllosilicate are sensitive to the lattice parameters and/or lattice angles as well as proton positions. Therefore, it is important to conduct geometry optimisation on the diffraction-derived structures that contain protons before NMR calculations. The talc structure from which the NMR parameters were derived in the study by Walter, Turner and Oldfield (1988) shows a very similar ^{17}O NMR spectral response from its hydroxyl oxygen to that of the precipitate(s) formed during MgEM glass dissolution (up to 16 weeks). The static ^{1}H-^{25}Mg CP spectrum of the ^{25}Mg-enriched MgEM sample leached for the same duration also

shows the best match with the simulated ^{25}Mg spectrum as a superposition of the two Mg sites in talc[§] stoichiometrically. However, both comparisons are made only among the limited Mg-containing phyllosilicate structures (Mg endmembers) available including only talc and clinochlore and others including brucite, and hydroxyl-clinohumite.

The crystallographic structures of other potential precipitates of Mg silicates (clay) from the thermodynamic calculations, with the information of proton positions, for example, by neutron diffraction, should be tested by subjecting them to the same Ab initio NMR calculation procedures for comparison.

[§] This talc structure is from Rayner and Brown (1973).

Chapter 8

8. Discussion and concluding remarks

8.1. Effect of Mg on glass structure and primary dissolution

The observation of ^{25}Mg NMR shifts in the MgEM glass consistent with 4-fold Mg coordination with oxygen confirms a network forming role for Mg. Indeed, the structural roles of the alkaline-earth ions Ca^{2+} and Mg^{2+} have been shown to be different in multiple 3/4-component soda-lime and (alumino)silicate melts and glasses. In particular, the latter has a very high tendency to form tetrahedra with oxygen anions，as with Si and Al，to construct the glass network while the former mainly acts as a network modifier. The network forming characteristics of Mg were manifested in the elastic properties, degree of (de)polymerisation and simulated glass structures as well as viscosities of the melts of the corresponding compositions upon Mg substitution for Ca or Al (Binsted, Greaves and Henderson, 1985; Pedone *et al.*, 2008; Kuryaeva, 2009). Higher-coordinated Mg was also inferred by the overall charge balance scheme derived from a multinuclear examination of the local environments of glass components. However, the exact distribution of Mg into these two roles was not obtained because of the difficulty in obtaining a highly resolved (2D) ^{25}Mg NMR spectrum due to *S*/*N* constraints and a lack of information on the overall degree of network modification (fraction of NBOs) in the glass. In this relatively complex 6-component borosilicate glass, the boron coordination environment was also affected by the different structural roles adopted by Ca and Mg in that the fraction of $^{[3]}$B increased with the relative Mg content. Similar structural changes have also been observed for aluminoborosilicate glasses when network modifier cations with higher field strength were added at the expense of cations with lower field strength. Conversion of $^{[4]}$B to $^{[3]}$B was understood to be promoted by the creation of NBO (negative charge) around cations with higher field strength (Wu and Stebbins, 2009; Morin, Wu and Stebbins, 2014). While this could be the mechanism operating for higher-coordinated Mg, the poorer charge compensating capability of Mg relative to Ca, as shown by Figure 4-14 and Figure 4-15, also favoured the $^{[4]}$B to $^{[3]}$B conversion in the MgEM glass. The difference in the average shift position of the static ^{139}La NMR spectra in Figure 4-12 suggests the different structural roles for the sole REE in the glass when a high content of Mg is present. Combining the charge balance discussion based on Table 4-6, it is intriguing that upfield (lower frequency) shifts of

^{139}La NMR spectra correspond to over-coordinated La. Charge compensating La tends to adopt more downfield shifts, as in the case of high Mg contents.

Boron coordination has been shown to have no impact on its tendency to be leached from the glass and the initial dissolution rate across the simplified glass series remains invariant within error at ~2.4 g/m^2/d. Both findings suggest that the systematic compositional and local structural changes from CaEM to MgEM glasses, at least to the extent discussed in Chapter 4, are not the primary causes of the much poorer aqueous durability reported in the literature and Chapter 5 for Mg-containing glasses over longer time scales.

8.2. Effect of Mg on alteration layers formation

On passing through the initial forward dissolution phase, glass dissolution is then thought to be retarded due the formation of a protective gel layer formation on the surface, which acts as a transport barrier for water species and glass constituents. However, for the hydrolysed glass structure to be protective of the underlying glass, re-construction and densification are required. Therefore, in order to understand the drastically different degree of dissolution between Mg- and Ca-based (as the alkaline-earth constituent) glass described in Chapter 5 and elsewhere in the literature, it is imperative to identify the effects of Mg on the densification of the gel layer. As pointed out in 1.4.1, this well-recognised prerequisite for the establishment of a residual rate of dissolution could be affected by local Si saturation and presence of phyllosilicates, while Mg in the aqueous environment (leached from glass or in the leachant) was found to promote the formation of Mg-containing clays.

The capability of solid-state NMR to detect specific nuclei and short-range chemical environments was proven to be immensely powerful for identifying the precipitates formed on the glass surface, which was 'X-ray amorphous' and present in very small amounts. A multinuclear (^{1}H, ^{29}Si, ^{25}Mg and ^{17}O) approach combined with ab initio NMR calculations suggested that the phyllosilicate formed on the simplified MW25 glass was a talc-like (clay) phase rather than a clinochlore-like (chlorite) phase. Despite the lack of accurate structural information (proton positions) of other smectite group and sepiolite clay candidates amenable to calculations, the fundamental difference between these two types of phyllosilicates is their different layered structure. While talc, and other clays of interests, possess a typical 2:1 layered structure, the Mg endmember clinochlore can be regarded as a brucite layer sandwiched by two 2:1 talc layers (Brigatti, Galán and Theng, 2013) (see Figure 7-2 and Appendix IV). Although the effects of interlayer cations within smectite group and sepiolite on the hydroxyl oxygen

NMR interactions should be further investigated, the 2:1 layers of talc are charge neutral and hence devoid of charge-balancing interlayer cations.

The precipitation of a talc-like amorphous phase operated to reduce the efficacy of the protective layer in, at least, two ways. It consumed Si that could have created the protective layer at the altered glass-water interface, while the physical presence of a separate phase presented a mixed-phase microstructure that itself could provide the pathways for interdiffusion of water species and leached glass constituents at the reaction front. Clay minerals, including talc, because of their crystallographic features, have been shown to have one of the highest specific surface area among natural minerals and small size (typically 2~4 μm) and high porosity (Brigatti, Galán and Theng, 2013; Huggett, 2015; Tournassat *et al.*, 2015). Nevertheless, the loosely deposited precipitates shown in Figure 6-3 suggested that the former mechanism should be primary. On the other hand, ^{1}H, ^{29}Si MAS and 2D MQMAS NMR results demonstrated that re-construction of the hydrolysed glass to form the protective gel layer during MgEM glass dissolution took place but was restricted and interrupted, presumably, by the talc-like phase precipitation. The dissolution of the Mg-rich glasses was slowed down eventually, but the gel layer protectiveness was heavily impaired compared with that of the CaEM glass. The B release after 16 weeks was about one order of magnitude higher for the MgEM glass (7.960 vs 0.928 g/m^2), which compares well with the dissolution rates difference reported in the literature over longer time scales between MW and SON68 glasses.

8.3. Concluding remarks

The main findings from this work include:

1. Mg in the simplified MW25 glass (MgEM) adopts both network former and modifier roles. This is in contrast to Ca in its counterpart CaEM even though the structural role(s) of Ca was not directly identified. This was confirmed by the increased proportion of $^{[3]}B$, downfield shifts of the ^{139}La NMR spectrum, of the former, and the total charge balance scheme;
2. The pristine glass structure changes induced by Mg/Ca substitution and their respective different structural roles have little impact on the primary dissolution kinetics of the corresponding glasses. The initial dissolution rate(s) of the simplified glasses was determined to be the same within error at ~2.4 g/m^2/d;
3. The much greater (usually one order of magnitude) long-term dissolution in the literature and this thesis of Mg-containing glasses compared with their Ca-based

counterparts, therefore, was attributed to secondary effects. In particular, the secondary precipitates removed Mg and Si from solution;

4. The precipitates formed at relatively early stages of the MgEM glass dissolution (from 4 weeks up to 16 weeks with a starting *SA*/*V* of 1200 m^{-1}) adopted a talc-like (clay) as opposed to a clinochlore-like (chlorite) structure. As an output of this work, talc could be used as a solubility-limiting phase in modelling the MW25 glass dissolution;
5. Although such precipitates were thought to reduce the protectiveness of the gel layer (altered glass), re-construction of the hydrolysed structure was believed to have taken place. This was shown by semi-quantitative ^{1}H NMR results between 4- and 16-week leached MgEM samples and ^{17}O NMR signal of bridging oxygens.

8.4. Ideas for future work

The effects of Mg substituting Ca in simplified MW25 glass domain, and potentially other Mg-containing glasses, would be better understood with the quantitative knowledge of Ca in different structural roles. Attention should also be paid to the homogeneity of the synthesised glasses in terms of glass-glass phase separation, which could potentially lead to Si-rich and B-rich regions. While these structural changes are immune to routine XRD examinations, they would lead to structure dependent dissolution kinetics. Due to the time constraint of this work, the dissolution experiments were only conducted in static batches with glass samples in powder form, up to 16 weeks in time.

Whilst speeding up the dissolution kinetics, using powder sample excluded the applicability of some characterisation techniques that have been widely adopted in the literature for investigating altered glass surface including Time-of-Flight Secondary Ion Mass Spectroscopy (ToF-SIMS) and Atom Probe Tomography (ATP) etc. These techniques usually only produce information on overall elemental composition and physical structure of the alteration layers, whilst NMR gives the speciation and the link to geochemical modelling. On the other hand, preparing the samples in finer powders could increase the amount of altered material for a given sample mass and leaching time (see 5.2) and hence increase the NMR sensitivity for characterising such secondary materials. Using ^{17}O-enriched water as the leaching agent was only applied to the 16-week dissolution experiments, which limited the useful solid-state ^{17}O NMR techniques e.g. ^{1}H-^{17}O CP(MAS) and MQMAS to samples leached only for this duration. In terms of the solution (leachate) analysis, not only the elemental concentrations but also the isotopic (ratio) variations could be monitored to capture the timing and extent of ionic diffusion, elemental retention/incorporation and secondary precipitation because such reactions lead to

kinetic isotope effects, such as $^{10}B/^{11}B$, fractionation* (O'Neil, 1986). Last but not the least, NMR calculations based on ab initio DFT ought to be carried out on more clay structures to assist with ^{17}O and ^{25}Mg NMR experimental results.

Based on the work presented in this thesis, the measures that could potentially improve our understanding of the Mg effects on radioactive waste glass (MW25) structure and alteration processes (especially during passivating gel layer formation) include:

1. Making CaEM glass with ^{43}Ca-enriched precursor(s) and conducing ^{43}Ca NMR experiments to distinguish the Ca roles between charge compensator and creating NBO. Other ^{25}Mg NMR experiments should also be attempted including MQMAS and CP under MAS conditions;
2. Monitoring glass-glass phase separation with Mg/Ca variation by conducting ^{29}Si NMR experiments on the pristine glasses, i.e. observing Q^n species distribution;
3. Using ^{17}O-enriched water as the leaching agent for CaEM and MgEM dissolution experiments of shorter (e.g. 1-4 week(s)) and longer durations to capture the difference in the extent, nature and evolution of the hydrolysis and precipitation reactions by ^{17}O solid-state NMR;
4. Setting up dissolution experiments using finer glass powders (e.g. 3.5~5.5 μm as in (Collin *et al.*, 2018)) to achieve greater (total) alteration in preparation for solid characterisation by NMR. Using monolith glass samples (MgEM/MW25) to facilitate other surface characterisation techniques including ToF-SIMS and ATP etc.;
5. Performing NMR calculations on more Mg clay minerals using ab initio DFT codes (e.g. CASTEP) to explore the effects of interlayer cations on -^{17}OH and ^{25}Mg-OH NMR spectral responses;
6. Continuing the B isotope work by determining the ratio of the pristine ^{10}B-enriched ISG glass and extending it (Mg isotope) to the MgEM/MW25 glass.

* B isotope experiments were already done with a lab-synthesised ^{10}B-enriched borosilicate glass mimicking the composition of ISG. The results are not presented in this thesis due to the undetermined B isotope ratio of the pristine glass, by the time of submission.

References

A. Medek, J.S. Harwood and L. Frydman (1995) 'Multiple-Quantum Magic- Angle Spinning NMR: A New Method for the Study of Quadrupolar Nuclei in Solids', *Journal of the American Chemical Society*, 117(5), pp. 12779–12787.

Abraitis, P. K. *et al.* (2000) 'The kinetics and mechanisms of simulated British Magnox waste glass dissolution as a function of pH, silicic acid activity and time in low temperature aqueous systems', *Applied Geochemistry*, 15(9), pp. 1399–1416. doi: 10.1016/S0883-2927(99)00118-3.

Amoureux, J.-P., Fernandez, C. and Steuernagel, S. (1996) 'Z Filtering in MQMAS NMR', *Journal of Magnetic Resonance, Series A*. Academic Press, 123(1), pp. 116–118. doi: 10.1006/jmra.1996.0221.

Amoureux, J. P. and Fernandez, C. (1998) 'Triple, quintuple and higher order multiple quantum MAS NMR of quadrupolar nuclei', *Solid State Nuclear Magnetic Resonance*. Academic Press, 10(4), pp. 211–223. doi: 10.1016/S0926-2040(97)00027-1.

Andrew, E. R., Bradbury, A. and Eades, R. G. (1958) 'Nuclear magnetic resonance spectra from a crystal rotated at high speed', *Nature*. Nature Publishing Group, 182(4650), p. 1659. doi: 10.1038/1821659a0.

Angeli, F. *et al.* (2006) 'Influence of glass composition and alteration solution on leached silicate glass structure: A solid-state NMR investigation', *Geochimica et Cosmochimica Acta*, 70(10), pp. 2577–2590. doi: 10.1016/j.gca.2006.02.023.

Apperley, D., Harris, R. and Hodgkinson, P. (2012) *Solid-State NMR: Basic Principles and Practice*. Momentum Press. doi: 10.5643/9781606503522.

Aramendía, M. A. *et al.* (1997) 'Characterization of Spanish sepiolites by high-resolution solid-state NMR', *Solid State Nuclear Magnetic Resonance*, 8(4), pp. 251–256. doi: 10.1016/S0926-2040(97)00009-X.

Ashbrook, S. E. *et al.* (2005) 'High-resolution ^{17}O MAS NMR spectroscopy of forsterite (α-Mg_2SiO_4), wadsleyite (β-Mg_2SiO_4), and ringwoodite (γ-Mg_2SiO_4)', *American Mineralogist*, 90(11–12), pp. 1861–1870. doi: 10.2138/am.2005.1915.

Ashbrook, S. E. *et al.* (2007) 'First-principles calculations of solid-state ^{17}O and ^{29}Si NMR

spectra of Mg_2SiO_4 polymorphs', *Phys. Chem. Chem. Phys.*, 9(13), pp. 1587–1598. doi: 10.1039/B618211A.

Ashbrook, S. E. *et al.* (2015) 'New insights into phase distribution, phase composition and disorder in $Y_2(Zr,Sn)_2O_7$ ceramics from NMR spectroscopy', *Physical Chemistry Chemical Physics*. The Royal Society of Chemistry, 17(14), pp. 9049–9059. doi: 10.1039/c4cp05827e.

Ashbrook, S. E. and Farnan, I. (2004) 'Solid-state ^{17}O nuclear magnetic resonance spectroscopy without isotopic enrichment: Direct detection of bridging oxygen in radiation damaged zircon', *Solid State Nuclear Magnetic Resonance*. Academic Press, 26(2), pp. 105–112. doi: 10.1016/j.ssnmr.2004.06.003.

Ashbrook, S. E. and McKay, D. (2016) 'Combining solid-state NMR spectroscopy with first-principles calculations – a guide to NMR crystallography', *Chemical Communications*. The Royal Society of Chemistry, 52(45), pp. 7186–7204. doi: 10.1039/C6CC02542K.

Ashbrook, S. E. and Smith, M. E. (2006) 'Solid state ^{17}O NMR - An introduction to the background principles and applications to inorganic materials', *Chemical Society Reviews*, 35(8), pp. 718–735. doi: 10.1039/b514051j.

ASTM C1285-02 (2002) 'Standard Test Methods for Determining Chemical Durability of Nuclear , Hazardous , and Mixed Waste Glasses and Multiphase Glass Ceramics : The Product Consistency Test (PCT) 1', *ASTM, Conshohocken, USA, 2002*, 15, pp. 1–26. doi: 10.1520/C1285-14.2.

Berglund, B. and Vaughan, R. W. (1980) 'Correlations between proton chemical shift tensors, deuterium quadrupole couplings, and bond distances for hydrogen bonds in solids', *The Journal of Chemical Physics*, 73(5), pp. 2037–2043. doi: 10.1063/1.440423.

Binsted, N., Greaves, G. N. and Henderson, C. M. B. (1985) 'An EXAFS study of glassy and crystalline phases of compositions $CaAl_2Si_2O_8$ (anorthite) and $CaMgSi_2O_6$ (diopside)', *Contributions to Mineralogy and Petrology*. Springer-Verlag, 89(2–3), pp. 103–109. doi: 10.1007/BF00379446.

Björkman, T. (2011) 'CIF2Cell: Generating geometries for electronic structure programs', *Computer Physics Communications*, 182, pp. 1183–1186. doi: 10.1016/j.cpc.2011.01.013.

Bonhomme, C. *et al.* (2012) 'First-principles calculation of NMR parameters using the gauge including projector augmented wave method: A chemists point of view', *Chemical Reviews*,

112(11), pp. 5733–5779. doi: 10.1021/cr300108a.

Bray, P. J. *et al.* (1982) 'NMR studies of the structure of non-metallic glasses', *Nuclear Instruments and Methods in Physics Research*. North-Holland, 199(1–2), pp. 1–15. doi: 10.1016/0167-5087(82)90173-9.

Brigatti, M. F., Galán, E. and Theng, B. K. G. (2013) 'Structure and Mineralogy of Clay Minerals', *Developments in Clay Science*. Elsevier, 5, pp. 21–81. doi: 10.1016/B978-0-08-098258-8.00002-X.

Brigden, C. and Farnan, I. (2014) 'Experimental studies of the durability of UK HLW and ILW glasses . Task 4 – The effect of magnesium Final Report', *NDA RWMD report*, RWM005105(2), pp. 1–68.

Brunet, F. *et al.* (2008) 'Solid-state NMR characterization of a controlled-pore glass and of the effects of electron irradiation', *Solid State Nuclear Magnetic Resonance*. Academic Press, 33(1–2), pp. 1–11. doi: 10.1016/j.ssnmr.2007.12.001.

Bunker, B. C. *et al.* (1990) 'Multinuclear nuclear magnetic resonance and Raman investigation of sodium borosilicate glass structures', *Physics and Chemistry of Glasses*, 31(1), pp. 30–41.

Cailleteau, C. *et al.* (2008) 'Insight into silicate-glass corrosion mechanisms', *Nature Materials*, 7(12), pp. 978–983. doi: 10.1038/nmat2301.

CamGrid — IT Help and Support (2018). Available at: https://help.uis.cam.ac.uk/service/supporting-research/research-support/camgrid/camgrid (Accessed: 29 June 2018).

Catti, M. *et al.* (1995) 'Static compression and H disorder in brucite, $Mg(OH)_2$, to 11 GPa: a powder neutron diffraction study', *Physics and Chemistry of Minerals*. Springer-Verlag, 22(3), pp. 200–206. doi: 10.1007/BF00202300.

Change, D. of E. & C. (2014) *Implementing Geological Disposal*.

Clark, S. J. *et al.* (2005) 'First principles methods using CASTEP', *Zeitschrift für Kristallographie - Crystalline Materials*, 220(5/6). doi: 10.1524/zkri.220.5.567.65075.

Cochran, M. A. *et al.* (1988) 'Tensile bond strengths of five porcelain repair systems.', *Operative dentistry*. Academic Press, 13(4), pp. 162–167. doi: 10.1016/j.jmr.2008.03.001.

Cochran, R. G. and Tsoulfanidis, N. (1999) *The nuclear fuel cycle : analysis and management*. American Nuclear Society.

Collin, M. *et al.* (2018) 'Structure of International Simple Glass and properties of passivating layer formed in circumneutral pH conditions', *npj Materials Degradation*. Springer US, 2(1), p. 4. doi: 10.1038/s41529-017-0025-y.

Conradt, R. (2008) 'Chemical durability of oxide glasses in aqueous solutions: A review', *Journal of the American Ceramic Society*. John Wiley & Sons, Ltd (10.1111), 91(3), pp. 728–735. doi: 10.1111/j.1551-2916.2007.02101.x.

Cormier, G., Capobianco, J. A. and Monteil, A. (1993) 'Molecular dynamics simulation of the trivalent europium ion doped in silica and sodium disilicate glasses', *Journal of Non-Crystalline Solids*, 152(2–3), pp. 225–236. doi: 10.1016/0022-3093(93)90256-W.

Curti, E. *et al.* (2006) 'Long-term corrosion of two nuclear waste reference glasses (MW and SON68): A kinetic and mineral alteration study', *Applied Geochemistry*, 21(7), pp. 1152–1168. doi: 10.1016/j.apgeochem.2006.03.010.

d'Espinose de Lacaillerie, J.-B., Fretigny, C. and Massiot, D. (2008) 'MAS NMR spectra of quadrupolar nuclei in disordered solids: The Czjzek model', *Journal of Magnetic Resonance*. Academic Press, 192(2), pp. 244–251. doi: 10.1016/J.JMR.2008.03.001.

Daval, D. *et al.* (2013) 'Linking nm-scale measurements of the anisotropy of silicate surface reactivity to macroscopic dissolution rate laws: New insights based on diopside', *Geochimica et Cosmochimica Acta*. Pergamon, 107, pp. 121–134. doi: 10.1016/j.gca.2012.12.045.

Davis, M. C. *et al.* (2009) 'Magnesium silicate dissolution investigated by ^{29}Si MAS,^{1}H-^{29}Si CPMAS, ^{25}Mg QCPMG, and ^{1}H-^{25}Mg CP QCPMG NMR', *Physical Chemistry Chemical Physics*. The Royal Society of Chemistry, 11(32), pp. 7013–7021. doi: 10.1039/b907494e.

Debure, M. *et al.* (2012) 'Borosilicate glass alteration driven by magnesium carbonates', *Journal of Nuclear Materials*. North-Holland, 420(1–3), pp. 347–361. doi: 10.1016/j.jnucmat.2011.09.032.

Dickin, A. P. (1981) 'Hydrothermal leaching of rhyolite glass in the environment has implications for nuclear waste disposal', *Nature*. Nature Publishing Group, 294(5839), pp. 342–347. doi: 10.1038/294342a0.

Donald, I. W., Metcalfe, B. L. and Taylor, R. N. J. (1997) 'The immobilization of high level

radioactive wastes using ceramics and glasses', *Journal of Materials Science*, pp. 5851–5887. doi: 10.1023/A:1018646507438.

Du, J. and Cormack, A. N. (2005) 'The structure of erbium doped sodium silicate glasses', *Journal of Non-Crystalline Solids*, 351(27–29), pp. 2263–2276. doi: 10.1016/j.jnoncrysol.2005.05.018.

Duer, M. J. (ed.) (2001) *Solid-State NMR Spectroscopy Principles and Applications*. Oxford, UK: Blackwell Science Ltd. doi: 10.1002/9780470999394.

Van Eck, E. R. H., Smith, M. E. and Kohn, S. C. (1999) 'Observation of hydroxyl groups by ^{17}O solid-state multiple quantum MAS NMR in sol-gel-produced silica', *Solid State Nuclear Magnetic Resonance*, 15(3), pp. 181–188. doi: 10.1016/S0926-2040(99)00055-7.

Eckert, H. *et al.* (1988) 'Water in silicate glasses: quantitation and structural studies by proton solid echo and magic angle spinning NMR methods', *The Journal of Physical Chemistry*, 92(7), pp. 2055–2064. doi: 10.1021/j100318a070.

Farnan, I. (1997) 'Oxygen bridges in molten glass', *Nature*, 390 (November), pp. 14–15.

Fenzke, D. *et al.* (1984) 'NMR intensity measurements of half-integer quadrupole nuclei', *Chemical Physics Letters*, 111(1–2), pp. 171–175. doi: 10.1016/0009-2614(84)80458-3.

Fernandez, C. and Amoureux, J. P. (1996) 'Triple-quantum MAS-NMR of quadrupolar nuclei', *Solid State Nuclear Magnetic Resonance*. Academic Press, 5(4), pp. 315–321. doi: 10.1016/0926-2040(95)01197-8.

Ferrand, K., Abdelouas, A. and Grambow, B. (2006) 'Water diffusion in the simulated French nuclear waste glass SON 68 contacting silica rich solutions: Experimental and modeling', *Journal of Nuclear Materials*. North-Holland, 355(1–3), pp. 54–67. doi: 10.1016/j.jnucmat.2006.04.005.

Filgueiras, M. R. T., La Torre, G. and Hench, L. L. (1993) 'Solution effects on the surface reactions of three bioactive glass compositions', *Journal of Biomedical Materials Research*, 27(12), pp. 1485–1493. doi: 10.1002/jbm.820271204.

Fleury, B. *et al.* (2013) 'SON68 glass dissolution driven by magnesium silicate precipitation', *Journal of Nuclear Materials*. North-Holland, 442(1–3), pp. 17–28. doi: 10.1016/J.JNUCMAT.2013.08.029.

Fournier, M. *et al.* (2016) 'Glass dissolution rate measurement and calculation revisited', *Journal of Nuclear Materials*. North-Holland, 476, pp. 140–154. doi: 10.1016/j.jnucmat.2016.04.028.

Freude, D. and Haase, J. (1993) 'Quadrupole Effects in Solid-State Nuclear Magnetic Resonance', in *NMR Basic Principles and Progress*. Springer, Berlin, Heidelberg, pp. 1–90. doi: 10.1007/978-3-642-50046-6_1.

Frugier, P. *et al.* (2005) 'The effect of composition on the leaching of three nuclear waste glasses: R7T7, AVM and VRZ', *Journal of Nuclear Materials*, 346(2–3), pp. 194–207. doi: 10.1016/j.jnucmat.2005.06.023.

Frydman, L. and Harwood, J. S. (1995) 'Isotropic Spectra of Half-Integer Quadrupolar Spins from Bidimensional Magic-Angle Spinning NMR', *Journal of the American Chemical Society*, 117(19), pp. 5367–5368. doi: 10.1021/ja00124a023.

Fujino, K. *et al.* (1981) 'X-ray determination of electron distributions in forsterite, fayalite and tephroite', *Acta Crystallographica Section B: Structural Crystallography and Crystal Chemistry*. International Union of Crystallography, 37(3), pp. 513–518. doi: 10.1107/S0567740881003506.

Fukushima, E. and Boden, N. (1982) *Experimental pulse NMR: A nuts and bolts approach, Biochemical Education*. Addison-Wesley Pub. Co., Advanced Book Program. doi: 10.1016/0307-4412(82)90186-8.

Geisler, T. *et al.* (2010) 'Aqueous corrosion of borosilicate glass under acidic conditions: A new corrosion mechanism', *Journal of Non-Crystalline Solids*. Elsevier B.V., 356(28–30), pp. 1458–1465. doi: 10.1016/j.jnoncrysol.2010.04.033.

Geisler, T. *et al.* (2015) 'The mechanism of borosilicate glass corrosion revisited', *Geochimica et Cosmochimica Acta*. Pergamon, 158, pp. 112–129. doi: 10.1016/J.GCA.2015.02.039.

Geissberger, A. E. and Bray, P. J. (1983) 'Determinations of structure and bonding in amorphous SiO_2 using ^{17}O NMR', *Journal of Non-Crystalline Solids*. North-Holland, 54(1–2), pp. 121–137. doi: 10.1016/0022-3093(83)90087-X.

Gin, S. *et al.* (2011) 'Nuclear glass durability: New insight into alteration layer properties', *Journal of Physical Chemistry C*, 115(38), pp. 18696–18706. doi: 10.1021/jp205477q.

Gin, S. *et al.* (2012) ‘Effect of composition on the short-term and long-term dissolution rates of ten borosilicate glasses of increasing complexity from 3 to 30 oxides’, *Journal of Non-Crystalline Solids*. North-Holland, 358(18–19), pp. 2559–2570. doi: 10.1016/J.JNONCRYSOL.2012.05.024.

Gin, S., Abdelouas, A., *et al.* (2013) ‘An international initiative on long-term behavior of high-level nuclear waste glass’, *Materials Today*. Elsevier Ltd., 16(6), pp. 243–248. doi: 10.1016/j.mattod.2013.06.008.

Gin, S., Ryan, J. V., *et al.* (2013) ‘Contribution of atom-probe tomography to a better understanding of glass alteration mechanisms: Application to a nuclear glass specimen altered 25 years in a granitic environment’, *Chemical Geology*. Elsevier B.V., 349–350, pp. 99–109. doi: 10.1016/j.chemgeo.2013.04.001.

Gin, S., Jollivet, P., Fournier, M., Angeli, F., *et al.* (2015) ‘Origin and consequences of silicate glass passivation by surface layers’, *Nature Communications*, 6. doi: 10.1038/ncomms7360.

Gin, S., Jollivet, P., Fournier, M., Berthon, C., *et al.* (2015a) ‘The fate of silicon during glass corrosion under alkaline conditions: A mechanistic and kinetic study with the International Simple Glass’, *Geochimica et Cosmochimica Acta*, 151, pp. 68–85. doi: 10.1016/j.gca.2014.12.009.

Gin, S., Jollivet, P., Fournier, M., Berthon, C., *et al.* (2015b) ‘The fate of silicon during glass corrosion under alkaline conditions: A mechanistic and kinetic study with the International Simple Glass’, *Geochimica et Cosmochimica Acta*. Pergamon, 151, pp. 68–85. doi: 10.1016/j.gca.2014.12.009.

Gin, S. *et al.* (2016) ‘The controversial role of inter-diffusion in glass alteration’, *Chemical Geology*, 440, pp. 115–123. doi: 10.1016/j.chemgeo.2016.07.014.

Gin, S. *et al.* (2017) ‘Atom-Probe Tomography, TEM and ToF-SIMS study of borosilicate glass alteration rim: A multiscale approach to investigating rate-limiting mechanisms’, *Geochimica et Cosmochimica Acta*, 202, pp. 57–76. doi: 10.1016/j.gca.2016.12.029.

Gin, S., Ribet, I. and Couillard, M. (2001) ‘Role and properties of the gel formed during nuclear glass alteration: Importance of gel formation conditions’, *Journal of Nuclear Materials*, 298(1–2), pp. 1–10. doi: 10.1016/S0022-3115(01)00573-6.

Grambow, B. (2006) ‘Nuclear Waste Glasses’, *Elements*, 2, pp. 357–364. doi: 10.1016/B978-0-12-341826-5.50007-7.

Griffin, J. M. *et al.* (2009) ‘Solid-state ^{17}O NMR spectroscopy of hydrous magnesium silicates: Evidence for proton dynamics’, *Journal of Physical Chemistry C*, 113(1), pp. 465–471. doi: 10.1021/jp808651x.

Guo, R. *et al.* (2018) ‘The effect of magnesium on the local structure and initial dissolution rate of simplified UK Magnox waste glasses’, *Journal of Non-Crystalline Solids*. North-Holland, 497, pp. 82–92. doi: 10.1016/J.JNONCRYSOL.2018.03.002.

Haeberlen, U. (1976) *High resolution NMR in solids : selective averaging*. Academic Press.

Hahn, E. L. (1950) ‘Spin echoes’, *Physical Review*. American Physical Society, 80(4), pp. 580–594. doi: 10.1103/PhysRev.80.580.

Harder, H. (1972) ‘The role of magnesium in the formation of smectite minerals’, *Chemical Geology*. Elsevier, 10(1), pp. 31–39. doi: 10.1016/0009-2541(72)90075-7.

Harrison, M. T. (2014) ‘The Effect of Composition on Short- and Long-term Durability of UK HLW Glass’, *Procedia Materials Science*. Elsevier, 7, pp. 186–192. doi: 10.1016/j.mspro.2014.10.025.

Harrison, M. T. (2014) ‘Vitrification of High Level Waste in the UK’, *Procedia Materials Science*, 7, pp. 10–15. doi: 10.1016/j.mspro.2014.10.003.

Hartmann, S. R. and Hahn, E. L. (1962) ‘Nuclear double resonance in the rotating frame’, *Physical Review*, 128(5), pp. 2042–2053. doi: 10.1103/PhysRev.128.2042.

Hayashi, S. and Hayamizu, K. (1991) ‘Chemical-Shift Standards in High-Resolution Solid-State Nmr (1) ^{13}C, ^{29}Si and ^{1}H Nuclei’, *Bull. Chem. Soc. Jpn.* The Chemical Society of Japan, pp. 685–687. doi: 10.1246/bcsj.64.685.

Hazen, R. M. (1976) ‘Effects of temperature and pressure on the crystal structure of forsterite’, *American Mineralogist*, 61, pp. 1280–1293.

Hellmann, R. *et al.* (2012) ‘Unifying natural and laboratory chemical weathering with interfacial dissolution-reprecipitation: A study based on the nanometer-scale chemistry of fluid-silicate interfaces’, *Chemical Geology*. Elsevier, 294–295, pp. 203–216. doi: 10.1016/j.chemgeo.2011.12.002.

Hellmann, R. *et al.* (2015) 'Nanometre-scale evidence for interfacial dissolution-reprecipitation control of silicate glass corrosion', *Nature Materials*, 14(3), pp. 307–311. doi: 10.1038/nmat4172.

HTCondor - Home (2018). Available at: https://research.cs.wisc.edu/htcondor/ (Accessed: 8 August 2018).

Huggett, J. M. (2015) 'Clay Minerals', *Reference Module in Earth Systems and Environmental Sciences*. Elsevier. doi: 10.1016/B978-0-12-409548-9.09519-1.

IAEA (2009) 'IAEA Safety Standards: Classification of Radioactive Waste - No. GSG-1', *General Safety Guide IAEA*, p. 68. doi: ISBN:978-92-0-109209-0.

Van Iseghem, P. *et al.* (2006) 'Chemical durability of high-level waste glass in repository environment: Main conclusions and remaining uncertainties from the GLASTAB and GLAMOR projects', in *Scientific Basis for Nuclear Waste Management XXIX*. Cambridge University Press, pp. 293–304. doi: 10.1557/PROC-932-95.1.

Van Iseghem, P. *et al.* (2009) 'Glamor - or how we achieved a common understanding on the decrease of glass dissolution kinetics', in *Ceramic Transactions*. John Wiley & Sons, Ltd, pp. 115–126. doi: 10.1002/9780470538371.ch12.

Iwalewa, T. M., Qu, T. and Farnan, I. (2017) 'Investigation of the maximum dissolution rates and temperature dependence of a simulated UK nuclear waste glass in circum-neutral media at 40 and 90°C in a dynamic system', *Applied Geochemistry*, 82, pp. 177–190. doi: 10.1016/j.apgeochem.2017.05.018.

Jäger, C. *et al.* (1993) '^{17}O satellite transition spectroscopy of amorphous SiO_2', *Journal of Non-Crystalline Solids*. North-Holland, 155(1), pp. 95–98. doi: 10.1016/0022-3093(93)90476-E.

Jégou, C., Gin, S. and Larché, F. (2000) 'Alteration kinetics of a simplified nuclear glass in an aqueous medium: Effects of solution chemistry and of protective gel properties on diminishing the alteration rate', *Journal of Nuclear Materials*, 280(2), pp. 216–229. doi: 10.1016/S0022-3115(00)00039-8.

Jollivet, P. *et al.* (2012) 'Effect of clayey groundwater on the dissolution rate of the simulated nuclear waste glass SON68', *Journal of Nuclear Materials*. North-Holland, 420(1–3), pp. 508–518. doi: 10.1016/j.jnucmat.2011.10.026.

Jollivet, P., Gin, S. and Schumacher, S. (2012) ‘Forward dissolution rate of silicate glasses of nuclear interest in clay-equilibrated groundwater’, *Chemical Geology*. Elsevier, 330–331, pp. 207–217. doi: 10.1016/j.chemgeo.2012.09.012.

Kentgens, A. P. M. and Verhagen, R. (1999) ‘Advantages of double frequency sweeps in static, MAS and MQMAS NMR of spin I=3/2 nuclei’, *Chemical Physics Letters*, 300(3–4), pp. 435–443. doi: 10.1016/S0009-2614(98)01402-X.

Kirkpatrick, R. J. *et al.* (1986) ‘Magic-Angle Sample-Spinning Nuclear Magnetic Resonance Spectroscopy of Silicate Glasses: A Review’, in *Structure and Bonding in Noncrystalline Solids*. Boston, MA: Springer US, pp. 303–327. doi: 10.1007/978-1-4615-9477-2_16.

Kohanoff, J. (2006) *Electronic structure calculations for solids and molecules: Theory and computational methods, Electronic Structure Calculations for Solids and Molecules: Theory and Computational Methods*. Cambridge University Press. doi: 10.1017/CBO9780511755613.

Kohn, S. C., Dupree, R. and Smith, M. E. (1989) ‘Proton environments and hydrogen-bonding in hydrous silicate glasses from proton NMR’, *Nature*. Nature Publishing Group, 337(6207), pp. 539–541. doi: 10.1038/337539a0.

Kohn, W. and Sham, L. J. (1965) ‘Self-consistent equations including exchange and correlation effects’, *Physical Review*, 140(4A). doi: 10.1103/PhysRev.140.A1133.

Kroeker, S. and Stebbins, J. F. (2000) ‘Magnesium coordination environments in glasses and minerals: New insight from high-field magnesium-25 MAS NMR’, *American Mineralogist*, 85(10), pp. 1459–1464. doi: 10.2138/am-2000-1015.

Kump, L. R., Brantley, S. L. and Arthur (2013) ‘Chemical Weathering, Atmospheric CO_2, and Climate’, *Annual Review of Earth and Planetary Sciences*, 28(1), pp. 611–667. doi: 10.1146/annurev.earth.28.1.611.

Kuryaeva, R. G. (2009) ‘The state of magnesium in silicate glasses and melts’, *Glass Physics and Chemistry*. SP MAIK Nauka/Interperiodica, 35(4), pp. 378–383. doi: 10.1134/S1087659609040051.

Lefebvre, F. *et al.* (1987) ‘Investigation of variable angle sample spinning (VASS) NMR of quadrupolar nuclei. I. Theory’, *The Journal of Chemical Physics*. American Institute of Physics, 86(11), pp. 6070–6076. doi: 10.1063/1.452446.

Lemmens, K. (2001) ‘The effect of clay on the dissolution of nuclear waste glass’, *Journal of Nuclear Materials*. North-Holland, 298(1–2), pp. 11–18. doi: 10.1016/S0022-3115(01)00590-6.

Lutze, W. *et al.* (1985) ‘Alteration of basalt glasses: Implications for modelling the long-term stability of nuclear waste glasses’, *Nature*. Nature Publishing Group, 314(6008), pp. 252–255. doi: 10.1038/314252a0.

Maciel, G. E. and Sindorf, D. W. (1980) ‘Silicon-29 NMR study of the surface of silica gel by cross polarization and magic-angle spinning’, *Journal of the American Chemical Society*. American Chemical Society, 102(25), pp. 7606–7607. doi: 10.1021/ja00545a056.

Mackenzie, K. J. D. and Meinhold, R. H. (1994) ‘^{25}Mg nuclear magnetic resonance spectroscopy of minerals and related inorganics: a survey study’, *American Mineralogist*, 79(3–4), pp. 250–260.

MacKenzie, K. J. D. and Smith, M. E. (2002) *Multinuclear solid-state NMR of inorganic materials*. Pergamon.

Mägi, M. *et al.* (1984) ‘Solid-state high-resolution silicon-29 chemical shifts in silicates’, *Journal of Physical Chemistry*, 88(8), pp. 1518–1522. doi: 10.1021/j150652a015.

Man, P. P. (1998) ‘Scaling and labeling the high-resolution isotropic axis of two-dimensional multiple-quantum magic-angle-spinning spectra of half-integer quadrupole spins’, *Physical Review B - Condensed Matter and Materials Physics*, 58(5), pp. 2764–2782. doi: 10.1103/PhysRevB.58.2764.

Man, P. P. (2006) ‘Quadrupole Couplings in Nuclear Magnetic Resonance, General’, *Encyclopedia of Analytical Chemistry*, pp. 12224–12265. doi: 10.1002/9780470027318.a6111.

Maricq, M. M. and Waugh, J. S. (1979) ‘NMR in rotating solids’, *The Journal of Chemical Physics*, 70(7), pp. 3300–3316. doi: 10.1063/1.437915.

Massiot, D. (1996) ‘Sensitivity and lineshape improvements of MQ-MAS by rotor-synchronized data acquisition’, *Journal of Magnetic Resonance - Series A*, 122(2), pp. 240–244. doi: 10.1006/jmra.1996.0202.

Massiot, D. *et al.* (1996) ‘Two-dimensional magic-angle spinning isotropic reconstruction sequences for quadrupolar nuclei’, *Solid State Nuclear Magnetic Resonance*, 6(1), pp. 73–83.

doi: 10.1016/0926-2040(95)01210-9.

Massiot, D. *et al.* (2002) ‘Modelling one- and two-dimensional solid-state NMR spectra’, *Magnetic Resonance in Chemistry*, 40(1), pp. 70–76. doi: 10.1002/mrc.984.

Mehring, M. (1983) *Principles of High Resolution NMR in Solids*. Berlin, Heidelberg: Springer Berlin Heidelberg. doi: 10.1007/978-3-642-68756-3.

Millot, Y. and Man, P. P. (2002) ‘Procedures for labeling the high-resolution axis of two-dimensional MQ-MAS NMR spectra of half-integer quadrupole spins’, *Solid State Nuclear Magnetic Resonance*, 21(1–2), pp. 21–43. doi: 10.1006/snmr.2001.0043.

Molières, E. *et al.* (2014) ‘Investigation of local environment around rare earths (La and Eu) by fluorescence line narrowing during borosilicate glass alteration’, *Journal of Luminescence*. Elsevier, 145, pp. 213–218. doi: 10.1016/j.jlumin.2013.07.051.

Monkhorst, H. J. and Pack, J. D. (1976) ‘Special points for Brillouin-zone integrations’, *Physical Review B*. American Physical Society, 13(12), pp. 5188–5192. doi: 10.1103/PhysRevB.13.5188.

Moran, R. F., Dawson, D. M. and Ashbrook, S. E. (2017) ‘Exploiting NMR spectroscopy for the study of disorder in solids’, *International Reviews in Physical Chemistry*. Taylor & Francis, 36(1), pp. 39–115. doi: 10.1080/0144235X.2017.1256604.

Morin, E. I., Wu, J. and Stebbins, J. F. (2014) ‘Modifier cation (Ba, Ca, La, Y) field strength effects on aluminum and boron coordination in aluminoborosilicate glasses: The roles of fictive temperature and boron content’, *Applied Physics A: Materials Science and Processing*. Springer Berlin Heidelberg, 116(2), pp. 479–490. doi: 10.1007/s00339-014-8369-4.

NDA (2016) *Geological Disposal: Generic Post-closure Safety Assessment, NDA Report*.

Neuville, D. R., Cormier, L. and Massiot, D. (2004) ‘Al environment in tectosilicate and peraluminous glasses: A ^{27}Al MQ-MAS NMR, Raman, and XANES investigation’, *Geochimica et Cosmochimica Acta*. Pergamon, 68(24), pp. 5071–5079. doi: 10.1016/j.gca.2004.05.048.

Nirex (2005) *Outline Design for a Reference Repository Concept for UK High Level Waste/Spent Fuel*.

NIST (2018) *Thermophysical Properties of Fluid Systems*. Available at:

https://webbook.nist.gov/chemistry/fluid/ (Accessed: 28 January 2019).

O'Neil, J. R. (1986) 'THEORETICAL AND EXPERIMENTAL ASPECTS OF ISOTOPIC FRACTIONATION.', *Reviews in Mineralogy*, 16, pp. 1–40.

Ojovan, M. I. and Lee, W. E. (2005) *An Introduction to Nuclear Waste Immobilisation*. Elsevier. doi: 10.1016/B978-008044462-8/50008-9.

Pallister, P. J., Moudrakovski, I. L. and Ripmeester, J. A. (2009) 'Mg-25 ultra-high field solid state NMR spectroscopy and first principles calculations of magnesium compounds', *Physical Chemistry Chemical Physics*, 11(48), pp. 11487–11500. doi: 10.1039/b916076k.

Pedone, A. *et al.* (2008) 'Role of magnesium in soda-lime glasses: Insight into structural, transport, and mechanical properties through computer simulations', *Journal of Physical Chemistry C*. American Chemical Society, 112(29), pp. 11034–11041. doi: 10.1021/jp8016776.

Perdew, J. P., Burke, K. and Ernzerhof, M. (1996) 'Generalized gradient approximation made simple', *Physical Review Letters*, 77(18), pp. 3865–3868. doi: 10.1103/PhysRevLett.77.3865.

Pfrommer, B. G. *et al.* (1997) 'Relaxation of crystals with the quasi-Newton method', *J. Comput. Phys.*, 131, pp. 233–240.

Phillips, B. L. *et al.* (1997) '^{29}Si and ^{1}H NMR spectroscopy of high-pressure hydrous magnesium silicates', *Physics and Chemistry of Minerals*. Springer-Verlag, 24(3), pp. 179–190. doi: 10.1007/s002690050031.

Pickard, C. J. and Mauri, F. (2001) 'All-electron magnetic response with pseudopotentials: NMR chemical shifts', *Physical Review B*, 63, pp. 1–13. doi: 10.1103/PhysRevB.63.245101.

Pines, A., Gibby, M. G. and Waugh, J. S. (1973) 'Proton-enhanced NMR of dilute spins in solids', *The Journal of Chemical Physics*. American Institute of Physics, 59(2), pp. 569–590. doi: 10.1063/1.1680061.

Profeta, M. *et al.* (2002) 'Accurate first principles prediction of ^{17}O NMR parameters in SiO_2: Assignment of the zeolite ferrierite spectrum', *Journal of the American Chemical Society*. American Chemical Society, 125(2), pp. 541–548. doi: 10.1021/ja027124r.

Putnis, A. (2014) 'Why mineral interfaces matter', *Science*, 343(6178), pp. 1441–1442. doi: 10.1126/science.1250884.

Rayner, J. H. and Brown, G. (1973) 'THE CRYSTAL STRUCTURE OF TALC', *Clays and Clay Minerals*. PergamonPress. PrintedinGreatBritain, 21, pp. 103–114.

Ruiz-Agudo, E. *et al.* (2016) 'Control of silicate weathering by interface-coupled dissolution-precipitation processes at the mineral-solution interface', *Geology*, 44(7), pp. 567–570. doi: 10.1130/G37856.1.

Rumble, J. R. (2018) *CRC handbook of chemistry and physics : a ready-reference book of chemical and physical data.* Available at: https://www.crcpress.com/CRC-Handbook-of-Chemistry-and-Physics-99th-Edition/Rumble/p/book/9781138561632 (Accessed: 22 August 2018).

Schaller, T. and Stebbins, J. F. (1998) 'The Structural Role of Lanthanum and Yttrium in Aluminosilicate Glasses: A ^{27}Al and ^{17}O MAS NMR Study', *The Journal of Physical Chemistry B*, 102(52), pp. 10690–10697. doi: 10.1021/jp982387m.

Scheetz, B. E. *et al.* (1984) 'The Role of Boron in Monitoring the Leaching of Borosilicate Glass Waste Forms', *MRS Proceedings*. Cambridge University Press, 44, p. 129. doi: 10.1557/PROC-44-129.

Schmelz, C. E. and Stebbins, J. F. (1993) 'Gel synthesis of an albite ($NaAlSi_3O_8$) glass: An NMR analysis', *Geochimica et Cosmochimica Acta*. Pergamon, 57(16), pp. 3949–3960. doi: 10.1016/0016-7037(93)90345-W.

Schofield, J. M. *et al.* (2016) *Experimental studies of the chemical durability of UK HLW and ILW glasses, AMEC/103498/03 Issue 1*. Available at: https://rwm.nda.gov.uk/publication/experimental-studies-of-the-chemical-durability-of-uk-hlw-and-ilw-glasses-interim-progress-report-amec103498ipr02-revision-3/.

Scholze, H. (1988) 'Glass-water interactions', *Journal of Non-Crystalline Solids*. North-Holland, 102(1–3), pp. 1–10. doi: 10.1016/0022-3093(88)90105-6.

Sears, R. E. J., Kaliaperumal, R. and Manogaran, S. (1988) '^{1}H shielding anisotropy in $Mg(OH)_2$: The isolated OH-group', *The Journal of Chemical Physics*, 88(4), pp. 2284–2288. doi: 10.1063/1.454062.

Segall, M. and Probert, M. (2002) 'First-Principles Simulation : Ideas , Illustrations and the CASTEP Code', *Journal of Physics: Condensed Matter*, 14(July 2015), pp. 2717–2744. doi: 10.1088/0953-8984/14/11/301.

Shannon, R. D. (1976) ‘Revised effective ionic radii and systematic studies of interatomic distances in halides and chalcogenides’, *Acta Crystallographica Section A*, 32(5), pp. 751–767. doi: 10.1107/S0567739476001551.

Shannon, R. D. and Prewitt, C. T. (1969) ‘Effective ionic radii in oxides and fluorides’, *Acta Crystallographica Section B Structural Crystallography and Crystal Chemistry*. International Union of Crystallography, 25(5), pp. 925–946. doi: 10.1107/S0567740869003220.

Shimoda, K. *et al.* (2007) ‘Structural investigation of Mg local environments in silicate glasses by ultra-high field ^{25}Mg 3QMAS NMR spectroscopy’, *American Mineralogist*, 92(4), pp. 695–698. doi: 10.2138/am.2007.2535.

Shimoda, K., Nemoto, T. and Saito, K. (2008) ‘Local structure of magnesium in silicate glasses: a ^{25}Mg 3QMAS NMR study.’, *The journal of physical chemistry. B*, 112(22), pp. 6747–6752. doi: 10.1021/jp711417t.

Sombret, C. G. (1993) ‘The Vitrification of High-Level Wastes in France: from the Lab to Industrial Plants’, in *BNS/OECD-NEA Symposium on the Safety of the Nuclear Fuel Cycle*. Available at: https://inis.iaea.org/collection/NCLCollectionStore/_Public/25/047/25047841.pdf (Accessed: 19 January 2019).

Spearing, D. R., Farnan, I. and Stebbins, J. F. (1992) ‘Dynamics of the α-β phase transitions in quartz and cristobalite as observed by in-situ high temperature ^{29}Si and ^{17}O NMR’, *Physics and Chemistry of Minerals*. Springer-Verlag, 19(5), pp. 307–321. doi: 10.1007/BF00204008.

Stebbins, J. F. *et al.* (2000) ‘Quantification of five- and six-coordinated aluminum ions in aluminosilicate and fluoride-containing glasses by high-field, high-resolution ^{27}Al NMR’, *Journal of Non-Crystalline Solids*. North-Holland, 275(1–2), pp. 1–6. doi: 10.1016/S0022-3093(00)00270-2.

Stebbins, J. F. (2007) ‘NMR Studies of Oxide Glass Structure’, in *Solid-State NMR Spectroscopy Principles and Applications*, pp. 391–436. doi: 10.1002/9780470999394.ch8.

Sternheimer, R. (1950) ‘On Nuclear Quadrupole Moments’, *Physical Review*. American Physical Society, 80(1), pp. 102–103. doi: 10.1103/PhysRev.80.102.2.

Studio, M. (2014) ‘CASTEP Guide’, *Materials Studio*. San Diego, pp. 1–219. doi: 10.1016/0020-7519(82)90051-0.

Sturniolo, S. *et al.* (2016) 'Visualization and processing of computed solid-state NMR parameters: MagresView and MagresPython', *Solid State Nuclear Magnetic Resonance*. Elsevier, 78, pp. 64–70. doi: 10.1016/j.ssnmr.2016.05.004.

Thien, B. *et al.* (2010) 'Structural identification of a trioctahedral smectite formed by the aqueous alteration of a nuclear glass', *Applied Clay Science*. Elsevier B.V., 49(3), pp. 135–141. doi: 10.1016/j.clay.2010.04.016.

Thien, B. M. J. *et al.* (2012) 'The dual effect of Mg on the long-term alteration rate of AVM nuclear waste glasses', *Journal of Nuclear Materials*. Elsevier B.V., 427(1–3), pp. 297–310. doi: 10.1016/j.jnucmat.2012.05.025.

Timken, H. K. C. *et al.* (1987) 'Solid-state oxygen-17 nuclear magnetic resonance spectroscopic studies of alkaline earth metasilicates', *The Journal of Physical Chemistry*. American Chemical Society , 91(5), pp. 1054–1058. doi: 10.1021/j100289a010.

Tournassat, C. *et al.* (2015) 'Surface Properties of Clay Minerals', in *Developments in Clay Science*. Elsevier, pp. 5–31. doi: 10.1016/B978-0-08-100027-4.00001-2.

Vega, A. J. (1992) 'CP/MAS of quadrupolar S = 3/2 nuclei', *Solid state nuclear magnetic resonance*, 1(1), pp. 17–32. doi: 10.1016/0926-2040(92)90006-U.

Vega, A. J. (2010) 'Quadrupolar Nuclei in Solids', in *Encyclopedia of Magnetic Resonance*. Chichester, UK: John Wiley & Sons, Ltd. doi: 10.1002/9780470034590.emrstm0431.pub2.

Vega, S. (1981) 'Multiple-quantum cross-polarization NMR on spin systems with I=1/2 and S=3/2 in solids', *Physical Review A*. American Physical Society, 23(6), pp. 3152–3173. doi: 10.1103/PhysRevA.23.3152.

Vernaz, E. *et al.* (2001) 'Present understanding of R7T7 glass alteration kinetics and their impact on long-term behavior modeling', *Journal of Nuclear Materials*. North-Holland, 298(1–2), pp. 27–36. doi: 10.1016/S0022-3115(01)00643-2.

Vienna, J. D. *et al.* (2013) 'Current understanding and remaining challenges in modeling long-term degradation of borosilicate nuclear waste glasses', *International Journal of Applied Glass Science*. John Wiley & Sons, Ltd (10.1111), 4(4), pp. 283–294. doi: 10.1111/ijag.12050.

Van De Walle, C. G. and Blöchl, P. E. (1993) 'First-principles calculations of hyperfine parameters', *Physical Review B*, 47(8), pp. 4244–4255. doi: 10.1103/PhysRevB.47.4244.

Walter, T. H., Turner, G. L. and Oldfield, E. (1988) 'Oxygen-17 cross-polarization nmr spectroscopy of inorganic solids', *Journal of Magnetic Resonance (1969)*. Academic Press, 76(1), pp. 106–120. doi: 10.1016/0022-2364(88)90205-3.

Wu, J. and Stebbins, J. F. (2009) 'Effects of cation field strength on the structure of aluminoborosilicate glasses: High-resolution ^{11}B, ^{27}Al and ^{23}Na MAS NMR', *Journal of Non-Crystalline Solids*. North-Holland, 355(9), pp. 556–562. doi: 10.1016/J.JNONCRYSOL.2009.01.025.

Xue, X. and Stebbins, J. F. (1993) '^{23}Na NMR chemical shifts and local Na coordination environments in silicate crystals, melts and glasses', *Physics and Chemistry of Minerals*. Springer-Verlag, 20(5), pp. 297–307. doi: 10.1007/BF00215100.

Yesinowski, J. P., Rossman, G. R. and Eckert, H. (1988) 'Characterization of hydrous species in minerals by high-speed ^{1}H MAS-NMR', *Journal of the American Chemical Society*, 110(5), pp. 1367–1375. doi: 10.1021/ja00213a007.

Zanazzi, P. F. *et al.* (2006) 'Structural effects of pressure on triclinic chlorite: A single-crystal study', *American Mineralogist*, 91(11–12), pp. 1871–1878. doi: 10.2138/am.2006.2191.

Zanazzi, P. F. *et al.* (2007) 'Structural effects of pressure on monoclinic chlorite: A single-crystal study', *American Mineralogist*, 92(4), pp. 655–661. doi: 10.2138/am.2007.2341.

Zarzycki, J. (Jorzy) (1991) *Glasses and the vitreous state*. Cambridge University Press. Available at: https://www.cambridge.org/gb/academic/subjects/engineering/materials-science/glasses-and-vitreous-state?format=HB&isbn=9780521355827 (Accessed: 23 January 2019).

Zeng, Q., Nekvasil, H. and Grey, C. P. (1999) 'Proton Environments in Hydrous Aluminosilicate Glasses: A ^{1}H MAS, ^{1}H/ ^{27}Al, and ^{1}H/ ^{23}Na TRAPDOR NMR Study', *The Journal of Physical Chemistry B*, 103(35), pp. 7406–7415. doi: 10.1021/jp990726l.

Zwicky, H. U. *et al.* (1988) 'Corrosion behaviour of British Magnox Waste Glass in Pure Water', *MRS Online Proceedings Library*. Cambridge University Press, 127, p. 129. doi: 10.15713/ins.mmj.3.

Appendices

Appendix I

^{11}B MAS NMR spectra of Mg75Ca25, Mg50Ca50, Mg25Ca75 and CaEM glasses with their respective fit and sub-components. Each fit is composed of four sub-components including one Quad 1st line, one Gaus/Lor line and two Q mas 1/2 lines available in the DMFIT programme.

Mg75Ca25

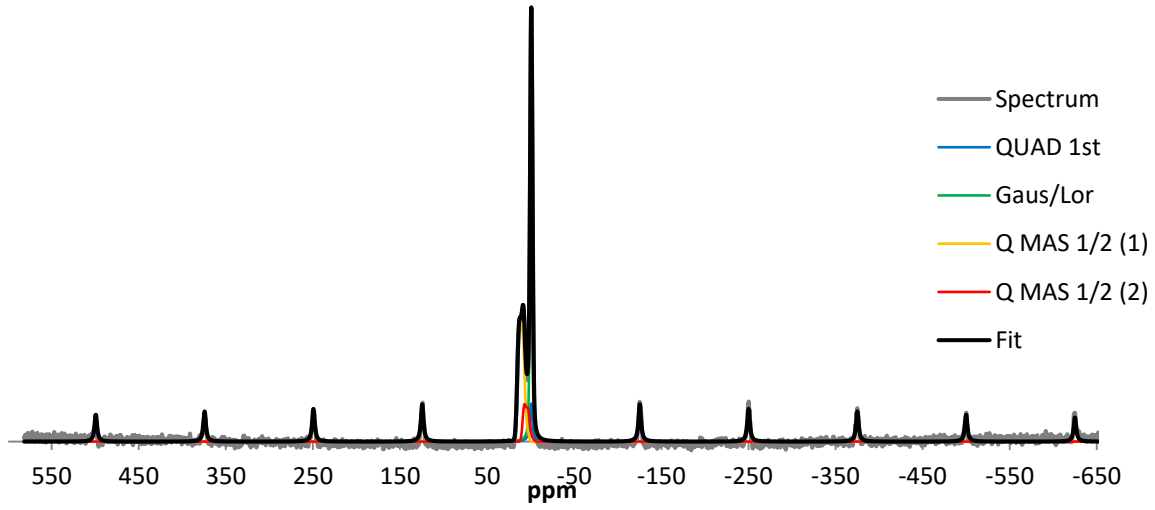

Mg50Ca50

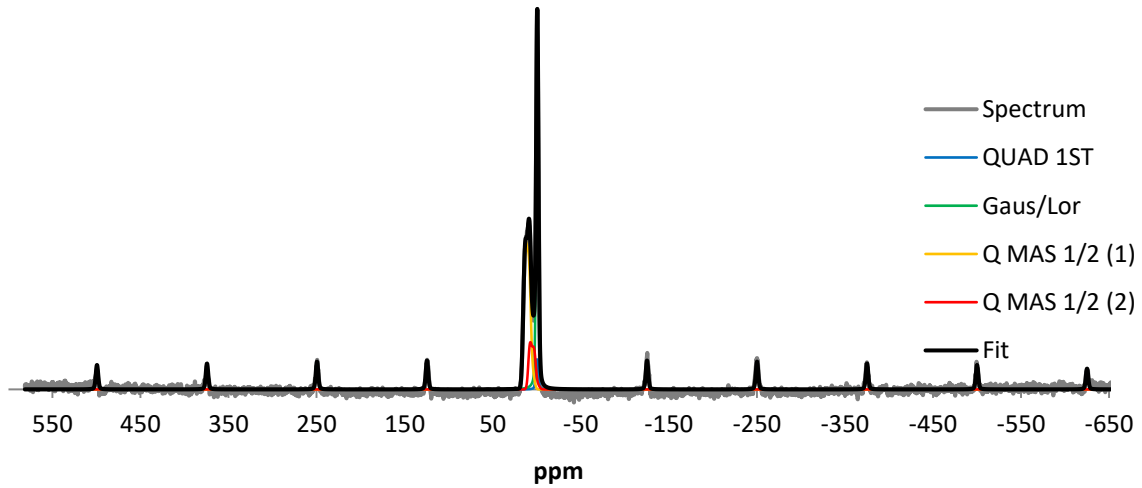

Mg25Ca75

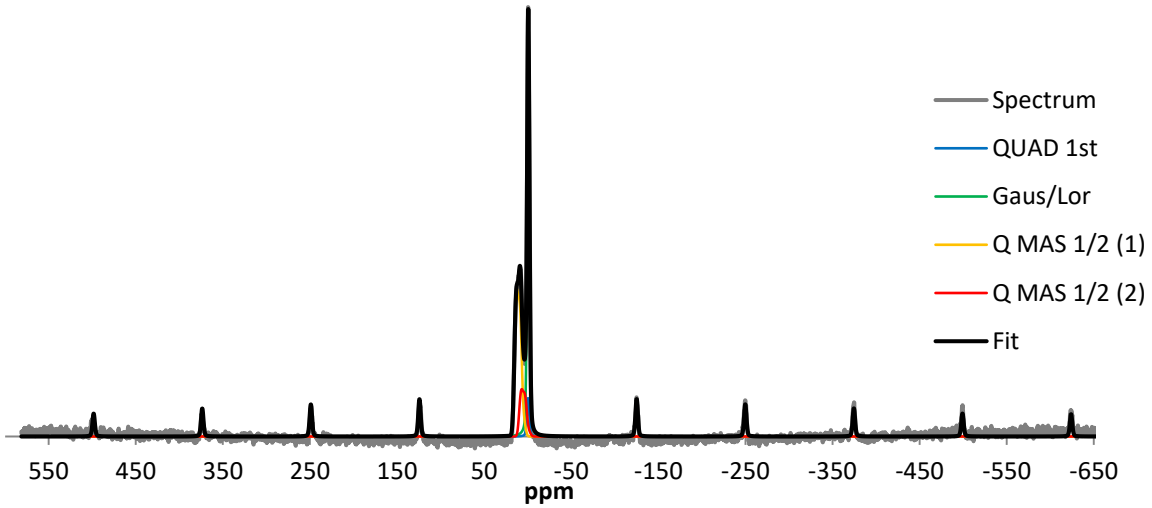

MgEM

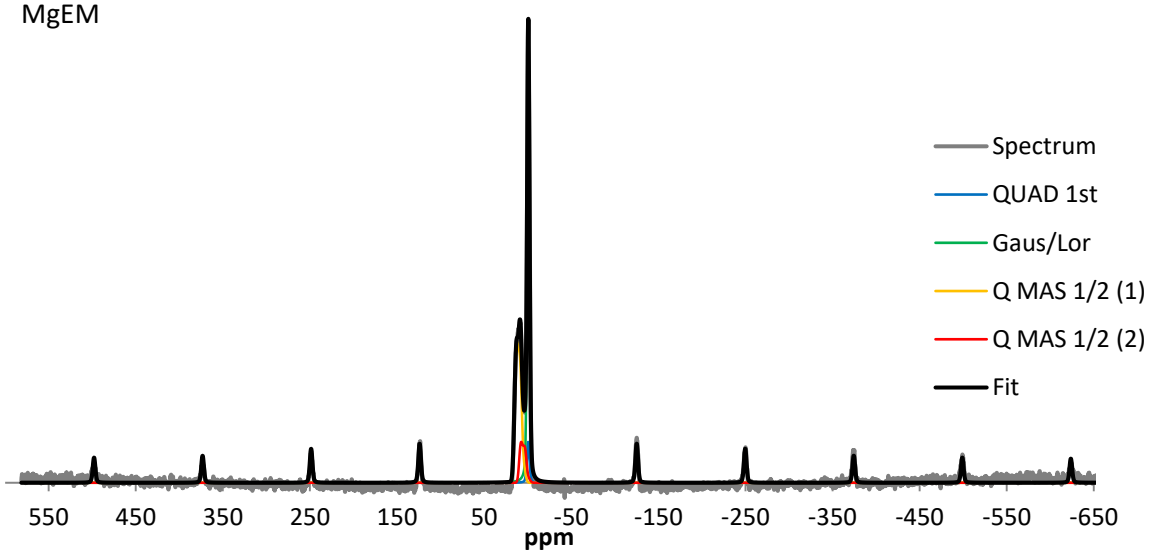

Appendix II

Curve fitting of the Mg50Ca50 and MgEM glasses ^{27}Al MAS NMR spectrum with 2 CzSimple lines available in the DMFIT programme: $^{[4]}$Al in dashed red and $^{[6]}$Al in dashed green. The grey line is the experimental spectrum while the superimposed overall fit is displayed in dashed black.

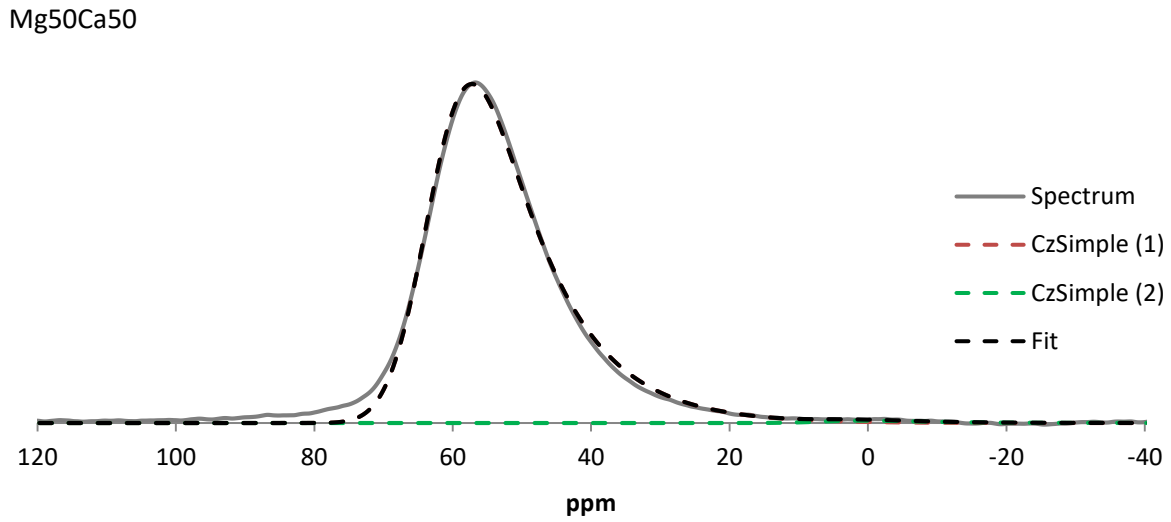

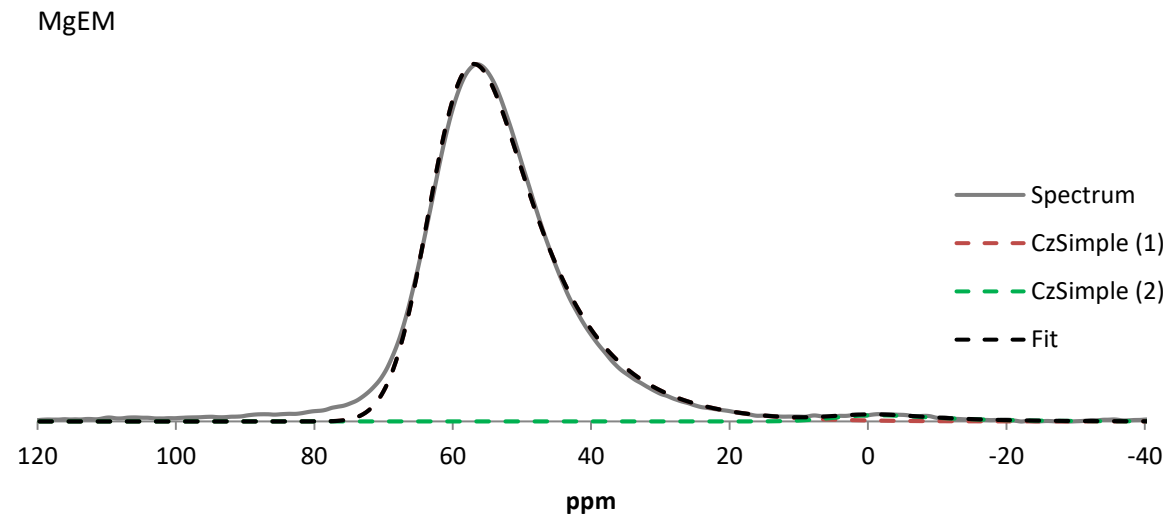

Appendix III

The isotropic projection of the 2D ^{17}O 3QMAS spectra of MgEM glass leached in ^{17}O-enriched water for 16 weeks shown in Figure 6-20.

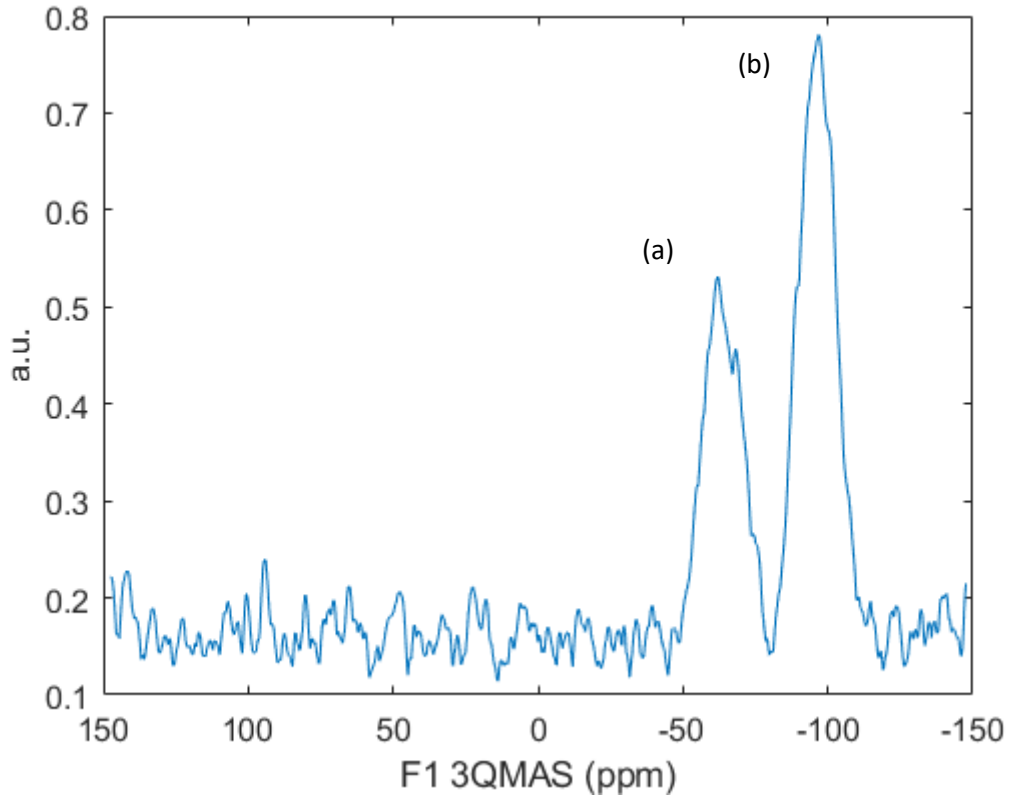

The anisotropic projection of the 2D ^{17}O 3QMAS spectra of MgEM glass leached in ^{17}O-enriched water for 16 weeks shown in Figure 6-20.

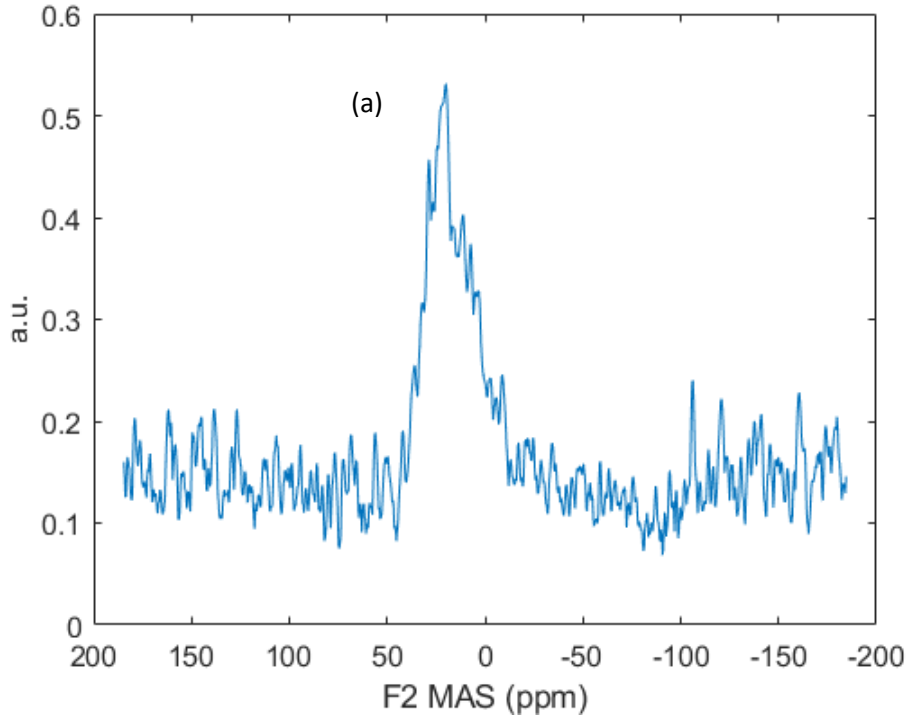
(a)
a.u.
0.6
0.5
0.4
0.3
0.2
0.1
0
200
150
100
50
0
-50
-100
-150
-200
F2 MAS (ppm)

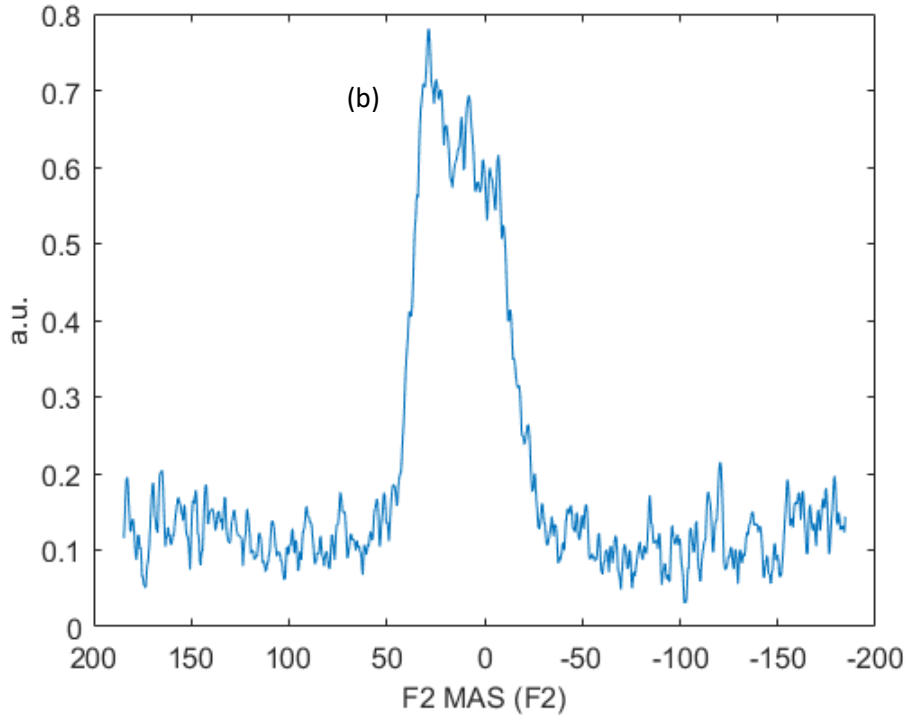
(b)
a.u.
0.8
0.7
0.6
0.5
0.4
0.3
0.2
0.1
0
200
150
100
50
0
-50
-100
-150
-200
F2 MAS (F2)

Appendix IV

The convergence test using total energy and stress as the criteria for brucite and two types of chlorite (see 7.2.1), with respect to the number (density) of the k-points in the first Brillouin zone.

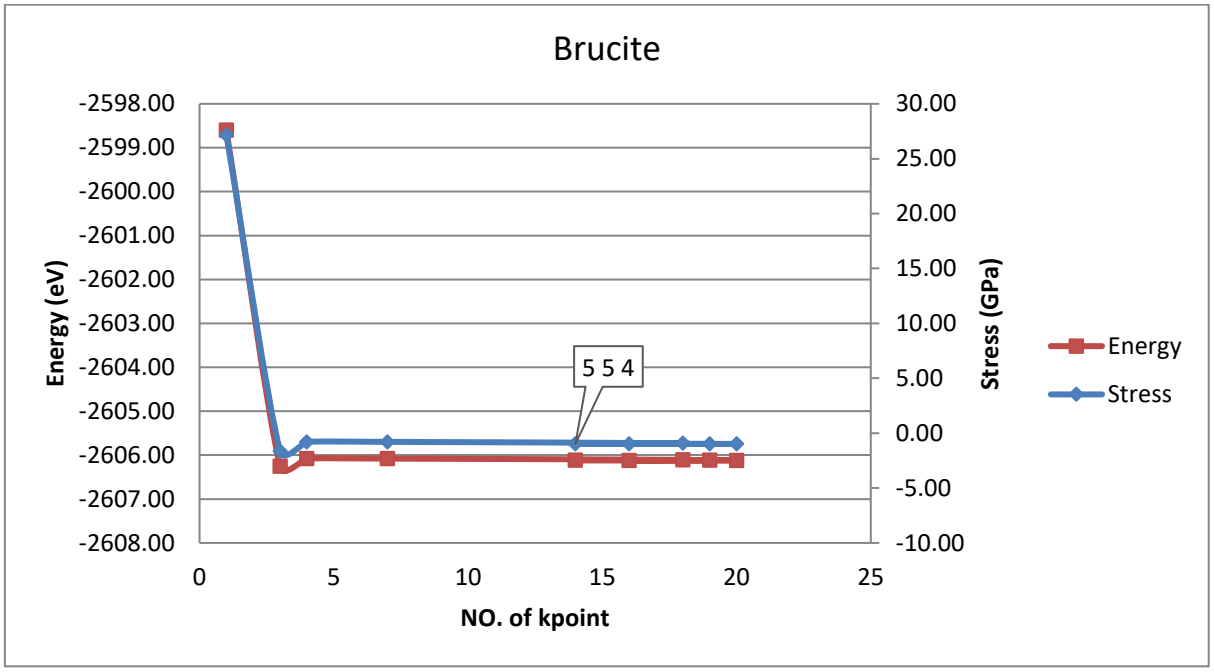

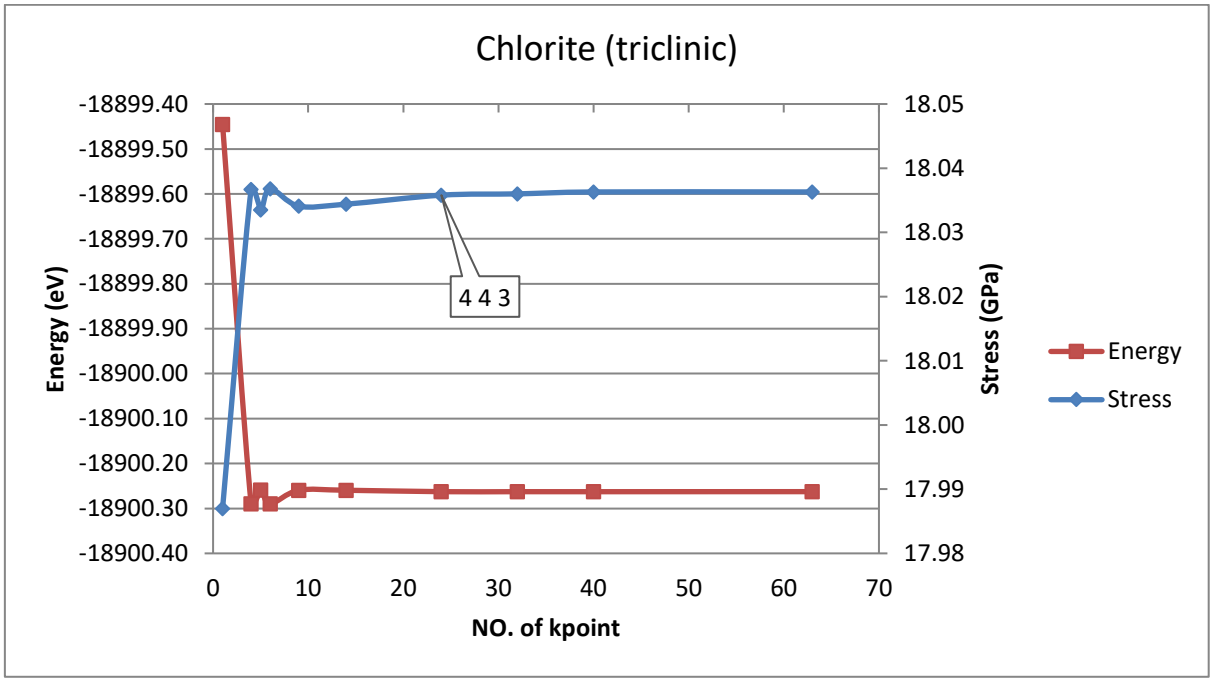

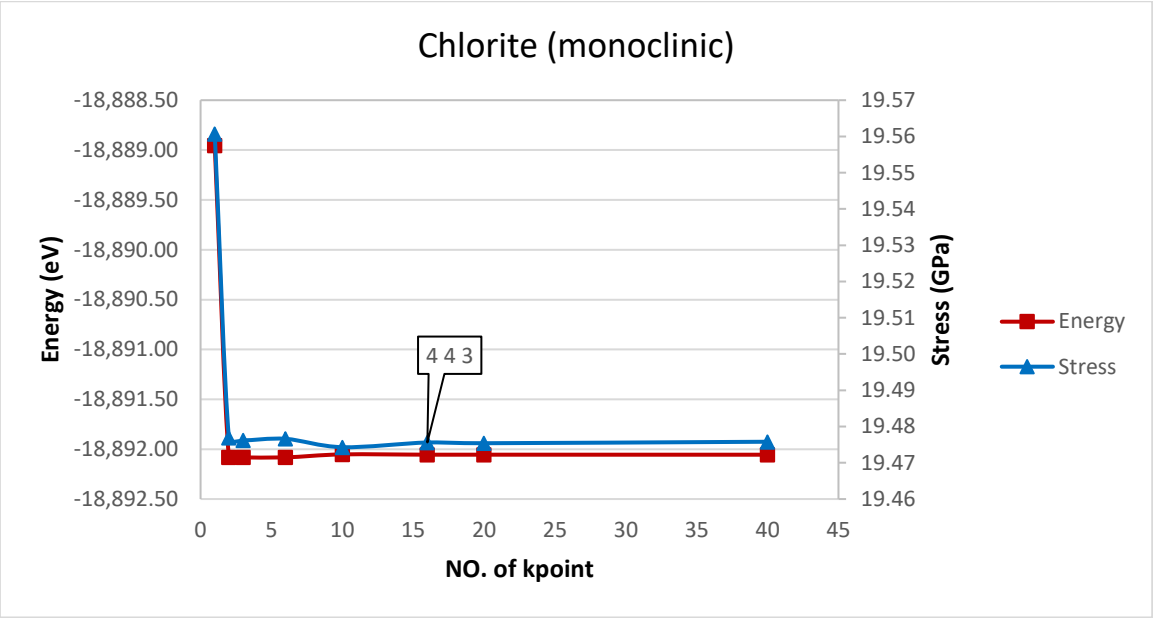
Chlorite (monoclinic)
-18,888.50
-18,889.00
-18,889.50
-18,890.00
-18,890.50
-18,891.00
-18,891.50
-18,892.00
-18,892.50
Energy (eV)
19.57
19.56
19.55
19.54
19.53
19.52
19.51
19.50
19.49
19.48
19.47
19.46
Stress (GPa)
0
5
10
15
20
25
30
35
40
45
NO. of kpoint
4 4 3
Energy
Stress

Appendix IV

The (primitive) unit cell structure and atomic coordinates of brucite and two types of chlorite (see 7.2.1) before and after geometry optimisation.

Brucite

Before GO

α = 90.000°

β = 90.000°

γ = 120.000°

a = 3.142Å

b = 3.142Å

c = 4.766Å

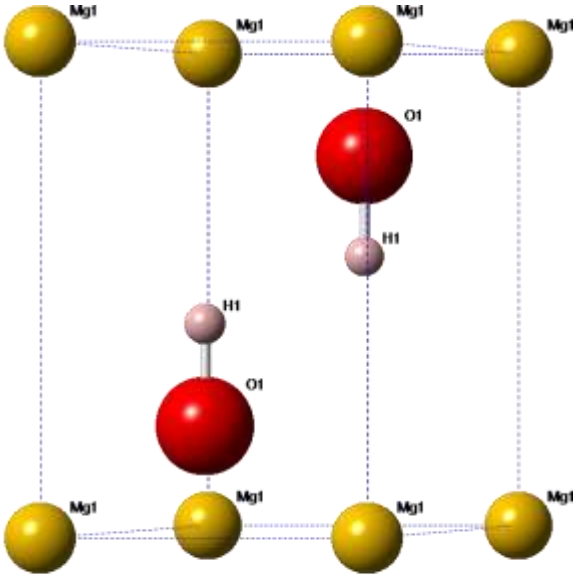

Element	Label	x	y	z
H	H1	0.3333	0.6667	0.4303
H	H1	0.6667	0.3333	0.5697
Mg	Mg1	0	0	0
Mg	Mg1	1	0	0
Mg	Mg1	0	1	0
Mg	Mg1	1	1	0
Mg	Mg1	0	0	1
Mg	Mg1	1	0	1
Mg	Mg1	0	1	1
Mg	Mg1	1	1	1
O	O1	0.3333	0.6667	0.2216
O	O1	0.6667	0.3333	0.7784

After GO

α = 90.000°

β = 90.000°

γ = 120.000°

a = 3.188Å

b = 3.188Å

c = 4.815Å

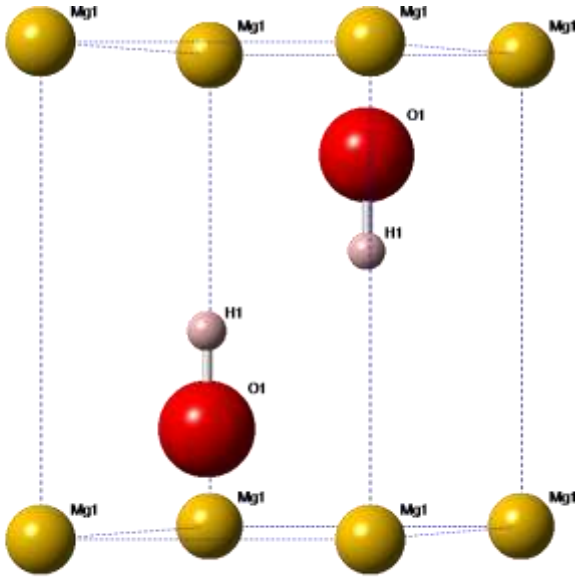

Element	Label	x	y	z
H	H1	0.333333	0.666667	0.4174
H	H1	0.666667	0.333333	0.5826
Mg	Mg1	0	0	0
Mg	Mg1	1	0	0
Mg	Mg1	0	1	0
Mg	Mg1	1	1	0
Mg	Mg1	0	0	1
Mg	Mg1	1	0	1
Mg	Mg1	0	1	1
Mg	Mg1	1	1	1
O	O1	0.333333	0.666667	0.216223
O	O1	0.666667	0.333333	0.783777

Chlorite: clinochlore (triclinic)

Before GO

α = 93.764°

β = 93.418°

γ = 120.034°

a = 5.329Å

b = 5.331Å

c = 14.381Å

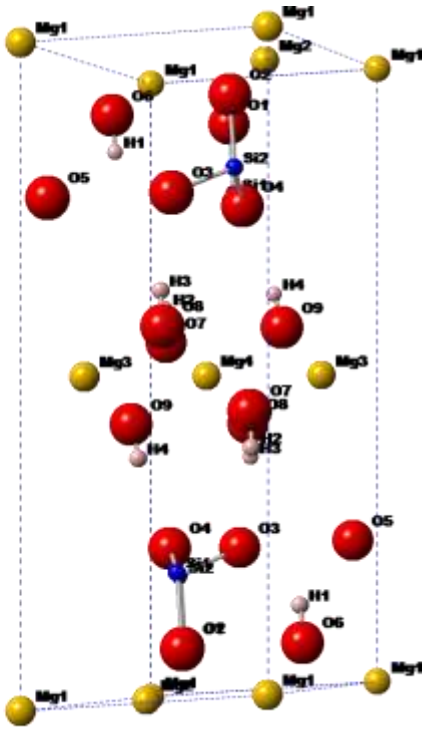

Fractional Coordinates (Before GO)

Element	Label	x	y	z
H	H1	0.6340	0.9600	0.8680
H	H1	0.3660	0.0400	0.1320
H	H2	0.8790	0.8770	0.6260
H	H2	0.1210	0.1230	0.3740
H	H3	0.7870	0.4550	0.3750
H	H3	0.2130	0.5450	0.6250
H	H4	0.5490	0.2370	0.6230
H	H4	0.4510	0.7630	0.3770
Mg	Mg1	0.0000	0.0000	0.0000
Mg	Mg1	1.0000	0.0000	0.0000
Mg	Mg1	0.0000	1.0000	0.0000
Mg	Mg1	1.0000	1.0000	0.0000
Mg	Mg1	0.0000	0.0000	1.0000
Mg	Mg1	1.0000	0.0000	1.0000
Mg	Mg1	0.0000	1.0000	1.0000
Mg	Mg1	1.0000	1.0000	1.0000
Mg	Mg2	0.6673	0.3345	1.0000
Mg	Mg2	0.3327	0.6655	0.0000
Mg	Mg3	0.1670	0.8334	0.5000
Mg	Mg3	0.8330	0.1666	0.5000
Mg	Mg4	0.5000	0.5000	0.5000
O	O1	0.9744	0.6406	0.9232
O	O1	0.0256	0.3594	0.0768
O	O2	0.3080	0.3074	0.9231
O	O2	0.6920	0.6926	0.0769
O	O3	0.8802	0.5480	0.2326

O	O3	0.1198	0.4520	0.7674
O	O4	0.5892	0.3904	0.7672
O	O4	0.4108	0.6096	0.2328
O	O5	0.0583	0.9211	0.7674
O	O5	0.9417	0.0789	0.2326
O	O6	0.6422	0.9752	0.9267
O	O6	0.3578	0.0248	0.0733
O	O7	0.8532	0.8538	0.5696
O	O7	0.1468	0.1462	0.4304
O	O8	0.8073	0.4763	0.4304
O	O8	0.1927	0.5237	0.5697
O	O9	0.5232	0.1930	0.5692
O	O9	0.4768	0.8070	0.4308
Si	Si1	0.9362	0.6017	0.8086
Si	Si1	0.0639	0.3983	0.1914
Si	Si2	0.2697	0.2686	0.8086
Si	Si2	0.7303	0.7314	0.1914

After GO

α = 93.437°

β = 93.118°

γ = 120.014°

a = 5.387Å

b = 5.385Å

c = 15.820Å

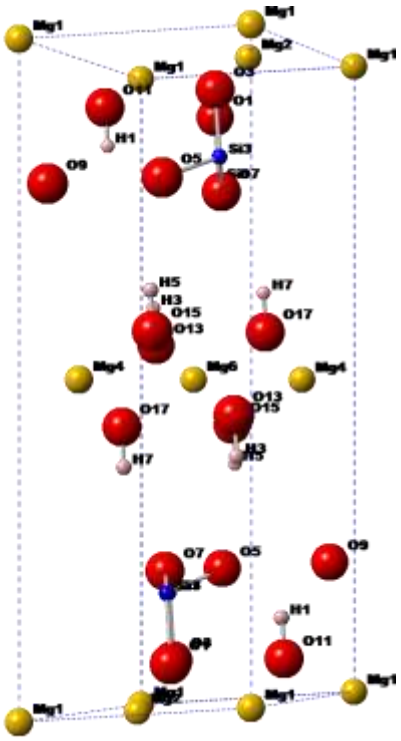

Fractional Coordinates (After GO)

Element	Label	x	y	z
H	H1	0.376444	0.045646	0.127570
H	H1	0.623556	0.954354	0.872430
H	H3	0.122850	0.122526	0.371729
H	H3	0.877150	0.877474	0.628271
H	H5	0.795152	0.459259	0.371799
H	H5	0.204848	0.540741	0.628201

H	H7	0.460077	0.795055	0.371692
H	H7	0.539923	0.204945	0.628308
Mg	Mg1	0.000000	0.000000	0.000000
Mg	Mg1	1.000000	0.000000	0.000000
Mg	Mg1	0.000000	1.000000	0.000000
Mg	Mg1	1.000000	1.000000	0.000000
Mg	Mg1	0.000000	0.000000	1.000000
Mg	Mg1	1.000000	0.000000	1.000000
Mg	Mg1	0.000000	1.000000	1.000000
Mg	Mg1	1.000000	1.000000	1.000000
Mg	Mg2	0.667008	0.333990	0.999852
Mg	Mg2	0.332992	0.666010	0.000148
Mg	Mg4	0.833496	0.166776	0.500034
Mg	Mg4	0.166504	0.833224	0.499966
Mg	Mg6	0.500000	0.500000	0.500000
O	O1	0.024161	0.358553	0.070511
O	O1	0.975839	0.641447	0.929489
O	O3	0.690014	0.689951	0.070503
O	O3	0.309986	0.310049	0.929497
O	O5	0.896341	0.565582	0.209695
O	O5	0.103659	0.434418	0.790305
O	O7	0.402669	0.578530	0.209564
O	O7	0.597331	0.421470	0.790436
O	O9	0.908904	0.071743	0.209238
O	O9	0.091096	0.928257	0.790762
O	O11	0.354927	0.022991	0.065987
O	O11	0.645073	0.977009	0.934013
O	O13	0.144774	0.143871	0.432986
O	O13	0.855226	0.856129	0.567014
O	O15	0.811029	0.477075	0.433044
O	O15	0.188971	0.522925	0.566956
O	O17	0.478141	0.810955	0.432954
O	O17	0.521859	0.189045	0.567046
Si	Si1	0.057880	0.393669	0.174703
Si	Si1	0.942120	0.606331	0.825297
Si	Si3	0.724315	0.726258	0.174694
Si	Si3	0.275685	0.273742	0.825306

Chlorite: clinochlore (monoclinic)

Before GO

α = 93.135°

β = 93.135°

γ = 119.985°

a = 5.384Å

b = 5.384Å

c = 15.646Å

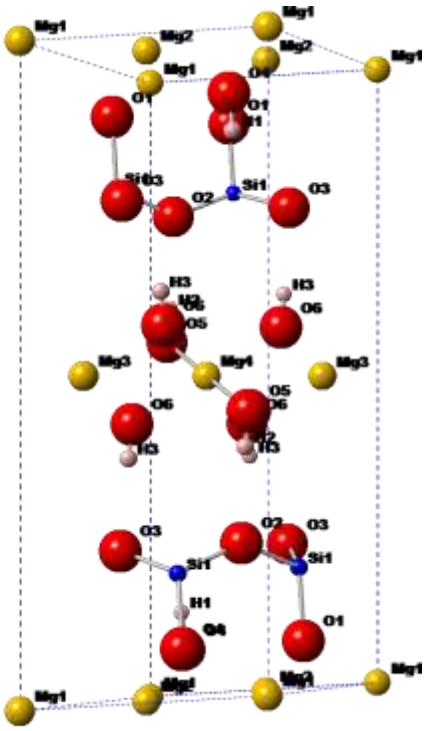

Fractional Coordinates (Before Go)

Element	Label	x	y	z
H	H1	0.285000	0.285000	0.866000
H	H1	0.715000	0.715000	0.134000
H	H2	0.820000	0.820000	0.622000
H	H2	0.180000	0.180000	0.378000
H	H3	0.812000	0.470000	0.378000
H	H3	0.530000	0.188000	0.622000
H	H3	0.188000	0.530000	0.622000
H	H3	0.470000	0.812000	0.378000
Mg	Mg1	0.000000	0.000000	0.000000
Mg	Mg1	1.000000	0.000000	0.000000
Mg	Mg1	0.000000	1.000000	0.000000
Mg	Mg1	1.000000	1.000000	0.000000
Mg	Mg1	0.000000	0.000000	1.000000
Mg	Mg1	1.000000	0.000000	1.000000
Mg	Mg1	0.000000	1.000000	1.000000
Mg	Mg1	1.000000	1.000000	1.000000
Mg	Mg2	0.667310	0.332690	0.000000
Mg	Mg2	0.667310	0.332690	1.000000
Mg	Mg2	0.332690	0.667310	0.000000
Mg	Mg2	0.332690	0.667310	1.000000
Mg	Mg3	0.166540	0.833460	0.500000
Mg	Mg3	0.833460	0.166540	0.500000
Mg	Mg4	0.500000	0.500000	0.500000
O	O1	0.642000	0.975200	0.923220
O	O1	0.975200	0.642000	0.923220
O	O1	0.358000	0.024800	0.076780

O	O1	0.024800	0.358000	0.076780
O	O2	0.210000	0.210000	0.232800
O	O2	0.790000	0.790000	0.767200
O	O3	0.258600	0.727400	0.767300
O	O3	0.727400	0.258600	0.767300
O	O3	0.741400	0.272600	0.232700
O	O3	0.272600	0.741400	0.232700
O	O4	0.309900	0.309900	0.926600
O	O4	0.690100	0.690100	0.073400
O	O5	0.848300	0.848300	0.569300
O	O5	0.151700	0.151700	0.430700
O	O6	0.803900	0.477500	0.430400
O	O6	0.522500	0.196100	0.569600
O	O6	0.196100	0.522500	0.569600
O	O6	0.477500	0.803900	0.430400
Si	Si1	0.604830	0.938290	0.808480
Si	Si1	0.938290	0.604830	0.808480
Si	Si1	0.395170	0.061710	0.191520
Si	Si1	0.061710	0.395170	0.191520

After GO

α = 93.459°

β = 93.459°

γ = 119.985°

a = 5.335Å

b = 5.335Å

c = 14.370Å

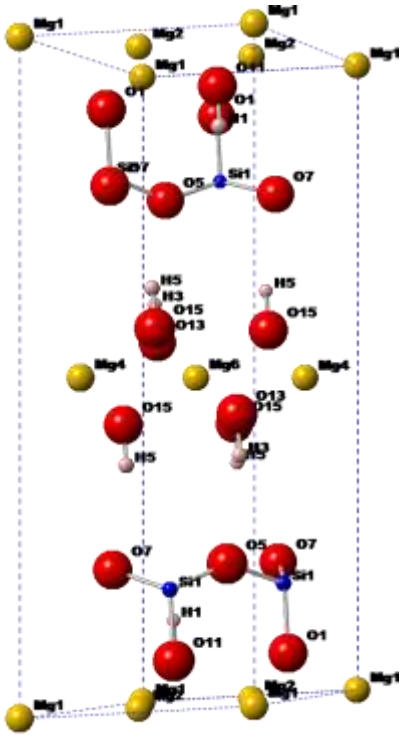

Fractional Coordinates (After GO)

Element	Label	x	y	z
H	H1	0.706386	0.706386	0.129076
H	H1	0.293614	0.293614	0.870924
H	H3	0.119799	0.119799	0.370024
H	H3	0.880201	0.880201	0.629976
H	H5	0.790436	0.456928	0.370527

H	H5	0.209564	0.543072	0.629473
H	H5	0.456928	0.790436	0.370527
H	H5	0.543072	0.209564	0.629473
Mg	Mg1	0.000000	0.000000	0.000000
Mg	Mg1	1.000000	0.000000	0.000000
Mg	Mg1	0.000000	1.000000	0.000000
Mg	Mg1	1.000000	1.000000	0.000000
Mg	Mg1	0.000000	0.000000	1.000000
Mg	Mg1	1.000000	0.000000	1.000000
Mg	Mg1	0.000000	1.000000	1.000000
Mg	Mg1	1.000000	1.000000	1.000000
Mg	Mg2	0.666678	0.333322	0.000000
Mg	Mg2	0.333322	0.666678	0.000000
Mg	Mg2	0.666678	0.333322	1.000000
Mg	Mg2	0.333322	0.666678	1.000000
Mg	Mg4	0.833411	0.166589	0.500000
Mg	Mg4	0.166589	0.833411	0.500000
Mg	Mg6	0.500000	0.500000	0.500000
O	O1	0.021562	0.355318	0.071286
O	O1	0.978438	0.644683	0.928714
O	O1	0.355318	0.021562	0.071286
O	O1	0.644683	0.978438	0.928714
O	O5	0.223948	0.223948	0.211910
O	O5	0.776052	0.776052	0.788090
O	O7	0.240180	0.731982	0.211662
O	O7	0.759820	0.268018	0.788338
O	O7	0.731982	0.240180	0.211662
O	O7	0.268018	0.759820	0.788338
O	O11	0.687745	0.687745	0.066840
O	O11	0.312255	0.312255	0.933160
O	O13	0.144967	0.144967	0.431929
O	O13	0.855033	0.855033	0.568071
O	O15	0.812144	0.478838	0.432432
O	O15	0.187856	0.521162	0.567568
O	O15	0.478838	0.812144	0.432432
O	O15	0.521162	0.187856	0.567568
Si	Si1	0.054147	0.387445	0.176606
Si	Si1	0.945853	0.612555	0.823394
Si	Si1	0.387445	0.054147	0.176606
Si	Si1	0.612555	0.945853	0.823394